The Deposition, Characterisation and Biocompatibility of Hydroxyapatite and Silicon Doped Hydroxyapatite Thin Film Coatings for Orthopaedic Applications

Samuel Christopher Coe, BSc (Hons)

Thesis submitted to the University of Nottingham for the Degree of Doctor of Philosophy, April 2008

Acknowledgements

I would like to thank Prof. David Grant, Dr. Colin Scotchford and Dr. Gavin Walker for their continued help and expertise throughout this project. Further thanks should go to all the technical staff whom have assisted me to operate equipment correctly and safely with particular thanks to Keith Dinsdale, George Anderson, Martin Roe, Nigel Neate, Julie Thornhill, Tom Buss, Rory Screaton and Graham Malkinson.

Many thanks go to Teer Coatings Ltd. for financial support and to Dennis Teer and Sue Field for expertise in the field of thin film deposits. Special mention is made to Joanne Hampshire who patiently and tirelessly produced large numbers of samples for this project.

The work of Dr. Chris Jeynes at the Surrey Ion Beam Centre is greatly acknowledged with regard to the collection and analysis of data for ion beam compositional analysis of thin film samples.

I would like to express my great appreciation to my friends and family who have supported me emotionally and financially throughout my studies at university. Particular mention is made to Dr. Katie Rollins who has continually encouraged me and pushed me in the right direction. Finally, I would like to express my gratitude to my parents, Dr. Caroline Saffell and Mr. Chris Coe for their constant belief in me, whatever my choice in life.

Abstract

Silicon doped hydroxyapatite (SiHA) could be used as a thin film coating on load bearing bone implants to provide a bioactive layer enabling bone to form a direct bond with the implant/bone interface thus increasing implant lifetime by lowering the chances of aseptic loosening. This study has been undertaken to investigate silicon additions to RF magnetron sputtered hydroxyapatite (HA) thin films. Detailed characterisation was carried out on SiHA thin films to establish the structural, chemical, mechanical and compositional properties. Silicon content was altered by adjusting the power density applied to silicon targets in a co-deposition process resulting in SiHA films containing 0.0, 1.8, 4.2 and 13.4 wt.% silicon. All as-deposited thin films were found to be amorphous. After annealing at 600°C in flowing argon for 2 h, it was found that films exhibited a single phase HA structure. The addition of silicon inhibited HA crystallite growth and acted to lower the stability of HA films in aqueous solutions. The 13.4 wt.% SiHA thin film did not recrystallise until a heat treatment at 800°C.

From the work presented here, it is proposed that, in post-plasma-deposited heat treated films, silicon substitutes as silicate species into the HA lattice. As-deposited silicon containing thin films were found to be amorphous and have a polymeric silicate configuration, suggesting that, silicate groups may be randomly distributed throughout the amorphous film. After post-deposition annealing silicon containing films were in a monomeric state suggesting silicate groups had substituted for phosphate tetrahedra in the HA lattice. Furthermore, an HA-like phase was found to be present. Contrary to these findings, FTIR analysis did not manifest any silicate-based bands. This may, however, be due to the fact that technique used only samples a very small amount of material and, due to the low doping quantities of silicon in the HA films. Furthermore, Ca/P ratios consistently differed from the stoichiometric value of HA (1.67). This combined evidence raises

the question of whether the post-deposition heat-treated films have a true HA-like structure. More work is required in order to truly understand the structures present in heat-treated SiHA thin films.

HA thin film composition is commonly measured in terms of the Ca/P ratio. Energy dispersive X-ray analysis (EDX) and XPS were evaluated in terms of accuracy in conjunction with Rutherford backscattering spectroscopy (RBS) to measure the Ca/P ratio of HA thin films to establish the most appropriate technique for accurate compositional analysis. This was was found to the RBS, achieving an accuracy of within 2 %, with EDX averaging 8 % and XPS ranging from 25 - 42%. It was concluded that XPS gave such large differences in values because the top few atomic layers of thin films was of a different composition than the bulk of the coating.

A Human osteoblast cell (HOB) model was used to establish the *in vitro* cellular response of SiHA thin films. Initially, HA and SiHA thin films annealed at 600°C were compared. Cells attached and proliferated well on HA surfaces compared to SiHA surfaces, however, improved cell growth was seen with increasing silicon content. Dissolution studies showed that SiHA thin films were highly unstable in cell culture media and it is thought that the films dissolved, and where cell adhesion and growth did occur it was because cells adhered to the titanium substrates beneath the films. This was then compared with HA and SiHA thin films annealed at 700°C. No significant difference was found between the two surfaces in terms of cell growth or protein expression indicating that silicon content and crystallinity play an important role in the cellular response of SiHA thin film.

Table of Contents

List of Abbreviations

AB	Alamarblue™
ACP	Amorphous Calcium Phosphate
ADMIDAS	Adjacent metal ion dependant adhesion site
ALP	Alkaline phosphatase
BPM	Balanced Planar Magnetron PVD rig
Ca/P	Calcium phosphorus ratio
CPTi	Grade 1 commercially pure titanium
DC	Direct current
DMEM	Dulbecco's modified eagles' medium
ECM	Extracellular matrix
EDX	Energy dispersive X-ray analysis
EDX_n	EDX performed with GaP and wollastonite standard profiles
EDX_s	EDX performed with HA P120 standard profiles
EELS	Electron energy loss spectroscopy
ERD	Elastic recoil detection
FA	Fluoroapatite/Fluorohydroxyapatite
FBS	Foetal bovine serum
FIB	Focused ion beam
FTIR	Fourier transform infrared spectroscopy
HA	Hydroxyapatite
HBSS	Hank's balanced salt solution
HOB	Human osteoblast cell
IgG	Immunoglobulin G
IgM	Immunoglobulin M
IMFP	Inelastic mean free path

LIMBS	Ligand associated metal binding site
MIDAS	Metal ion dependant adhesion site
NHS	National Health Service
PIXE	Particle induced X-ray emission
PLA	Poly(lactic acid)
PLGA	Poly(lactic-co-glycolic acid)
PMMA	Poly(methylmethacrylate)
PO_4^{3-}	Phosphate ions
PTFE	Poly(tetrafluoroethylene)
PTH	Parathyroid hormone
RBM	Rat bone marrow cells
RBS	Rutherford backscattering spectroscopy
RF	Radio frequency
RGD	Arg-Gly-Asp attachment site
RHEED	Reflective high energy electron diffraction
RSF	Relative sensitivity factors
SAM	Self-assembled monolayer
SEM	Scanning electron microscopy
SiHA	Silicon doped Hydroxyapatite
SiO_4^{-4}	Silicate ions
α or β TCP	α or β- Tricalcium phosphate
TCP	Tissue Culture Plastic
TEM	Transmission electron microscope
TiO_2	Titanium dioxide (Rutile)
TJR	Total joint replacement
THR	Total hip replacement
TKR	Total knee replacement
UDP	Uniform deposition and plasma systems
UHMWPE	Ultra-high molecular weight poly(ethylene)

XPS	X-ray photoelectron spectroscopy
XRD	X-ray diffraction

1. Introduction

The field of biomaterials is a worldwide multi-billion dollar industry. Just under a decade ago, the lives of over 20 million patients were sustained, supported or significantly improved by biomaterials. It is estimated that this figure increases at 10 % per year. Worldwide, the market of initial and follow-up of organ replacement and prostheses exceeds $ 300 billion US dollars per year and represents between 7-8 % of total worldwide healthcare spending. In the United States alone, the costs of therapies enabled by organ replacement technology exceed 1 % of the gross national product [1]. These figures highlight the importance of biomaterial development. Research in this area is constantly ongoing to enhance current and concept materials for future generations, improving the longevity of implants and the quality of the patient's life. This area of materials science is characterised by medical needs, materials characterisation and design, basic research, advanced technological development, patient expectation, ethical considerations, industrial involvement and federal regulation [2]. Such multidisciplinary research requires expertise and techniques from a wide variety of subjects such as materials science, chemistry, molecular and cell biology, mathematics, engineering, biomechanics, computer modeling, manufacturing, medicine and genetics. Biomaterial devices are available for joint and limb replacements, artificial arteries and skin, contact lenses, and dentures which aim to replace damaged or diseases tissues. However, prostheses may also be used for enhancement of the body of which the most well known is the breast implant.

One of the many issues faced with regard to foreign objects being inserted into the body is the reduction or elimination of adverse effects caused by a stimulated immune response. Many such effects can be reduced with careful material selection; however the current trend is to use the response of the body to improve

the initial success of implant materials which could lead to a longer device lifetime reducing the need for revision surgery. In the case of load bearing implants, such as in total hip replacement (THR) or total knee replacement (TKR), further complications such as the mechanical requirements of the material to bear load can reduce the number of materials available. It is often the case that materials that possess the mechanical properties are not always the most biologically compatible in these sites. A possible solution is to coat mechanically sound devices with materials which will be more biologically favorable. A considerable amount of work has already gone into this area but many problems such as selection of the most appropriate correct coating technique is required to control properties such as coating adhesion, composition and topography which may ultimately influence the biological response of the surface.

1.1. Joint Replacement

In England between 1991 and 2000 the incidence of primary THR increased by 18% from 31,211 to 38,425, while the incidence of revision THR more than doubled from 3678 in 1991 to 9507 in 2000. Primary TKR doubled and revision TKR increased by 300% in the period [3].

In 2005 the National Joint Registry (NJR) was formed, which is now one of the largest of its kind in the world, collating THR and TKR data for England and Wales. Table 1-1 shows the most recent figures for 2006 and 2007. This illustrates that in the England and Wales alone there is a large number of surgeries thus highlighting the importance of the need for appropriate materials to be used for these devices to ensure long term success.

NHS	2006	2007
Total completed operations	93022	92975
THR	45751	44614
TKR	47466	48524

Independent		
	2006	2007
Total completed operations	35251	37299
THR	18919	19037
TKR	16699	18532

Table 1-1. Total number of THR and TKR in England and Wales for 2006 and 2007 for the NHS and the private sector recorded by the National Joint Registry (NJR) [4].

Joint replacement is required when a natural joint fails either due to trauma or disease, requiring surgery to restore some if not all function to the affected area. Successful replacement of fingers, ankles, shoulders, elbows, knee and hips have all been carried out. The current study is primarily concerned with replacement of the knee or the hip joints; however the work here could easily be adapted for other areas of the body. The knee and hip joint is commonly replaced when the articular cartilage between the joint surfaces wears away causing joint gap narrowing leaving bone on bone contact and resulting in considerable discomfort and pain for the patient. Clinically this presents as a loss of mobility impairing simple every day functions such as walking or dressing oneself. The most common cause of wear in the joint is due to arthritis. There are over 200 types of arthritis but the most relevant in TJR are osteo- and rheumatoid arthritis. Osteoarthiritis is the most common of the two and is caused by normal wear and tear of the joint. In the knee the cartilage gradually thins and roughens while the bone thickens. Bone at the edge of the joint grows outwardly forming bony spurs called osteophytes. The synovium swells and an increase in synovial fluid occurs. The joint gradually changes shape and becomes disfigured causing immobility. In smaller joints the body can repair itself making smaller joint replacements less common in joints such as fingers. However, in larger joints self repair is not as

successful requiring surgical intervention. Rheumatoid arthritis is a chronic autoimmune disease which causes inflammation in the cartilage of patients. It is three times more common in women than men and may start at any age with onset typically occurring between 40 to 65 years of age. B-lymphoctyes are triggered which produce immunoglobulin G and M (IgG, IgM) proteins which are deposited in the tissue. This leads to the activation of the complement cascade and the recruitment of phagocytes. This further exacerbates inflammation leading to edema, vasodilation and infiltration of activated T-cells. In chronically affected joints, the delicate synovium thickens and develops many villous folds. The synovial lining cells produce various secretions, including IL-1 and TNF-α which aid to stimulate collagenase and stromelysin sysnthesis, which contribute to cartilage destruction, osteoclast-mediated bone absorption, synovial inflammation, and prostaglandins (which potentiate inflammation). Fibrin deposition, fibrosis, and necrosis are also present. Through these inflammatory mediators, hyperplastic synovial tissue (pannus) erodes cartilage, subchondral bone, articular capsule, and ligaments.

Replacement creates a new surface significantly reducing chronic pain and allowing mobilisation of the patient commonly within 24 h of surgery dependant on joint and fixation type. Implant lifetime is about 10-15 years but this is predominantly dependant on patient lifestyle. If the implant fails a revision surgery is required, which involves removal of the old device and replacing it with a new prosthesis. The average age of patients undergoing such initial surgeries are commonly between 60-80 years of age. In the more elderly, the chances of a revision surgery are lowered because the patient is unlikely not to outlive their implant.

Risks and complications associated with this type of joint replacement may lead to premature failure of the joint. If the joint becomes infected it may need to be

removed and another joint inserted, but this is uncommon only occurring in 1-2 % of surgeries, due to precautionary procedure such as the use of antibiotics, given before and after the operation and extra aseptic precautions are taken in orthopaedic operating theatres to reduce this risk. Complications directly related to the prosthesis such as loosening, dislocation, wear and breakage are all possible mechanisms of failure. Loosening is the most common failure mechanism in joint replacement. This causes pain to the patient and eventually will require a revision surgery. Dislocation of the joint tends to occur soon after the operation if at all. In this instance the orthopaedic surgeon will relocate the joint without further problems for the patient. As with any moving surface, friction is created leading to wearing of the joint. This is a slow process, however, depending on the articulating surfaces (e.g. metal on metal or metal on polymer) different rates will occur. It has been shown that wear particles migrate along implant interfaces leading to osteolysis which is the major cause of aseptic loosening particularly around the acetabular component [5]. A great deal of work has been carried out in this area to understand the mechanisms behind particle induced aseptic loosening. Particles migrate along the bone/implant interface inducing the formation of a fibrous membrane. This fibrous layer may act as a pathway for implant debris [6]. Aseptic loosening is most common in cemented devices, however, may also occur in uncemented components. Unlike cemented prostheses, uncemented implants do not result in a fibrous capsule reducing the migration of wear particle. However, if osteolysis occurs the result is expansive and destructive lesions, which typically balloon into the trabecular bone of the illium. Even so, the failure rates of cemented implants are significantly higher than uncemented devices [7]. Therefore, recent work has tended to focus on uncemented implants.

In younger patients who require a total joint replacement (TJR), and with increasing population life expectancy, it is probable that a revision surgery will be

required. In the UK over 45,000 THR are performed every year and it is estimated that 20 % of all THR require revision after 20 years [8]. This poses many problems; the quality and density of bone surrounding an implant is often reduced over time, leading to increased bone fragility lowering the chance of a successful re-operation. In addition revision surgeries are more expensive than the first procedure as patients require another operation that leads to increased recovery time and surgeon expertise. One line of thought is that by enhancing the initial response of the implant, this could lead to increased longevity of implant by reducing loosening lowering the need for revision surgery.

1.2. Biomaterials Terms and Definitions

The field of biomaterials contains many terms which are specific to this area of work. Therefore a brief explanation of two commonly used terms has been compiled.

"A biomaterial is a nonviable material used in a medical device intended to interact with biological systems" [9].

Biomaterials are often referred to in terms of their 'biocompatibility'. Equally this has been defined as:

"Biocompatibility is the ability of a material to perform with an appropriate host response in a specific application" [9].

1.3. Historical Background

Biomaterials have been in use for over 2000 years [2] and even before the pre-Christian era. Throughout history materials have been found to be used with the body to replace lost function. The Aztecs, Chinese and Romans commonly used

gold in dentistry. Wooden teeth and glass eyes have also been discovered throughout the course of history. In 1860 Lister became a pioneer for aseptic surgery which significantly improved the survival rate of many patients but notably compound fracture victims. However, it was not until the 1900s when the use of biomaterials really expanded with the use of bone plates and biomaterials for joints. During World War II it was found that poly(methylmethacrylate) (PMMA) did not provoke an immune response when shrapnel became implanted in soldier's bodies. In the 1960s Charnley revolutionised hip replacements by using stainless steel, PMMA and ultra-high molecular weight polyethylene (UHMWPE) for the use of a hip arthoplasty. Even so, it was not until 1975 that the Society of Biomaterials was formed. This organisation aimed to bring together the larger number of disciplines listed at the beginning of this chapter. The biomaterials world has historically concentrated on replacement and, in more recent times, enhancement, but as we begin the 21st century the discipline looks set to become a regenerative science [10]. Unfortunately the idea of implanting a regenerative material as a long term solution into load bearing bones is currently not clinically viable and so we must concentrate on improving current solutions until this time arises.

1.4. Classes of Biomaterials

Materials used for bone applications are categorised into four groups: autografts, allografts, xenografts and alloplastics.

Autografts involve removal of tissue from one site and transferring it to another within an individual. A common example of this is skin grafts in which skin layers may be transferred to a site of trauma or disease to restore function to that area. For bone tissue autografts, common sites available for donation are the iliac crest, tibia and ribs. Bone autografts have the advantage of being osteogenic,

osteoinductive and osteoconductive and do not illicit a host immune response. Drawbacks of using this type of graft are a second surgical procedure is required to prepare the graft with related donor site morbidity and only limited amounts of tissue may be removed. For the patient, this generally means increased time in surgery, increased morbidity, longer recovery time and increased scarring.

Allografts, which are also known as homografts, are the transplantation of tissue from one individual, either alive or deceased, to another within a species. The donated tissue is then processed and prepared to remove for implantation and used within a finite time period. Allografts are an attractive option when compared to autografts as they only require a single surgical procedure per patient, reducing discomfort, recovery times and post-operative problems such as infection. Furthermore, increased availability allows room for error. Unfortunately significantly inactivating pathogens in the donated tissue and reducing foreign body response poses a great challenge for scientists developing these tissues.

Xenografts are the transferring of tissue from one species to another. Common examples of this include porcine and bovine heart value transplants into humans which have proved successful. The advantages are similar to allographs in that there is an increased donor number. However, issues related to pathogens associated with the implant and trans-species infection has reduced the potential offered by these types of biomaterials. Moreover, ethical issues and religious views can further limit xenograft use.

Due to restrictions of other donor types, researchers have begun to give increasing attention to alloplastics. These materials are synthetically produced devices which can be manufactured into many shapes and sizes out of an almost infinite number of material or material combinations. The advantage of this graft type is that there is unlimited resource. In addition pathogen contamination does

not pose a serious threat, as these materials should be designed to allow sterilisation. Disadvantages include unwanted foreign body immune response upon implantation. The human body is a complex system and often alloplastics are very simplified replications of single components of this system. This means the device may not always accurately mimic the mechanical properties, composition or role of the replaced tissue. This study in part aims to address some of these principal issues.

1.5. Current Materials in Joint Replacement

Current joint replacement methods adopt a variety of materials depending the procedure, patient and surgeon. An example of a common joint replacement is the hip joint replacement system, is shown in figure 1-1.

Figure 1-1. A selection of hip implant prostheses showing individual femoral and acetabular components. Taken from [11].

The device consists of two components, the femoral shaft and the acetablular cup, each can be manufactured from a variety of materials. Materials relating to the hip and other joint replacement devices are discussed in this section.

1.5.1. Metals

Metals have been the material of choice throughout the history of joint replacement. While ceramics and glasses can have exceptional compressive properties, only metals and some composite materials possess the mechanical strength required to withstand the high loads imposed in uniaxial directions in load bearing joints. Many metals and alloys have been used, each with slightly different properties and biological response. Disadvantages in selecting metals include harmful ion release [12] and a lower quality biological response compared with other types of materials. Most commonly, the long femoral element is made of Co–Cr alloys or Ti alloys. There is no agreement as to which material is better suited for this purpose with both having advantages over the other. The cup component is made up of alumina or zirconia ceramic, UHMWPE, polytertrafluoroethylene (PTFE) or Co–Cr alloy [8]. The ball component, which fits into the cup, has conventionally been made of metals or ceramics mentioned above. Various material systems have been investigated such as metal on polymer, metal on metal and ceramic on ceramic joints. Problems associated with metal on polymer surface have already been discussed in section 1.1. Metal on metal surfaces create wear particles, however, these are smaller in size and less frequent than polymer wear particles. An advantage is that these particles can be considered less harmful than polymer particulates; although concerns have been raised about the production of metallic ions which are found in surrounding tissues. Ceramic on ceramic implants, however, have a very low wear rate without the production of metallic ions. In some instances these surfaces have been known to fracture. Clearly material selection is an ongoing problem that requires thought and care. Metallic implants are significantly stiffer than bone which can lead to stress shielding. The regenerative and remodelling processes in bone are in part triggered by loading, i.e. bone subjected to loading or stress regenerates and bone not subjected to loading results in atrophy. The concept of stress shielding is further discussed in section 2.2.5. Ti6Al4V is often the metal of choice

due to its relative low weight, low corrosion potential, lower elastic modulus and high strength. However, while titanium is osteoconductive, meaning bone can remodel along the interface of this material, it cannot directly bond to bone which can result in loosening of the prosthesis. A potential solution to this problem is to coat the metal with a material which can form a direct bond with bone thus reducing the chance of loosening. The focus of this thesis aims to look at potential solutions to this problem by investigating hydroxyapatite (HA) coatings on titanium implants. The coating of HA onto implant materials is not a new idea, however, problems are associated with coatings currently used clinically. HA coatings are commercially plasma-sprayed, however, the resultant coatings often are poorly adhered and commonly fail at the coating to implant interface. This thesis looks to address such problems by investigating alternative coating methods.

1.5.2. Polymers

Polymers have the lowest mechanical properties, in terms of strength and elastic modulus, of all the material classes. This severely limits their use to low wear surfaces. In medicine, common polymers used are: acrylic, nylon, silicone, polyurethane, UHMWPE, and polypropylene which are used for medical tubing, grafts, blood vessels, breast, ear, chin and nose implants. Polymers are commonly used as a replacement acetabular cup and utilises PMMA bone cement to hold the prosthesis in place. Previously, acetabular cups were manufactured from metals, however, the high friction coefficient of metals led to surgeons reverting back to polymer materials. Acetablular cups are most commonly made from UHMWPE although recently some ceramic materials have also been used which possess lower wear rates. Significant concerns are associated with the effect of UHMWPE wear particles which may lead to adverse effects in the body such as loosening of the device ultimately leading to failure. Since the late 1980s, large diameter

second generation metal/metal surfaces have attracted the attention of researchers and surgeons. A larger diameter reduces the friction of the joint reducing metal wear, however, the joint must still be small enough to fix comfortably in the patient without comprisming joint stiffness. Volumetric wear on polymer/metal (17.9 mm^3 $year^{-1}$) surfaces is significantly higher than metal/metal surfaces (0.03 mm^3 $year^{-1}$) [13]. Metal/metal surfaces also have the advantage of producing smaller (<0.1 μm) wear particles as opposed to UHMWPE wear particles, which are in the range of 0.5 to 10 μm, and have been shown to induce the secretion of interlukin-6 in macrophages which lead to osteolysis. However, problems associated with metal ion release still raise concerns, and this has been shown with elevated chromium and cobalt levels in blood serum and urine. Such effects may lead to inhibition of bone growth, hypersensitivity and carcinogenicity [13].

1.5.3. Ceramics and Glasses

Ceramics used for orthopaedic implant materials include HA, tricalcium phosphate (α- or β-TCP), alumina, Bioglass™ and other bioactive glasses. Conventional engineering ceramics such as alumina were initially attractive biomaterial options due to their excellent properties of high strength, good biocompatibility and stability in physiological environments. Due to lack of chemical bonding between sintered alumina and bone tissue, its applications are limited. However, alumina can be polished to a high surface finish and possesses excellent wear resistance and therefore is often used for wear surfaces in joint replacement prostheses. Femoral heads for hip replacements and wear plates in knee athroplasties have been fabricated using alumina. In the last 30 years, a move towards ceramic materials which bone tissue can achieve a direct bond with, such as HA and Bioglass™ have attracted the attention of biomaterial researchers. Due to the brittle nature and low strength properties compared to metallic materials this

often restricts bioceramics to non-load bearing sites. By coating ceramic materials on metal implants a combination of mechanically sound properties and bone bioactivity can be achieved.

1.5.4. Composites

Bone is a composite due to the incorporation of different materials, which is, a combination of organic and inorganic material. Therefore, it is logical that biomaterial scientists concentrate their efforts to mimicking the composition of bone tissue. Bone repair composite materials can be classed into three categories, functionally graded composites, polymer-ceramic composites and biomimetic composites or composites with biological macromolecule inclusions [8]. Functionally graded composites are continuously graded in composition from one side of the material to the other giving different properties for each end of the material. This has the advantage of combining bone bonding ability with mechanical functionality for a specific site within the body. Graded compositions of fluorapatite and β-TCP have been used to combine the bioactive properties with bioresorbable ability repectively [14]. Other examples include composites combining the bioactivity of HA with the mechanical properties of titanium in a graded composite [15]. These composite materials have proved to be a promising area within biomaterials research, however, more work is needed to approach the elastic modulus of bone as these materials currently well exceed these values. The second class of composite in joint repair is polymer-ceramic composites. Polymers generally have low elastic moduli but are lower than that of bone thus making them attractive materials for the use of bone repair. However, their strength and stiffness is often a limiting factor. Therefore ceramic and polymer materials have been combined, potentially overcoming this problem. Polymers such as poly(lactic acid) (PLA) are commonly combined with HA or calcium carbonate which are loaded at high weight percentages to improve mechanical properties [16, 17].

Restrictions of mechanical strength limit the clinical use of these materials. Biomimetic composites or biologically impregnated composites are materials that aim to mimic bone in composition and biological function. One complex example composite system is nano-carbonated hydroxyapatite/collagen/poly(lactic-co-glycolic acid) (PLGA). This composite was manufactured in order to tailor bioresorption properties [18] with the individual components being specifically chosen to alter these properties, however they possess the additional advantage of being materials that could be easily broken down by the body after degradation. Other, non-resorbable composite structures have also been developed such as poly(ether-ether-ketone) (PEEK)/carbon fibre (CF). This material has shown increased wear performance compared to UHMWPE and HA/high density polyethylene (HDPE) but also encourages an enhanced bone response.

1.6. Project Objectives

While many material systems offer attractive properties, as discussed above, HA has attracted much attention due to its excellent bioactive ability for the application of bone repair and bone replacement. Due to reduced mechanical performance in comparison to metals, HA has been restricted to non-load bearing implants. This problem can be overcome by applying an HA coating onto metallic materials with superior mechanical strength and stiffness. Currently plasma spraying is the only commercial coating process suitable for this process, but coatings are compromised by the inclusion of undesired calcium phosphate phases leading to bioresorption and variable tissue response. In addition, these coatings are often poorly bonded to the metallic substrates leading to failure in the form of cracking at the coating/substrate interface. Physical vapour deposition (PVD) offers an attractive alternative resulting in dense, defect free, well adhered single phase coatings with controllable deposition parameters.

In the last decade it has been found that small weight percent additions of silicon to HA can be used to enhance the initial response between bone tissue to HA. A large amount of research has been concerned with bulk materials, however, only recently has the attention of researchers moved to the use of these doped materials for coatings.

The aims of this project were:

- Optimise the deposition process to allow for good quality and controllable HA coatings.
- To determine the effect of post-deposition treatments on coatings and a range of substrates.
- To investigate the effect of silicon dopants on coating structure, composition and mechanical properties.
- Characterise the chemical, compositional, structural and mechanical properties of HA and doped HA thin films.
- To determine the *in vitro* biological response of osteoblast-like cells to coating surfaces to identify compositions and treatments that may be desirable for *in vivo* testing.

2. Literature Review

2.1. Introduction

This chapter gives detail of literature currently available regarding bone and bone cells, HA and silicon doped HA (SiHA) materials for bone repair applications. Each section is summarised below:

Section 2.2. reviews the well established literature of bone growth and development with a particular focus on long bones in the leg which will be most relevant to TKR and THR operations. Section 2.3. introduces the material hydroxyapatite (HA) which is reviewed with regard to its crystal structure, biocompatible properties and use for bone replacement applications. These uses include coatings and thin films on implantable materials designed for total hip and total knee arthoplasties and other load bearing sites where the biocompatible nature of the device can be improved without compromising mechanical properties. The characterisation of HA and calcium phosphate thin films with regard to compositional analysis will also be provided. The use of three techniques is discussed and how their accuracy and ability to analyse thin film samples can affect values, such as the calcium to phosphorus ratio. This ratio has been shown to be important when considering the biological response of cells and therefore careful determination of such values is vital to the prediction of implant material success. Section 2.4. describes the role of silicon in the body and more specifically in bone development, highlighting its importance as a trace element which maybe essential for ossification. Details have been given of how this may be incorporated into materials such as HA to enhance its bioactive properties leading to the potential success of materials for implantation *in vivo*. Section 2.5. looks at silicon substituted or doped HA materials, how they are characterised and their *in vitro* and *in vivo* cellular response. Section 2.6. investigates HA as a coating material

and briefly summarises the advantages and disadvantages of various coating techniques. Section 2.7. provides a detailed background regarding the phenomenon of sputtering and how it may be applied in practice to produce thin films for use as biomaterial surfaces with an emphasis on HA and silicon doped HA films. The properties and biological response of such films are then discussed and how improvements could be made to these material systems to enhance their ability to form a direct bond with bone. Section 2.8. discusses HA thin film deposits in terms of composition, crystal structure and morphology. The properties and bone cell response to HA thin films are compared for *in vitro* and *in vivo* applications. Section 2.9. introduces silicon doped HA thin films deposited by RF magnetron sputtering. Details of deposition techniques, film characterisation and cellular response is provided. Finally, section 2.10. will give a summary of all the literature drawing conclusions and assessing possible future work required in the field of silicon doped HA thin films.

2.2. The Structure and Growth of Bone

To manufacture an implantable device that will be inserted into a bony area it is first important to understand the anatomical structure, histology and mechanical properties of bone. Bone provides all higher vertebrates with a specialised support system which protects internal organs and facilitates muscle action and body movement. Bone can be considered as an organ which can repair and remodel itself to accommodate the mechanical demand imposed on it, making it one of the most metabolically active tissues in the body.

2.2.1. Bone Anatomy and Histology

2.2.1.1. Bone Composition and Microstructure

Bone is a complex material with many levels of organisation. The composition of bone differs depending on species, age, dietary history [19] and the presence of disease [20], however, general values can be given. The main constituents are collagen (20 wt.%), calcium phosphate (69 wt.%) and water (9 wt.%) [21]. Other organic materials exist in small quantities (1-2 wt.%). These organic components are made up of 58 wt.% proteins, 40 wt.% lipids and trace amounts of sugars, citrate and lactate ions [22]. Collagen fibres, predominantly type I, are considered to be the matrix and may vary from 100 to 2000 nm in diameter. Stiffness is supplied by bone mineral crystals, which were previously thought to be pure hydroxyapatite (HA) but are now referred to as apatite due to unique acid-phosphate groups [23]. These mineral crystals, which are approximately 20-40 nm long and 1.5-5 nm thick [24], are deposited parallel to the collagen fibres. Figure 2-1 shows the hierarchical structure of bone from the macrostructure down to the apatite and collagen nano- and sub-nano structures.

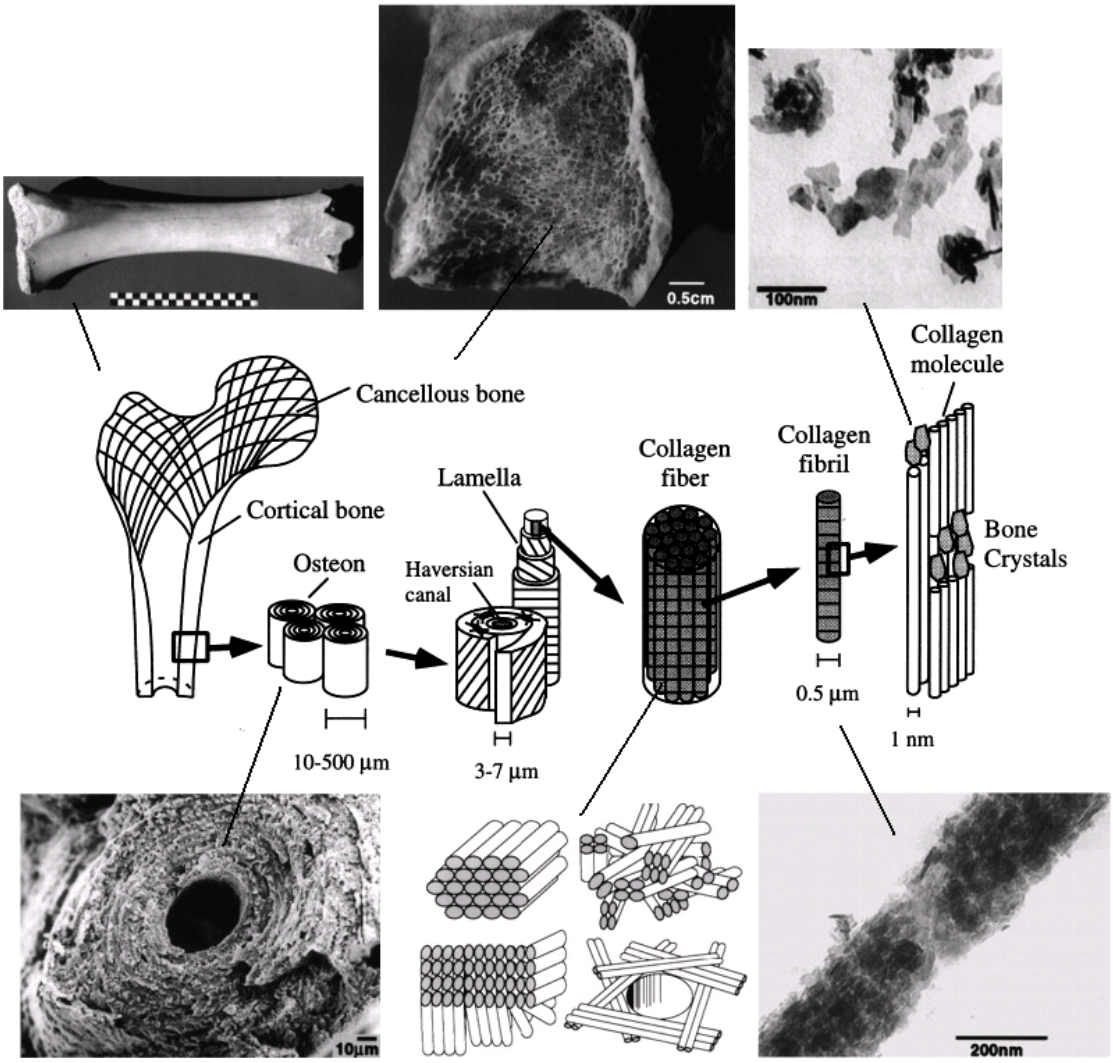

Figure 2-1. Combined schematic and micrographs of the hierarchical structural organisation of bone: from left to right, cortical and cancellous bone; osteons with Haversian systems; lamellae; collagen fibre assemblies of collagen fibrils; bone mineral crystals, collagen molecules. Adapted from [25, 26].

2.2.1.2. Bone Type

Two mature types of bone exist; compact and cancellous. Compact bone, sometimes known as cortical bone is largely found in the shafts of long bones. Cancellous bone, also known as trabecular or spongy bone, is found in the vertebrae and at the ends of long bones. This variety of bone contains numerous pores which are filled with either red or fatty marrow [24], which are responsible for the synthesis of red and white blood cells. Both of these types of bone can be made up from a second sub-class termed woven (primary) or (secondary) lamellar

bone. Woven bone is considered to be immature and unstructured, which can be found in the prenatal and neonatal stages, in newly formed bone and in the metaphysial region of growing bones in healthy individuals. More structured lamellar bone begins to form about 1 month after birth and actively replaces woven bone [20].

2.2.2. The Anatomy of Long Bones

For the purpose of this thesis only the anatomy of long bones is considered, however detail of short, flat and irregular bone types can be found elsewhere [27].

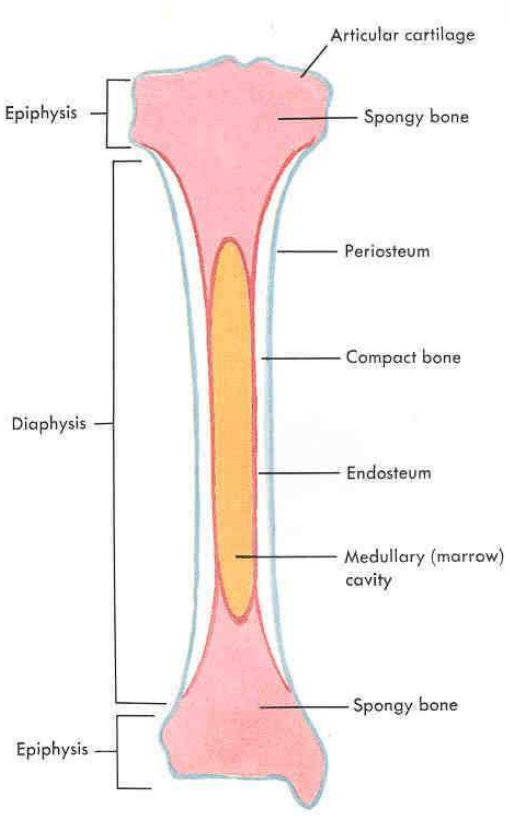

Figure 2-2. A schematic of a long bone showing the ephiphysis and diaphysis regions. Taken from [28].

Long bones are present in the arms and thigh and are made up of two distinct areas the diaphysis and the epiphysis (figure 2-2). The diaphysis is the central

section which is made up of a hollow section of cortical bone. This central cavity contains the medullary arterial supply and is occupied chiefly by fatty marrow. The epiphysis is the end section on the bone which is comprised of trabecular or spongy bone. The epiphysis is made up of hyaline cartilage which is important for bone lengthening during childhood, then upon bone maturation progressing into adulthood. The entire bone, except the joint ends where articular cartilage is present, is surrounded by the periosteum. The periosteum consists of an inner osteogenic layer (cambium), which provides appositional growth before maturity, and an outer fibrous layer which is purely supportive. The presence of the active cambium, with longitudinal arterioles, makes the periosteum thick. However, within the mature long-bone the cambium is thin and tenuous.

2.2.3. Cell Types and their Function

Four cell types exist within bone (figure 2-3). These osteoregulatory cells include osteoblasts, osteocytes, osteoclasts and lining cells [23]. Osteoblasts form a cell layer over bone surfaces upon which matrix is being formed and are responsible for the deposition of new osteoid. Active osteoblasts contain large numbers of mitochondria, Golgi apparatus and rough endoplasmic reticula [23], which are responsible for the production of procollagen molecules. These are extruded into the extracellular space and, after proteolysis and polymerisation occur, this results in the formation of collagen fibrils. Proteoglycans are exocytosed from osteoblasts, and a combination of these molecules and the collagen fibrils result in a mineralisable matrix. Amorphous calcium phosphates are then deposited from the plasma membrane of the cell which is then transformed into crystalline hydroxyapatite. During this process about 10 % of osteoblasts become incorporated into the bone matrix and these are referred to as osteocytes, which lie in sites termed lacunae and make up 90 % of bone cells in the adult skeletal system [23]. These cells undergo changes, which allow long cytoplasmic

processes to extend from the cell to other osteoblast and osteocyte processes forming tight gap junctions in small channels in the bone matrix called canaliculi. This network is known to act as a regulatory mechanism allowing the control of the flow of mineral ions between the extracellular fluid and bone [29].

Bone resorption and remodeling is controlled by giant multinucleated cells called osteoclasts, which act to remove bone material under both normal and pathological conditions via enzyme synthesis [30]. These cells are often found individually or in low numbers [31] and lie in pits called Howship's lacuna, an area created by the digestion of underlying bone. The plasma membrane is comprised of two areas: a ruffled border, consisting of finger like membranous folds that extend varying distances into the cytoplasm, and a sealing zone which has a dense cytoplasm that surrounds the site of bone resorption. The sealing zone acts to isolate the resorption pit and the matrix is dissolved through acidification with hydrochloric acid of the extracellular environment. Following this, a lysosomal protease, cathespin K, degrades the organic component. The by-products; Ca^{2+}, H_3PO_4, H_2CO_3 and water, are transported to the opposite side of the osteoclast leaving a resorptive lacuna. The osteoclast then detaches and moves to a new site leaving osteoblasts to replace the resorbed bone [32].

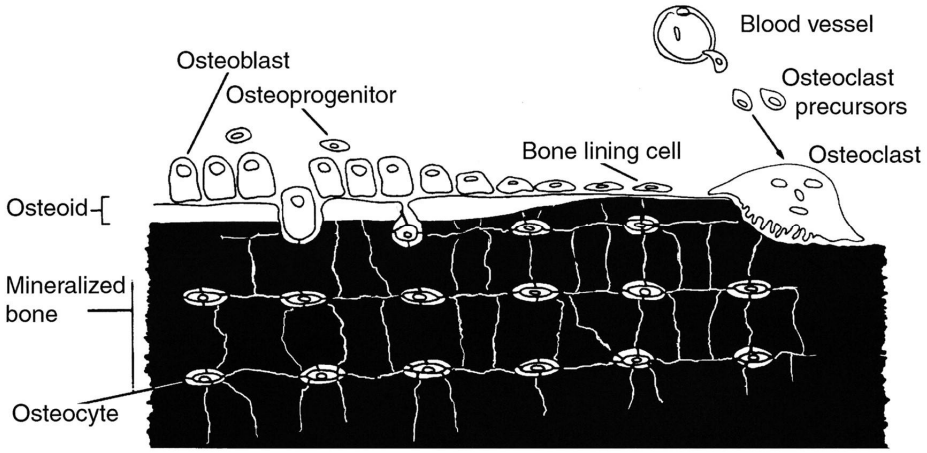

Figure 2-3. The origin and location of bone cells. Taken from [23] reproduced with permission from Popoff [33].

The fourth cell type, lining cells, are inactive osteoblast cells. These cells are elongated thin cells which cover bone surfaces of the mature skeleton and they are linked to either themselves or osteocytes via cytoplasmic extensions or gap junctions. As these cells are virtually inactive they contain fewer organelles compared to osteoblasts. It has been suggested that these cells may be precursors for osteoblasts, regulate bone crystal growth or simply function as a barrier system between bone matrix and extracellular fluid [33, 34]. Equally it is thought that parathyroid hormone (PTH) can activate lining cells to secrete enzymes capable of removing osteoid in preparation of osteoclastic action [35].

2.2.4. Bone Development and Repair

Bone development can occur by either intramembranous or endochondral ossification. Intramembranous ossification produces bone directly, particularly in the case of the skull and some irregular bones. Initially mesenchymal cells migrate to the site of eventual ossification where they differentiate into osteogenic cells which then specialise into osteoblasts secreting organic matrix. This results in trabeculae which fuse to form cancellous bone. Angiogenesis occurs leading to vascularisation of the spaces between the cancellous bone. At the bone periphery mesenchymal cells condense to form the periosteum. Eventually the bone will be transformed into cortical bone as the body takes on adult form [36].

Endochondral ossification uses cartilage as an intermediate and is responsible for the formation of most bones. This process is illustrated in figure 2-4. At the site of development mesenchymal cells group together in a process called prechondrogenic condensation to form the shape of the bone and differentiate into chondroblasts. These cells secrete cartilage matrix to produce a template consisting of hyaline cartilage. At the end of their cell life chondrocytes calcify this matrix and undergo apoptosis. This occurs because the new, denser, surrounding

calcified area slows the diffusion of nutrients to the central cells leading to malnourishment. Near the centre of the cartilage matrix periosteal arteries grow into the calcified area. As a result, osteogenic cells within the perichondrium are stimulated to differentiate into osteoblasts which lay down a thin shell of compact bone under the perichondrium termed the periosteum. Capillaries then stimulate the growth of the primary ossification centre, where the cartilage will be replaced with bone material. Osteoblasts deposit matrix over the remaining cartilage body forming trabeculae. As the ossification centre proceeds to the end of the bone structure, osteoclasts make small medullary cavities, within the trabecular bone which fills with red bone marrow. When branches of the epiphyseal artery enter an epiphysis, a secondary ossification centre develops in a similar way to the primary ossification centre [36].

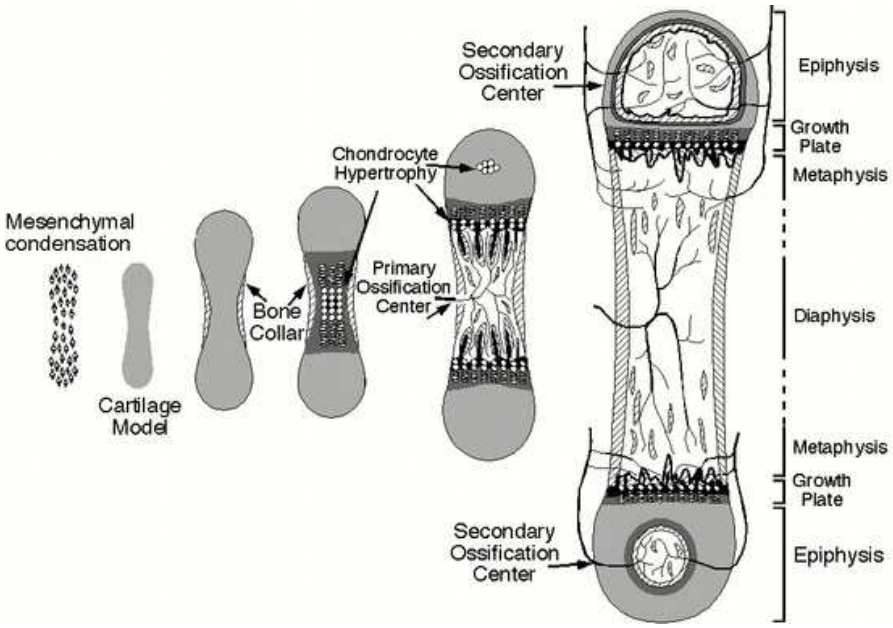

Figure 2-4. The process of endochondrial ossification from prechondrogenic condensation to final growth of cortical bone. With permission from Roland Baron.

There are several key differences between primary and secondary ossification centres. Primary ossification occurs in the diaphysis, while secondary ossification occurs in the epiphysis. Hyaline cartilage is not fully replaced in the epiphysis. This

leads to the formation of articular cartilage and separates it from the diaphysis as the epiphyseal plate. The epiphyseal plate will be replaced with bone over time as the individual approaches adulthood.

Bone healing can be divided in to primary or secondary healing. Primary healing occurs when the fracture is mechanically rigid and no interfragmentary space is present such as when rigid internal fixation is applied. The most common type of healing, secondary healing, occurs when a fracture is relatively stable for example when a fracture is in a plaster cast [37] this pathway proceeds via endochondral bone repair (callus formation) which is mediated by the inner periosteal layer and marrow tissues in a similar mechanism to endochondral ossification as described above. These tissues synthesis cartilage and then woven and lamellar bone in voids or space between bone material [38].

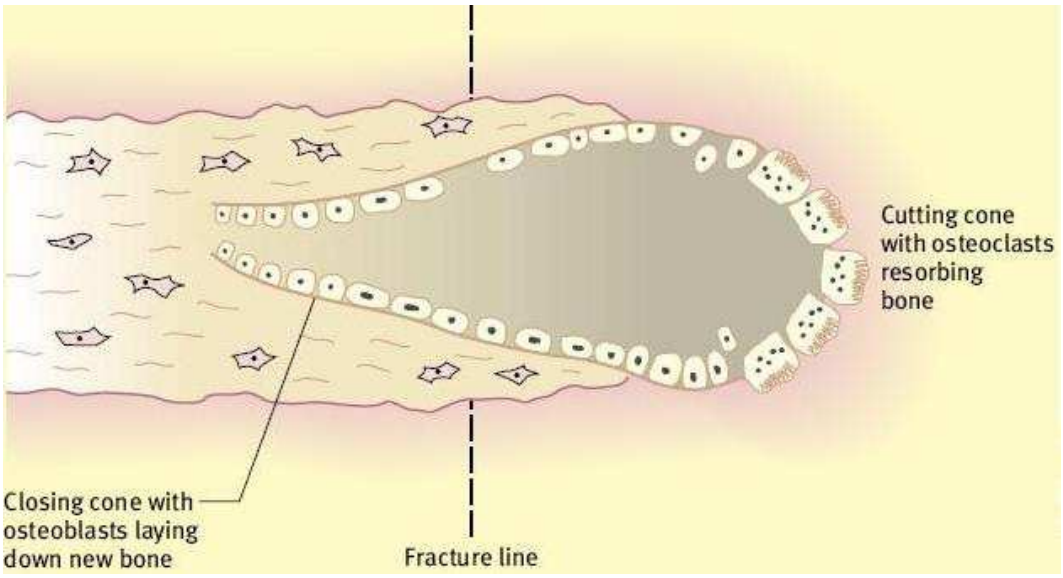

Figure 2-5. Schematic diagram showing a cutting cone tunnelling the bone from left to right. Taken from [37].

Primary bone healing occurs when the interfragmentary gap is 0.1 nm – 200 μm but where fracture is stable and rigid [38]. Strain is very low and there is no functional requirement for a bridging callus. Osteoclasts can tunnel across the fracture line and form a cutting cone (figure 2-5). Osteoblasts then follow laying

down bone extracellular matrix reestablishing continuity between Haversian systems. Angiogenesis is absent and bone formation proceeds without cartilage formation. Complete fracture healing with the formation of cortical bone occurs up to seven years after trauma and the same biological process occurs in normal bone remodeling [37].

2.2.5. Mechanical Properties of Bone in Comparison to Common Biomaterials

As bone is not a monolithic material but a composite structure that can adapt, the mechanical properties vary according to location in the body and species. Further factors, including type of bone, age, lifestyle, the presence of water, disease and trauma will also have an effect on the properties of bone [39]. Bone consists of apatite, collagen and water. Apatite has a Young's modulus of 80 GPa and collagen of 1.5 GPa; therefore the modulus of healthy bone cannot exceed 80 GPa. Values within the literature vary greatly due to the factors detailed above and the testing method applied. However, cortical bone has been shown to have a Young's Modulus between 14-20 GPa in a tensile situation whilst during bending this is as low as 5.4 GPa [25]. These figures have been supported by Suchanek *et al*. [21] giving values of 17.0-18.9 GPa. Trabecular (cancellous) bone has a lower value than cortical bone due to its higher porosity. For example vertebral trabecular bone was measured to have a modulus of 13.5 GPa [40].

When selecting an implant material for a load bearing application the mechanical properties are paramount. Implants for TJR must bear the joint load and must match or exceed the mechanical properties of bone. Failure to meet these criteria will ultimately end in implant failure. This explains why the majority of load bearing implants are predominately metallic. Table 2-1 demonstrates that most of the commonly used metals well exceed the elastic modulus of bone and this can

potentially lead to stress shielding. This occurs because there is a disproportionate degree of load sharing between the implant and bone [2]. Wolff's law states that bone will remodel itself to adapt to changes in stress, hence bone tissue surrounding an implant with a Young's Modulus greater than the bone will be reabsorbed, thus lowering the strength of the surrounding bone [41].

Material		Ultimate Tensile Strength / MPa	Modulus / GPa	Elongation / %
Metals				
	Co-Cr alloy			
	Cast	600	220	8
	Forged	950	220	15
	Stainless Steel	850	210	10
	Titanium	900	110	15
Polymers				
	Bone cement (PMMA)	20	2	2-4
	Polyethylene	30	0.4	15-100
Ceramic				
	Alumina	300	350	<2
	Hydroxyapatite	40-50	117	<0.5
Biological				
	Cortical Bone	100 – 150	10-24	1-3
	Trabecular	8-50	13.5	2-4
	Tendon, ligament	20-35	2-4	10-25

Table 2-1. The mechanical properties of selected biomaterials and cortical and cancellous bone. Adapted from [20].

While materials such as polymers and composites have been suggested as alternatives as they more closely match the modulus of bone (table 2-1), only metals and some composites are suitable materials for load bearing implantation.

2.2.6. Osteoblast Development *in Vitro*

In culture conditions osteoblasts are almost indistinguishable from fibroblasts. Figure 2-6 shows images of osteoblasts after day 1 and after day 14 of culture showing the pre-confluent (proliferative) and over confluent states (differentiating). Figure 2-6a shows some cells which have spread and some cells which have remained rounded before they begin to spread. Phenotypically osteoblasts may only be distinguished from fibroblasts by an extracellular matrix and only two osteoblastic-specific transcripts have ever been found. These are Cbfa1, a transcription factor for osteoblast differentiation, and osteocalcin, a molecule that inhibits osteoblast function and is only expressed in terminally differentiated osteoblasts [42].

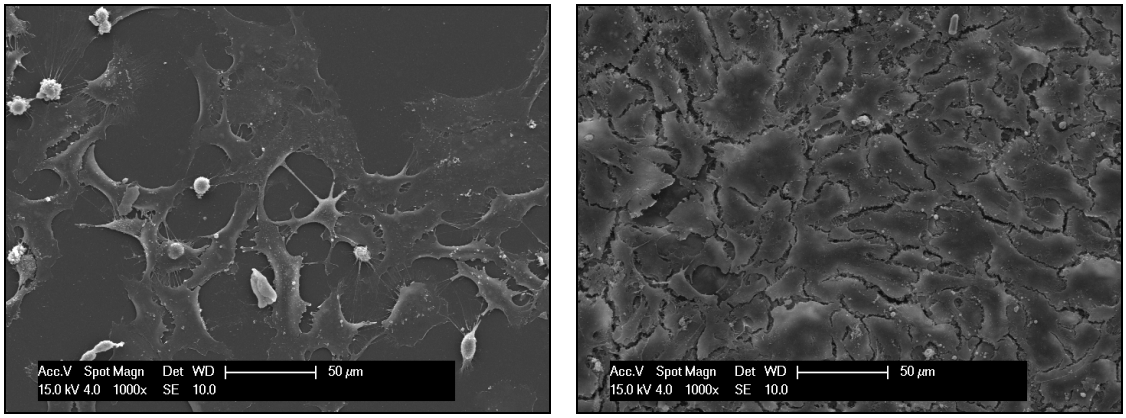

a **b**

Figure 2-6. SEM micrographs of dehydrated and fixed a) proliferating pre-confluent cells after day 1 and b) multi-layering human osteoblast culture after 14 days of culture on Thermanox plastic *in vitro.*

Three stages of osteoblast development are essential for normal growth *in vitro* conditions after initial attachment of cells; proliferation, matrix development and mineralisation (figure 2-7) [43]. During the first stage all cells in culture contribute equally in pre-confluent proliferation and express genes required for the support of cell cycle progression (H4 histone, c-fos, c-myc) and extracellular

matrix biosynthesis (proα1(1) and proα2(1)) for the formation of protein collagen type I [44]. This allows continual growth and cell division within the culture. The second stage occurs at the onset of matrix mineralisation. Following this proliferation period genes associated with the maturation and organisation of the bone matrix are up-regulated such as alkaline phosphatase. The final stage involves matrix mineralisation, or more specifically the deposition of mineral apatite particles. At this point proteins such as osteocalcin and osteopontin are expressed. At restriction points between proliferation and matrix development, maturation and mineralisation, additional cellular signalling must occur to stimulate progression to the next stage of development [43].

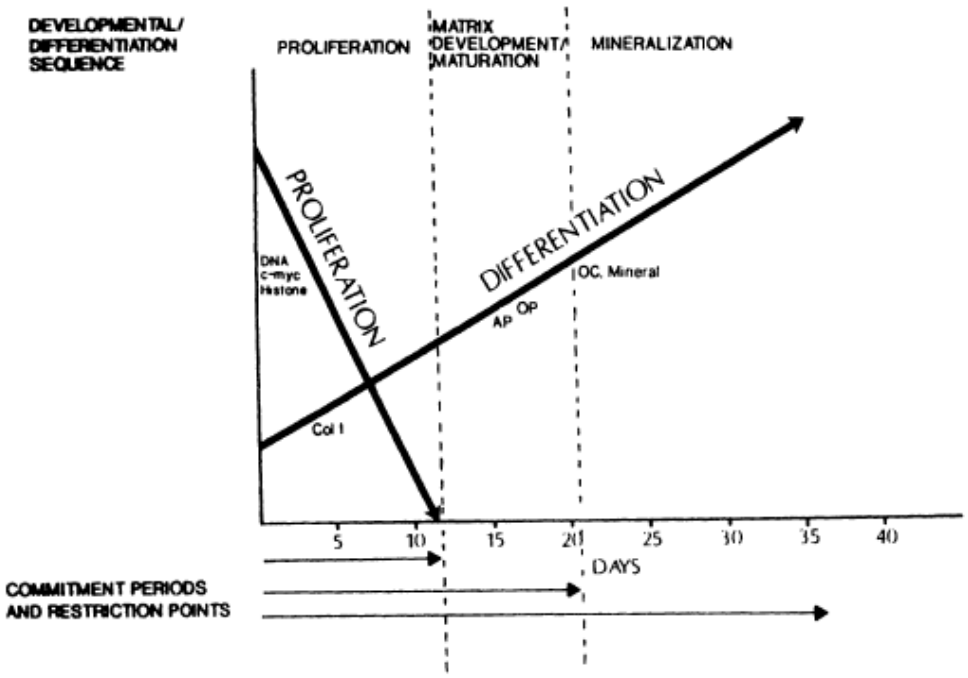

Figure 2-7. The three key stages of osteoblast development *in vitro* from day 0 to day 35. Taken from [44] adapted from [45].

This development pathway is dynamic and both proteins and biomaterial surfaces have been shown to change the points at which proliferation is downregulated and the mineralisation process can occur. Ishizuya *et al.* [46] showed that by exposing rat osteoblasts to parathyroid hormone for 1 h, osteoblast differentiation could be inhibited by suppression of alkaline phosphatase activity and other crucial proteins

essential for differentiation. Other work has shown that osteoblasts grown on type I collagen exhibit an earlier and enhanced expression of the osteoblast differentiated phenotype [47]. The aim of the present study is ultimately to enhance the development pathway *in vitro* with a long term view to ensuring the long term success of the implant material by using silicon as a dopant in HA material.

2.2.7. Osteoblast Attachment/Adhesion to Material's Surfaces in Vitro

Adhesion of osteoblast cells to material surfaces is of crucial importance for cell viability and development [48]. The process of cells initially interacting with surfaces can be thought of as short (attachment) or long-term (adhesion) chain of events. Short term events involve physiochemical linkages such as covalent, ionic and van der Waal's attractions between the cell and material. Longer term adhesion involves a cascade of biological molecules which lead to cell signalling and upregulation of transcription factors which ultimately control gene expression [49]. This longer term adhesion process is described below.

Cells adhere via adhesion proteins which adsorb onto substrata within seconds of exposure [48]; *in vitro* fibronectin and vitronectin have been shown to be important adhesion proteins. Moreover, Grothos *et al.* [50] found that osteoblast-like cells adhered preferentially to fibronectin compared with other proteins such as type I , type IV collagen and vitronectin, poorly with type V collagen and laminin but did not adhere to type III collagen. Some of these proteins have chemotactic or adhesive properties because they contain sequences such as the well characterised Arg-Gly-Asp (RGD) sequence which can bind specifically with cell membrane receptors such as integrins (figure 2-8) [49]. Other sequences

include ICAMs, DGEA and EILDV, however, such binding sequences are less well understood [36].

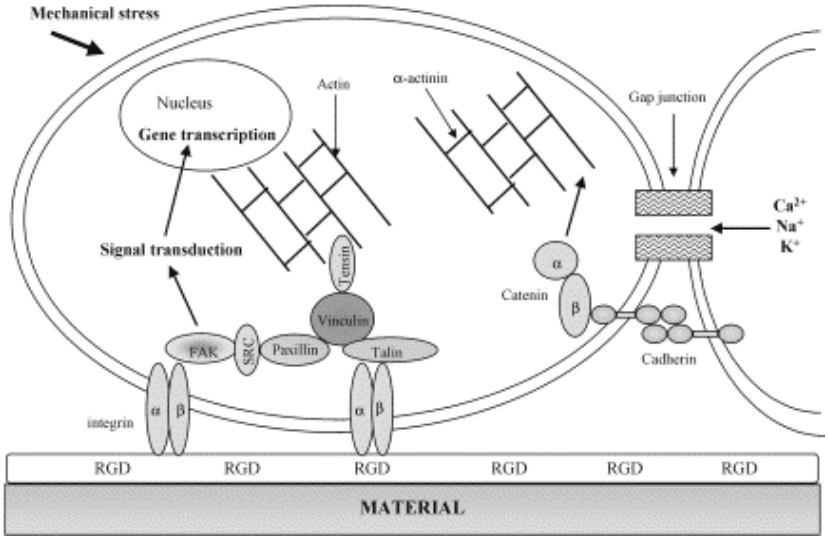

Figure 2-8. A schematic of attachment proteins involved in the material/cell adhesion process. Taken from [49].

Integrins are membrane heterodimers comprised of non-covalently bonded α and β subunits (figure 2-9). Many subunit families exist with a total of 24 α subunits and 9 β subunits [51]. Combinations of these subunits allow protein specific binding, for example integin α_5 β_1 can bind fibronectin in many cell types but $\alpha_v\beta_3$ can bind to a host of proteins such as collagens, vitronectin, laminin and fibronectin [52]. Details of integrin sub-families and protein specificity are reviewed by Hynes *et al.* [52] and more recently by Anselme *et al*. [49].

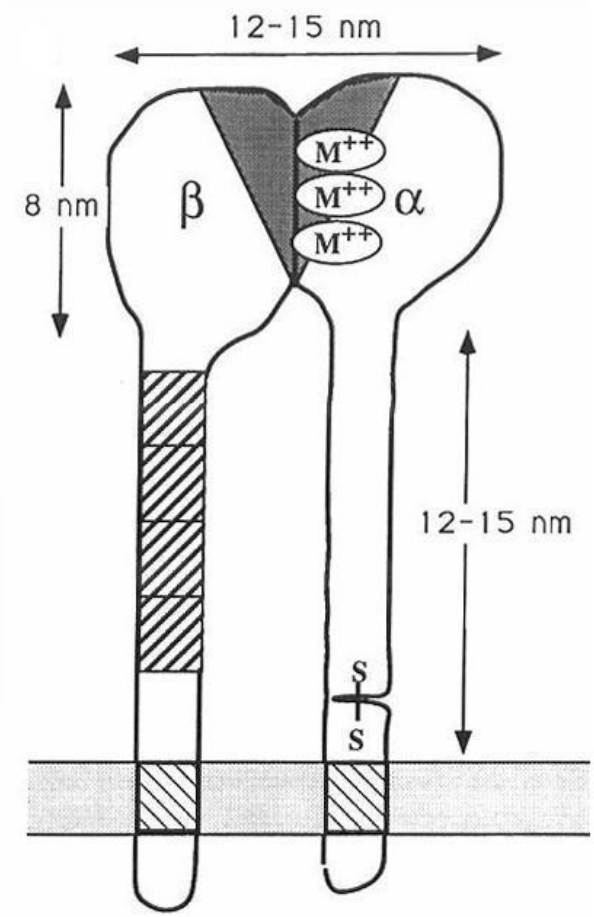

Figure 2-9. The α and β subunits making up the integrin. M^{++} are divalent metal binding sites (either Ca^{++} or Mg^{++}). The shaded area the ligand binding site and the dashed areas are the cystine rich sites. Adapted from [52].

Numerous authors have investigated the effect of different functional groups on protein absorption and cellular adhesion. Alkanethiol self assembled monolayers (SAMs) can be altered to have different end groups and then attached to gold surfaces. The following discussed studies all used gold surfaces as a platform for functionalisation. Albumin is more abundant in serum and adsorbs within seconds but attachment proteins displace this such as fibronectin [53]. Scotchford *et al*. [54] observed fibronectin from pure solution attached to functional groups in the order of COOH>OH>CH_3 and albumin from pure solution in the order of OH>COOH>CH_3. Osteoblast affinity followed the trend of fibronectin attachment. Keselowsky *et al*. [55] found that fibronectin binding affinity was in the order of

OH>COOH=NH_2>CH_3 with cell attachment following the same trend. These results differ from Scotchford *et al*. with OH groups having a higher affinity to fibronection that COOH groups. It was suggested that Scotchford *et al*. did not control for the density of adsorbed fibronectin, which for the same coating concentration is greater for COOH than an OH monolayer. When fibronectin binds to nonpolar CH_3 the $\alpha_5\beta_1$ integrin ligand is destroyed due to unfolding, lowering cell adhesion [55]. Moreover, it has been found hydrophobic surfaces denature adsorbed proteins. Wertz and Santore [56] demonstrated higher protein unfolding with CH_3 groups compared to OH groups.

Crystal structures of $\alpha_5\beta_3$ in a bound and unbound state provided the first atomic view of integrin interactions with synthetic RGD sequences. Firstly, the integrin acquires three divalent metal ions that coordinate the binding to the RGD site. The Asp of the RGD peptide establishes a direct contact with the ion located at a site termed the metal ion dependant adhesion site (MIDAS) which is flanked by two neighbouring ions located at the ligand-associated metal binding site (LIMBS) and the adjacent MIDAS (ADMIDAS) [57, 58]. The exact role of the latter two binding sites is unclear but it has been shown that ADMIDAS regulates affinity binding to the RGD sequence [59].

Adhesion sites between cells and substratum are termed focal adhesion points. The distance between the cell and the substratum is approximately 15 nm which is about the height of an integrin receptor. This linkage site leads to cell signalling transduction pathways which involve intracellular anchor proteins such as talin, paxillin, viculin and tensin (figure 2-8). These proteins are known to mediate interactions between actin filaments and integrins [49]. By this route, maintenance of cell shape and adhesion can be regulated.

Many of the signalling functions of integrins depend on focal adhesion kinase (FAK). FAK is a major tyrosine-phosphorylted protein and is linked to cell migration. It was found that cells deficient in FAK attached with higher numbers of focal adhesions thus making the cell spreading and migration slow [51].

2.3. Apatite Materials and Hydroxyapatite

Generally, apatite material is in the form of calcium phosphate and is present in a large number of biological systems and mineral apatite in bone has been discussed in section 2.2.1. Calcium phosphates and their occurrence in the body are detailed in table 2-2.

Calcium Phosphate	Chemical Formula	Occurrences
Apatite (HA)	$(Ca, Z)_{10}(PO_4, Y)_6(OH,X)_2$	enamel, dentine, bone, dental calculi, stones, urinary calculi, soft tissue calcifications
Octacalcium phosphate, OCP	$Ca_8H_2(PO_4)_6.5H_2O$	dental and urinary calculi
Brushite, dicalcium phosphate dihydrate, DCPD	$CaHPO_4.2H_2O$	dental calculi, chronocalcinosis, crystalluria, decomposed bones
Whitlockite, Tricalcium phosphate, ß-TCP	$(Ca, Mg)_9(PO_4)_6$	dental and urinary calculi, salivary stones, dentinal caries, arthritic cartilage, soft tissue calcifications
Amorphous calcium phosphate, ACP	$(Ca,Mg)?(PO_4,Y')?$	soft tissue calcifications
Calcium pyrophosphate di hydrate, CPPD	$Ca_2P_2O_7.2H_2O$	pseudo-gout deposits in synovial fluids
Z = Na, Mg, K, Sr, etc, Y = CO_3, HPO_4, X = Cl, F, Y' = P_2O_7, CO_3		

Table 2-2. Calcium phosphates and their location within the human body. Taken from [60].

It is no coincidence that calcium phosphate materials have been used in medicine and dentistry for over 90 years with applications including dental implants, periodontal treatment, alveolar ridge augmentation, maxillofacial surgery, otolaryngology, rhinology and orthopaedics [2] because calcium phosphate phases can be selected depending on whether a resorbable or a stable ceramic is required. The most stable of all calcium phosphates at human body pH (7.3) is HA, which has led this material to be one of the most researched biomaterials to date.

2.3.1. Crystal Structure of Apatites

Apatite is the most abundant naturally occurring phosphate on Earth. It provides a major source of phosphorus to the global phosphorus cycle and therefore apatite is crucial for the production of fertilizers, detergents and phosphoric acid [61]. A commonly investigated biological apatite is HA [$Ca_{10}(PO_4)_6OH_2$]. It is sometimes also referred to as hydroxylapatite [62-64], calcium hydroxyapatite or apatite and has a similar composition to bone. It is a brittle ceramic with a calculated density of 3.219 g cm^{-3}. Synthetically HA is considered to be a stoichiometric material, whereas biological apatites are generally considered non-stoichiometric [65] due to vacancies or substitutions which can commonly occur. HA is monoclinic with lattice parameters of a = 9.4214 Å, b = 2a, c = 6.8814 Å, γ = 120° and a lattice volume of 528.8 $Å^3$. Although, Elliott [66] found that b is marginally larger than 2a. HA, like all apatites, has a hexagonal system with space group $P6_3/m$ thus defining it as a material family (figure 2-9) [22].

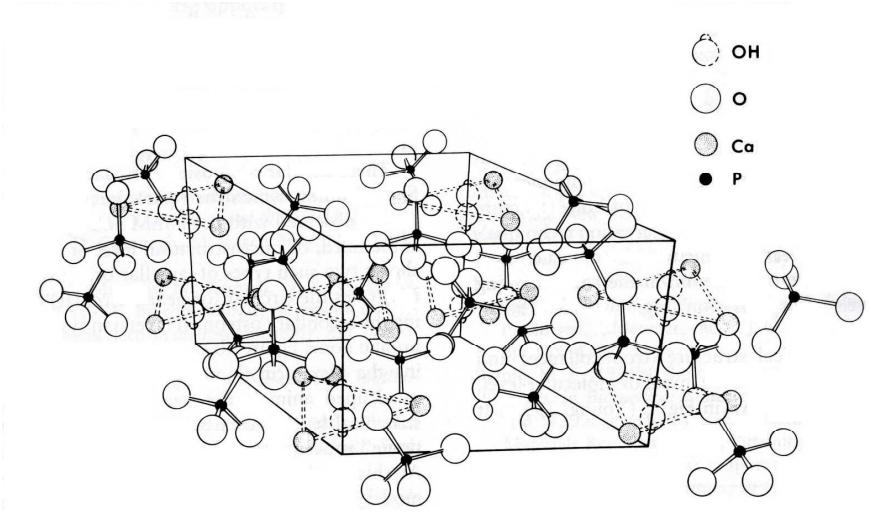

Figure 2-9. The hexagonal hydroxyapatite structure with $P6_3/m$ space group. Each OH^- position is only statistically 50 % occupied as indicated by the dotted outline of half of each OH^- group. Taken from [2].

The atomic arrangement of apatite is formed on three cation polyhedra (figure 2-10), which are the PO_4 tetrahedron, the $Ca(1)O_9$ polyhedron and the $Ca(2)O_6X$ polyhedron, where X is OH^-, Cl^- or F^-. Wyckoff positions are used to describe

crystal structures without the use of Miller indices (xyz). The PO_4 tetrahedron has a central P atom in the special 6h Wyckoff position and is surrounded by four oxygen atoms. The ten calcium atoms present in the structure are split into two polyhedra. Ca(1) is present with the central cation in the 4*f* Wyckoff (1/3, 2/3, z) position and nine oxygen atoms surround it in a tricapped trigonal prism, a structure termed the $Ca(1)O_9$ polyhedron. This polyhedron shows little response to substitutions. The second polyhedron, $Ca(2)O_6X$ sees Ca(2) again in the 6h special position of the $P6_3/m$ space group and is surrounded by six oxygen atoms with one column anion.

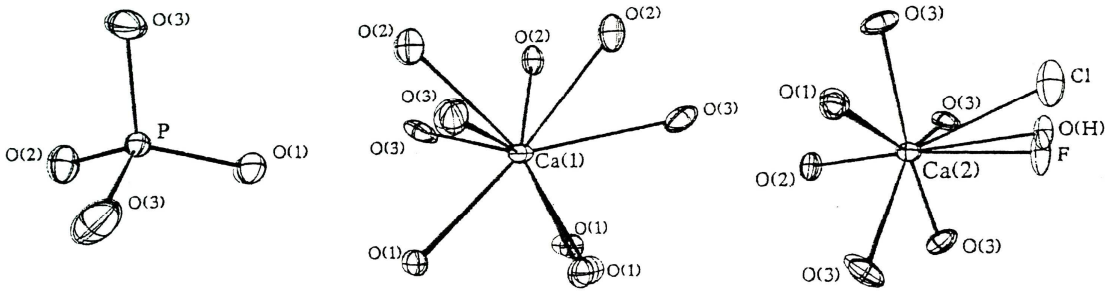

a **b** **c**

Figure 2-10. Schematic of a) phosphate tetrahedron, b) Ca(1) and c) Ca(2) polyhedra for the three apatite sub-structures in the HA crystal lattice. Also included in c) are possible anion substitutions of Cl^-, F^- or OH^- and their respective positions. Taken from [67].

Substitutions preferentially affect this polyhedron. The Ca(2) cations form triangles on the planes at z = 1/4 and z = 3/4 (figure 2-11). Each of the three calcium atoms at the corners of the triangles are bonded to the central anion in the 00z column (or c-axis). In the case of HA this anion is the OH^- group. This chemical species, however, is too large to fit into the cation triangles defined by the Ca atoms. Therefore, the OH^- group will either lie above or below the triangle plane destroying the $P6_3/m$ symmetry. Although the ideal space group is $P6_3/m$ pure forms of HA often crystallise into a $P2_1/b$ structure because of the asymmetry caused by the OH anions being unable to occupy Ca(2) cation triangles. Only fluorapatite can achieve $P6_3/m$ symmetry because the F^- anion is

significantly smaller than OH^-. In HA and chloroapatite, however, it has been found that all anions occupying the c-axis column do so with a sense of order. This ordering leads to a tilting of the polyhedra caused by the positioning of one column causing the adjacent column to become ordered in the opposite sense thereby doubling the b-axis, hence a $P2_1/b$ structure will be observed. However in reality, all natural HA materials contain sufficient vacancies and impurities to destroy this ordering thus reverting it back to a $P6_3/m$ space group [68], as shown in figure 2-9.

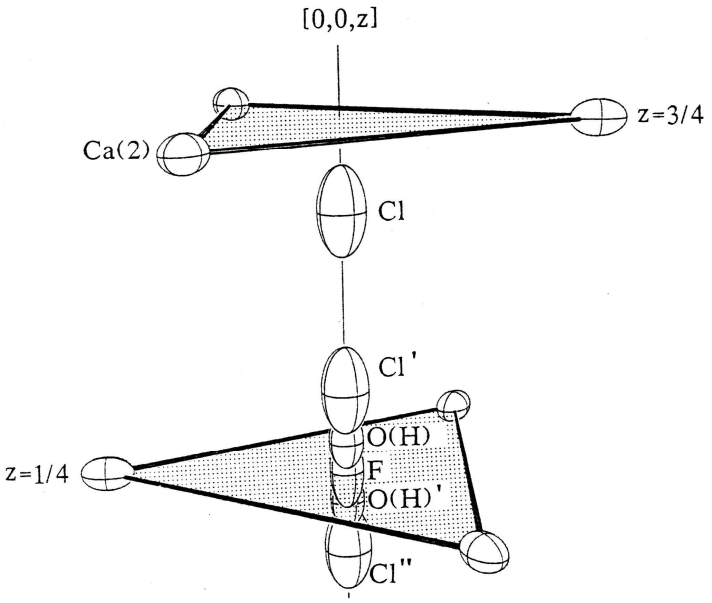

Figure 2-11. Position of anions relative to Ca(2) triangles. F^- can fit in the central positions whereas Cl^- and OH^- anions sit above an below. The severity of anion displacement is dominated by atomic size.

The structure and chemistry of apatite $M_{10}(ZO_4)_6X_2$ allows numerous substitutions thus leading to a potentially huge number of compounds with an enormous variety of materials which can be found all over the world. This can be achieved due to the remarkable amounts of distortion that the apatite structure can withstand. Such substitutions include divalent cations; Sr^{2+}, Pb^{2+} ,Ba^{2+} and Mn^{2+} to name a few which displace the M or Ca^{2+} component in apatite. Equally, monovalent, such as Na^+ and Li^+, trivalent, tetravalent and hexavalent substitutions all commonly

occur in nature replacing calcium [69]. The X component of the apatite structure is as equally interchangeable. This is commonly dominated by the three anions Cl^-, F^- and OH^-, however, this site is not exclusive to these groups with monovalent Br^-, I^-, O_2^-, BO_2^-, NCO^-, NO_3^- and NO_2^-, divalent O_2^{2-}, CO_3^{2-}, S^{2-} anions all having the capability to occupy the c-axis (00z) channels [69]. Substitution of c-axis sites is referred to as type A substitution. While substitutions of this nature are important, this study is concerned with the substitutions of the Z site atom. As with the previous types of substitutions, a host of anions can be accommodated. Examples include PO_4^{3-} AsO_4^{3-}, VO_4^{-3}, MnO_4^{3-}, CrO_4^{3-}, SO_4^{2-}, SeO_4^{2-}, CrO_4^{2-}, BeF_4^{2-}, GeO_4^{4-}, SiO_3N^{5-} however the most interesting to this study is the silicate group, SiO_4^{4-} because we can use this as a mechanism to easily introduce silicon into the apatite structure. The substitution of silicate for phosphate tetrahedron is known as a B-type substitution and has been confirmed with data obtained from both natural apatites and artificial synthesis [69]. In fact such substitutions can be found in bone throughout the body which is discussed briefly in section 2.5.

2.3.2. Calcium Phosphorus Ratios

Chemical Name	Acronym	Chemical Formula	Ca/P ratio	Relative Biocompatibility	Relative Solubility (pH 7)
Monocalcium phosphate monohydrate	MCPM	$Ca(H_2PO)_2.H_2O$	0.50	-	High
Monocalcium phosphate anhydrate	MCPA	$Ca(H_2PO_4)_2$	0.50	-	-
Dicalcium phosphate dihydrate, brushite	DCPD	$CaHPO_4.2H_2O$	1.00	-	Medium
Dicalcium phosphate anhydrate, monetite	DCPA	$CaHPO_4$	1.00	-	-
Octacalcium phosphate	OCP	$Ca_8(HPO_4)2(PO_4)_4.5H_2O$	1.33	-	Low/Medium
β-Tricalcium phosphate	β-TCP	$Ca_3(PO_4)_2$	1.50	Good	Medium
α-Tricalcium phosphate	α-TCP	$Ca_3(PO_4)_2$	1.50	Good	Medium
Amorphous calcium phosphate	ACP	$Ca_x(PO_4)_{y.n}H_2O$	1.2-2.2	-	High
Calcium deficient hydroxyapatite	CDHA	$Ca_{10-x}(HPO_4)_x(PO_4)_{6-x}(OH)_{2-x}(0<x<1)$	1.5-1.67	-	-
Hydroxyapatite	HAP	$Ca_{10}(PO_4)_6(OH)_2$	1.67	Excellent	Low
Oxyapatite	OXA	$Ca_{10}(PO_4)_6O$	1.67	Very Good	-
Tetracalcium phosphate	TTCP	$Ca_4(PO_4)_2O$	2.00	-	High
Calcium oxide	CaO	CaO	-	Poor	High

Table 2-3. The chemical and biological properties of some calcium phosphates adapted from [70, 71].

Stoichiometric HA has a calcium to phosphorus ratio of 1.67 due to the 10 calcium and 6 phosphorus atoms present in the apatite structure. The calcium to phosphorus ratio (Ca/P) of calcium phosphate and HA bulk or coatings material can determine the success of initial attachment and proliferation of osteoblasts and other cell lines [72]. The Ca/P value will also indirectly determine both solubility [73, 74] and mechanical properties [72]. Table 2-3 provides information regarding relative solubility and biocompatibility of different bulk calcium phosphate compounds [70]. Often the *in vivo* response of a calcium phosphate can be predicted by its solubility [71]. More detailed information regarding the solubility of selected calcium phosphate phases is shown in figure 2-12. Hydroxyapatite is the most desirable phase leading to excellent biocompatibility, thermal stability and low solubility. In the case of thin films the Ca/P ratio is commonly not 1.67 which may be the result of mixed phases or a calcium/phosphorus deficient HA being present.

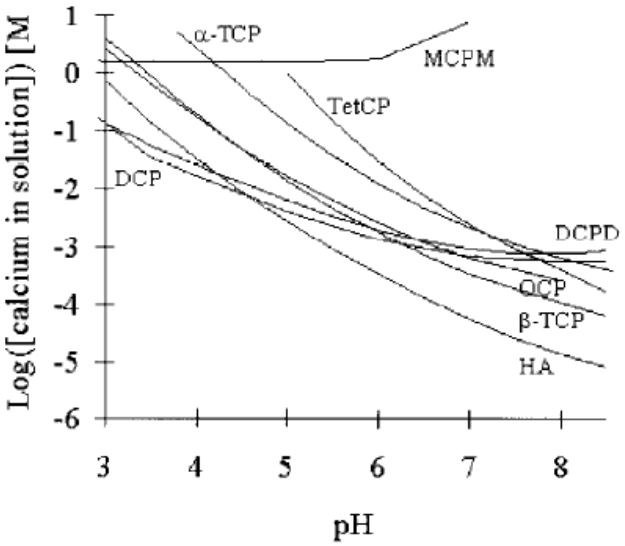

Figure 2-12. Solubility isotherms of several calcium phosphates in water. The solubility is expressed by the total amount of calcium ions in the solution. Human body pH = 7.3. Taken from [71].

2.3.3. Thermal Properties of Hydroxyapatite

HA has a thermal stability ranging from 900 - 1450°C. Yang *et al*. [75] produced an HA powder via a coprecipitation method which was stable up to 1200°C while Tampieri *et al*. [76] produced powders that were stable up to 1450°C. Thermal stability is affected by Ca/P ratio, pH and impurities [75]. Decomposition follows the equation 2.1, of which there are two stages; the first a reversible expulsion of water producing oxyapatite and the second the irreversible decomposition. This is controlled by diffusion of water from the reaction zone at the surface of the ceramic sample [77].

Eqn 2.1. $HA \rightarrow 2\ \alpha-\beta-TCP + TTCP + H_2O$

Where $\alpha-\beta-TCP$ is $\alpha-\beta-$ tricalcium phoshate, TTCP is tetracalcium phosphate.

2.3.4. Formation of a Carbonated Apatite Layer on Hydroxyapatite

HA is a bioactive material meaning bone can form a direct bond with this material. It has proved to be a successful implant material as this direct bone bonding enhances the device/bone interface lowering the long term chances of aseptic loosening (section 1.1). When implanted HA ceramics form a carbonated apatite layer on their surfaces. These reactions, occurring *in vitro* and *in vivo*, have been associated with bioreactivity. This process proceeds by the production of acids, by cells or elsewhere, which directly precipitates or hydrolyses acidic calcium phosphate phases. Finally, the formation of a carbonated apatite occurs, which becomes intimately associated with the organic matrix. Carbonate ions and Mg^{2+} ions, which originate from the biological fluid may also be present in this formation [22].

2.3.5. Mechanical Properties of Hydroxyapatite

The mechanical properties of dense sintered hydroxyapatite have been briefly mentioned in section 2.2.7. Akao *et al*. [78] measured compressive, flexural and torsional strengths to be 509, 113, and 70 MPa respectively and bending strengths of up to 196 ± 33 MPa have been quoted [79]. One solution to improve the mechanical properties of HA materials is to grow single crystals. This eliminates surface flaws, micropores, inclusions or strain in grain boundaries which all can contribute to failure in ceramic materials. Bending tests on HA single crystals yielded a bending strength of 500 ± 184 MPa and a Young's modulus of 60.2 ± 11.7 MPa [80] which are significantly higher than dense material. It is suggested that such crystals could be used in load bearing applications, however, they are not used clinically as they would be extremely expensive and brittle fracture could have severe side effects.

2.3.6. Accurate Measurement of Thin Film Calcium to Phosphorus Ratios

Thin film characterisation is often more problematic than analysis of bulk materials. Small quantities of material mean that techniques used for bulk analysis may not have a high enough sensitivity. In addition thin films by convention are < 1 μm which means that some analysis techniques penetrate further than film depth leading the substrate to also be characterised, thus reducing the quality of the resultant data leading to less accurate semi-quantitative analysis. Moreover, bulk materials are commonly in powdered form. Powders can easily be mixed and so fewer measurements are required as the material is already randomised. In the case of thin films, material cannot be mixed and composition can change slightly at different areas on the film. This requires more replicates to be measured to ensure good characterisation of a batch. Generally, the most important compositional value that can be taken from

HA thin film studies is the Ca/P ratio. Many techniques have been used to calculate Ca/P ratios of HA and calcium phosphate thin film materials including, energy dispersive X-ray analysis (EDX) [81], Rutherford backscattering spectrometry (RBS), elastic recoil detection (ERD) [82-84] and X-ray photoelectron spectroscopy (XPS) [83]. These techniques are summarised in table 2-4 with emphasis on accuracy and traceability of error. Terms like 'accuracy' and 'traceability' can be taken to have a variety of meanings. Often the terms precision and accuracy are confused, being used to mean the same entity. Therefore it is important to define such terms. For the purpose of this study the term accuracy is taken to mean '*the ability of a technique to obtain a correct value within the constraints of the machine resolution for the material area analysed'*. While precision is '*the ability of a measurement to be consistently reproduced*'. Traceability is '*the ability of a researcher to account for all variables that may contribute to error associated with a result*'. This subsequently allows one to adjust for such factors thus increasing the accuracy of a given technique. Different values have been measured for a given thin film calcium phosphate sample with different techniques [85], but no studies have investigated the accuracy of such techniques for the measurement of Ca/P ratios. One of the major factors contributing to this is the analysis depth, however, it has been claimed on numerous occasions that RF magnetron sputtered coatings yield homogeneous compositions through the depth of the coating [86, 87] an therefore regardless of analysis depth values obtained should be similar. Concerns have been raised that inaccuracies in the above techniques could lead to false or misleading characterisation of HA and calcium phosphate thin films.

The following sections describe in detail the practical implications of quantification of three commonly used techniques for the analysis of Ca/P ratios in thin films; EDX, RBS and XPS.

Acronym	Name	Typical incident particle	Detected particle	Depth analysed	Depth profiling	Analysis precision	Normal analysis accuracy	Traceability
XPS	X-ray photo-electron spectroscopy	Cu characteristic X-ray	Photoelectron	near surface: first ~10 monolayers	Sputtering etching (destructive)	1%	10%	Depends on IMFP and RSFs
EDX EPMA	Energy dispersive X-ray analysis, or electron probe microanalysis	10-20 KeV electrons	Characteristic X-rays	~1 μm: depends on excitation volume of probing electron beam	No	2%	10%	Depends on sample matched standards and homogeneity
RBS	Rutherford backscattering spectrometry	1.5 MeV $^4He^+$	Backscattered $^4He^+$	~0.75 μm: depends on range of probing particle beam	Yes	1%	2%	Absolute
α-ERD	α particle induced elastic recoil spectrometry	1.5 MeV $^4He^+$	Recoiled H from target	~0.5 μm: depends on range of probing particle beam and analytical geometry	Yes	1%	5%	Absolute (non-Rutherford cross-sections and larger geometry and calibration uncertainties)
HI-ERD	Heavy ion induced ERD	35 MeV Cl^{5+}	Recoiled atoms (Z<Cl) from target	~0.25 μm: depends on range of probing particle beam and analytical geometry	Yes	1%	5%	Absolute (but large stopping power uncertainty)
PIXE	Particle induced X-ray emission	3 MeV H^+	Characteristic X-rays	~20 μm: depends on excitation volume of probing beam	No	1%	10%	As EDX, but excitation volume geometry given by the probing beam

Table 2-4. A summary of ion beam and X-ray analysis techniques complete with limitations and accuracy.

2.3.6.1. Energy Dispersive X-ray Analysis (EDX)

EDX can be a useful analysis technique if samples are flat, smooth and homogeneous. Spatial resolutions of typically 1 μm allow small area analysis and trace elements to be detected down to 100 ppm. The depth resolution is within the micron range but does depend on the material and accelerating voltage.

Characteristic X-ray emissions are measured by silicon particle detectors. Detectors are not without problems such as incomplete charge collection (ICC), electronic drift and absorption of X-rays by contaminant build-up on the silicon crystal. The use of standards to create calibration profiles reduces this source of error, as long as the calibration occurs as the same time as the measurement, which is not always practically viable.

Quantitative EDX is a complex process. Accelerating voltages play a crucial role in the data obtained. If too low, insufficient X-rays will be created producing too few counts to analyse. Increasing the accelerating voltage leads to inclusion of the substrate material in the thin film analysis [88]. However, it is suggested that to excite a given element characteristic X-ray an accelerating voltage three times higher than the KeV of the element should be used [89]. Elemental sample composition can affect the X-ray spectrum produced which can be adjusted for with a high degree of success in homogeneous materials.

For bulk materials it is possible to obtain statistical precision of ± 1 %. However, various factors govern the accuracy of the final result. Instrumental instabilities are estimated at < ± 1 % but the largest uncertainly arises from correction of matrix factors. These matrix corrections are commonly achieved by ZAF corrections, where ZAF denotes the atomic number (Z), absorption (A) and fluorescence (F). Individual components are calculated from suitable physical models. It is difficult to estimate uncertainty, but in favourable cases it is approximately ± 1-2 %. The largest uncertainty of this correction is caused by absorption calculations which obey the law:

Eqn 2.2. $$I = I_0 \exp [-(\mu/\rho)\rho x]$$

Where I_0 = initial intensity and I is the intensity after travelling a distance x through an absorber of density ρ with a mass absorption coefficient (μ/ρ) [90]. Mass absorption coefficients are measured but can have differences of up to 20 %. This will have a significant effect on quantitative analysis.

2.3.6.2. Rutherford Backscattering Spectroscopy (RBS)

The energy of a backscattered particle is determined by the kinematics of the nuclear interaction, and the inelastic energy loss of the particle to the target electronic lattice on its inward and outward path through the target to and from the interaction site. This inelastic energy loss ε(E, Z_1, Z_2), where E is the particle energy and Z_1, Z_2 are the atomic numbers of the particle and target atom respectively, is determined from a linear combination of losses of each element of the target, and is taken from the stopping and range of ions in matter (SRIM) energy loss semi-empirical database [91], whose accuracy is currently about 4 %. The nuclear and electronic energy losses can be treated independently to a good approximation, and the electronic energy losses are determined by integrating ε along the path length of the particle.

The spectrum expected from any particular sample can be readily calculated, however, various parameter values are required to do so. The sample composition is required as a function of depth (to calculate the electronic energy loss), the number of particles striking the sample and the solid angle of the detector (to determine the yield as a function of energy). The geometry of the ion beam, target and detector must be known, and the probability of scattering can be calculated analytically from the Coulomb potential.

The great utility of RBS is due to the existence of very simple and reliable detectors (reverse biased silicon diodes) which can detect particles with effectively

100 % efficiency, and determine their energy with an energy resolution of about 1 % and with very good linearity.

Interpretation of experimental spectra requires solving the inverse problem of calculating spectra from a known target. Unfortunately, because the detected energy of a particle is determined both by the mass of the scattering nucleus and the depth of that nucleus in the target, this is a mathematically ill-posed problem with no analytical solution. However, Jeynes *et al*. [24] have developed a code based on simulated annealing which reliably solves this inverse problem, and it is now possible to extract accurate depth profiles routinely.

The limitations of the accuracy of RBS are at greater depths, where plural and multiple nuclear scattering events become significant. The effect is the same with electrons however ions are much heavier and so it is possible to neglect multiple scattering and still get accuracy of < 0.5 % in the near-surface region (~ 750 nm). The other major limitation of accuracy is in the semi-empirical database of electronic energy losses. However, in many cases (including this one) we need to analyse only the relative shape of the spectrum, not its absolute height. In this instance we need only ratios of energy loss for different elements in the target, and ratios are generally known to be < 0.5 %. Another effect is electronic screening of the nuclear charge, but this is reasonably well known at < 0.25 % for Ca, P and O light ions.

2.3.6.3. X-ray Photoelectron Spectroscopy (XPS)

XPS is a non destructive, surface sensitive technique which typically examines the top 10 atom layers of a surface on most samples [92]. XPS can be used to obtain information about the chemical state of the atoms which gives this method an advantage over the previously described surface analysis techniques. Its limitation is that information about lower surfaces cannot be deduced without destructive

etching methods which may alter compositions ultimately reducing the accuracy of the result.

Compositional analysis of XPS data can be complicated. For the purpose of elemental compositional quantitative analysis three main steps must be taken. Firstly, an appropriate background must be fitted accounting for secondary electrons and inelastically scattered electrons. Multiple background types are available, of which linear and Shirley [93] are the most commonly used. This selection process can incur large amounts of systematic error as discussed by Powell and Seah [94]. Secondly, peak fitting must take place and this is normally achieved with Gaussian-Lorentzian line functions. If binding energies are known constraints may be made to ensure a better fit. Lastly, data are adjusted using one of two methods. The most accurate approach is to use standard materials to measure peak intensity and adjust accordingly. However, this is not always practically possible because surfaces must be flat, atomically clean and homogeneous and in addition standards often have little relation to materials that are being analysed. Relative sensitivity factors (RSFs) offer a practical solution. RSFs are obtained from known standards, or less frequently, calculated, and adjusted for individual system geometries. This is a very time consuming and complicated process. A study looking at the accuracy of RSFs and standards measured by the user using AuCu alloys found calculating compositions using standards achieved an uncertainty from ± 1.75 to 2.43 % while using RSFs measurements were within ± 8.82 to 10.4 % [95].

RSFs may also be calculated. The major limiting factor in calculating RSFs is the inelastic mean free path (IMFP). This is defined as the average of the distances measured along the trajectories that electrons with a given energy travel between

inelastic collisions in a substance [96]. Values may be measured or calculated but reliable data are difficult to obtain. A number of approximations has been made for calculating these parameters but the uncertainty of these processes can only be estimated. Again measured values are subject to uncertainty that can only be calculated, which is in the region of 10 – 20 % [97]. Moreover, IMFP calculated for bulk materials have been shown to differ for surface layers but this is strongly element dependant. The uncertainty of measured and calculated IMFPs are discussed in detail by Powell and Jablonski for near solid surfaces [98].

2.4. The Role of Silicon in the Body and its Effects upon Bone

2.4.1. Toxicity

For decades silicon has been considered in terms of its toxicity and has previously been thought to be an environmental contaminant, rather than an essential ultra-trace element. Oral ingestion of silicon is unlikely to result in toxic effects [99], however this may lead to conditions such as renal calculi, which has been associated with excessive silicon intake. Stewart *et al*. [100] showed by feeding rats 2700 mg of Si/kg urolithiasis could be induced. Subsequently, a reduction in silicon lowered this effect. The Food and Nutrient Board have no recommended adequate silicon intake for humans, although silicon requirement is estimated to be between 2-20 mg day^{-1} [99, 101].

2.4.2. Metabolism

Many dietary forms of silicon are known to exist; silica, tetraethylorthosilicate, monosilicic acid, sodium zeolite A and metasilicate. These are often derived from plant foods such as cereals, cereal products (especially beer), green beans and some mineral waters [102]. Dietary intake appears to have large affect on the amount of silicon absorbed into the body. Studies have shown that orthosilicic acid is the most readily available source of silicon to humans. It is unclear how much silicon is absorbed but research has shown this to be low amounts [103]. Silicon is broken down into monomeric silicon in the gastrointestinal tract and then absorbed, however the majority of ingested silicon is excreted in the urine typically within 3 - 8 h of ingestion. The mechanism of absorption is unknown and may be either by passive diffusion or active uptake. The degree of silicon polymerisation has been shown to influence the uptake of silicon with monomeric silicon being most easily absorbed and polymeric silicon most poorly absorbed [104].

2.4.3. Silicon and its effects on Growth and Bone Development

Silicon may be beneficial for healthy arteries [105], hair, nails and skin [106]. In general, silicon has been linked with the development and regulation of connective tissues of which most significantly bone and skeletal development [102]. The role of silicon within the skeletal system was first noted by Carlisle [107] who found that the osteoid of young chicks contained 0.5 wt % silicon content. This decreased when moving away from the active growth front. Later studies by Carlisle [108] and Schwarz and Milne [109] showed that silicon deprivation in chicks and rats lead to abnormalities in bone and cartilage development which impaired the normal growth of the animals. More recent studies have not managed to repeat such dramatic effects; including no effect on growth to mild abnormalities in bone and cartilage [110]. It has been suggested that the original studies of Carlisle and Schwarz and Milne may additionally have been depleted in other essential nutrients thus having cumulative adverse effects on growth and making the results difficult to interpret [102]. Alternatively, due to the ubiquity of silicon in the environment, low level silicon diets can be difficult to achieve and this may explain why no change in growth in chicks and rats was observed in subsequent studies [102]. Multiple studies have shown that increased silicon levels have beneficial effects on collagen synthesis [111] and that deficiency causes a reduction in connective tissue formation [112]. Silicon seems to affect the extracellular matrix formation of bone but may also have a role in the mineralisation events with accelerated mineralisation shown in rats [113]. Not only is silicon related to osteoblast up-regulation but studies have shown it to have a negative effect on bone resorption by a reduction of osteoclast numbers [114, 115].

While there are much data available concerning the role of silicon in animal models, research in humans is less prevalent. Work has shown that administering monomethyltrisilanol by intramuscular or intravenous injection and orally at 5.5

mg/day for four months to osteoporotic subjects increased trabecular bone volume when compared to untreated controls [116]. Subsequently, the bone mass density of femoral heads in osteoporotic women significantly increased after receiving 50 mg of monomethyl trisilanol twice weekly via intramuscular injection for 4 months [117]. A recent study by Jugdaohsingh *et al*. [118] reported higher dietary silicon intake resulting in higher bone mineral density at the hip of men and pre-menopausal women, but surprisingly not in post-menopausal women.

A number of authors have reported the positive effect which silicon has on osteoblast and chrondrocyte cells. Reffitt *et al*. [119] added orthosilicic acid at 10-20 μM concentrations to MG-63 human osteosarcoma cells, fibroblasts and bone marrow stromal cells. In all cases collagen type I production was significantly higher than in unsupplemented cells. Furthermore, the MG-63 cells exhibited increased differentiation as measured by osteocalcin and alkaline phosphatase activity.

Evidently there is a great deal of proof that silicon plays a beneficial role in the increased proliferation and differentiation of osteoblasts both *in vitro* and *in vivo*. Therefore, silicon could be used as a cheap solution to aid the success of implant fixation and improve the quality of the surrounding bone tissue leading to a reduction in revision surgery. The following section will discuss this use of silicon in materials which could be suitable for orthopaedic applications.

2.4.4. Silicon in Biomaterials

The use of silicon in materials for bone repair is well established. Most notable is the bioceramic Bioglass®, which was discovered by Hench in 1969 and first used clinically in 1985. The material led to the concept of bioactive materials [120] and is available in multiple compositions but is mainly comprised approximately within

the ranges of 30-55 wt % SiO_2, 19.5-24.5 wt % Na_2O, 14.7-24.5 wt % CaO and 6 wt % P_2O_5. The bioactivity of these materials, which are characterised by the ability of the material to form interfacial bonding with bone tissues, is in part due to the silicon content of the material. In the sequential interface reactions that take place at the surface of the tissue and the bioactive material (figure 2-13), silicon plays an important role in the initial steps leading to the generation and crystallisation of the extracellular matrix.

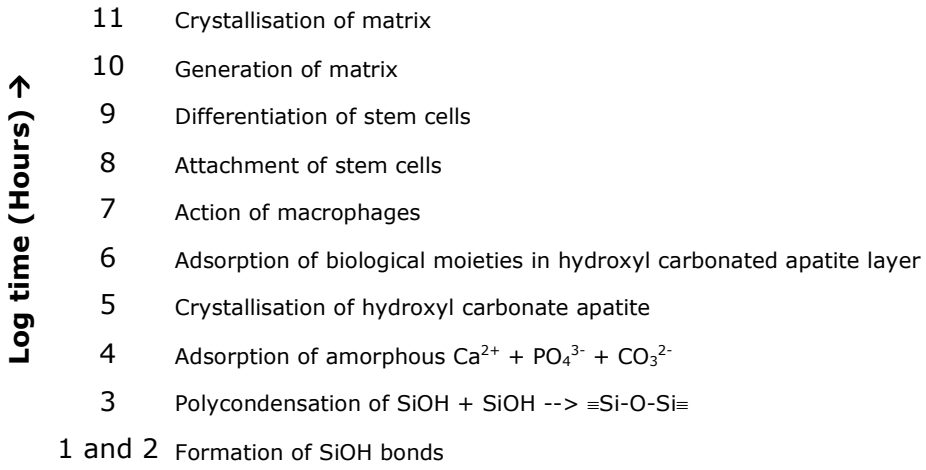

Figure 2-13. The interfacial reactions involved in forming a direct bond between tissue and bioactive glasses *in vivo*. Taken from [121].

Silicon in these materials has been shown to have other advantages; Xynos *et al*. [122] dissolved Bioglass® 45S5 in cell culture medium, which was shown to have an 88 fold increase in silicon content. Subsequently it was demonstrated that 190 genes out of 1,176 osteoblast genes were present at higher levels than the control cells. Upregulated genes included CD44, mitogen activated protein (MAP), kinase-activated protein kinase 2, integrin β1 and RCL growth-related c-myc responsive gene. Only 5 genes were found to be downregulated. Although calcium and phosphate ions were present at increased levels, it was postulated that gene upregulation was related to the silicon ion content. Keeting *et al*. [123] showed osteoblasts to significantly increase their degree of proliferation and differentiation after 48 h when cultured in the dissolution product of a silicon containing

compound, Zeolite A. Moreover, it was found that silicon induced the release of transforming growth factor β1 (TGF-β1). This topic is expanded in section 2.5, however silicon substituted HA is exclusively discussed rather than biomaterials generally.

2.5. Silicon Doped and Substituted Hydroxyapatite

2.5.1. Silicon substituted Hydroxyapatite

While Bioglass® has had a large degree of success as a bioactive material, its use in load bearing sites is very restricted. One solution would be to coat this material onto more mechanically suitable substrates as discussed in section 2.6.1., however attempts to date have been reasonably unsuccessful due to cracking of the coating due to the brittle nature of glass [124, 125]. Therefore, the use of HA materials is more commonplace and a potential method to improve the bioactivity of HA is to dope it with silicon. More specifically phosphate groups could be substituted by silicate groups. However, it is important that this ionic substitution does not affect the thermal stability of HA resulting in the decomposition to undesirable secondary phases [126]. Several attempts have been made by researchers to produce silicon doped HA materials. Ruys [127] prepared a silicon-doped HA by a sol-gel method but secondary phases of calcium silicophosphate [$Ca_5(PO_4)_3SiO_2$] and α- or β-TCP were formed depending on the silicon doping level. It was suggested that silicon substituted into the HA lattice in the place of phosphate groups did not occur. Tanizawa *et al*. [128] and Sugiyama *et al*. [129] produced a silicon doped HA by hydrothermal methods again suggesting substitution had taken place, however the Ca/(P + Si) ratio was measured at 1.71 which is higher than the 1.67 of HA, indicating that substitution had not occurred. Other approaches have included the co-substitution of ions but all failed to substitute silicon successfully [130, 131]. Gibson *et al*. [126] successfully prepared 0.4 wt.% silicon substituted HA (SiHA) via an aqueous precipitation reaction. Rietvelt refinement of the diffraction data resulted in a small decrease along the a axis and an increase in the c-axis and it is thought this is due to the substitution of larger silicate groups for the phosphate groups. In addition, a reduced number of OH groups where present in the SiHA and it was suggested that this was due to a charge balance effect. When the group SiO_4^{4-} replaces the

PO_4^{3-} group a difference of -1 is created. In order to restore charge order the easiest way of the HA structure to accommodate this is to lose 1 OH^- group. This method of producing SiHA has been subsequently reproduced by numerous authors [132, 133].

Values ranging from 0.1 to 4.9 wt.% silicon incorporation have been reported in the literature [126, 134] which relate to the method developed by Gibson *et al*. [126]. After inclusion of about 5 wt.% silicon the HA material becomes thermally unstable and degrades. Silicon acts to stabilise phases such as α- or β-TCP and CaO, which commonly appear in HA materials with high quantities of doping. Unfortunately, it is not easy to identify a substituted or non-substituted HA material. Gibson *et al*. [126] suggested that a lack of secondary phases indicated that phosphate groups had been replaced by silicate groups. Rietvelt analysis is commonly used to refine XRD data to calculate lattice parameters which again is a good indication of substitution. Balas *et al*. [135] and Botelho *et al*. [136] used XPS chemical analysis to deduce whether substitution had occurred. It was suggested that at low binding energies (101 eV) the silicon was in a monomeric SiO_4 formation and therefore likely to be substituted whereas at higher binding energies (103 eV) silicon was in a polymeric SiO_2 form and could not fit into the HA lattice. Less conclusive methods are FTIR and Raman spectroscopy [137], which can show the presence of Si-O bonding but also a reduction of OH groups. One issue is, however, that Si-O peaks tend to overlap with P-O vibration peaks and so this is rather a speculative method. While data can be obtained about the chemical structure of silicon in SiHA ceramics its exact position is not well understood. Vallet-Regi and Arcos [138] suggested that silicon may either lie in grain boundaries or be homogeneous throughout the HA structure, however recent selected area electron diffraction studies showed that silicon was present in equal distributions across the sample [139]. To the current author it appears that while the evidence for silicon substitution suggests that if such events are

occurring, this evidence is circumstantial and more in-depth studies are required to understand the exact location and position of silicon in the HA structure.

2.5.2. Biological Response to Silicon substituted Hydroxyapatite

2.5.2.1. *In Vitro*

Interestingly, only a small amount of literature is available for *in vitro* testing of SiHA materials. Gibson *et al*. [140] demonstrated that by substituting silicate groups for phosphate groups an enhanced osteoblast cell activity could be observed. Furthermore, Balas *et al*. [135] found that 0.8 wt.% SiHA allowed the formation of a carbonated apatite layer on its surface more readily than HA samples. However, it was also found that unsubstituted 1.6 wt.% SiHA did not show any difference when compared to an HA control. This may indicate that silicon should be in a monomeric (soluble) form as opposed to polymeric (insoluble), to enhance osteoblast activity.

2.5.2.2. *In Vivo*

Multiple works have examined the response of SiHA granules and ceramics and all studies suggest that SiHA materials elicit an enhanced biological response compared to HA. However, it appears that no optimum value of silicon substitution has been identified for the use with bone. Gibson *et al*. [141] investigated HA and 1.2 wt.% SiHA by implanting cylinders of the ceramic material into the distal femurs of 6 month old New Zealand White rabbits. It was found that after 7 days significantly higher amounts of new bone formation were discovered at the SiHA/bone interface, however, not on the HA/bone interface. After 14 days bone ingrowth was found in both samples but again it was significantly higher for the SiHA sample. After 3 weeks the animals were sacrificed and cross sections were made of implanted plugs. Figure 2-14 shows bone ingrowth into HA and SiHA

inserts after 3 weeks of implantation illustrating the increased bone ingrowth in the SiHA samples compared to the HA sample.

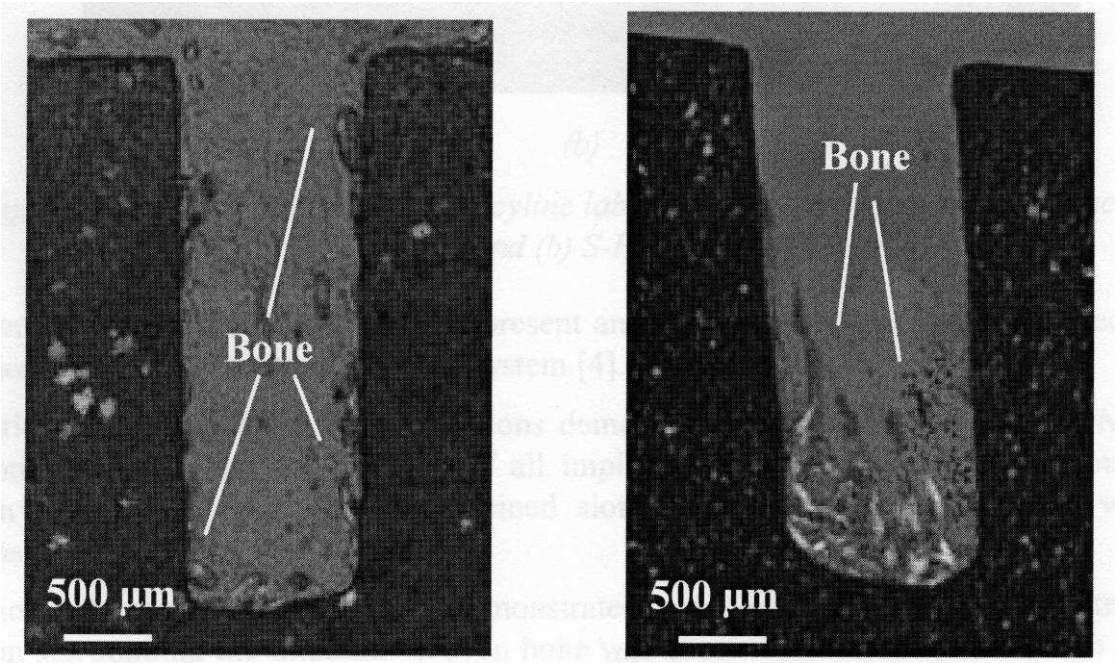

a **b**

Figure 2-14. Comparison of a) HA and b) 1.2 wt% SiHA inerts implanted into the distal end of the femur of New Zealand White rabbits after 3 weeks implantation. Taken from [141].

Further studies have shown similar trends with more bone ingrowth and bone coverage found when comparing 0.8 wt.% SiHA with HA granules in a rabbit model [142]. Patel *et al*. [143] looked at HA, 0.8 and 1.2 wt.% SiHA. Bone ingrowth and coverage was seen to be significantly increased for the SiHA samples, however there was no significant difference for the 0.8 and the 1.2 wt.% at 6 and 12 weeks of implantation into ovine models. A comprehensive study by Hing *et al*. [133] investigated multiple amounts of silicon substitution in New Zealand White rabbits. HA, 0.2, 0.4, 0.8 and 1.5 wt.% SiHA compositions were used to obtain an optimum value for bone ingrowth and mineral apposition rate after 1, 3, 6 and 12 weeks *in vivo*. It was seen that 0.8 wt.% SiHA supported significantly ($P<0.05$) higher amounts of bone ingrowth compared with all other samples and so this was concluded as an optimum value. As no other study has

investigated silicon content in so much detail few comparisons can be made with the literature. Porter *et al*. [139] used high resolution transmission electron microscopy to study the interface of SiHA materials apposed to bone using 1.5 wt.% SiHA samples that had been implanted in sheep. Organised collagen fibrils were found after 6 weeks of implantation at the interface of the SiHA samples and bone but not the HA samples, however collagen was found at bone after 12 weeks.

All current studies strongly suggest that SiHA materials allow more rapid bone ingrowth and bone regeneration than conventional HA ceramics. However, an optimal value of silicon substitution is yet to be identified. Further studies are needed to see if what this value or range may be.

2.5.3. Mechanisms of Bone Apposition to Silicon substituted Hydroxyapatite

Substituting silicon into HA has been shown to have various effects on the properties of HA materials. Porter *et al*. [144] used TEM to study the microstructure of a 0.8 wt.% SiHA material. It was found that a larger number of triple junctions (figure 2-15) were observed in SiHA material when compared with HA materials and it was proposed that this increase in defects could increase the solubility of the material leading to its excellent bone apposition rate. Wen and Liu [145] suggested that grain boundary structure was the predominant influence on the dissolution behaviour of apatite and that solubility is directly linked to the 'bioactiveness' of such ceramics [71]. This effect is not exclusive to SiHA and work has shown that other substitutions such as aluminium and carbonate can also increase the number of dislocations and grain boundaries which can lead to increased dissolution rates [146]. Furthermore, Porter *et al*. showed SiHA dissolution followed the order 1.2 wt.% SiHA > 0.8 wt.% SiHA > HA, both *in vitro*

using simulated body fluid at pH 7.3 and *in vivo* in various models. This was attributed to a less ordered grain structure and increased number of lattice defects [144, 147-149].

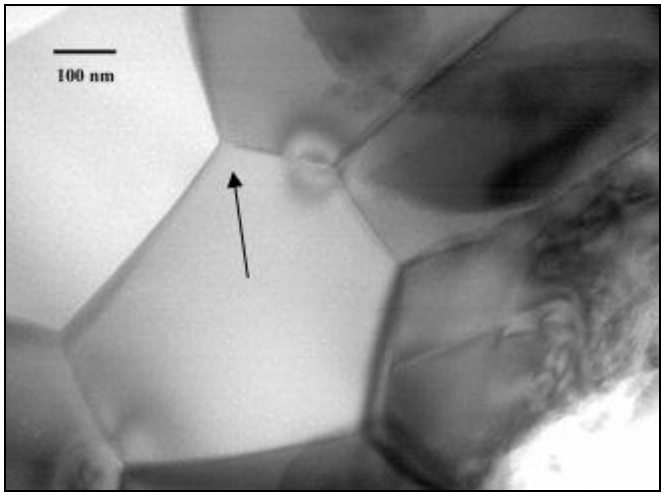

Figure 2-15. TEM dark field micrograph of 1.5 wt.% Si-HA showing an example of a triple junction. Black arrow denotes a triple junction. Taken from [144].

A number of theories exists as to why HA is a bone bonding material, the most common of which is the 'dissolution-reprecipitation' theory which can occur both *in vitro* and *in vivo*. Dissolution of calcium and phosphate ions from the surface of such ceramics leads to a local increase in ion concentration which allows the reprecipitation of a carbonated apatite layer on the HA surface [150]. However, carbonated apatite layers have been show to form on non-calcium phosphate surfaces after a few days suggesting this localised increase in ions may not need to occur [151]. Alternative theories have subsequently been proposed; Amarh-Boulai *et al*. [152] suggested that an amorphous apatite layer forms on the surface of ceramics and is transformed to a crystalline apatite. The surface composition and morphology could affect protein adhesion and conformation which could then act as template nucleation sites resulting in bone bonding. Thus it appears that dissolution is important for osseointegration but other factors may be related to the process of bone bonding [153]. It is still unclear how silicon helps to improve bone apposition. Three possible mechanisms may play a crucial

role; modification of surface topography resulting in decreased grain size, acceleration of the dissolution–reprecipitation process due to a decrease in grain size and the effect of silicon substitution on collagen organisation around the implant [153]. A smaller grain size may influence protein conformation and cellular adhesion to the Si-HA implant surface and contribute to increase bone apposition [153]. Silicon in SiHA materials may directly act as nucleation sites for carbonated apatite precipitation [154]. Indeed, the importance of Si-OH bonding in Bioglass® has already been discussed (section 2.4.4.). Finally, silicon itself has been shown to be important in the formation of new bone. It may be that silicon can actively lead to differences in collagen formation around the implant surface and this again has been discussed in section 2.4.3. While a number of mechanisms have been suggested to explain why SiHA materials allow faster bone apposition compared to HA ceramics no conclusive information is yet available.

2.6. Hydroxyapatite as a Coating

In load bearing joints, such as the hip, a metal or composite implant is essential to take the load if the joint is to be replaced. However, many metals are bioinert leading to the formation of a fibrous capsule around the device which is undesirable and may reduce the long-term success of the prosthesis [2]. Furthermore metallic implants are required to be cemented into place using PMMA cement. This allows secure fixation of implants and acts to transfer the load from the implant to the bone via the bone/implant/cement. As shown in section 2.2.5. bone cement has a modulus lower than that of bone and can act to reduce stress shielding. The cement may also act as a shock absorbing layer between the elastic bone and the stiff implant [155]. However, there are still problems related to the use of bone cement. When the cement is cured the reaction is exothermic and can produce temperatures in the range of 70 – 120 $^{\circ}$ C. Collagen is known to denature at 56 $^{\circ}$ C and so concerns have been raised about the thermal damage cement may cause. Furthermore, aseptic loosening is suggested to be accelerated by monomer mediated bone damage. Upon setting of the bone cement shrinkage can occur which can act to but strain on the bone/cement interface, however this may only be a theoretical concern. These problems have led researchers to look for alternatives such as press fit implants that do not require cementation [155].

HA has been shown to be bioactive [156] allowing a direct bond to be formed between surrounding tissue and the implanted ceramic, making it an excellent candidate for a bone repair material. However, as previously discussed, HA is brittle and has a modulus higher than that of bone, thus restricting the use of HA to non-load bearing implants. One possible solution to this problem is to coat HA materials onto metallic substrates thus combining the excellent mechanical properties of metals and the bioactivity of HA. Furthermore, this method eliminates the need for bone cements and can achieve higher fixation strengths

[157] and reduced healing times [158], translating into improved post operative mobility and reduced pain for the patient, in comparison to uncemented metallic prostheses. Many coating methods are available which are discussed below. Currently the only commercially viable coating option is plasma spraying.

Plasma sprayed HA coatings have shown good success clinically [159, 160] as measured by bone ingrowth and a lack of adverse effects caused by HA particle release. This process was first carried out with HA material by de Groot *et al.* [63] depositing a thin layer onto a titanium substrate. Plasma spraying belongs to a family of coating processes called thermal spraying. This group includes other processes such as high velocity oxy-fuel (HVOF) and flame spraying. All the above techniques work on the fundamental principles of a heat source, a way of accelerating particles at high velocities, the coating of material in a powder, wire or occasionally liquid form. Plasma spray has provided the highest quality of coating of all the thermal spray techniques with reduced impurity and porosity levels.

Unfortunately, plasma sprayed HA coatings, are not without their problems. Different crystallinities and undesired phases such as α- and β-TCP and CaO caused by thermal decomposition of HA [161], which has been directly correlated with their dissolution potential [162] may lead to a variations in cellular response. Moreover, poor bond strength at the implant/coating interface, voids, cracks and variation in composition from vendor to vendor [163] has led researchers to investigate alternative coating methods. Pulsed laser deposition [81, 164-166], sol-gel/dip coating processes [167-170], electrophoretic deposition [171-175] and chemical vapour deposition (CVD) [176] have all been used and produced coatings with varying degrees of success. Table 2-5 details advantages and disadvantages of some currently available coating techniques. One increasingly

popular option is to use radio frequeny (RF) magnetron sputtering [177-184]. This method produces thin films and coatings that are well adhered, dense, defect free and homogeneous in composition [86, 178]. This process is discussed in detail in the subsequent section.

Technique	Thickness	Advantages	Disadvantages
Thermal Spraying (Plasma Spraying)	30-500 μm	High Deposition Rates, low cost; commercially viable	Line of sight technique, high temperatures induce decomposition, rapid cooling produces amorphous coatings
Cold Spraying	30-500 μm	Low temperature so no thermal decomposition, high deposition rates	Poor coating adhesion due to low relative coating density
Sputter Deposition (PVD)	0.05-3 μm	Uniform coating thickness on flat substrates, dense coating	Line of sight technique, expensive, time consuming, amorphous coatings
Pulsed Laser Deposition	0.05-5 μm	Coating with crystalline and amorphous; coating with dense and porous	Line of sight technique
Dip Coating	0.05-0.5 mm	Inexpensive, coatings applied quickly, can coat complex structures	Requires high sintering temperatures, thermal expansion mismatch
Sol-gel	<1 μm	Can coat complex shapes, low processing temperatures, relatively cheap as coating are very thin	Some processes require controlled atmosphere processing; expensive raw materials
Electrophoretic Deposition	0.1-200 mm	Uniform coating thickness; rapid deposition rates, can coat complex substrate.	Difficult to produce crack free coatings, requires high sintering temperatures
CVD	n/a	Novel technique	Complicated pre-cursors, low Ca/P ratios, high sintering temperatures
Biomimetic coating	< 30 μm	Low processing temperatures, can form bone like apatite, complex shapes can be coated, can incorporate growth factors	Time consuming, requires constant renewal of simulated body fluid
Hot Pressing and Hot Isostatic Pressing	0.2-2.0mm	Produces dense coatings	High temperature required, thermal expansion mismatch, elastic property differences, expensive, removal/interaction of encapsulation material

Table 2-5. Advantages and disadvantages of coating techniques currently available for medical devices. Adapted from [185].

2.7. Magnetron Sputtering

2.7.1. A Brief History of Sputtering

The first report of sputter coating was produced by Grove [186]. He observed that sputtered material emitted from the tip of a wire held in close proximity to a highly polished silver surface produced a coloured ring structure. No significant studies on these thin films were reported as he was more interested in the voltage properties of the system. In 1854 Faraday reported a deposition using plasma, later followed by the first sputtering apparatus being detailed by Wright in 1877 used to form mirror surfaces. Edison produced the first methodology to use sputtering a commercial entity, manufacturing 'gold molded records' in 1902.

2.7.2. The Fundamentals of Sputtering

Sputtering is a non-thermal vaporisation process in which surface atoms are physically ejected from the surface by momentum transfer from an energetic bombarding species of atomic/molecular size [187]. Figure 2-16 shows a simplified idea of the sputtering process. Sputtering normally involves the use of a glow discharge or ion beam to generate a flux of ions or energetic neutrals capable of impinging on a material surface or target. When high energy incident ions or neutrals collide with the target surface, atoms or clusters of atoms are ejected by impact transfer [188]. Atoms will only be ejected if the collision energy is greater than the material's lattice energy. These ejected atoms can then be re-deposited onto another surface which is termed a substrate. With the use of many incident ions re-deposited material can be built up on the substrate which is termed sputter deposition. This material is typically less than 1 μm in thickness and thus is referred to as a thin film [189].

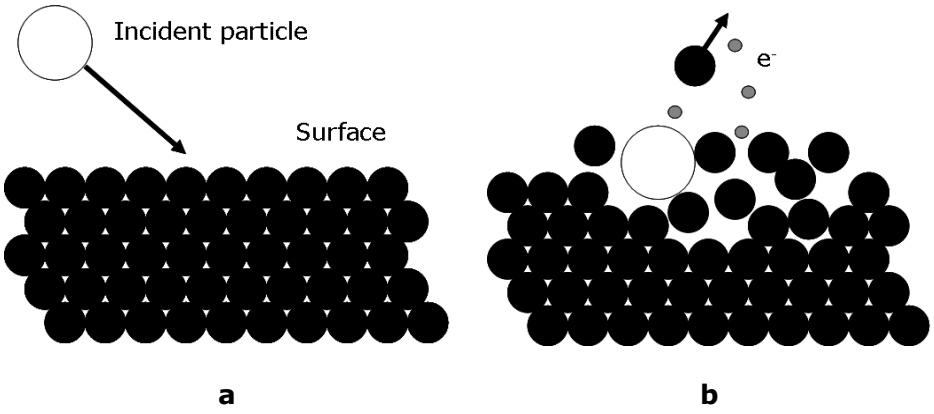

Figure 2-16. Schematic showing a simplistic idea of a possible outcome of the sputtering process at an atomic level, where a) illustrates a presputtering event and b) the affects of an incident particle immediately after collision, showing sputtered atoms and secondary electrons.

Advantages	Disadvantages
Low temperature deposition	Low deposition rates 5-50 nm min^{-1}
Elimination of droplet formation such as in Plasma Spray	High initial costs due the need for a vacuum system
Multi-component films can easily be formed	Line of sight process
Thickness uniformity	Energy efficiency low
High adhesion properties	Amorphous coating without post deposition treatments
Almost anything can be sputtered with the exception of some organic compounds	Difficult to control stoichiometry due to preferential sputtering

Table 2-6. Advantages and disadvantages of sputtering. Adapted from [187, 189].

Sputtering is a highly versatile process which can be used to deposit many materials. However, the initial cost for such systems is higher than nearly all other coating systems [189]. Deposition rates are low which can add to the overall cost of a device or component if a thicker film is required. Some materials can be extremely difficult to use as targets because they substantially outgas in the vacuum environment; a problem for which many polymers would encounter. A

brief list of sputter deposition advantages and disadvantages are shown in table 2-6.

2.7.3. Sputtering Systems

2.7.3.1. Direct Current (DC) Sputtering

The simplest form of sputtering system is the direct current (DC) sputtering technology which employs a conductive target material to sputter deposit thin films. Two electrodes, a cathode and anode, are situated in a deposition chamber which is subsequently evacuated to a base pressure of typically 10^{-6} Torr (1.3 x 10^{-4} Pa) or better. The chamber is then filled with a noble gas, normally argon, at a pressure typically between 1 to 200 mTorr (0.13 to 26.66 Pa). A highly negative DC voltage is applied across the target, typically hundreds to thousands of Watts, making it the cathode in the electrical system and the substrate material is attached to an electrically grounded anode completing the circuit. This causes electrons to be ejected from the cathode which then act to ionise argon atmosphere producing positive argon ions. These ions are then attracted to the cathode at energies dependant on the voltage across the system. As these ions travel towards the target material they commonly recombine with electrons thus producing energetic neutrals. On impact, some target material is removed. As the system is in a vacuum, target material will be deposited everywhere in the chamber. These sputtered atoms are generally composed of neutral single atoms however a small percentage of ions exist. In the case of copper sputtered at 100 eV, 95 % of the population are single copper atoms while 5 % are Cu_2 molecules. At higher voltages atom clusters are more common [190].

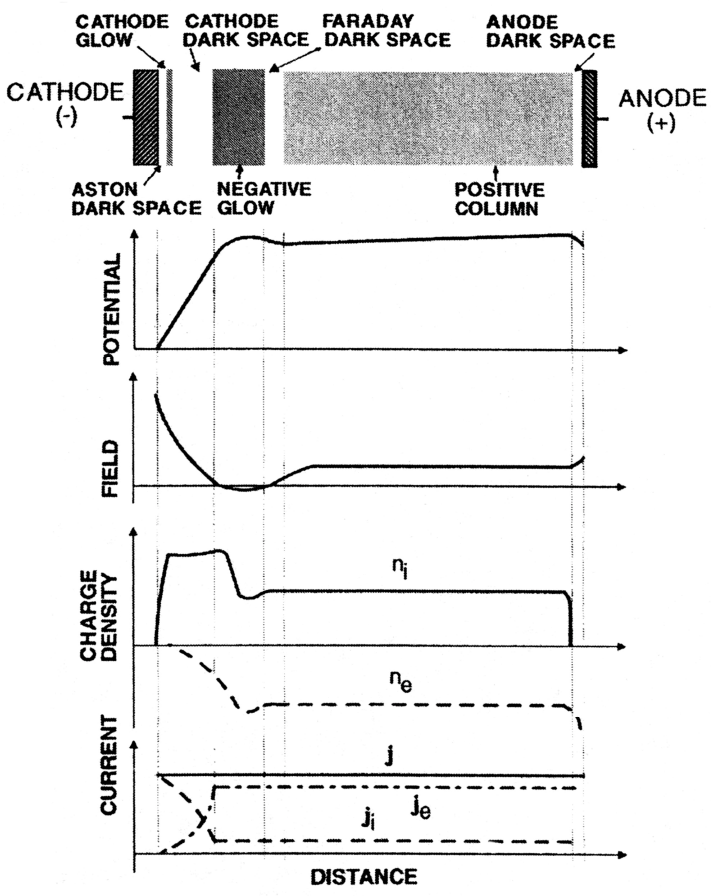

Figure 2-17. The structure of a DC glow discharge with corresponding potential, electric field, charge and current distributions. Taken from [191].

Figure 2-17 shows the structure of a DC glow discharge between a cathode and anode. The Aston dark space closest to the cathode contains low energy electrons and high energy positive ions each moving to opposite electrodes. A cathode glow region precedes this dark space. The coloured glow is caused by neutralisation of positive ions. In the cathode dark space electrons are energised to the point where they begin to impact ionise neutrals, however there is relatively little ionisation so this region is dark. There is a large drop in voltage across this dark region which is commonly referred to as the cathode sheath. The resultant electric field acts to accelerate ions towards the cathode. In the negative glow region a visible emission is seen due to interactions between secondary electrons and neutrals leading to excitation and de-excitation. Further along is the Faraday dark

space, positive column and the anode. Often the substrate is placed in the negative glow region and so these do not normally appear [191].

When ions and energetic neutrals impact with the cathode or target many scenarios may occur of which sputtering is one. These events are shown in figure 2-18. The particle can be reflected, which generally occurs when the particle is of lower atomic mass than the target material. A secondary electron, characteristic X-ray or photon may be ejected or incident particle may become implanted into the surface. Structural rearrangements such as atom vacancies, interstitials or changes in stoichiometry in compound targets may occur. These three changes are known as radiation damage. The sputtering process will result in material being ejected in all projections with a smaller quantity arriving at the substrate surface thus forming a thin film [189]. The erosion rate of ions removing target materials can be characterised by the sputtering yield S which is defined as the mean number of emitted atoms per incident particle. This value can vary hugely between different incident particles and target materials, but experimentally lie between 10^{-5} and 10^{3} atoms per incident particle [192].

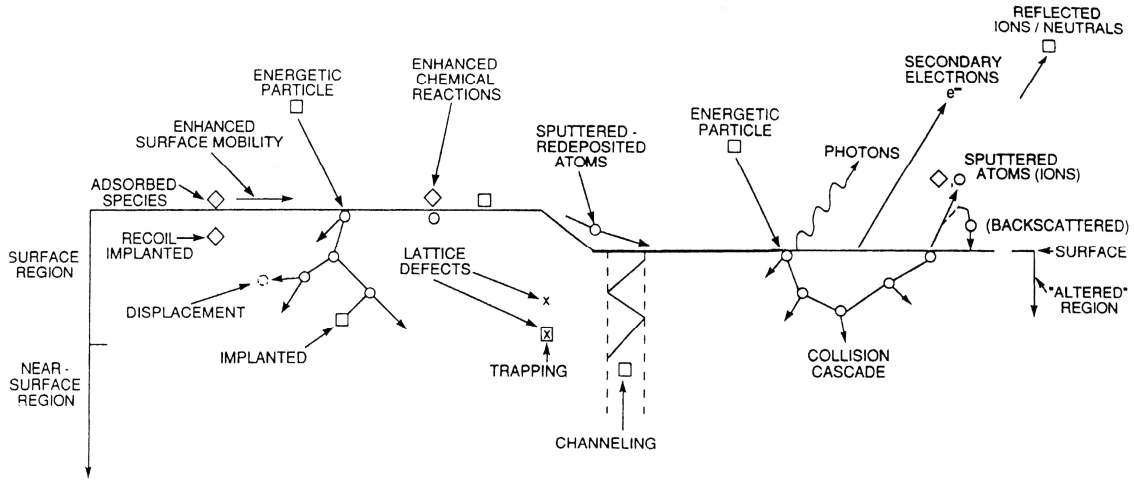

Figure 2-18. The interaction between ions and a target surface during the sputtering process. Taken from [191].

2.7.3.2. Radio Frequency (RF) Sputtering

HA is an insulating material and so DC power supplies cannot be used unless a voltage of 10^{12} can be achieved. A positive charge builds up on the target surface causing arcing. One of two solutions may be applied to overcome this problem. The first is to pulse the DC current between positive and negative voltages. This allows charge build up at the surface of the target to be dissipated. The second, and most popular solution, is to use a radio frequency (RF) power supply up to a frequency of 50 MHz. A common set up is shown in figure 2-19. In most cases this is 13.56 MHz as this is the value assigned by the Federal Communications Commission so as not to interfere with telecommunications [189]. By alternating the target potential the surface can be neutralised. This is optimised so that the potential is negative for long periods of time to allow sputtering with a small time at positive voltage to dissipate charge. The RF diode sputtering system requires an impedance-matching network between the power supply and discharge chamber. The impedance of the RF power supply is almost always 50 Ω. The impedance of the glow discharge is in the order of 1 to 10 k Ω [190].

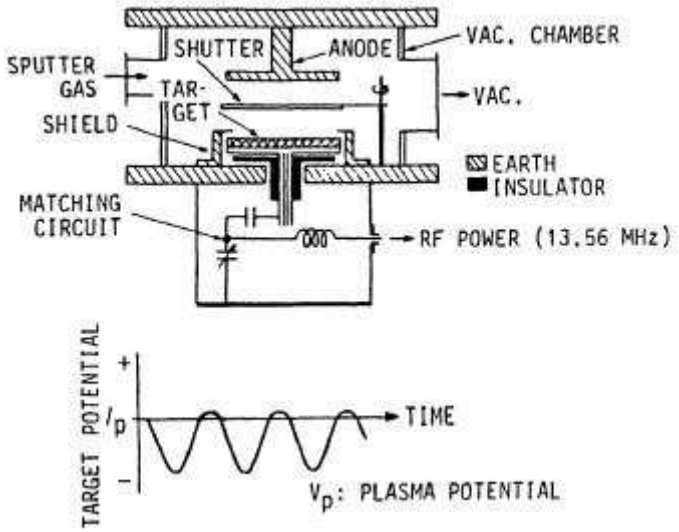

Figure 2-19. A RF sputtering system setup with target potential. Taken from [191].

RF power supplies have the advantage of lower operational pressures, between 1-15 mTorr (0.1-2.0 Pa), when compared to DC discharges which operate at 100-200 mTorr (13.3-26.7 Pa), since the RF electrical field in the discharge chamber increases the collision probability between secondary electrons and gas molecules [190].

2.7.4. Magnetrons

When an electric field is used in combination with a magnetic field secondary electrons are directed into a cycloidal path leading to high ionising efficiency [193] confining the glow discharge to the near target region. This magnet is known as a magnetron. Magnetrons allow higher deposition rates due to the magnetic confinement created when compared with sputtering alone. As the 'magnetic trapping' is increased, the path length and residence time of the electrons in the near-cathode plasma region is multiplied and so is the probability to undergo ionisation collisions which in turn increases the sputtered flux by up to ten times and therefore increasing the deposition rate [194]. The planar magnetron (figure 2-20) is the most common type of magnetron which is generally circular or rectangular in geometry and can range from 2.5 cm to 8 m in diameter. All planar magnetrons erode preferentially where the magnetic field is parallel to the target surface. This results in the formation of a racetrack in the annulus region. Many studies have examined the erosion of targets on planar magnetrons and developments such as cylindrical target geometries have been created which increase sputtering rates and target lifetime. However non-planar targets are often expensive to manufacture limiting their use in commercial applications.

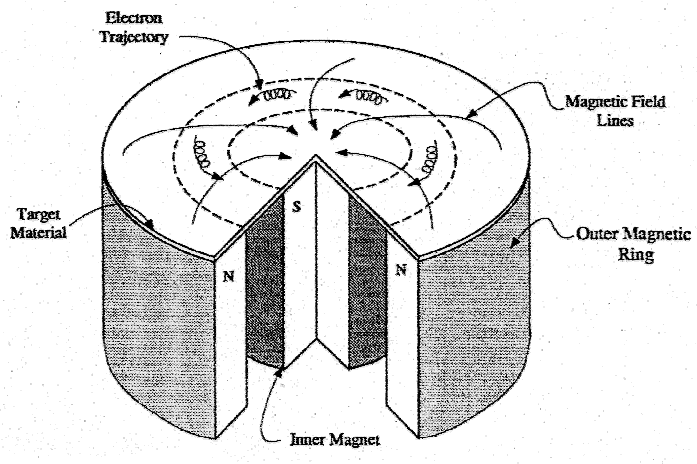

Figure 2-20. A circular planar magnetron illustrating the magnetic confinement and the resulting electron trajectories. Taken from [187].

Two types of magnetron are available; balanced and unbalanced. A balanced magnetron has uniform strength within the magnetron affected area but this leads to decreased current density of the ion flux arriving at the substrate with increasing source to substrate distances. However, this problem can be overcome by the use of an unbalanced magnetron where magnetic stray fields are used to concentrate ion flux density further away from the target surface and closer to the substrate. Two types of unbalanced magnetron configurations are available (figure 2-21); type I (figure 2-21a), which is distinguished by a strong inner pole and weak outer pole and type II (figure 2-21b) which is the converse arrangement. Type II configurations are of the most use for industrial applications because ion to deposited atom ratios can be as high as 2:1 whereas this is only 0.25:1 for the type I magnetrons at a specified distance from the sample [187].

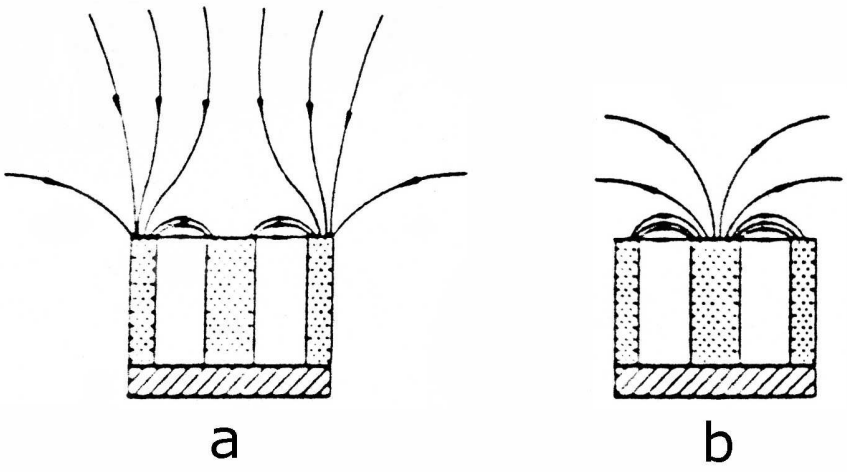

Figure 2-21. The two types of unbalanced magnetron a) type I and b) type II.

2.7.4. Thin Film Growth

Three thin film growth mechanisms have been identified; the Volmer-Weber, Frank-Van der Merwe and Stranski-Krastanov. In depth descriptions of each mechanism can be found elsewhere [191]. However, all follow a similar sequence of events. Soon after exposure of the substrate to the plasma, small but highly mobile clusters or islands form on the substrate surface. In the initial stages these clusters incorporate incoming atoms and molecules. Islands then go through a coalescence stage where islands grow connecting with neighbouring clusters. This occurs via a liquid like phenomenon, especially at high substrate temperatures. As this process continues a network is formed with some unfilled channels, with continuing deposition the channels and voids become filled forming a uniform film. This sequence of event occurs in the first few hundreds of angstroms of deposition [191].

Movchan and Demchishin proposed a structure zone model describing the structure of growing films for vacuum deposited films. Thorton and Messier later

proposed a model for sputter deposited films (figure 2-22). This classifies microstructure dependant on argon pressure and substrate temperature. In the model zone 1 shows a thin film with a columnar microstructure with round and tapered grains. The columns are closely packed with spaces or open boundaries between each column. Zone 1 microstructures are formed at substrate temperatures (T_S/T_M) less than 0.3 and partial pressures in excess of 10 mTorr (1.3 Pa). This microstructure is formed due to adatoms coating the surface not having sufficient mobility to overcome substrate surface features. Films possessing this structure have a high surface area, mossy appearance and poorly defined crystal structure.

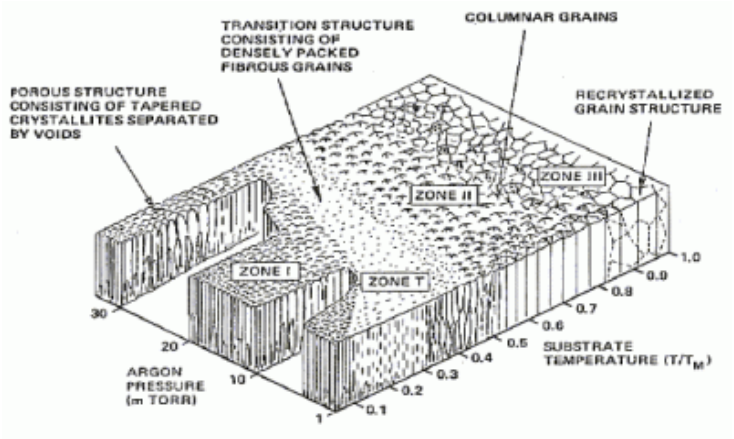

Figure 2-22. Thornton-Messier structure zone model for sputter deposited films.

A zone T microstructure is characterised by dense fibrous columnar grains which are a transitional stage between zone 1 and 2 structures. Zone T is formed when the growing film is bombarded with energetic ions and neutrals leading to erosion of the surface. As a result this zone has fewer voids resulting in a smooth film with a high density. Zone 2 films are close packed, more dense and columnar in morphology in contrast to zone 1 films. Zone 2 growth is dominated by adatom surface diffusion in the T_S/T_M region of 0.5 – 0.8. Therefore films are denser due to depositing adatoms having increased surface mobility. Zone 3 films are formed

when T_S/T_M is larger than 0.8. Here bulk diffusion is dominant in determining microstructure resulting in dense microstructures similar to that of bulk materials.

2.8. RF Magnetron Sputtering of Hydroxyapatite Thin Films

Many researchers have investigated RF magnetron sputtered HA thin films. Pioneering work occurred over two decades ago, and films are still been investigated. This area has been further developed with the use of interlayers [195] between the substrate and coatings and dopants, such as yttrium [196], titanium [197], magnesium [198] and silicon [199] which have been added to films to improve bioactivity, stability and mechanical properties. The following section looks at RF magnetron sputtering with particular regard to HA thin films.

2.8.1. Sputtering Parameters

Discharge power, sputtering pressure, gas composition and target material are all important parameters which can affect resultant thin films. These have been discussed in the subsequent sections.

2.8.1.1. Discharge Power

Discharge power affects the composition and the deposition rate of HA thin films. With increasing power density the flux of positive particles colliding with the target will increase thus increasing the sputtering yield (Y). Therefore, the probability that a single atom will impinge on the substrate is increased again thus increasing the deposition rate. At a given pressure a relationship has been suggested for DC discharges to predict film growth rate, G:

Eqn 2.3.
$$G \approx \frac{\wp_d < X_{th} >}{g\rho(1+\gamma_e)E^{'}}$$

Where $\wp_d$ is applied power density, X_{th} is the mean distance for cathode sputtered atoms to travel before they obtain the same kinetic energy of the

surrounding gas, g is the cathode to anode distance, ρ is the atomic density of the target (atoms cm^{-3}), γ_e is the Townsend secondary electron emission coefficient and E' is the average sputtering energy (~ 1 KeV).

Van Dijk *et al.* [182, 183] demonstrated a weak correlation between increasing power density and calcium to phosphate ratio (Ca/P) suggesting that other factors such as plasma-sprayed target composition variation played a part in determining film composition. This weak correlation was again observed by Ozeki *et al*. [70] at powers between 50 - 100 W (target dimensions not given), with Ca/P ratios ranging from 1.7 - 2.4, but which decreased slightly at 150 W. Recently an improved correlation was observed by Yamaguchi *et al*. [200] who showed a notable increase in Ca/P ratio from 1.11 to 1.59 with power densities ranging from 2.55 - 5.09 W cm^{-2}. Ca is more probable to reach the substrate than P due to its higher atomic mass. Furthermore, when on the surface of the growing film it is less likely to be removed, whereas phosphorus is known to be re-sputtered from the film. As the power density is increased these events occur more frequently with the net effect of more Ca present in the film and less P. It was suggested that other factors are responsible for the change is Ca/P ratio with increasing power density such as target purity and sputtering consistency [183].

2.8.1.2. Sputtering Pressure

Sputtering pressure affects many parameters, such as coating thickness, composition and discharging effect related to the sputtering target [201]. Figure 2-23 shows the variation of deposition rate with sputtering pressure for a non magnetron sputtering DC discharge. At pressures increasing from 20 – 100 mTorr (2.7-13.3 Pa) the deposition rate of sputtered material is increased. This plateaus between 100 and 120 mTorr (13.3-16.0 Pa) and the decreases after this point. At low pressures the cathode sheath is wide and so ions and neutrals are lost the

sputter chamber walls. Moreover, the distance travelled between collisions is large and electrons collected at the anode are not replenished by impact of energetic particles colliding with the target so the plasma is not self sustaining. As the pressure is increased the distance travelled between collisions is smaller so more ions are generated and a larger current can flow. If the pressure exceeds 120 mTorr (16.0 Pa) the ions undergo increased collisional scattering and so less make it to the substrate surface.

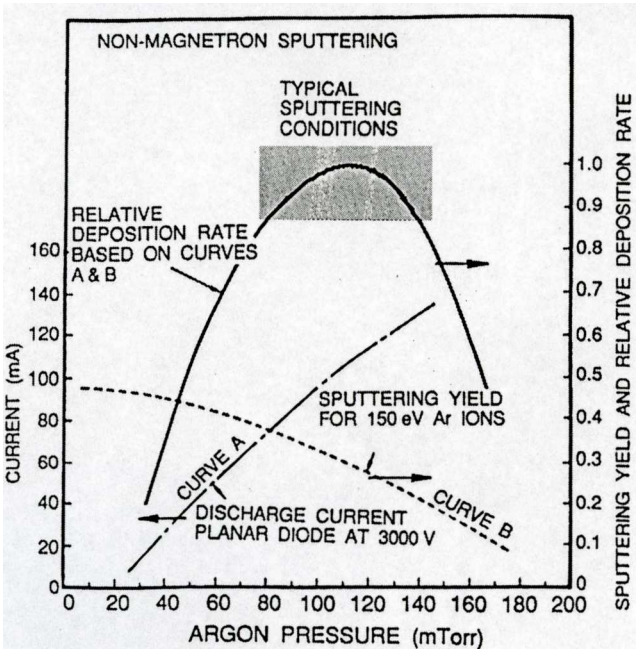

Figure 2-23 Influence of sputtering pressure and current on deposition rate for a DC non magnetron sputtering system.

RF discharges can operate at lower sputtering pressures and so the optimal sputtering pressure is considerably lower than a DC discharge. Moreover, the use of a magnetron increases ionisation thus lowering the need for higher sputtering pressures. Van Dijk *et al*. [182] studied the influence of argon pressure on the sputtering of HA thin films between 1.95 and 19.5 mTorr (0.3 and 2.6 Pa) at power densities between 2.5 and 10.2 W cm^{-2}. It was reported that deposition rate increases with argon pressure. Ozeki *et al*. [70] studied argon pressures between 3.7 and 37.5 mTorr (0.5 and 5.0 Pa) at power densities of 2.5 – 7.64 Wcm^{-2}. The study found that deposition rate decreased with increasing argon

pressure. As both authors did not use directly comparable power densities it is difficult to establish the optimal argon gas pressure at a given power density.

Compositional differences can also be observed with increasing sputtering pressure. The composition of HA thin films can be measured in terms of the Ca/P ratio. This Ca/P ratio directly follows the deposition rate approaching stoichiometric HA at low or higher pressures. When the sputtering pressure increases there is an increase in the number of argon ions colliding with the target. At the same time the number of argon ions deflecting back from the target increases and the thin film becomes re-sputtered away form the substrate surface. As phosphorous (RAM = 30.1) is lighter than calcium (RAM = 40.1) the phosphorus is more affected by the re-sputtering. Van Dijk *et al*. [182] found the Ca/P increased with increasing pressure whereas, Ozeki *et al*. [70] found that Ca/P ratios decreased with increasing argon pressure. This difference was explained by varying deposition rates (discussed above).

2.8.1.3. Substrate Biasing

The anode or substrate can be biased by application of a DC in non-reactive situations or RF power supply in reactive situations. Typically this is in the region of -50 to -300 V. This acts to vary the flux and energy of depositing charged species. Biasing can alter a larger number of film properties such as adhesion to the substrate, film density, hardness, residual stresses, morphology, gas content and composition [191].

2.8.1.4. Gas Composition

Sputtering can be carried out with almost any atom or molecule. However, noble gases are the only viable option to avoid reactive sputtering which may lead to films with little similarity when compared to the target materials. The sputtering

yield increases with the atomic mass of the sputtering gas. Non-reactive sputtering is generally carried out in argon atmospheres as this noble gas is readily available and inexpensive [189].

Studies have shown that for HA thin films the Ca/P ratio can be reduced by the inclusion of oxygen into the argon atmosphere [181, 202]. This effect became pronounced up to 5 vol.% (of 'argon' (*sic*) pressure) oxygen after which no benefit was observed [181], the theory being that increased oxygen allows reactive sputtering to occur between phosphorus and oxygen forming heavier phosphate species $(PO_4)^{-3}$ reducing the re-sputtering effect from the substrate and phosphorus not making it to substrates due to argon ion and neutral collisions, thus improving the stoichiometry of the films. A later study reported that 1% oxygen inclusion into an argon atmosphere lowered the Ca/P ratio from 2.03 to 1.77 [202]. Oxygen is an electron scavenger which reduces the number of electrons available for ionisation and therefore lowers the sputtering yield, which overall decreases the deposition rate of sputtered material.

2.8.1.5. Substrate Temperature

Substrate temperature is important for resultant HA thin films. In conventional systems the substrate is mounted on a water cooled substrate holder. A combination of heat from the target and heat generated by bombardment of high energy secondary electrons leads to heating of the substrate. In RF systems the substrate temperature can rise to 700°C. This effect can be reduced by cooling the substrate or applying a negative bias to the substrate reducing the number of secondary electron collisions with the substrate. The introduction of the magnetron can also act to lower the substrate temperature as this confines electrons and in normal RF magnetron sputter systems at low power densities substrate temperatures do not exceed 300°C [190]. Lo *et al*. [195] used FTIR to

investigate substrate heating between 67 and 241°C. It was shown that increasing the substrate temperature during deposition HA thin films became more hydroxylated, however no significant differences were found between phosphate bonding.

2.8.1.6. Targets

Targets approaching full density will have the highest deposition rate compared to a low density target. For experimental setups powder targets are sometime adopted due there easy production. Good practice is to run targets for a period of time before sputtering onto a substrate to sinter the surface through bombardment [190]. Thermally insulating targets must be cooled and run at lower powers as excessive heat can crack the ceramic.

Few studies have examined the effect of sputtering on the composition of target material. Ozeki *et al*. [70] observed that when sputtering at 150 W (target dimensions not given) and 5.0 Pa for 2 h a single phase HA target was transformed to a combination of HA, TCP and CaO. Further investigation revealed that at higher powers the amount of HA material that decomposed increased. It was also shown that α- and β-TCP was preferentially sputtered compared to CaO due to a lower atomic binding energy. The author concluded that local heating of the target must be in the region of 1400 °C for thermal degradation to occur. A more recent study [179] highlighted the problem of target degradation by showing that phosphate and hydroxyl groups were removed from the target during sputtering. An increase in the target Ca/P ratio was seen increasing from 1.67 to 2. The rate of degradation decreased with increased use of the target and it was suggested that targets could be reused without being replaced after every run because coating properties did not alter significantly between runs.

2.8.2. Hydroxyapatite Thin Film Observations

2.8.2.1. As-Deposited Structure and Recrystallisation of Thin Films

Below power densities of ~ 8 - 10 W cm^{-2}, HA as-deposited thin films are reported to be amorphous. Above this value heating of the substrate can occur transforming the deposited films into a semi-crystalline or fully crystalline state [183]. The amorphous nature of as-deposited films is due to the destruction of the HA structure into individual atomic components that are then randomly deposited onto the substrate. Van Dijk *et al*. [183] found that films sputtered at 7.64 W cm^{-2} were X-ray amorphous and films deposited at 10.19 W cm^{-2} films began to show a degree of crystallinity. The substrate temperature at 10.19 W cm^{-2} was measured to be 290 °C which produced enough energy to induce recrystallisation. It was also found that higher discharge powers lead to higher target temperatures. Other authors [202, 203] also noted as-deposited coatings to be X-ray amorphous, and it has been reported that a characteristic amorphous hump can appear at 30.5 ° 2θ in XRD plots [204]. One simple method to induce recrystallisation is post-deposition heat treatments. Yang *et al.* [203] heat treated the coatings for 1 h at 350 °C with and without water vapour and found that recrystallisation was not induced. At 450 °C in the presence of water vapour coating partial recrystallisation was observed in the film, but it was not until temperatures of 500 and 600 °C that a crystalline HA structure was observed. In addition, many authors have shown that heat treatments in the presence of water vapour can act to increase film crystallinity [203, 205], although it has been noted that no structural benefit occurs [185]. It is thought that this occurs because water molecules are more thermally conductive at a given temperature when compared to argon atmospheres. Lo *et al* [195] used FTIR to investigate post-annealing temperature ranging from 80 to 600°C. They found no significant difference between phosphate bonding at any of the temperatures, however at 500°C and above carbonate peaks could be observed. They found that the Ca/P ratio increased with

increasing annealing temperature. In summary, coatings begin crystallisation at about 300 – 400°C with or without water vapour and approach a full coating crystallinity between 500 – 600°C with or without water vapour, although these temperatures will depend on deposition parameters, coating thickness, composition, film residual stress and substrate material.

2.8.2.2. Crystallographic Orientation

It is common for thin films to be preferentially orientated along a given crystallographic plane. Crystal orientation has been reported by a number of workers for annealed HA thin films [161, 164, 177, 187, 188], with a preferred orientation was seen in the <001> direction where the c-axis is perpendicular to the substrate. Preferential orientation occurs to allow a reduction in micro-strain caused by a mismatch in the thermal expansion coefficient of HA and titanium substrates. When films are deposited initially preferential orientation occurs to reduce surface energy but as the film increases in thickness microstrain becomes the dominant factor. The majority of work observed this to be with the (002) plane being the most intense peak but Nelea *et al*. [205] found that on silicon substrates the (002) plane was not dissimilar to an HA powder, however, the (004) plane was twice as intense as expected. When films were grown on TiAlFe substrates a more pronounced orientation was noted for the (002) plane. Wolke *et al*. [206] showed that by rotating the substrate during the sputtering process preferential orientation could be prevented. While no explanation was offered for this it is probably due to the rotating substrate moving in and out of the sputtering plume thus not being continually heated thus reducing preferential orientation.

2.8.2.3. Grain Size

Grain or crystallite size can be calculated using the Scherrer equation or by measurement of transmission electron microscope (TEM) images. Ozeki *et al*. [207] calculated crystallite sizes to be between 40 – 100 nm and 30 - 50 nm for XRD calculations and TEM studies along the c-axis respectively. The difference in result could be explained by inaccuracy introduced by the Scherrer equation. Similarly, other authors [165, 205] have quoted values between 20 – 30 nm when calculated by the Scherrer equation. These figures are comparable to the mineral apatite crystals in bone which have been measured at 20 – 40 nm (section 2.2.1.1.).

2.8.2.4. Compositional Differences

Calcium is often preferentially sputtered onto the substrate leading to higher Ca/P ratios than that of stoichiometric HA. Various reasons have been given for this, in which a single or a multitude of mechanisms may have an effect. Phosphorus maybe re-sputtered from the substrate by negatively charged oxygen ions. Feddes *et al*. [208] studied the affect of phosphorus re-sputtering between argon pressures of 0.375 – 3.75 mTorr (0.1 – 0.5 Pa) and 2.54 W cm^{-2} providing evidence that phosphorus re-sputtering from the thin film decreases with increasing argon pressure leading to lower Ca/P ratios at higher sputtering pressures. It was shown that this re-sputtering from the substrate was caused by negatively charged oxygen particles (which originated from the target) which are suggested to be more abundant at low argon pressures, while at high argon pressures less energetic neutrally charged oxygen particles were present at higher concentrations which have little or no effect on the re-sputter rate of HA films. Phosphorus may also be decomposed by the glow discharge [182]. Being a lighter element than calcium, phosphorus and will suffer more from argon ion and neutral collisions. Calcium may have a higher sputter potential than phosphorus. Finally,

increased amount of calcium can enter the HA structure substituting for OH groups present along the c-axis [165], however this would require the loss of a Ca^{2+} atom elsewhere or $2H^{+}$ to charge compensate this effect.

Substrate type has also been shown to affect the composition of sputtered films. Films sputtered onto polyethylene, polytetrafluoroethylene and silicon showed variations in Ca/P. This was explained by two mechanisms. Negative charging of insulating substrates reduced the bombardment of negative oxygen ions originating from the target. This affects the amount of P in the resultant film. In the case of the polytetrafluoroethylene substrate, F was found to escape which was explained by interaction with the uv light from the plasma. It was thought F reacted with P and is removed from the film [209].

2.8.3. The Biological Response to Hydroxyapatite Thin Films

2.8.3.1. *In Vitro*

There are only a few studies looking into the biological response of cells to RF magnetron sputtered HA thin films in comparison to the amount of work characterising such films. Hulshoff *et al*. [210] used rat bone marrow (RBM) cells to assess the cytotoxicity of RF magnetron sputtered HA coating in comparison to plasma-sprayed HA coatings and uncoated titanium substrates. Amorphous and crystalline coatings were investigated. In an attachment and proliferation study of 8 h and 5 days no significant difference in cell number was observed between any of the samples. Morphology studies at 18 days showed sputtered coatings and plasma-sprayed coatings to exhibit ECM formation. However, no difference was seen between the two types of coating. Lo *et al*. [211] compared pulsed laser deposited HA surfaces with RF magnetron sputtered films. It was found that sputtered films supported significantly higher cell growth and ALP production than pulsed laser films. Furthermore, it was found as-deposited sputtered films lead to

a more favourable cellular response than films annealed at 400°C in argon for 1 h. Differences were explained in terms of crystallinity of samples. Annealed pulsed laser films were found to be 87 - 98% crystalline whereas RF sputtered films were only 65 % crystalline. It was argued very low crystallinities affected sample stability whereas too high and cellular response is affected. It was concluded that intermediate crystallinities provided the best conditions for cellular growth and mineralisation. A more in depth investigation looked at differences in Ca/P ratio of coatings with RBM cells [202]. The study looked at HA coatings with Ca/P ratios of 2.09, 1.77 and 1.79 with a titanium substrate as a control. It was found that the control was demonstrated to have significantly ($P<0.05$) higher proliferation values than any of the HA coatings. However, bone mineralisation was seen to take place on all HA films but not titanium substrates, as measured by tetracycline staining and imaging using a confocal laser scanning microscope. No significant difference ($P>0.05$) between the Ca/P ratio of HA coatings and the amount of ECM production was measured. Moreover, integrin expression during initial cell-material interactions was reported to be unaffected by the surface characteristics of HA films or titanium substrates [212].

2.8.3.2. *In Vivo*

In vivo studies are crucial to the understanding and development of RF magnetron sputtered coatings. A study compared grit blasted titanium substrates with sputtered coating implants in a goat model showing improved initial fixation and healing response for the coated implants when implanted into trabecular bone [213, 214]. Another study [215] implanted tapered conical screws coated with plasma-sprayed and amorphous sputtered HA of similar roughness into the trabecular bone of femurs of nine goats. Implants were evaluated at 3 months of implantation. Histomorphometry revealed a higher percentage of bone contact for the plasma sprayed implants compared with the HA sputtered screws ($P<0.05$).

Measurement of the amount of bone revealed significantly ($P<0.05$) more bone mass around the HA sputtered implants. Studies in rabbit models have also been carried out [216], again comparing as-sputtered and plasma-sprayed HA coatings. Seventy two cylindrical implants were inserted into medial femoral condyles of 18 New Zealand White rabbits. Histological implant evaluation was carried out after 3, 6 and 9 weeks. It was concluded that sputter coatings had the same bone healing process as plasma-sprayed implants. It has been hypothesised that the dissolution of HA coatings could play an important role in the bioactivity of such coatings enhancing early bone tissue formation and tissue bonding. This early stimulation of bone has a positive affect on the overall bone healing process [185].

2.9. The Co-deposition of Silicon doped Hydroxyapatite Thin Films

Silicon doped hydroxyapatite thin films production via a magnetron sputtering route is a relatively new field of interest. Others have investigated applying such coatings using techniques such as electrophoretic deposition and plasma spraying (section 2.8). The current section aims to summarise the recent work of Porter and Thian based at Cambridge University.

2.9.1. The Production of Silicon doped Hydroxyapatite Thin Films

The use of a RF magnetron sputter co-deposition system to produce SiHA films was first carried out by Porter *et al*. [217] who used a pure silicon target and a dense HA target to produce films of varying silicon content. By positioning the substrates either closer or further from the silicon target it was possible to obtain silicon contents from 11.45 to 1.95 at.%. Silicon additions to HA thin films ranging from 0.4 to 4.9 wt.% have been comprehensively investigated. This was achieved by modifying the method of Porter *et al*. [217] and altering the power density applied to the silicon magnetron. Briefly, a slip cast hydroxyapatite target [218] and a pure silicon target of dimensions 55 x 35 mm and 2 mm in thickness were used. An RF power supply was applied to the HA target and run at 60 W. A DC power supply was used for the silicon target and operated at 3, 9 or 15 W to create 0.8, 2.2 and 4.9 wt.% SiHA films [219]. Deposition was carried out in pure argon with an operating pressure of 4.5×10^{-3} Torr (0.6 Pa).

2.9.2. Silicon doped Hydroxyapatite Thin Film Observations

At low doping levels it is common that HA and SiHA thin films largely exhibit the same properties on a macro-scale, for example preferential crystal orientation along the c-axis of HA can still be observed [199]. However, subtle differences can

be observed when examined on the nano-scale. The inclusion of silicon has been shown to alter crystal structure in bulk materials which was discussed in section 2.5. which has also been shown to inhibit HA crystal growth [220] although no quantitative studies have been carried out. This has the effect of leading to increased solubility of thin films when compared with HA coatings alone. Moreover, wettablity has been shown to increase on SiHA thin films [221], meaning such coatings are more hydrophilic than HA films. A contact angle of 47.6 ± 2.52 ° was reported for HA and 29.45 ± 3.10 ° for SiHA. To date characterisation of SiHA thin films has generally been limited to identifying silicon content, crystal structure and chemical bonding.

As previously discussed SiHA materials are more soluble than HA. Thian *et al*. [222] investigated Ca, P and Si ion release for as-deposited and annealled 0.8 wt.% SiHA film over 28 days in simulated body fluid using inductively coupled plasma optical emission spectroscopy. Between days 1-5 the Ca and P content remained constant but decreased up to day 28. The Si content remained constant over the time period. As-deposited films showed higher quantity of ions in solution compared to annealed films. This study did not measure this compared to an HA control and therefore comparisons cannot be made.

2.9.3. The Biological Response to Silicon doped Hydroxyapatite Thin Films

The cellular response to bulk SiHA materials has already been discussed in section 2.5.2. This section provides detail of cellular interactions with SiHA thin films. Currently no *in vivo* biological studies have yet been carried out with SiHA thin film coatings, however many studies have been performed *in vitro*. SiHA thin films have been shown to enhance the proliferation and differentiation of osteoblasts grown on their surfaces [199, 219, 220, 223, 224]. The ability of carbonated

apatite layers to form when SiHA is immersed in simulated body fluid (SBF) compared with uncoated titanium and hydroxyapatite thin films has also been increased [222].

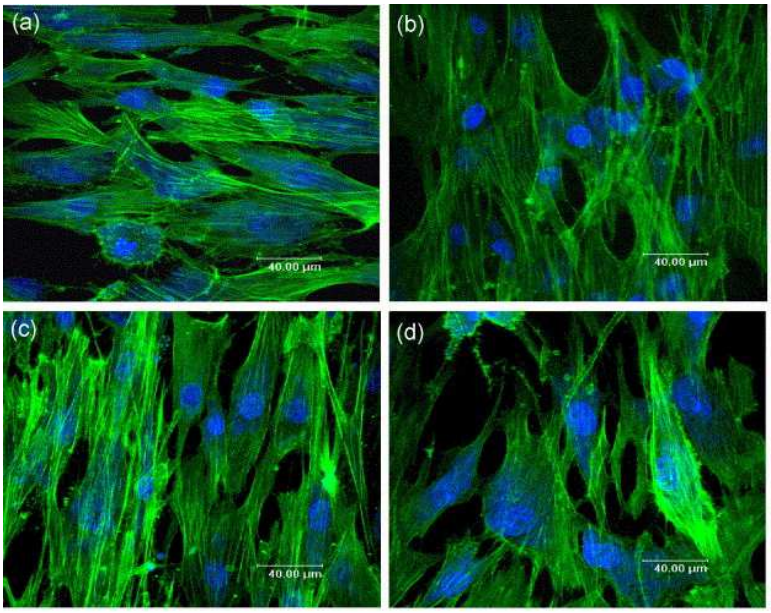

Figure 2-24. Immunostained images of nuclear DNA (blue) and actin cytoskeleton (green) in HOB at day 1, where (a) 0.8 wt.% Si–HA; (b) 2.2 wt.% Si–HA; (c) 4.9 wt.% Si–HA; (d) HA. [219].

In a 4 day growth study comparing 0.8, 2.2 and 4.9 wt.% SiHA films which were heat treated at 600°C for 3 h in moist argon, and using HA as a control surface it was found that all SiHA surfaces had significantly ($P<0.05$) increased growth activity at both 2 and 4 days, however no significant difference ($P>0.05$) was found between the different doping levels [219]. Both HA and SiHA surfaces showed clear distinct actin filaments, which were seen to be well aligned along the cell axis in cells on the SiHA surfaces (figure 2-24) compared to the cells on HA surfaces which were more diffuse, with fewer and shorter filaments [219]. Both HA and SiHA surfaces led to mineralisation, however this effect was more prominent on the SiHA surface [219]. It was suggested that SiHA surfaces allowed increased amounts of serum proteins to attach owing to the formation of a bound silicate network structure on the SiHA surface. It has been shown that released silicate ions from the coatings combined with oxygen ions have the capacity to

bind proteins together [225]. Similar studies have been published showing increased osteoblast growth on SiHA films up to 4.9 wt.% SiHA when compared to uncoated titanium substrates after 7 and 14 days [220]. It was seen that at 14 days cellular growth on the 4.9 wt.% SiHA film was significantly lower than growth on the titanium control. This decrease in cell growth for the 4.9 wt% SiHA film was explained by osteoblasts entering the mineralisation stage of development due to early deposition of extracellular matrix detected with SEM and EDX investigation. The study did not test for differentiation markers so such claims cannot be fully supported. Furthermore, immunofluorescence labelling indicated that after 1 day of culture the 2.2 and 4.9 wt.% SiHA films had well organised cytoskeletal components with increased actin organisation compared to the 0.8 wt% SiHA film. The increase in cellular response to SiHA films was assigned to a number of reasons. Firstly the continuous HA phase is a bioactive material possessing osteoconductive properties, thus promoting cell attachment, proliferation and differentiation. Secondly, the incorporation of silicon which plays an important role in the stimulation of bone cell metabolism and finally the inclusion of silicon acts to inhibit HA crystal growth thus increasing the solubility of HA. Increased dissolution can lead to preferential release of Ca^{2+}, PO_4^{-3} and SiO_4^{4-} ions into the culture media, hence allowing rapid formation of a carbonated apatite layer which is an ideal site for osteoblasts to grow and produce extra cellular matrix. Cell growth in the study was retarded at early stages on the SiHA surfaces and it was suggested this was due to the rapid dissolution of coatings rendering the surfaces unfavourable for osteoblast attachment. It was concluded that a silicon content of 2.2 wt.% was optimal for osteoblast growth as the dissolution rate was lowered [220]. An earlier study however showed SiHA surfaces at a doping level of 0.8 wt.% led to increased growth activity but the 1.2 wt.% SiHA surfaces were not significantly different ($P>0.05$) to roughened titanium controls at 3, 7 or 14 days [199]. It was suggested that this difference was due to the silicon difference, however, the aforementioned study [219]

indicates that silicon contents higher than 1.2 wt.% can yield enhanced cell growth compared to HA surfaces. This difference may be due to amount of crystalline material present in the SiHA samples opposed to the HA samples, with the HA becoming more amorphous with increasing silicon content. The 1.2 wt.% SiHA film is likely to be less crystalline and therefore less stable than the 0.8 wt.% SiHA film. Although it is still disputed, higher crystallinities can support higher levels of cell growth. Given that silicon inhibits HA crystallite size, work has been carried out assessing the degree of crystallinity in SiHA films. Films heat treated at 600 and 700°C for 3 h in a moist argon atmosphere were investigated with a osteoblast cell model. When compared to uncoated titanium it was found that cell growth was higher on heat treated surfaces. This became significant at 7 days. At 14 days, the surface heat treated at 600°C yielded a higher cellular response than the sample heat treated at 700°C, but no explanation was given [224]. The current author is inclined to use reasoning from other work of Thian *et al*. [220] suggesting this was because cells had entered a differentiation stage leading to a reduction in cell proliferation. While surfaces heat treated at 700°C produced higher cell growth than films at 600°C this was not shown to be statistically significant ($P>0.05$) at any time point. Thian *et al*. concluded that surfaces heat treated at 700°C had larger HA crystallites leading to increased stability of coatings and hence increase cellular growth.

In summary, one group has led the way in RF magnetron sputtered SiHA thin films showing increased cell growth, cystoskeletal organisation and potential differentiation on SiHA thin films compared to uncoated titanium and HA thin films. However, Thian *et al*. have claimed in two separated publications [199, 220] that 0.8 and 2.2 wt.% SiHA may both optimal coating compositions for osteoblast growth. Clearly these figures are conflicting and it is suggested that other factors may be related, such as crystallitinty and calcium phosphate composition.

2.10. Summary

This review has discussed the properties of bulk HA and SiHA materials and their bioactive nature leading to enhanced biological responses. Unfortunately, the nature of ceramic materials means that they are restricted to the application of non load bearing sites. One solution is to use such materials as a coating leading to a composite structure thus utilising the mechanical strength of metallic implants such as titanium but modifying the surface making it bioactive and hence improving the chances of a long term success of the implantable device.

Numerous authors have showed RF magnetron sputtering could be a potentially beneficial technique for applying coatings to future implantable devices. Current work has shown that HA coatings are bioactive and exhibit similar properties to bulk materials.

Many different compositions have been achieved for HA thin films due to differing sputtering parameters. However, it is still unclear what are suitable deposition parameters and how factors such as power density and sputtering environment affect resultant films. One important compositional parameter is the Ca/P ratio which can give rise to changes in the thermal stability, biological response, mechanical properties and dissolution potential. Further issues are encountered due to inaccuracies related to characterisation techniques. Researchers commonly use different techniques to obtain compositional data. The most common of which are XPS, EDX and RBS, however, no comparative studies have been undertaken to assess the accuracy of such techniques in relation to the Ca/P ratio of HA thin films.

SiHA thin films have been shown to elicit an enhanced cellular response compared to HA which may provide a way to increase bone response *in vitro* and *in vivo*

thus improving the longevity of implants for future generations. Work concerning RF magnetron sputtered SiHA thin films have only recently been investigated. Thin films systems often differ from bulk material systems due to the manufacturing process. Therefore, it is only assumed that silicate groups substitute for phosphate groups and it is not understood what may happen at higher silicon concentrations above 5 wt.%. Furthermore, optimal silicon values have been suggested but these are not in agreement. It appears that the higher silicon content may elicit a more favourable cellular response. Therefore, higher silicon additions and altered crystallinities will be investigated.

3. Materials and Methods

3.1. Introduction

In this chapter the experimental techniques and procedures are discussed. The section begins by describing how samples were prepared and lists the RF magnetron sputtering conditions for thin film production. The chapter then goes on to describe all characterisation techniques and then how samples were biologically tested. Extra detail has been included for the surface analysis techniques RBS, XPS and EDX as a study was carried out to evaluate the ability of each technique to record accurate compositional values for HA thin films, as discussed in section 2.3.6. Finally, details of how biological evaluation was carried out are described.

3.2. Materials and Thin Film Preparation

3.2.1. Substrate Preparation

Commercially pure grade 1 titanium sheet (Timet, UK) (CPTi) was wire eroded into 10 mm diameter discs with a thickness of 1 mm. Discs were then ground to a mirror finish (R_a = 16 ± 4 nm) using a series of silicon carbide paper (P240-P1200), polished with a mixture of colloidal silica (Buehler, Germany) and 10 % hydrogen peroxide (Fisher Scientific, UK) and finally water. Discs were cleaned for 30 min in acetone, IMS and distilled water and dried under flowing nitrogen (BOC, UK).

Silicon single crystal (100) orientated Cz wafer (Compart Technology Ltd., UK) was cut into squares approximately 10 x 10 mm in size with a diamond tipped scribe.

3.2.2. Thin Film Deposition

Three different RF magnetron sputtering systems were used in this study. The first system is a bespoke system based on a pair of planar magnetrons arranged parallel to one another as described in section 3.1.2.1. while section 3.1.2.2. details a commercially available system which has been modified for research purposes which is based on 4 vertically mounted magnetrons. A third system, which is described in section 3.1.2.3., was similar to the first system, again based on a dual magnetron setup and used for the production of coatings specifically for characterisation of compositions.

3.2.2.1. Balanced Planar Magnetron (BPM) Deposition Parameters

A coating system previously designed and constructed by Botterill [226] was used for the deposition of HA coatings (figure 3-1).

The rig consisted of a rolled stainless steel cylindrical chamber with internal dimensions of 400 mm diameter and a height of 400 mm. The system was a top loading unit with upper and lower vertically opposed balanced water cooled Ion Tech B325 planar magnetrons. Deposition was carried out using the lower magnetron, requiring targets either 63 or 75 mm in diameter depending on magnetron configuration.

Figure 3-1. BPM PVD deposition unit.

The chamber was pumped to a base pressure of 10^{-6} Torr (1.3×10^{-4} Pa) using an Edwards RV8 rotary pump and a water cooled Edwards EXT250 Turbomolecular pump. The chamber was then filled with high purity (99.99%) argon (BOC Pureshield, UK) at a user set deposition pressure between 1-10 mTorr (0.1-1.0 Pa). This atmosphere was regulated by a MKS Baratron type 627B temperature controlled capacitive manometer with an operating pressure of 0-1 Torr (0-133.3 Pa) sending data to an MKS 250 pressure controller reading system pressure. The

pressure controller was connected to a MKS 247C 100 sccm mass flow controller allowing a feedback loop to maintain a constant deposition pressure.

The lower magnetron was powered with either a RF Power Products Inc. RF5S 13.56 MHz RF power supply with 50 Ω matching unit or an ENI RPG-50 DC Plasma Generator 5 kW with optional pulse mode.

Substrates were mounted vertically above the lower magnetron with conductive silver dag at a working distance of 50 mm. Before deposition onto substrates, targets were sputter cleaned behind a protective shutter for 30 min to remove surface contamination and oxidants.

For the purpose of this study this rig will be referred to as the balanced planar magnetron (BPM) rig. Details of coatings for all systems described are shown in table 3-1.

Sample Description	Sample Ref. No.	HA Magnetron Power Supply	Silicon Magnetron Power Supply	Frequency (kHz)/Pulse Time (ns)	HA Power Density (W cm^{-2})	Si Power Density (W cm-2)	Base Pressure (Torr)	Gas Composition %	Argon Partial Pressure (Torr)	Oxygen Partial Pressure (Torr)	Duration (h)	Target Details	Estimated Thickness (µm)
HA	7014	Pulsed DC	n/a	150/1500	6.8	n/a	4.2×10^{-6}	100% Argon	2×10^{-3}	n/a	2	Plasma sprayed HA	0.2
HA	7017	RF	n/a	n/a	6.8	n/a	2.1×10^{-5}	100% Argon	2×10^{-3}	n/a	2	Plasma sprayed HA	0.3
HA	7019	RF	n/a	n/a	11.3	n/a	4.4×10^{-6}	100% Argon	2×10^{-3}	n/a	2	Plasma sprayed HA	0.8
HA	7125	RF	n/a	n/a	6.8	n/a	4.6×10^{-6}	87.8% Argon/12.2% Oxygen	2×10^{-3}	2.8×10^{-4}	2	Plasma sprayed HA	0.2
HA	7128	RF	n/a	n/a	4.5	n/a	2.3×10^{-5}	87.8% Argon/12.2% Oxygen	2×10^{-3}	2.8×10^{-4}	3	Plasma sprayed HA	0.2
HA*	8082	RF	Pulsed DC	150/1500	6.8	n/a	2.7×10^{-6}	87.8% Argon/12.2% Oxygen	2×10^{-3}	2.8×10^{-4}	2	Plasma sprayed HA	0.2
HA	8084	RF	Pulsed DC	150/1500	6.8	n/a	$<2 \times 10^{-5}$	87.8% Argon/12.2% Oxygen	2×10^{-3}	2.8×10^{-4}	2	Plasma sprayed HA	0.2
SiHA1	8092	RF	Pulsed DC	150/1500	6.8	0.06	4.0×10^{-5}	87.8% Argon/12.2% Oxygen	2×10^{-3}	2.8×10^{-4}	2	Plasma sprayed HA	0.2
SiHA1	8095	RF	Pulsed DC	150/1500	6.8	0.06	$<2 \times 10^{-5}$	87.8% Argon/12.2% Oxygen	2×10^{-3}	2.8×10^{-4}	2	Plasma sprayed HA	0.2
SiHA2*	8099	RF	Pulsed DC	150/1500	6.8	0.17	3.5×10^{-5}	87.8% Argon/12.2% Oxygen	2×10^{-3}	2.8×10^{-4}	2	Plasma sprayed HA	0.2
SiHA2	8102	RF	Pulsed DC	150/1500	6.8	0.17	$<2 \times 10^{-5}$	87.8% Argon/12.2% Oxygen	2×10^{-3}	2.8×10^{-4}	2	Plasma sprayed HA	0.2
SiHA3	8230	RF	Pulsed DC	150/1500	6.8	0.33	5.6×10^{-5}	87.8% Argon/12.2% Oxygen	2×10^{-3}	2.8×10^{-4}	2	Plasma sprayed HA	0.2

Sample Description	Sample Ref. No.	HA Magnetron Power Supply	Silicon Magnetron Power Supply	Frequency (kHz)/Pulse Time (ns	HA Power Density (W cm^{-2})	Si Power Density (W cm-2)	Base Pressure (Torr)	Gas Composition %	Argon Partial Pressure (Torr)	Oxygen Partial Pressure (Torr)	Duration (h)	Target Details	Estimated Thickness
SiHA3	8231	RF	Pulsed DC	150/1500	6.8	0.33	2.6×10^{-5}	87.8% Argon/12.2% Oxygen	2×10^{-3}	2.8×10^{-4}	2	Plasma sprayed HA	0.2
HA	BPM	RF	n/a	n/a	8.0	n/a	5×10^{-6}	100 % Argon	7×10^{-3}	n/a	6	Sintered HA powder	0.2
HA	CSIRO	RF	n/a	n/a	9.1	n/a	1×10^{-6}	100 % Argon	8×10^{-3}	n.a	0.33	Australian Surgical plasma spray	0.1

Table 3-1. A summary of all coating used in this study. 1 Torr = 133.3 Pa. *New target was used.

3.2.2.2. Uniform Deposition and Plasma Systems (UDP) Deposition Parameters

Coating deposition was performed in a UDP450/4 Teer Coatings Rig (figure 3-2) with chamber diameter of 450 mm and height of 570 mm. The chamber's external wall had a double skin of stainless steel plate with a gap between the layers to allow a flow of cooled water between them. The system had a front opening door to allow for samples to be conveniently loaded. All experiments used 4 magnetrons mounted vertically in the ports in the coating chamber wall. The standard magnetrons are planar and had target dimensions of 220 mm x 134 mm. The magnetron used for the HA target was a 75 mm circular magnetron. The system was configured with the closed field unbalanced magnetron design (figure 3-3), although the strength of the magnetrons used was different with the silicon target being a stronger magnetron than the HA magnetron. The silicon target was of dimensions 300 x 100 and 0.635 mm.

Before deposition the chamber was pumped to a minimum of 2×10^{-5} Torr (2.7×10^{-3} Pa). An Edwards 750 diffusion pump provided the vacuum for this system which is connected to the base of the chamber by an Edwards high-vacuum butterfly valve. This is backed with an Edwards E2M40 rotary pump which achieves a vacuum of approximately 10^{-2} Torr (1.3 Pa) before the high vacuum valve is opened. Chamber pressure is measured by Edwards Pirani and Penning gauges which operate at $< 10^{-3}$ Torr (0.1 Pa) and $> 10^{-4}$ Torr (0.01 Pa) respectively. The chamber was then backfilled with either argon or an argon/oxygen mixture using MKS 1179A12CS1BV 100 sccm mass flow controllers. Argon flow was set at 36 sccm for all coatings equating to 2×10^{-3} Torr (0.3 Pa). Where used, oxygen was flowed at 5 sccm with a partial pressure of 3×10^{-4} Torr (0.04 Pa).

Figure 3-2. The inside of the deposition chamber of a Teer Coatings UDP450/4 PVD unit.

To alter the composition of HA and SiHA coatings the powder density applied to the targets and the sputtering environment was altered. The HA target was powered by an Advanced Energies RF power supply unit with the silicon target powered by an Advanced Energy Inc DC Pinnacle pulsed DC power supply. Frequency and pulse time was constant at 150 kHz and 1500 ns respectively giving approximately 1500 on cycles per second. The remaining two magnetrons were earthed. A negative bias of -30 V was applied to the substrates.

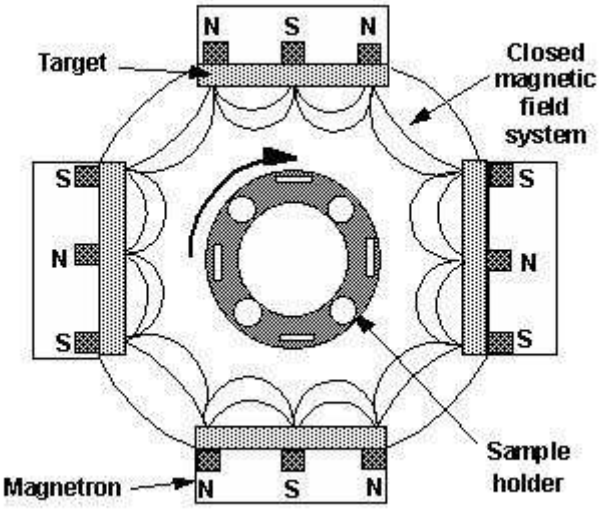

Figure 3-3. A Teer Coating Ltd closed field unbalanced magnetron arrangement as in the UDP450/4 rig. With permission from Teer Coatings Ltd.

Samples were mounted on a stainless steel plate as shown in figure 3-2 with double sided adhesive tape and oscillated at 4 rpm. Before deposition targets were run for a 2 min pre-sputter behind shutters.

For the purpose of this study this rig will be referred to as the UDP rig. Details of coatings for all systems described are shown in table 3-1.

3.2.2.3. CSIRO Deposition Parameters

Samples were deposited using an in house built rig based at CSIRO, Lindfield, Australia.

The deposition chamber was pumped to a base pressure of 10^{-6} Torr (1.3×10^{-4} Pa). Argon was backfilled into the chamber with a MKS 100 sccm mass flow controlled coupled to a MKS throttle type 252 A valve in feedback with a Baratron gauge MKS 127, with a range of 0-1 Torr (0-133.3 Pa).

The target was allowed a 10 min pre-sputter. The sample remained stationary throughout sputtering.

For the purpose of this study this rig will be referred to as the CSIRO rig. Details of coatings for all systems described are shown in table 3-1.

3.2.2.4. Target Manufacture

Targets used in this study are described below:

Untreated sintered and unsintered HA powder (Plasma Biotal, UK) were used. The powder was loosely compacted onto the magnetron surface and the target was run for 24 h to remove surface contamination and sinter the surfaces. This target type was used for the BPM rig.

HA targets were manufactured by plasma spraying HA powder (Plasma Biotal, UK or Australian Surgical Design, Australia) onto a circular copper backing plate 75 mm in diameter and 5 mm in thickness. The Plasma Biotal method gave targets with a coating thickness of 500 μm whereas the Australian Surgical Design targets had a coating thickness of 400 μm. This target type was used in conjunction with the UDP rig.

Where required, a single 99.999% pure homogeneous silicon target (Kurt J. Lesker, Netherlands) was used which were of dimensions 300 x 100 and 0.635 mm thick were purchased externally.

3.2.3. Post-Deposition Heat Treatments

Post-deposition, thin films were recrystallised by heat treatments at a range of temperatures with a set time of 2 h using a Lenton Thermal Design tube furnace

in an argon atmosphere. Argon was flowed at 100 sccm for 30 min before ramping to temperature at 20°C min^{-1}. Mass spectrometry indicated all gases and water vapour were at untraceable levels before ramping to temperature. Samples were left to cool naturally under argon.

3.3. Characterisation of HA and SiHA Thin Films

3.3.1. Profilometry

A Mitutoyo Surftest SV-600 profilometer equipped with Surfpak SZ v1.002 software was used to measure surface roughness of samples. The stylus had a 5 μm radius tip. A scan length of 2 mm with a scan speed of 0.2 mm s^{-1} and a range of 80 μm was used for all samples. Calibration was carried out prior to every session using a Mitotoyo Precision reference specimen with an R_a value of 2.95 μm. The R_a value is defined as the arithmetic average value of departure of the profile from the centre line.

To calculate deposition rates of BPM films substrates were partially masked with either Tippex™ or aluminium foil. Step profiles were taken at random positions and the mean was calculated.

3.3.2. Fourier Transform Infrared Spectroscopy (FTIR)

Attenuated total reflection (ATR) Fourier transform infrared spectroscopy (FTIR) was performed on the thin films using a Bruker Optics Tensor 27 spectrometer in glancing angle mode at 80 ° with a liquid nitrogen cooled MCT detector. The chamber was flushed with compressed air continually at 500 sccm to reduce background signal from water vapour. Samples scans were taken in triplicate for each coating with a total of 90 scans per coating ensuring repeatability of obtained data. Resultant spectra were analysed using an OPUS v4.2 programme.

Background spectra were subtracted by recording spectra from the sample holder and an uncoated CPTi disc. The following equation was applied to obtain sample spectra, e:

Eqn 3.1. $$\left(\frac{d-a}{b-a}\right)-\left(\frac{c}{b}\right)=e$$

Where a is the spectrum of the sample holder, b is the spectrum of the background sample (uncoated CPTi), c is the spectrum of the background sample again scanned immediately after b and d is the spectrum of the sample to be measured.

3.3.3. X-ray Diffraction (XRD)

A Bruker AXS D8 Advance X-ray diffractometer used in glancing angle X-ray diffraction mode to characterise thin films deposited into CPTi polished discs and single crystal (100) orientation silicon wafers. X-rays (λ = 1.5406 Å) were supplied by a copper source run at 40 KeV and 40 μA. The X-ray tube was fixed at 3 ° to the plane of the sample surface and fitted with 0.6 mm incidence divergence slit. Scans were performed with a 2θ of 20-55 °, a step size of 0.02 ° and a dwell time of 11 s. Samples were mounted on Perspex holders with plasticine and rotated at 30 rpm.

Temperature controlled XRD scans were performed on coating using a Bruker AXS D8 Advance diffractometer, as described above with the exception of 2 θ range and dwell time which was changed to 25-35 ° and 2 s respectively lowering the overall scan time so that any quick changes in crystal structure could be observed, however this is at the expense of resolution. The diffractometer was used with a modified mri RP-furnace equipped with tantalum box heater in a, water cooled, concealed chamber with kapton window for the passage of X-rays. Samples were positioned on an alumina crucible in the box heater. Sample height was adjusted accordingly using alumina powder. Prior to use, the chamber was purged using a Pfeiffer TMU 071 P Turbomolecular drag pump and backfilled with

helium gas (BOC, UK). An mri TCPU1 temperature controller was used to alter and monitor temperature within the chamber. Temperature scans were performed from room temperature to a maximum of 800 ° C to investigate the recrystallisation of thin films.

3.3.3.1. X-ray Diffraction Analysis

PC-APD version 3.5B DOS-based software was used to determine crystallite size of thin films using the Scherrer equation:

Eqn 3.2. $$t = \frac{0.9\lambda}{B\cos\theta}$$

Where B is the peak broadening (full width half maximum (FWHM) in radians), λ is the wavelength of the XRD source material and t is the crystallite diameter. B factors in instrumental broadening ($B = B_{0bs} - B_{inst}$) where B_{obs} is the observed line broadening which includes instrumental factors such as detector slit width, area of the specimen irradiated and possible $K\alpha_2$ X-rays. Usual procedure is to measure the instrumental broadening, B_{inst}, in a large grained material in which grain size broadening is assumed to be negligible. In practical terms absolute measures of grain sizes are not possible due to the presence of imperfections such as lattice strains which will contribute to line broadening [227].

3.3.4. Energy Dispersive X-ray Spectroscopy (EDX)

Theory

When an incident electron of tens to hundreds of KeV strikes an atom, inner shell electrons will become excited being ejected from that atom. As a result, vacancies remain and electrons from higher energy shells must drop down an energy step to accommodate these voids, in doing so a characteristic X-ray will

be omitted of a distinct energy, which is measured in KeV. Depending on how the atom has electronically reconfigured itself to its lowest energy state will affect the energy of the characteristic X-ray. There are three shells K, L and M which are in order of distance from the nucleus. If an electron is knocked out of the K shell it may either be filled by a L or an M shell electron. If the former occurs then this produces a Kα X-ray, whereas the latter will lead to a Kβ X-ray. In addition to this an L shell electron may be ejected. This can only be filled by a higher energy M shell electron which will produce an Lα X-ray (figure 3-4). It is commonplace to only analyse data obtained for Kα X-rays as they are the most abundant source of X-ray. Each element has a unique set of energy levels; each element produces X-rays at a unique set of energies, allowing a non-destructive measure of the elemental composition of a sample. [89, 228]

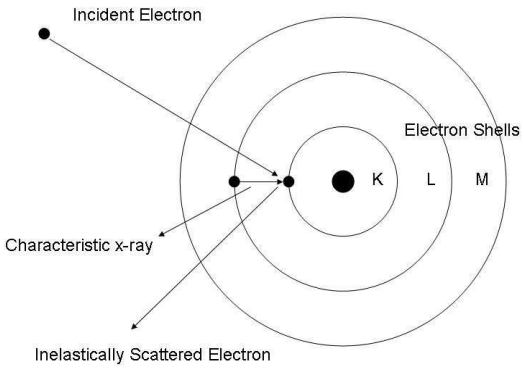

Figure 3-4. The production of characteristic X-rays which are recorded in EDX analysis. X-rays produced is this schematic are Kα X-rays.

When electrons hit the target material they will be decelerated. This deceleration causes the production of a continuous radiation called Bremsstrahlung (German word for braking) radiation. By energy conservation, whatever energy is lost when an electron decelerates must be taken away by the energy of a photon. The spectrum is continuous because not all electrons will lose the same amount of energy.

EDX equipment can be either a stand alone unit or it can be twinned with an electron microscope (Transmission electron microscope (TEM) or scanning electron microscope (SEM)), the advantage of this being a readily available electron beam source with adjustable electron beam energies. For this study an EDX unit was used with a SEM capable of producing beam energies of 25 KeV and therefore this setup will be considered. Further to an electron source an EDX unit must comprise of a vacuum chamber and detector. The vacuum used will be indicative of the type of electron microscope used but typically for an SEM this is in the region of 10^{-4} and 10^{-7} Torr (1.3×10^{-2} and 1.3×10^{-5} Pa) for a TEM. The detector used is generally a silicon particle detector. Briefly, if an X-ray penetrates the detector it produces electron-hole pairs, the number being proportional to the energy loss. An externally applied electric field separates the pairs before they recombine; electrons drift towards the anode, holes to the cathode; the charge is collected by the electrodes (charge collection). The collected charge produces a current pulse on the electrode, whose integral equals the total charge generated by the X-ray particle. [89]

Experimental

An Edwards E306 high vacuum evaporator unit was used to coat samples with a thin layer (~5 nm) of graphitic carbon prior to analysis. Carbon was used rather than gold/palladium because it is a lighter element and will absorb less characteristic X-rays [89]. Furthermore, gold Mα peaks appear at 2.12 KeV which will cause overlap with phosphate Kα peaks at 2.01 KeV thus increasing quantification uncertainty.

An Oxford Instruments energy dispersive X-ray microanalysis (EDX) system was used with a Si(Li) spectrometer crystal, an ultra-thin entrance window to allow detection of light elements down to Z=5 (boron) with a system energy resolution

of 60 eV. Analysis was performed using standards-based ZAF corrections to the order of two iterations on an Oxford Instruments Link ISIS v3.35 program.

For this study two sets of standards were used, a hydroxyapatite powder standard was obtained from Plasma Biotal (Batch No, P120) with a Ca/P ratio of 1.70 was used to set up Ca and P standard profile files. This was denoted as EDX_s. Composition was checked using previously compiled GaP and wollastonite calibration profiles, which are referred to as EDX_n, returning a Ca/P ratio of 1.63 ± 0.03 suggesting inaccuracies in the EDX_n standards for the used with HA samples. The electron beam (LaB_6 filament) voltage was run at 20 KeV with a working distance of 10 mm and a collecting time of 50 seconds. Ten randomly selected spots were analysed. Approximately 90,000 total spectrum counts were taken per sample area.

3.3.5. X-ray Photoelectron Spectroscopy (XPS)

Theory

X-ray absorption by an atom in a solid material leads to the ejection of an electron (photoionisation) either from a tightly bound core electron or a weakly bound valence electron. A small proportion of these electrons in the near surface region may escape the material in a vacuum system by a process called photoemission. The overall process is described as the photoelectric effect. Recording the energy of photoelectrons allows the build up of a spectrum where each element will have a characteristic energy footprint allowing the easy identification of all elements with the exception of helium and hydrogen. Furthermore, XPS is sensitive to chemical bonding of elements and the binding energy may vary according to the chemical state of an atom [92]. For an electrically insulating sample the equation below may be applied;

Eqn 3.3. $$K.E. = hu - B.E. - \Phi$$

Where K.E. is Kinetic energy of the emitted electron, B.E. is electron binding energy, h is Planks constant (6.62 x 10^{-34} J s), υ = frequency of the radiation and Φ is the work function of the spectrometer (typically 4.5 eV). This equation can be used to record a spectrum binding energy rather than kinetic energy. Standards are used to accurately calibrate the spectrometer energy scale. A reference point is generally used to charge correct insulating samples with a common carbon contamination peak termed adventitious carbon present in the spectrum at a binding energy of 285 eV.

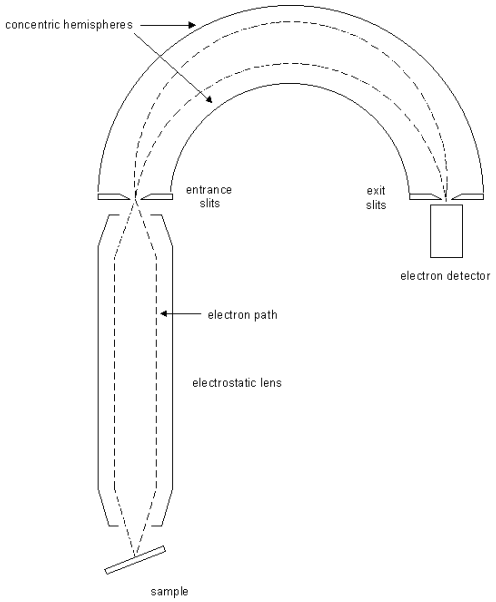

Figure 3-5. A concentric hemispherical analyzer (CHA) used for the detection of electrons in XPS.

XPS requires an X-ray emission source which is typically Al (1486.6 eV) or Mg (1253.6 eV). In some instances X-ray sources are monochromated by single or multiple Bragg reflections from suitable crystals, allowing only the Kα lines to be used for the production of photoelectrons, but at the expense of the number of counts. This allows increased resolution lowering the energy spread from 0.7 - 0.8 eV to about 0.2 eV. However, by moving the X-ray source in close proximity

to the sample (10 mm), sufficient photon flux can be achieved. This distance is restricted by the need for a Al or Be window (10 - 30 μm) which prevents secondary electrons being detected and provides a barrier between the outgassing X-ray source and the ultra-high vacuum (UHV) analysis chamber (> 10^{-9} Torr (1.3 x 10^{-7} Pa)). [229]. Emitted photoelectrons are analysed with a concentric hemispherical analyser (figure 3-5) (CHA) which can operate in constant retard ratio (CRR) or constant analysis energy (CAE). In the CRR mode the analyser pass energy is adjusted to maintain a constant value for the quantity of initial electron energy divided by the pass energy. That is if the retard ratio is 10, and 1000 eV electrons are to be detected, then the electrons will be slowed down to 100 eV, and the pass energy will be set to 100 eV. In the CAE mode, the pass energy is fixed. Hence, if the pass energy is 50 eV, then electrons of 1000 eV will have to be slowed down by 950 eV in order to be detected. The CRR mode gives constant resolving power and the CAE mode gives constant energy resolution [230].

Experimental

A Kratos Instruments Axis Ultra with a monochromated Al kα X-ray source run at 10 KeV and 15 mA with a charge compensator was used to investigate the top few nanometres of the sample surface. The instrument was operated in CAE mode with a pass energy of 20 eV for high resolution scans.

A VG Scientific ESCAlab with twin unmonochromated Mg/Al anode and argon etching capability was used to record spectra before and after etching. The instrument was run at 10 KeV and 18 mA in CAE mode with a pass energy 10 eV for high resolution scans. Etching was carried out for 10 minutes using a VG Scientific ion beam gun run at 4 KeV with an estimated etch rate of 0.1 nm min^{-1}.

Information about the chemical state and compositional data of the films were obtained between 0 – 1400 eV. All samples were charge corrected to the C 1s adventitious carbon peak which was set to a value of 285 eV. Ca 2p, O 1s and Ti 2p peaks were fitted with Shirley [93] backgrounds while linear backgrounds were used for the C 1s, P 2p and Si 2p regions. Region areas were selected manually and peak deconvolution was carried out using Gaussian-Lorentzian (GL30) line shapes.

Data analysis and compositional quantitification was carried out using CasaXPS v. 2.3.10. software with geometry adjusted Kratos and Schofield sensitivity factors, for the Kratos and ECSCAlab instruments respectively.

3.3.5.1. Stability of Calcium Phosphate Materials

It has been suggested that calcium phosphate materials decompose under X-rays generated in XPS analysis [231]. To establish the stability of Ca and P under Al kα X-rays a low Ca/P ratio calcium phosphate sputtered thin film sample was left exposed to an X-ray beam for a total of 3.5 h to observe the effects of electromagnetic radiation. XPS high resolution scans were taken of Ca 2p, C 1s, O 1s and P 2p regions repeatedly throughout. Scans lasted approximately 14 minutes giving a total of 23 scans. This experiment was repeated on two areas of the sample.

3.3.6. Rutherford Backscattering Spectroscopy (RBS)

Theory

RBS is a well established analytical technique [232] that is simply traceable and therefore particularly suitable for standards work. Briefly, an energetic light ion beam, typically 1.5 MeV He^+, is directed at a target, and the beam particles

scattered by the target atomic nuclei are detected (figure 3-6). For these ions the scattering process is coulombic, that is, the electrostatic repulsion of two charged nuclei completely accounts for the scattering. For more energetic particles the two nuclei may approach so close that the nuclear wave functions interact, in which case the cross-sections have to be determined by a quantum mechanical treatment. This is known as elastic (non-Rutherford) backscattering spectroscopy (EBS).

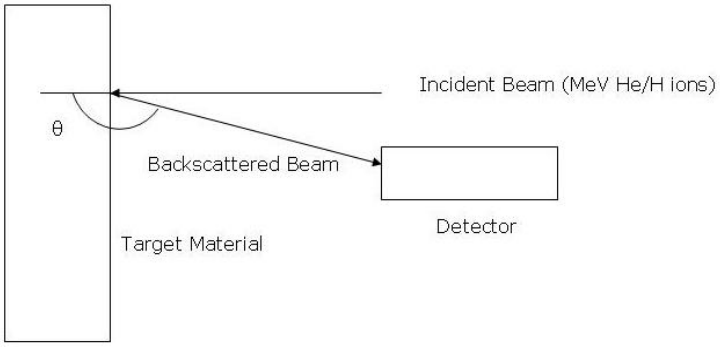

Figure 3-6. A typical backscattering event occurring with the use of RBS.

The energy of the backscattered particle is determined by the kinematics of the nuclear interaction, and the inelastic energy loss of the particle to the target electronic lattice on its inward and outward path through the target to and from the interaction site. This inelastic energy loss $\varepsilon(E, Z_1, Z_2)$, where E is the particle energy and Z_1, Z_2 are the atomic numbers of the particle and target atom respectively, is determined from a linear combination of losses to each element of the target and is taken from the stopping and range of ions in matter (SRIM) energy loss semi-empirical database [91]. The nuclear and electronic energy losses can be treated independently to an excellent approximation, and the electronic energy losses are determined by integrating ε along the pathlength of the particle.

The spectrum expected from any particular target can be readily calculated: the composition of the target must be known as a function of depth (to calculate the

electronic energy loss), the number of particles striking the sample and the solid angle of the detector (to determine the yield as a function of energy). Of course, the geometry of the ion beam, target and detector must be known, and the probability of scattering can be calculated analytically from the Coulomb potential.

The great utility of RBS is due to the existence of very simple and reliable detectors (reverse biased silicon diodes) which can detect particles with effectively 100 % efficiency, and determine their energy with an energy resolution of about 1 % and an excellent linearity.

Experimental

All RBS experiments were performed at the Surrey Ion Beam Centre (Surrey, UK). Calcium phosphate coatings and standards were analysed with a 2 MV Tandetron accelerator (High Voltage Engineering Europe). A helium ion beam ($^4He^+$) was run at a voltage of 1.554 MeV. Two silicon particle detectors positioned at scattering angles of 148.2 (RBS) and 172.8 º (Cornell) were used to assure accurate analysis. Beam current was < 30 nA with a nominal beam size of 1 mm. The solid angle of the RBS detectors 3.5 (RBS) and 1.25 msr (Cornell) was determined from Ti yield using TRIM90 stopping powers. Electronic calibration was carried out with an Au/Ni/SiO_2/Si sample [233]. This was determined very precisely using the Ca and O edges in the spectra. Electronic pileup was present and accounted for using an amplifier shaping time of 0.7 μs and a time resolution for pileup rejection of 0.5 μs, with the Amsel algortihm. Depth profiles were extracted automatically for spectra using IBA DataFurnace software which has been validated for accuracy by IRMM and BAM, the Belgian and German National Standards Laboratories [234].

3.3.7. Focused Ion Beam Scanning Electron Microscopy (FIB-SEM)

HA and SiHA thin films deposited onto CPTi substrates were initially sectioned using an FEI Quanta 200 3D FIBSEM fitted with a Quorum cryo-transfer unit, an Omniprobe micromanipulator and an INCA Oxford Instruments EDX analysis system as described in [235]. A schematic of the stage setup is shown in figure 3-7.

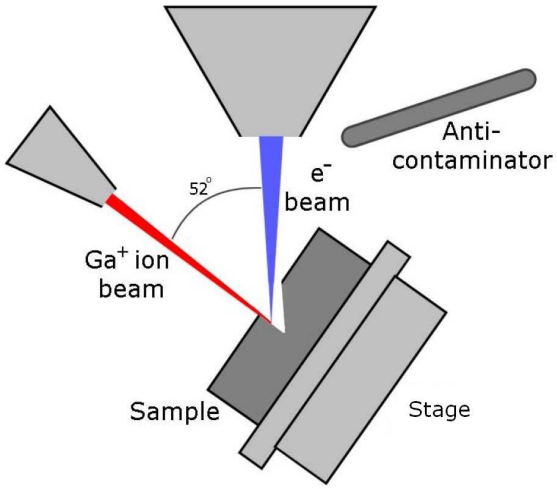

Figure 3-7. Schematic showing the geometrical configuration of the FIB-SEM stage. Taken from [235].

The FIBSEM was operated at an ion beam accelerating voltage of 30 KeV and electron beam accelerating voltages of 5-20 KeV. A coating of tungsten was-deposited *in situ* by chemical vapour deposition (CVD) to protect the HA coating. FEI-Runscript software was employed to mill inspection trenches, using reducing milling currents of 7 to 1 nA for rough sectioning, followed by milling currents of 0.5 nA to 30 pA in order to polish the lamella surfaces and to fashion U-shaped cuts into the lamella to facilitate lift-out. Sections were inspected using a JEOL 2000fx transmission electron microscope (TEM).

3.3.8. Transmission Electron Microscopy (TEM)

Cross sectional microstructural and chemical analysis was performed using a JEOL 2000-FX-II TEM operating at 200 KeV with the use of a LaB_6 thermal electron source.

3.3.9. Reflective High Energy Electron Diffraction (RHEED)

A RHEED unit coupled with a JEOL 2000fx TEM operated at 200 KeV was used to assess the surface crystallinity of films. Samples were held perpendicular to normal on a stage positioned immediately below the objective lens. Samples were tilted so that the shadow edge was positioned close to the primary beam to access near surface diffraction information. A GaN/GaAs single crystal standard reference sample with know d-spacings and a camera constant of 33.8 ± 0.5 cm was used to calculate thin films d-spacings.

3.3.10. Scanning Electron Microscopy (SEM)

A Phillips XL-30 scanning electron microscope (LaB_6) was used at accelerating voltages between 10-20 KeV depending on sample type. A working distance was set at 10 mm. Samples were mounted onto aluminum stubs with carbon adhesive tabs and then carbon coated with an Edwards E306 high vacuum evaporator unit to produce samples with a thin layer (~5 nm) of graphite carbon.

3.3.11. Hardness Testing

Hardness testing was carried out on a Micro Materials NanoTest™ nanoindentation system as shown schematically in figure 3-8. The system utilises a pendulum pivoted on frictionless bearings. At the top of the pendulum a coil is mounted, so that when a current is supplied, the coil will be attracted towards a permanent magnet which then will causes the pendulum to rotate on the

frictionless pivot. The indenter then moves towards the test specimen and penetrates the surface. The displacement of the indenter is then measured by a parallel plate capacitor with sub-nanometer resolution [236, 237].

The system uses a diamond tipped indenter to apply a progressive load to the material surface with a predetermined maximum load. Load and depth are continually monitored. As the indenter unloads the load and penetration depth will decrease as the material recovers elastically. Both hardness and Young's modulus can be calculated from this data [236].

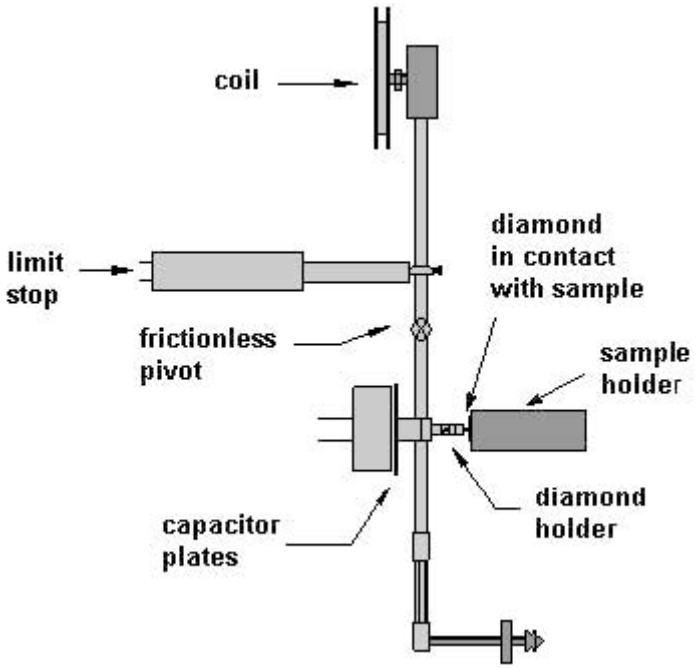

Figure 3-8. Schematic of the NanoTest™ system. [236]

Samples coated onto silicon (100) single crystal wafer were used for hardness testing. A 25 μm Berkovic 3-sided pyramidal diamond indenter was fitted and set to a maximum load of 0.3 mN with a ramp rate of 0.2 mNs^{-1}. A 5 s dwell time was given at the maximum load. A total of 25 indentations were made per sample.

Data analysis was carried out on Micro Materials Materials Testing Platform v.3.08 software using a power fitting law shown below:

Eqn 3.4. $$P = a(h - h_f)^m$$

where a, h_f and m are constants for values between 100 and 20 % of the unloading data. The true diamond contact depth is determined as follows:

Eqn 3.5 $$h_c = h_{\max} - \varepsilon(CP_{\max})$$

Where C is the compact compliance equal to 1/S which is the tangent at the maximum load (where S = contact stiffness). ε was given a value of 1 dependant on the geometry shape factor of the indenter. The diamond area function (DAF) (h) is determined by Micro Materials before installation.

The hardness (H) is calculated from the peak load and the projected area of tip contact,

Eqn 3.6. $$H = \frac{P_{\max}}{A}$$

Where A = DAF (h_c).

The Young's Modulus is obtained by analysing the unloading portion of the depth-load curve according to a relation which depends on the tip contact area,

Eqn 3.7. $$C = \frac{\pi^{0.5}}{2E_r A^{0.5}}$$

Where C = the contact compliance and E_r = the reduced modulus which is determined by,

Eqn 3.8.
$$\frac{1}{E_r} = \frac{1 - V_s^2}{E_s} + \frac{1 - V_i^2}{E_i}$$

Where V_s = Poission's ratio for the sample, V_i = Poisson's ratio for the indenter (0.07), E_s = Young's Modulus of the sample and E_i = Young's Modulus of the indenter (1141 GPa).

3.3.12. Adhesion Testing

Adhesion of the coating to the substrate was measured using the Micro Materials NanoTest™ described in section 3.3.1. The tip is applied at in increasing load and a xyz stage is moved in one direction at 10 μms^{-1}.

Coatings on CPTi substrates were used. Berkovic (10 and 25 μm) tips were used with maximum loads between 10-120 mN. A scratch length of 500 μm was used and the loading rate was varied to the constraints of the scratch length and the maximum load. Coating failure indicated adhesion values and this could be determined by either an erratic change in the load, tip penetration or from microscope inspection.

3.4. In Vitro Biocompatibility Assessment

3.4.1. Cell Culture and Maintenance

Human Osteoblast Cells (HOBs), from bone chips of the femoral heads of patients undergoing total hip arthoplasty were used in this study [238]. HOBs were cultured on tissue culture plastic (TCP) in 500 ml Dulbecco/Vogt Modified Eagle's Minimal Essential Medium (DMEM) supplemented with 10 % fetal bovine serum, 1 % L-Glutamine, 2% HEPES Buffer, 1 % non-essential amino acids, 2 % penicillin and streptomycin (Invitrogen, UK) and 75 mg ascorbic acid (Sigma, UK) and maintained at 37 °C and 5 % CO_2. The medium was changed every two days. Once confluent media was discarded, the cells were washed in phosphate buffer saline (PBS) and trypsanised for 4 mins at 37 °C with using 0.02 M bovine trypsin and scraped to remove from the flask base. An aliquot of 10 ml of fresh media was then added to the flask and the cells and media were transferred to a 20 ml universal and centrifuged in a Jouan CR422 centrifudge for 5 minutes at 1200 rpm creating approximately 2.4 g. The supernatant was then removed and the cell pellet was resuspended in 1 ml of fresh media. Cell number was assessed using a trypan blue exclusion stain which stains non-viable cells. An aliquot of 50 µl of trypan blue was mixed with 50 µl of cell suspension, applied to a haemocytometer and placed under a Nikon Eclipse TS100 microscope. A viable cell count was the calculated for the total number of cells. Appropriate adjustments were made to seed cells at the required cell density. Finally, 1 ml of media was used per well and plates were incubated at 37 °C for a given time period before an assay was applied.

3.4.2. Sample Sterilisation

Sterilisation was achieved by irradiating in uv light (λ = 320 - 280 nm) for 90 mins per sample side.

3.4.3. Elution Testing

Elution testing was performed to establish if selected samples were toxic or non-toxic. Samples were immersed in media for 48 h. After 24 h HOBs were seeded on to Thermanox slides at a cell density of 40,000 cells cm^{-2} in fresh media and left for one day. After a total of 48 h the media was changed for the media that had been on the samples. Metabolic activity of HOB cells was assessed by Alamarblue™ and DNA Hoechst staining 24 h after seeding. Cells were fixed and their morphology was viewed using SEM.

3.4.4. Initial Attachment

Samples were placed in 24 well plates (Nunc, UK) with one sample per well and 1 ml of media was added to each well. Tests were run in triplicate and repeated. Cells were seeded into wells at a cell density of 10,000 cells cm^{-2}. Plates were incubated for 90 minutes at 37 °C and 5 vol.% CO_2. After this period media was removed and the samples were washed in PBS three times and fixed in 4 wt.% paraformaldehyde for 10 min. Samples were washed again and then permealised for 5 min at -20 °C and washed. 0.1 wt.% propidium iodide was added for 1-2 s before washing and mounting samples on glass slides. A PBS solution containing 2 mg/ml of 1,4-diazabicyclo[2.2.2]octane (DABCO) was prepared at pH 8.6 and combined with glycerol in a 9:1 ratio of glycerol:DABCO/PBS. This solution and a coverslip were then applied for imaging. A Lecia DMLB optical microscope with a mercury lamp used in fluorescence mode with a BG38 filter at x10 magnification with a Nikon DXM1200 digital camera was used to image 25 random visual fields per sample. Cell counting was performed manually.

3.4.5. Metabolic Activity Assay

An Alamarblue™ assay was undertaken to assess the metabolic activity of HOBs over a 14 day time period. When added to cell cultures, the oxidised form of the Alamarblue™ (tetrazolium dye) enters the cytoplasm and is converted to the reduced form proportionally to cell metabolism by mitochondrial enzyme activity by accepting electrons from NADPH, FADH, FMNH, NADH as well as from the cytochromes [239]. This redox reaction is accompanied by a shift in colour of the culture medium from indigo blue to fluorescent pink which can be read on a fluorescence plate reader.

Duplicate samples were placed in 24 well plates and sterilised. TCP was used as a control surface. HOBs were seeded into wells at a density of 40,000 cells cm^{-2} and incubated at 37 °C and 5 vol.% CO_2. Media were changed every two days. At each respective time point (1, 4, 7, 10 and 14 days) the media was removed and samples were washed three times in PBS solution. 1 ml of a dilution of Alamarblue™ (Serotec, UK) and Hank's balanced salt solution (HBSS) (Gibco, UK) in the ratio of 1:10 was added to each well, including unseeded TCP wells and incubated for 80 minutes. Well plates were subsequently wrapped in foil and shaken at 300 rpm on a Heidolph Titramax 100 for 10 minutes in a dark environment. The Alamarblue™ solution was then removed and 100 µm from each well was aliquoted into a 96 well plate. Fluorescence was read using a Bio Tek Instruments FLx800 fluorscence plate reader using 560 nm excitation and 590 nm emission filters. Unreduced Alamarblue™ was subtracted from recorded values to remove background signal. Experiments were repeated twice.

3.4.6. Alkaline Phosphatase Assay

The Alkaline Phosphatase (ALP) assay was used as a measure of osteoblast differentiation at 1, 4, 7, 10 and 14 days. As osteoblasts produce this enzyme

they begin to enter the differentiation phase of the cell cycle. A substrate, 4-nitrophenlyphosphate mixed with diethanolamine buffer solution, was supplied with a Randox ALP alkaline phosphatase kit (Randox laboratories, UK) and mixed accordingly. This reacts with water in a dephosphorylation enzyme catalysed reaction:

Eqn 3.9. 4-nitrophenlyphosphate + H_20 → phosphate + 4-nitrophenolate

The production rate of 4-nitrophenolate is then determined photometrically which is directly proportional to ALP activity of cells on the sample. Photometry is the measurement of light. The radiant power of a wavelength of light is measured giving a relative intensity.

After each designated time point media was removed from culture plates and washed three times in PBS solution. Aliquots of 1 ml of sterile distilled water were added to each well. A freeze/thaw method was employed to ensure lyses of cells. Samples were frozen at -20 °C and then allowed to defrost at room temperature. This was repeated three times. Aliquots of 50 µl of solution were added to a 96 well plate per sample which was mixed with 50 µl of 4-nitrophenylphosphate mixed with an appropriate quantity of diethanolamine buffer solution. Plates were shaken at 300 rpm on a Heidolph Titramax 100 for 1 min in a dark environment. The eluminescence was measured using a Bio Tek ELx800 eluminescence plate reader with a primary wavelength of 405 nm and a reference wavelength of 630 nm.

3.4.7. DNA Hoechst Staining Assay

Cell proliferation can be determined by assaying the total DNA content at time points of 1, 4, 7, 10 and 14 days. DNA content is calculated by using standards based solutions of known DNA content.

At each time point media was removed and HOBs were washed in PBS three times and submerged in 1 ml of sterile distilled water. A freeze/thaw cycle was carried out in triplicate to lyse HOB cell walls. 100 µl of lysate was mixed with 100 µl of Hoechst 33258 stain (Sigma, Dorset, UK) and shaken at 300 rpm on a Heidolph Titramax 100 for 1 min in a dark environment. Fluorescence was then read on a Bio Tek Instruments FLx800 fluorescence plate reader with 360 nm excitation and 460 nm emission filters.

3.4.8. Scanning Electron Microscope Preparation

At selected time points media was removed and samples were washed three times in PBS and replaced with 3 wt.% glutaraldehyde in 0.1 M sodium cacodylate buffer. After 30 min this was replaced with 7 wt.% sucrose solution in 0.1 M sodium cacodylate buffer. Specimens were then washed three times for 5 min periods in 0.1 M cacodylate buffer solution and then immersed in osmium tetraoxide for 1 h. Post fixing, cells were dehydrated using an ethanol/distilled water gradient (20 vol.% x 2 min, 40 vol.% x 5 min, 60 vol.% x 5 min, 80 vol.% x 5 min 90 vol.% x 5 min and 100 vol.% x 5 min x 2). Specimens were then submerged in hexamethyldisilazane (HMDS) for 5 mins. This was then replaced with fresh HMDS and left to dry overnight.

Samples were mounted on aluminum stubs with carbon adhesive tabs and gold/palladium coated for 2 min in argon using an Emscope SC500 sputtering

device, giving a gold thickness of approximately 5 nm. Samples were viewed on a Philips XL-30 electron microscope as described in section 3.3.10.

3.4.9. Statistical Analysis

Statistical analysis was carried out using Prism® version 4.5.1 (Graphpad, California). Mean values, standard deviations (SD) and standard error of the mean (SE) were calculated using 3 replicates per time point. One way and two way analysis of the mean (ANOVA), with significance set at the 95 % confidence interval followed by a Tukey post test was used to measure significant differences between the control TCP, HA and SiHA surfaces.

4. Results

4.1. Introduction

This chapter arranges all results relevant to the current study into six separate sections. Section 4.2. details the characterisation of the two different targets used to produce BPM and UDP thin films. Section 4.3. summarises an investigation into the post-deposition heat treatment of HA thin films using techniques such as *in situ* XRD and FTIR. Section 4.4 describes the processes undertaken to optimise HA coatings and achieve the correct HA stoichiometry. This was carried out by changing deposition parameters such as discharge power and the sputtering environment. Section 4.5. summarises some of the characterisation techniques used and the accuracy at which compositional values may be quoted. Three techniques are investigated in order to assess possible uncertainty associated with each technique. Section 4.6. describes the results obtained from a large variety of techniques used to measure composition, chemical structure, the chemical bonding and surface morphology of HA and SiHA thin films. Finally, section 4.7. presents results for the initial attachment, proliferation and differentiation stages of HOBs on the surface of HA and SiHA thin films of varying composition and crystallinity.

4.2. Characterisation of Target Materials

4.2.1. Powder Targets

HA powder, obtained from Plasma Biotal Ltd., was analysed using SEM (section 3.3.10.) and XRD (section 3.3.3.) allowing particle morphology and phase purity to be checked. Figure 4-1 shows XRD plots for as received and HA powders sintered at 1350˚C for 3 h (section 3.2.3.). Both samples were single phase HA material matching to ICDD card 09-432. Post-sintering the reflections for the HA powder became more intense indicating a more crystalline material. Crystallite size was too large to be calculated by the Scherrer equation as particle size was >1 μm in length as seen in figure 4-2b. Post-sintering grain size increased to an approximate value of ca. 5 μm, which can be seen in figure 4-3b.

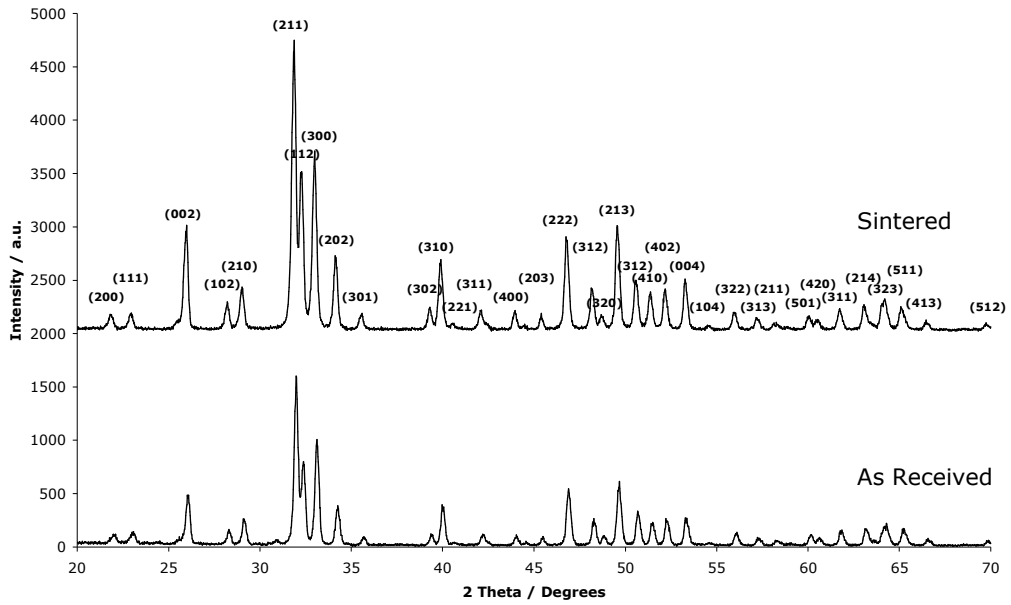

Figure 4-1. XRD plots of as received HA powder and HA sintered at 1350˚C for 3 h. Plane reflections are shown for respective HA diffractions. See appendices table A1 for further details.

SEM analysis of the as received powder showed HA to have a 'tapered crystal' like morphology. Crystallites tended to agglomerate in masses ranging from

approximately 1-10 μm in diameter (figure 4-2a) and individual crystallites measuring approximately 1 μm in length and 200 nm in width.

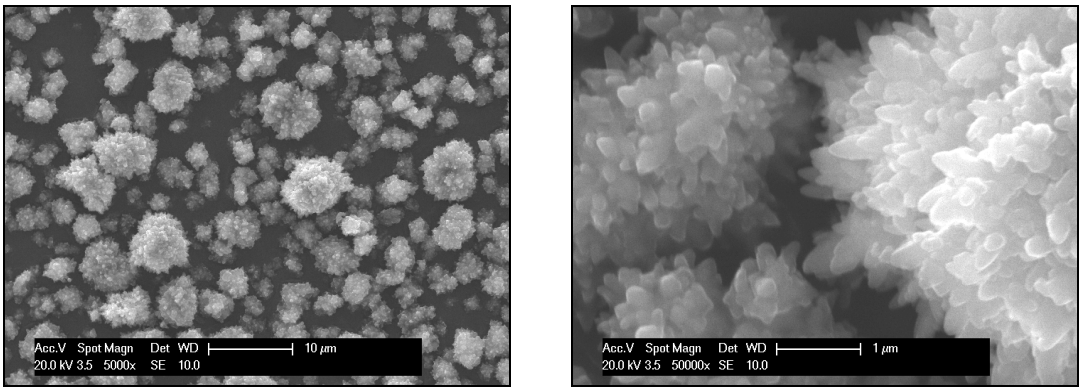

a **b**

Figure 4-2. SEM micrographs of as received HA powders mounted on adhesive carbon, a) showing clusters of particles and b) showing the individual crystals.

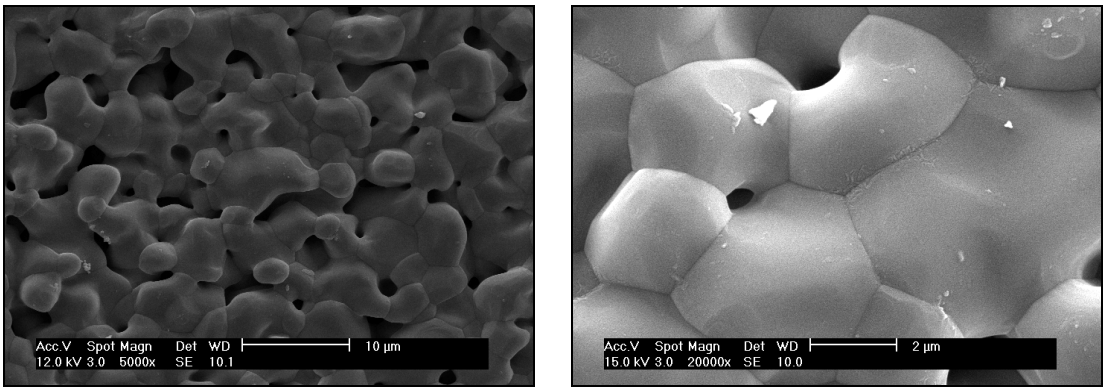

a **b**

Figure 4-3. SEM micrographs of pressed HA powders sintered at 1350˚C for 3 h, a) representative sintered structure and b) individual grains.

4.2.2. Plasma-sprayed Targets

Plasma-sprayed HA targets had a coating thickness of ca. 500 μm as determined by SEM (section 3.3.10.). XRD analysis showed the coating to be composed of a HA phase matching to ICDD card 09-432 and a small quantity of β-TCP matching

to ICDD card 09-169. A representative XRD pattern of a plasma-sprayed coating is shown in figure 4-4.

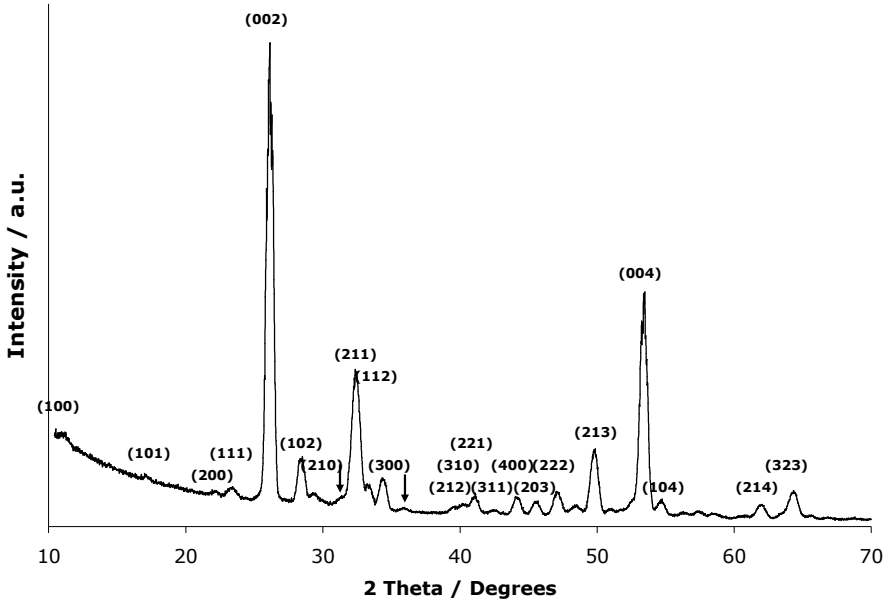

Figure 4-4. XRD pattern for a Plasma Biotal plasma-sprayed copper backed target. All major diffraction planes are indexed. Arrows indicate β-TCP secondary phase. See appendices table A3 for full details.

Coatings were preferentially orientated showing the (002) reflection to be the most intense and the (004) reflection the second most intense peaks. Compared to the HA powder diffraction peaks appeared broadened perhaps indicating a combination of smaller grain size and increased strain. Crystallite size was calculated using the (002) plane to be 23.4 nm, which is considerably smaller than the HA powders. Figure 4-5 shows typical SEM micrographs of the surface of plasma sprayed HA targets. It can be seen that coatings showed a splat morphology typical of plasma sprayed HA coatings. Cracking was observed across the surface. The Ca/P ratio was measured by EDX returning a value of 1.9 ± 0.1 (EDX_n) which is higher than the value of stoichiometric bulk HA.

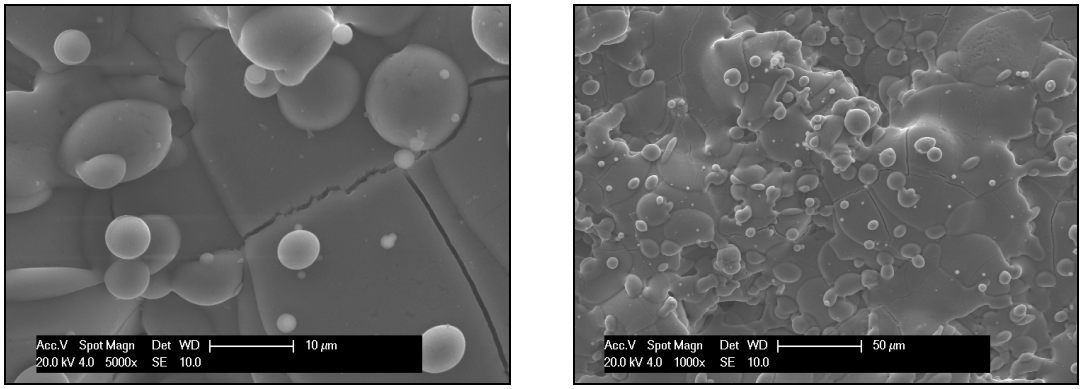

a **b**

Figure 4-5. An SEM micrograph of the surface of a Plasma Biotal plasma sprayed copper backed target. a) Cracks formed by residual stress in the coating and b) coating 'splat' morphology.

Having presented results for the characterisation of target materials, subsequent sections 4.3., 4.4., 4.5. and 4.6. details results for the characterisation of coatings deposited with the use of the aforementioned targets.

4.3. The Effects of Post-deposition Heat Treatment on Crystallinity of BPM HA Thin Films

Post-deposition annealing was carried out by *in situ* XRD to investigate the effect on crystallinity. BPM HA films were used with a Ca/P ratio of 2.43 ± 0.3 (EDX_n), as measured by EDX. Films were deposited onto silicon (100) single crystal wafers in order to identify the temperature range that HA thin films may recrystallise. Silicon wafers were used for two reasons; firstly reflections were only seen at 2θ values higher than 55 ° thus not overlapping with HA reflections and secondly silicon has a high melting point and low diffusion coefficient allowing the samples to be elevated to high temperatures without being affected by the substrate. Once established, this temperature region was explored in more detail with the use of furnace annealing followed by *ex situ* XRD and FTIR analysis on films deposited on CPTi samples.

4.3.1. X-ray Diffraction

4.3.1.1. *In Situ* XRD

HA films sputtered onto silicon (100) single crystal wafers were held at set temperatures for prolonged time periods and XRD peak growth was monitored. A sample was held at 400°C in an inert helium atmosphere and glancing angle XRD scan was performed every 16 minutes. A range between 27 and 34 ° 2θ was chosen to show crystal growth of the (102), (210), (211), (112) and (300) diffraction planes. Figure 4-6 shows a HA coated silicon (100) wafer held at 400°C for 800 min. It can be seen that the coating is amorphous with two distinct broad humps observed at approximately 28°and 32° 2θ. It can be seen that prolonged exposure did not cause the coating to alter from an amorphous state (figure 4-6).

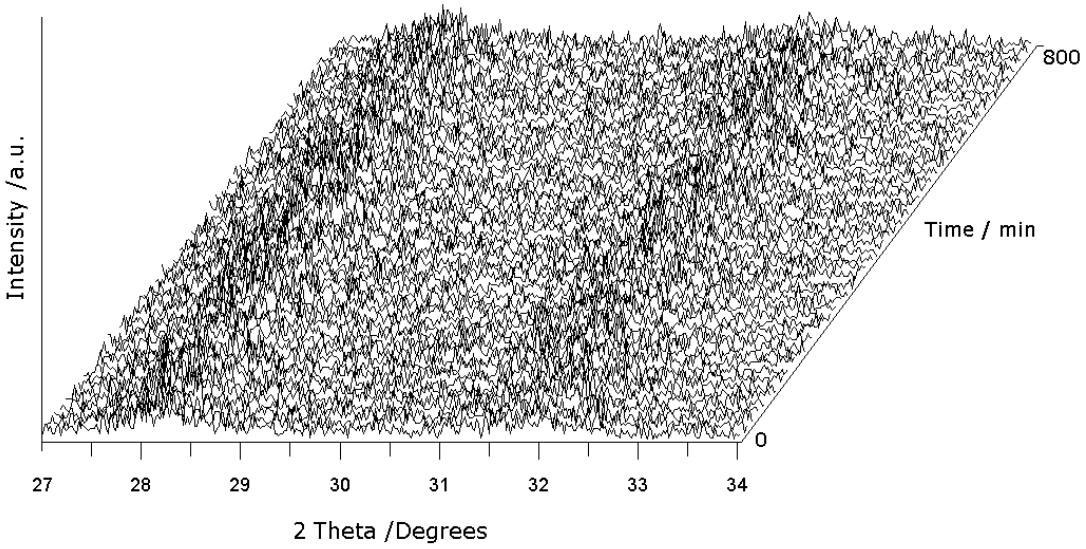

Figure 4-6. A staggered *in situ* XRD plot a HA thin film deposited onto a silicon (100) wafer and maintained at 400˚C under helium for 800 min.

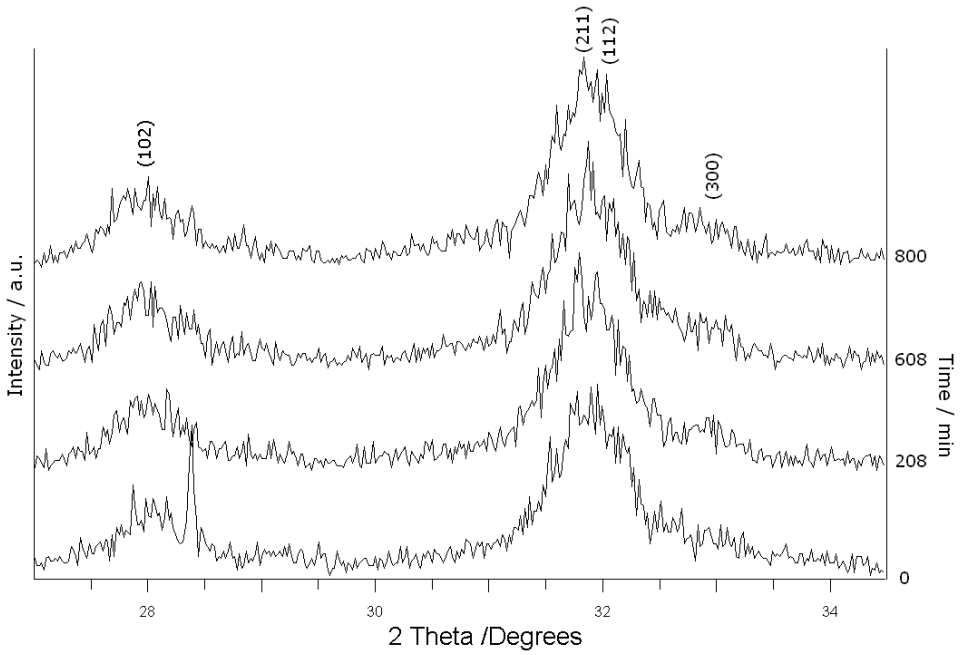

Figure 4-7. An *in situ* XRD plot of an HA thin film deposited onto a silicon (100) wafer held at 600˚C under helium for 800 min. Only 4 scans are shown to illustrate data more clearly. See appendices table. See appendices table A4 for full details.

A repeat experiment was then performed with a new HA thin film being held at 600˚C for a total of 800 min. The initial scan, shown in figure 4-7, showed the film to be crystalline with two distinct peaks corresponding to the (102) plane at

28.1° 2θ and a combination of the (211) (112) and (300) planes at 31.9, 32.2 and 33.1 ° 2θ (ICDD card 09-432, 2θ = 28.1, 31.8, 32.2 and 32.9° respectively), suggesting a single phase HA film. XRD peak shape gradually increased in intensity when held at this temperature over the 800 minutes.

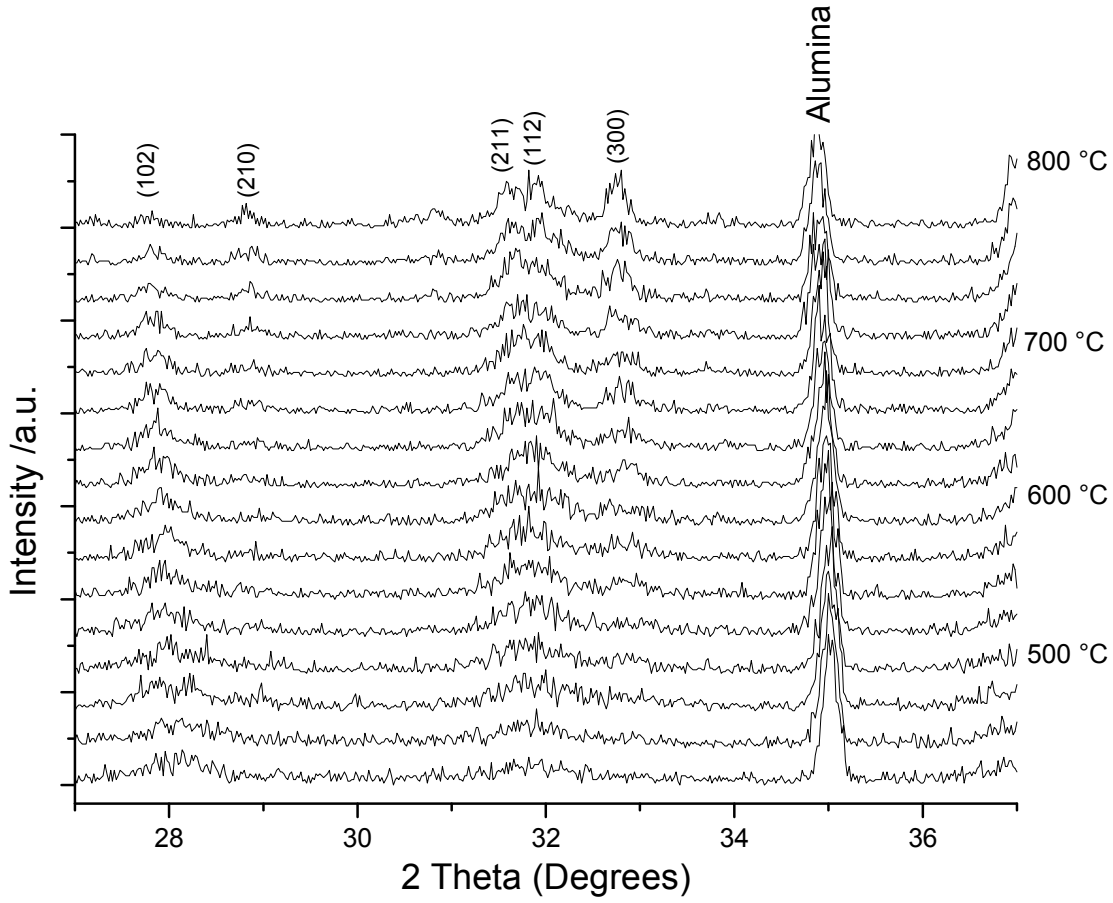

Figure 4-8. *In situ* glancing angle XRD plot of an HA thin film deposited onto a silicon (100) wafer at annealing temperatures from 425 to 800°C in a helium atmosphere at a temperature step of 25°C per scan.

The crystallinity of HA thin films at increasing temperatures was investigated. Samples were heated from 400 – 800°C with 25°C steps holding at each temperature to carry out a 16 min scan. XRD plots from 27 – 37 ° 2θ are shown in figure 4-8. At 400°C two amorphous humps were seen as before. By 500°C a third small hump appeared between 33 ° 2θ. Broad peaks became more clearly defined approaching 600°C. Further peak growth was seen up to 800°C at which

point the (102), (210), (211), (112) and (300) HA diffraction planes could all be clearly observed (ICDD card 09-432, 2θ = 28.1, 28.9, 31.8, 32.2, 32.9 and 34.0° respectively). The amorphous hump at 28° 2θ at the lower temperatures was seen to shift to lower 2θ value with increasing temperature appearing to form the (102) diffraction plane. A further peak attributed to alumina can be seen at 35° 2θ. This reflection arose from the alumina sample holder used or alumina powder used to adjust the sample height (section 3.3.3.)

The signal to noise ratio was low in all experiments due to the use of glancing angle mode, low coating thicknesses, the beryllium window leading to X-ray absorption and the use of helium gas. All these factors made it difficult to distinguish an exact temperature at which recrystallisation actively began, however, it was not possible to increase the time of scan as this would have had a large follow on effect for the total run time lowering the practicality of the technique.

4.3.1.2. X-ray Diffraction

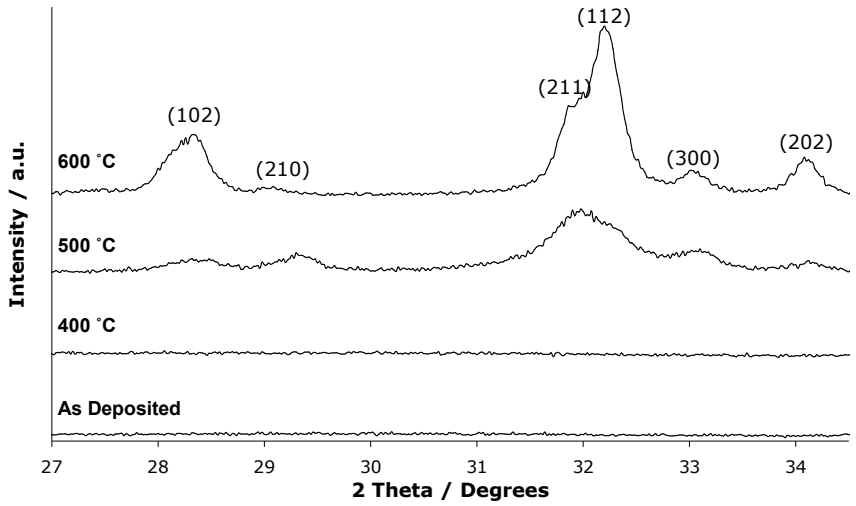

Figure 4-9. Expanded XRD plots for HA thin films deposited onto CPTi discs following post deposition heat treatments for 2 h in an argon atmosphere. See appendices table A5 for full details.

XRD was carried out on BPM HA films deposited onto CPTi to observe the effects of heat treatments had on the thin films. This proved advantageous compared to *in situ* XRD as higher signal to background ratios were possible. Figure 4-9 shows expanded axis XRD data for HA films sputtered onto CPTi discs following heat treatments at 400, 500 and 600°C for 2 h in a flowing argon atmosphere.

As-deposited samples were amorphous. After a heat treatment at 400°C the coatings remained amorphous. At 500°C small peaks matching to ICCD card 09-432 were observed, indicating a poorly crystalline or nano-crystalline HA phase was present, suggesting recrystallisation. A further heat treatment at 600°C lead to crystallite growth of the HA phase signified by more intense HA peaks. These peaks were attributed to (102), (210), (211), (112), (300) and the (202) HA crystal planes (ICDD card 09-432, 2θ = 21.8, 28.9, 31.8, 32.2, 32.9 and 34.0° respectively).

4.3.1.3. Fourier Transform Infrared Spectroscopy

Figure 4-10 displays infrared spectra for BPM RF sputtered HA films heat treated at various temperatures in flowing argon. Atmospheric water vibrations were observed between 1500 and 1400 cm^{-1}. As-deposited coatings showed two broad phosphate bands at 1136 and 1012 cm^{-1}. After a heat treatment at 400°C for 2 h a sharp OH peak was seen at 688 cm^{-1} along with a stretching carbonate band at 1406 cm^{-1}. At 500°C additional phosphate bands were seen to appear at 1084 and 940 cm^{-1}, while a sharp carbonate bending band appeared at 874 cm^{-1}. After a heat treatment at 600°C all bands became more pronounced and a further OH band appeared at 3642 cm^{-1} as shown in figure 4-10d'. See appendix table A2 for full details of peak assignments including references.

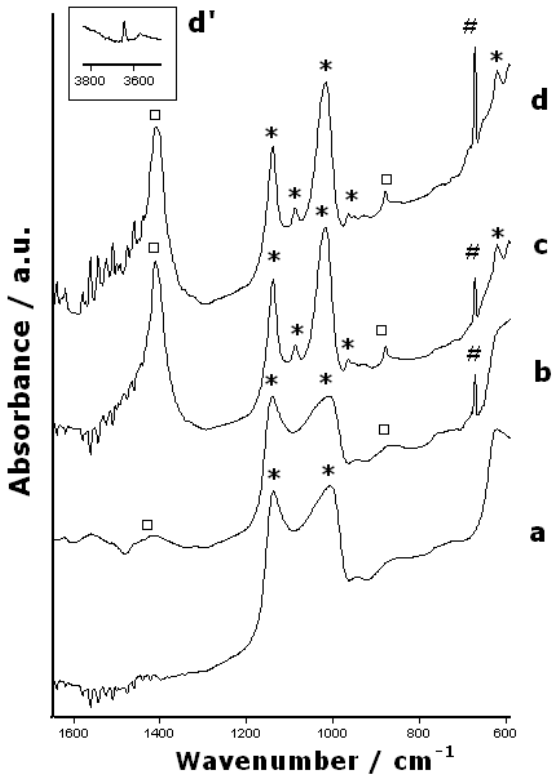

Figure 4-10. Absorbance infrared spectra of a) as-deposited, HA films heat treated at b) 400˚C, c) 500˚C, and d) at 600˚C for 2 h in flowing argon with d') showing the presence of an OH peak. □ corresponds to carbonate bonding, * to phosphate, and # to OH vibrations. See appendices table A2 for full details.

4.4. The Optimisation of UDP Thin Film Composition

Different PVD systems and deposition parameters can lead to compositional variations in HA films. Initial parameters were established using the BPM rig, however, as the UDP rig had the advantage of being able to deposit on a large number of substrates with a larger amount of control this system was adopted. Therefore, it was necessary to optimise the UDP thin films utilising understanding that was established from the BPM thin films. Parameters such as power supply, power density and gas composition were all investigated. XRD and EDX were used to identify crystal structure and composition.

4.4.1. The Effect of Power Supply

Pulsed DC and RF power supplies were investigated individually in order to identify their suitability for the production of HA thin films. Ball crater measurements showed that pulsed DC power supply (run at 6.8 W cm^{-2}) had an approximate deposition rate of 1.7 nm min^{-1} whereas the RF power supply (run at 6.8 W cm^{-2}) had a deposition rate of 2.5 nm min^{-1}. XRD analysis of both coatings as-deposited and after annealing at 600°C for the pulsed DC and RF power supplies are shown in figures 4-11 and 4-12 respectively.

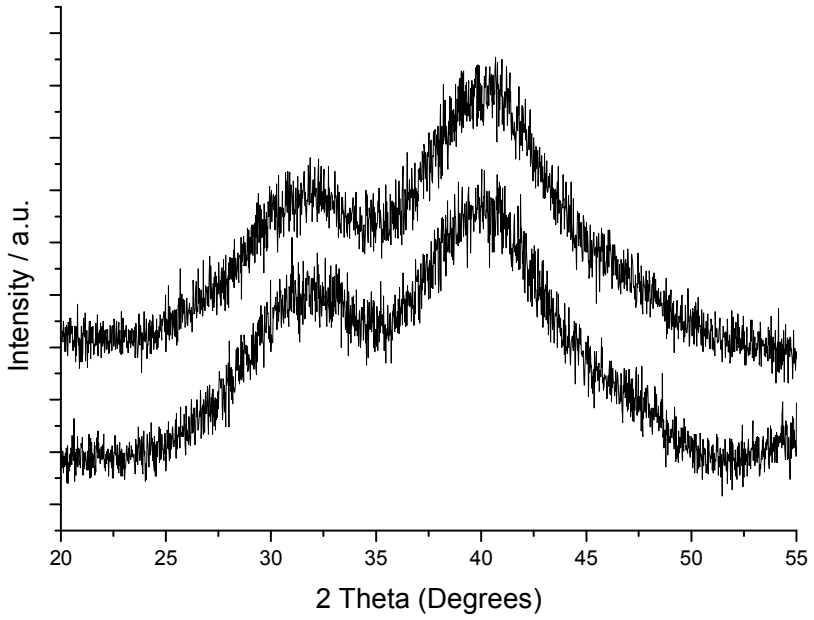

Figure 4-11. XRD plot of a thin film with a pulsed DC power supply run at a power density of 6.8 W cm^{-2} in as-deposited state and after annealing at 600˚C for 2 h in flowing argon deposited (Sample Ref. 7014)

It can be seen that as-deposited the pulsed DC film was amorphous. Two distinct humps were seen, the first probably corresponding to an amorphous HA structure. The second however is more likely to relate to a secondary calcium phosphate phase such as β-TCP or CaO. After annealing at 600˚C for 2 h the coating structure remained unchanged. Furthermore, depositions onto glass slides led to a film with a brown tinge indicating impurities in the coating. In comparison, the as-deposited RF magnetron sputtered coating was also amorphous, however this transformed to a (002) preferentially orientated HA crystal structure after heat treatment. Fewer HA crystal planes were observed when compared to ICDD card 09-432. Depositions of this coating onto glass slides were transparent. Table 4-1 shows deposition parameters and Ca/P ratio for all coatings in this section. It can be seen that the pulsed DC film had a very high Ca/P ratio of 2.43 compared to the stoichiometric value of HA which is 1.67,

whereas the RF magnetron sputtered coating was significantly lower at a value of 1.80.

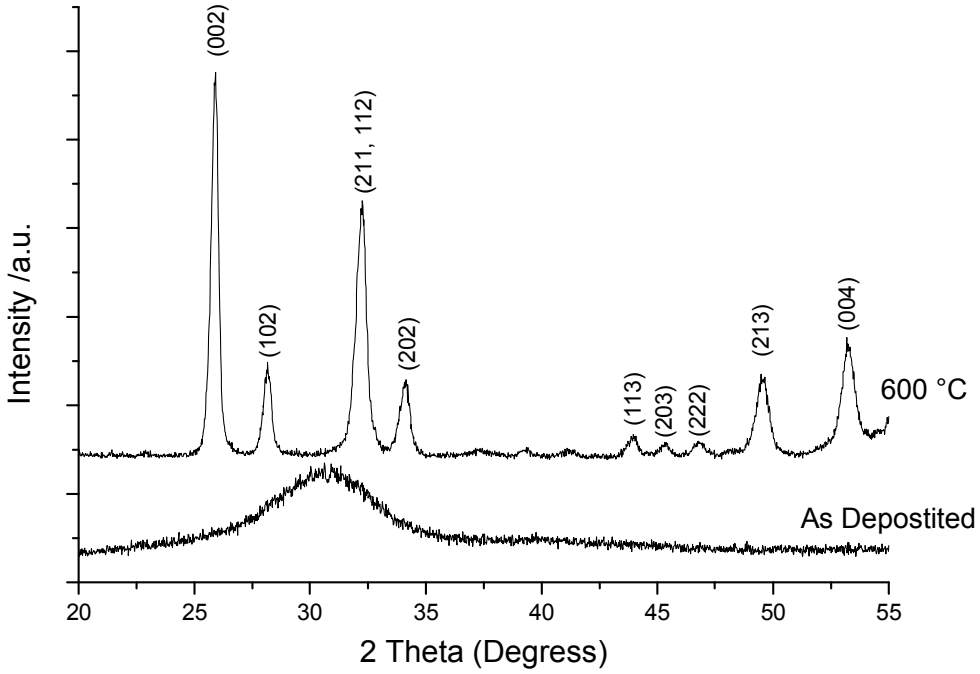

Figure 4-12. XRD plot of a thin film in as-deposited state and after annealing for 600˚C for 2 h in flowing argon produced with a RF power supply run at a power density of 6.8 W cm^{-2} in an argon atmosphere (Sample Ref. 7017). See appendices table A6 for full details.

Sample Description	Sample Ref. No.	Ca/P
Pulsed DC, 6.8 W cm^{-2}	7014	2.43 ± 0.05
RF, 6.8 W cm^{-2}	7017	1.80 ± 0.01
RF, 11.3 W cm^{-2}	7019	2.95 ± 0.03
RF, 6.8 W cm^{-2}, Oxygen	7125	1.68 ± 0.02
RF, 4.5 W cm^{-2}, Oxygen	7128	1.64 ± 0.01

Table 4-1. A brief summary of all films and deposition parameters with respective Ca/P ratios, as measured by EDX$_n$. See table 3-1 for full details.

4.4.2. The Effect of Power Density

Increasing the power discharge of RF sputtering from 6.8 W cm^{-2} (figure 4-12) to 11.3 cm^{-2} led to an increase in deposition rate from 2.5 to 6.7 nm min^{-2}. Figure 4-13 shows an XRD plot for a RF sputtered coating produced at a power density of 11.3 W cm^{-2}. It may be seen that crystal structure of the as-deposited coating displays a semi-crystalline HA structure due to the presence of an amorphous hump, but also displays (002), (102), (211), (112), (202), (213) and (004) reflections (ICDD card 09-432 2θ = 25.9, 28.1, 31.8, 32.2, 34.0, 49.5 and 53.2). The most intense reflection was from the (002) plane suggesting preferential orientation with respect to this crystal plane. After a heat treatment of 600˚C the coating was seen to crystallise further leading to more intense diffraction peaks and a larger number of diffraction planes. Unlike the coatings sputtered at 6.8 W cm^{-2} an additional calcium phosphate phase was seen at 2θ = 37.5 ˚ which corresponds to calcium oxide or β–TCP, however these two diffraction peaks overlap making identification difficult.

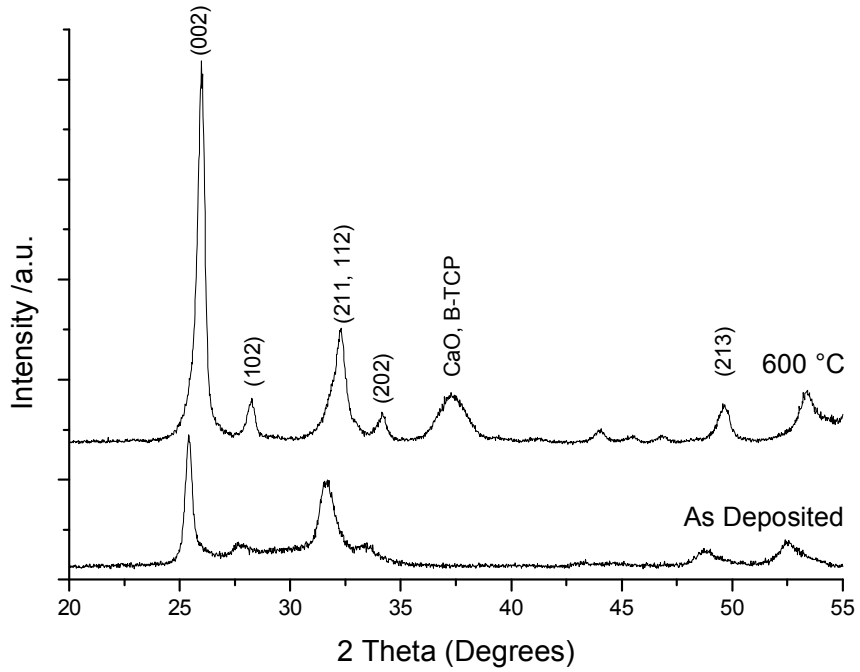

Figure 4-13. An XRD plot of an as-deposited and HA thin film annealed at 600˚C for 2h in flowing argon sputtered at 11.3 W cm^{-2} (Sample Ref. 7019). See appendices table A7 for full details.

4.4.3. The Effect of Gas Composition

It has been well documented that the inclusion of oxygen can aid stoichiometry of HA thin films (section 2.8.1.3). The parameters used for the sputtering of the HA coatings in argon were mimicked with the inclusion of 5 sccm of oxygen corresponding to a 12 vol.% oxygen atmosphere. Figure 4-14 shows XRD plots for an as-deposited and annealled HA coatings on a silicon (100) wafer. As-deposited coatings were amorphous, however, after heat treatment, a HA crystal structure could be identified matching ICDD card 09-432. A small quantity of β-TCP was also seen at a 2θ value of 31°. More diffraction planes were indexed compared to the HA coatings deposited without an oxygen atmosphere. Preferential orientation along the (002) plane suggested growth along the c-axis of the HA lattice. Moreover, the use of oxygen reduced the deposition rate from 2.5 nm min^{-1} to 1.7 nm min^{-1}.

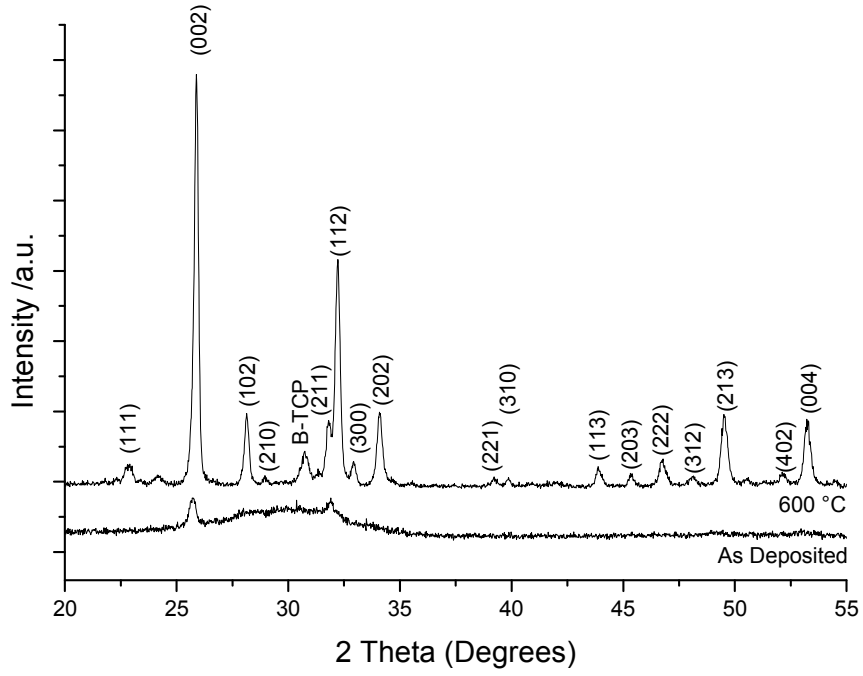

Figure 4-14. XRD plots of a HA thin film, sputtered at 6.8 W cm^{-2} in an argon/oxygen atmosphere in as-deposited state and annealed at 600°C for 2 h in flowing argon (Sample Ref. 7125). See appendices table A8 for full details.

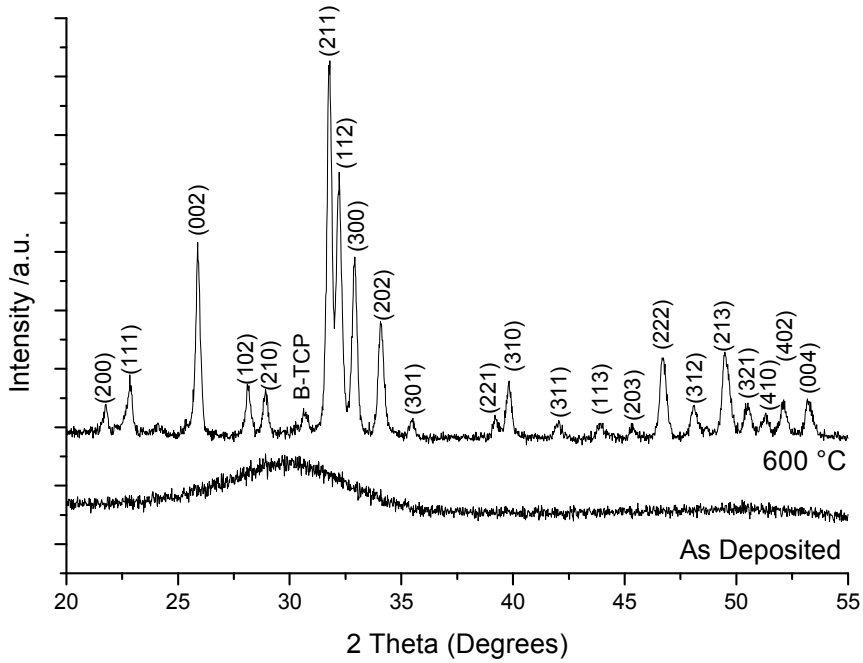

Figure 4-15. XRD plots of a HA thin film, sputtered at 4.5 W cm^{-2} in an argon/oxygen atmosphere as-deposited and annealed (Sample Ref. 7128). See appendices table A9 for full details.

Figure 4-15 shows an XRD plot of an HA coating sputtered at a power density of 4.5 W cm^{-2} in a 12 % oxygen/argon environment. The (211) plane was more intense than the (112). The reduction in power lowered the deposition rate slightly but not as much as changing the sputtering atmosphere. A small peak was attributed to β-TCP at 31° 2θ (ICDD card 09-0169, 31.0° 2θ)

RF magnetron sputtering systems often differ from rig to rig, and therefore it is important to perform sputtering runs at altered parameters to evaluate final coatings. Sputtering parameters were investigated such as the use of DC and RF power supplies, power densities between 4.5 – 11.3 W cm^{-2} and argon or argon/oxygen gas mixtures. It was found that coatings produced by RF magnetron sputtering at a power density of 6.8 W cm^{-2} and an argon/oxygen atmosphere allowed a HA crystal structure, stoichiometry and efficient deposition

rate to be achieved. This provided a good thin film system which could be modified with silicon dopant material.

4.5. Accurate Measurement of the Ca/P ratios of Thin Films

Although the deposition parameters for the HA thin films was optimised to allow for the best possible stoichiometry concerns over the methods employed to measure the Ca/P ratio was raised. Therefore, an investigation was carried out to evaluate the accuracy of the techniques commonly used to measure the Ca/P ratio of thin films.

The details of deposition parameters and thin film information for the three coatings investigated are detailed in table 4-2. Sample 1 and 2 were sputtered onto CPTi discs while sample 3 was coated onto silicon (100) orientated wafer. Full deposition details can be found in table 3-1 by using sample reference numbers. This allowed comparison not only of different thin film composition but also the effect of substrate.

Sample No.	Sample Ref. No.	Power Supply	Target Bias (V)	Power Density (W cm^{-2})	Gas Composition (%)	Duration (min)	Deposition Rate (nm min^{-1})	Rig/ Target Details
1	7017	RF	300	6.8	100% Argon	120	2.5	Teer Coating Ltd UDP450/4/ Plasma Biotal
2	7125	RF	300	6.8	87.8% Ar/12.2% O_2	180	1.1	Teer Coating Ltd UDP450/4/ Plasma Biotal
3	CSIRO	RF	300	9.1	100% Argon	20	5.0	In House Built/ (Australian Surgical)

Table 4-2. Summary of run parameters for calcium phosphate coatings. See table 3-1 for full deposition details.

4.5.1. Energy Dispersive X-ray Analysis (EDX)

Major peaks at 0.525, 2.01, 3.71, and 4.53 KeV representing O, P, Ca, and Ti Kα respectively were observed, as shown in figure 4-16. In addition a titanium escape peak was observed at 2.77 KeV. Sample 3 showed Si Kα peaks at 1.74

KeV as opposed to Ti lines as this sample was-deposited onto silicon wafer. The presence of Ti or Si peaks confirmed that the electron beam penetrates through the thickness of the films. Ti or Si peaks originating from the substrate were deconvoluted and discarded for quantification purposes. An escape peak strip was not performed as not to induce more potential error into the quantitification. Furthermore, this peak did not impinge on any of the peaks in question thus making this additional calculation unnecessary. Ca/P ratios were calculated by quantifying in "all elements mode" allowing determination of the atomic percentages of Ca and P only. This method was chosen as opposed to stoichiometric mode, which assumes that oxygen is bound to elements dependant on element valance, as accurate measurement of light elements (Z < Na) is limited in EDX systems [89]. Furthermore, the Ti Lα peaks (0.535 KeV) overlap with the O Kα peaks (0.525 KeV) thus increasing the uncertainty that oxygen percentages can be calculated.

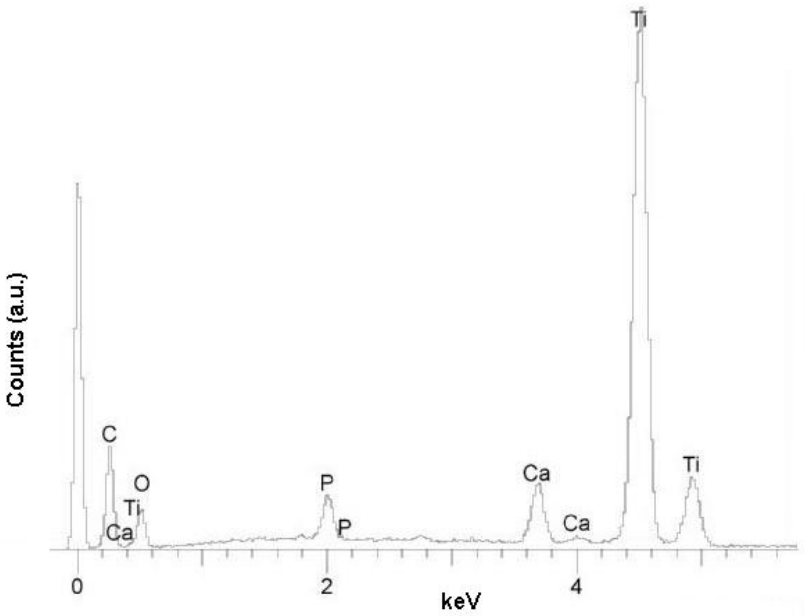

Figure 4-16. A typical EDX spectrum obtained for calcium phosphate thin film sputtered on a CPTi substrate showing major Ca, P, O, C and Ti Kα spectral lines.

4.5.2. Rutherford Backscattering Spectroscopy (RBS)

Figure 4-17 shows representative RBS spectra obtained for all samples. All spectra showed excellent reproducibility. All expected elements were detected (Ca, P and O) with the addition of small quantities of W (0.1 at.%) found at the film substrate interface of samples 1 and 2. Figure 4-18 shows depth profiles obtained by RBS for each sample at increasing intervals approaching the coating/substrate interface. RBS depth profiles have been fitted using the assumption that Ca is in the form of CaO or in a free state. P has been assumed to be in PO_4 tetrahedral configuration. Figure 4-18a and 4-18b show small variations of composition with depth. Sample 1 decreased in Ca and increases in CaO at approximately 1300 x 10^{15} atoms cm^{-2} and then returns to the same composition at approximately 2700 x 10^{15} atoms cm^{-2}. Similarly, sample 2 showed a small change at 1800 x 10^{15} atoms cm^{-2}. P concentration varied only slightly in all samples at any depth with no relation to the Ca and CaO variations. Sample 3 showed no variation with depth.

While sample 1 and 2 films varied slightly in composition with depth average atomic densities can be calculated by dividing average atoms cm^{-2} by the measured thickness of the films, as shown in table 4-3. All densities were not significantly different. All samples had a higher density than that of bulk phase HA which is 9.4 x 10^{22} atoms cm^{-2} at room temperature and atmospheric pressure [182].

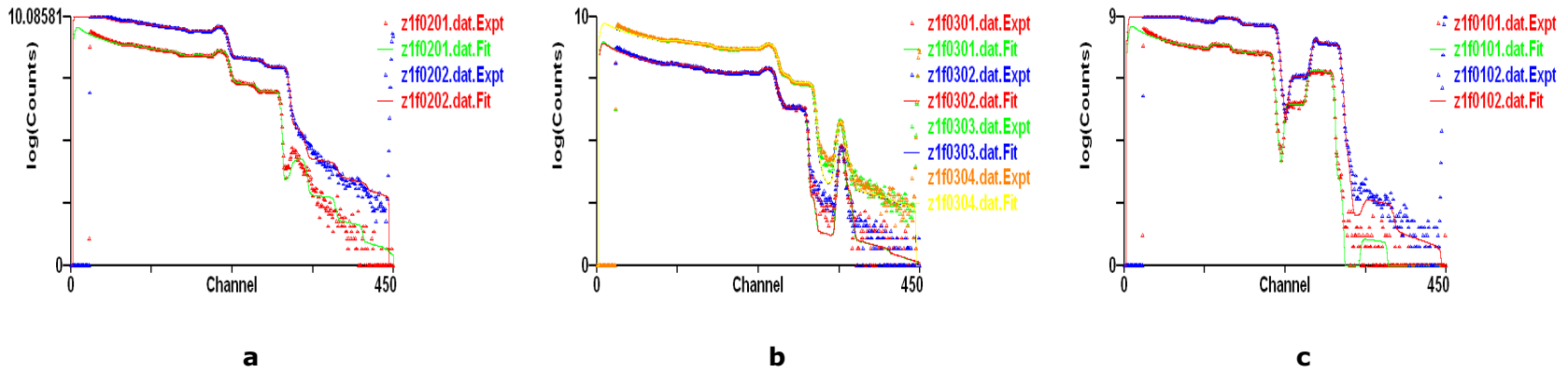

Figure 4-17. Representative RBS spectra for a) sample 1 on a CPTi disc, b) sample 2 on a CPTi disc and c) sample 3 on a silicon (100) wafer.

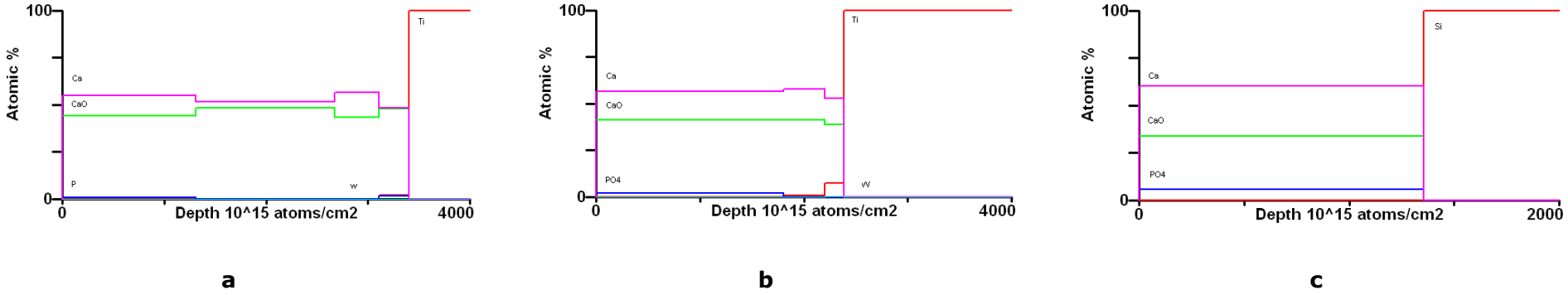

Figure 4-18. RBS depth profile of a) sample 1 on titanium substrate, b) sample 2 on titanium substrate and c) sample 3 on a (100) orientated silicon wafer.

Sample No.	Atomic Density / 1 x 10^{22} atoms cm^{-3}	Measured thickness / nm
1	11 ± 1	300
2	12 ± 1	200
3	14 ± 4	100

Table 4-3. Calculated atomic densities of films using thicknesses measurements obtained by a ball crater technique performed at Teer Coatings Ltd. with an accuracy of approximately ± 25 nm. Bulk phase HA has an atomic density of 9.4 x 10^{22} atoms cm^{-3} [182].

4.5.3. X-ray Photoelectron Spectroscopy (XPS)

Figure 4-19 shows a representative high resolution XPS spectrum obtained from the Kratos instrument of the O 1s, P 2p, Ca 2p and C 1s peaks for a calcium phosphate coating. The C 1s peak was used for charge correction at a value of 285 eV [240]. All peaks were fitted with Gaussian-Lorentzian (GL-30) line shapes. The Ca $2p_{3/2}$ and $2p_{1/2}$ doublet was fitted with a double component, separated by 3.55 eV. Furthermore, the P 2p peak was fitted with two components with a 0.84 eV separation corresponding to a doublet. Ca 2p and O 1s peaks were fitted with a Shirley [93] background to account for the larger background energy loss. C 1s and P 2p spectral lines were fitted with linear backgrounds. Sample 1 and 2 were found to have similar peak positions within 0.1 eV difference (table 4-4). However, the peak positions of sample 3 for the O 1s and the Ca 2p spectral lines were slightly higher suggesting a small variation in coating chemistry. Atomic percentages calculated with the Kratos relative sensitivity library corrected for system geometry are shown in table 4-5. The Kratos instrument was used to report peak positions because it has a monochromated beam thus increasing the accuracy of these measurements. Moreover, count rates were found to be generally higher than the ESCAlab apparatus leading to more accurate quantitification. Carbon contamination varied from 13.43 to 30.54 at.% on all the films. As there is a large amount of variation

in the carbon content of films, values were adjusted for comparison without carbon. When this calculation is performed sample 1 contained 65.2 at.% oxygen with samples 2 and 3 contained 65.4 at.%. However these values are not significantly different. The calcium content decreased from 21.9 at.% to 19.9 at.% from sample 1 to 3, however, the phosphorus content increased from 12.8 to 14.7 at.%.

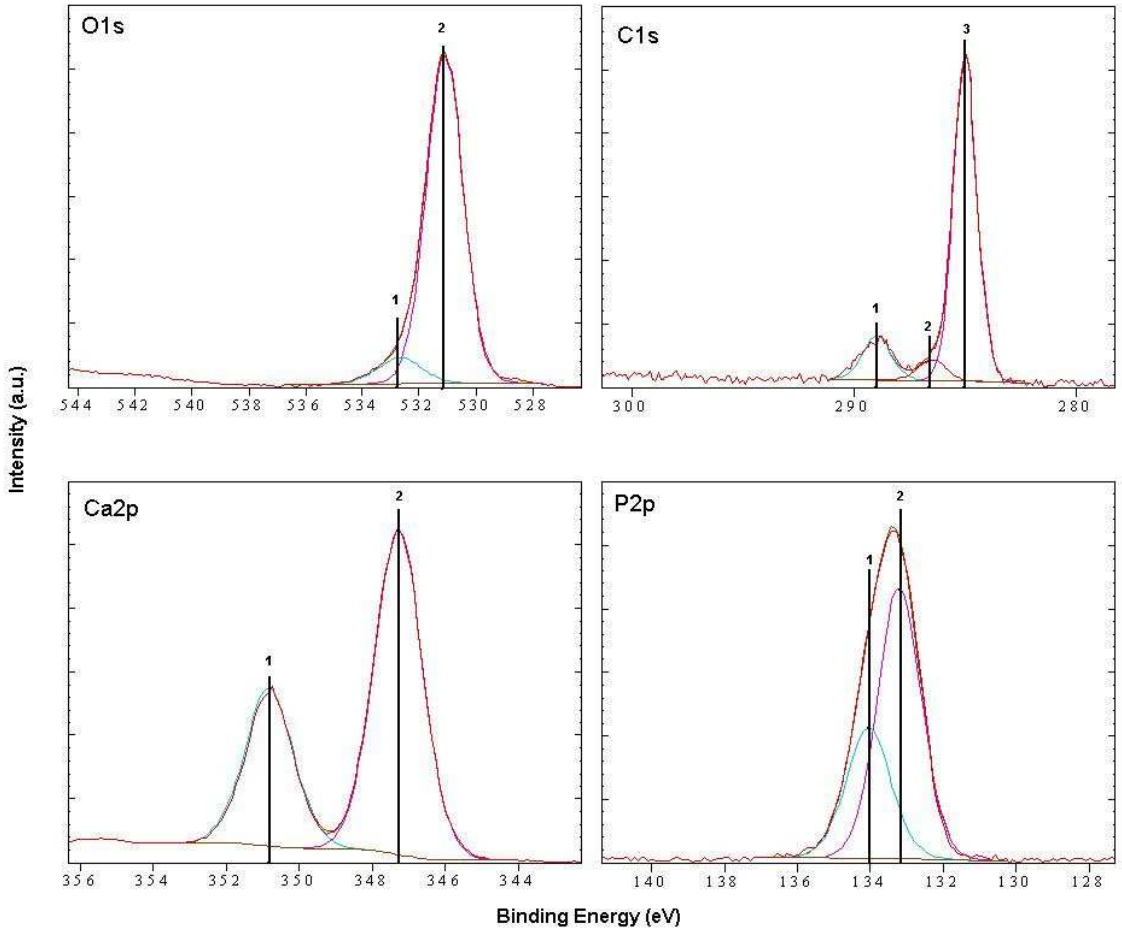

Figure 4-19. Representative high resolution O 1s, C 1s, Ca 2p and P 2p XPS data of calcium phosphate coated surfaces. Individual elements have been assigned numbers in accordance with fitted components. Each component represents a possible chemical species. These are assigned accordingly; O 1s 1: $Ca(OH)_2$ 2: PO_4, C 1s 1: C-O 2: Hydrocarbon 3: adventitious carbon, Ca 2p 1: Ca $2p_{1/2}$ 2: , P Ca $2p_{3/2}$ P 2p 1: P $2p_{1/2}$ 2: P $2p_{3/2}$.

Sample No.	Region	Binding Energy (eV)	±
1	O 1s PO_4	531.0	0.05
	O 1s $Ca(OH)_2$	532.6	0.05
	Ca $2p_{3/2}$ CaO	347.3	0.03
	Ca $2p_{1/2}$ CaO	350.8	0.03
	C 1s (Adventitious C)	285.0	0.02
	C 1s (Hydrocarbon)	288.9	0.03
	C 1s C-O	286.5	0.02
	P $2p_{3/2}$	133.2	0.02
	P $2p_{1/2}$	134.0	0.02
2	O 1s PO4 [203]	531.1	0.08
	O 1s CaO, $Ca(OH)_2$, $CaCO_3$, P_20_5	532.7	0.17
	Ca $2p_{3/2}$ CaO	347.4	0.05
	Ca $2p_{1/2}$ CaO	351.0	0.05
	C 1s (Adventitious C)	285.1	0.05
	C 1s (Hydrocarbon)	288.8	0.05
	C 1s C-O	286.6	0.05
	P $2p_{3/2}$	133.3	0.05
	P $2p_{1/2}$	134.1	0.05
3	O 1s PO_4 [203] $CaCO_3$	531.4	0.02
	O 1s CaO, $Ca(OH)_2$, $CaCO_3$	533.0	0.03
	Ca $2p_{3/2}$ $CaHPO_4$, $Ca_2P_2O_7$	347.6	0.02
	Ca $2p_{1/2}$ CaO	351.2	0.02
	C 1s (Adventitious C)	285.0	0.01
	C 1s (Hydrocarbon)	288.8	0.04
	C 1s C-O	286.5	0.01
	P $2p_{3/2}$	133.4	0.02
	P $2p_{1/2}$	134.2	0.02

Table 4-4. Kratos XPS binding energies of all O 1s, Ca 2p, P 2p and C 1s fitted components for all high resolutions scans.

Sample	Region	Atomic %	±
1	O 1s	54.04	0.15
	Ca 2p	18.15	0.05
	C 1s	17.21	0.15
	P 2p	10.61	0.05
2	O 1s	56.51	0.25
	Ca 2p	17.92	0.02
	C 1s	13.43	0.26
	P 2p	11.96	0.03
3	O 1s	45.44	0.32
	Ca 2p	13.80	0.20
	C 1s	30.54	0.50
	P 2p	10.21	0.08

Table 4-5. Atomic percentages of all samples determined by O 1s, Ca 2p, C 1s and P 2p high resolution spectra.

Figure 4-20 shows the effect of Kratos Al Kα X-rays (electromagnetic radiation), where λ = 8.3 Å for Al Kα X-rays run at 10 KeV, on a BPM HA coating as described in section 4.3 during normal XPS analysis. Carbon was used as a negative control. It can be seen that throughout the experiment the atomic percentage of P and Ca remained unchanged. It was concluded that calcium phosphate thin films are stable under electromagnetic radiation of this wavelength.

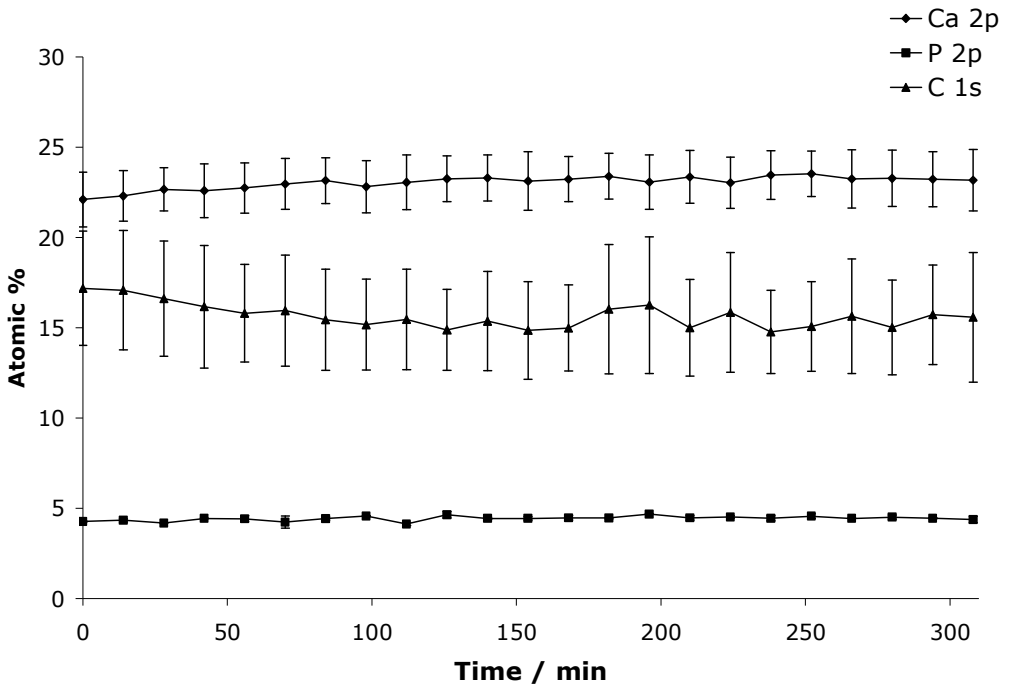

Figure 4-20. The effect of prolonged exposure of X-rays during normal XPS analysis on a calcium phosphate coating for a period of 3.5 h. Ca 2p, P 2p and C 1s data is shown and plotted as mean ± standard error of mean.

4.5.4. Calcium to Phosphorus Ratios

Table 4-6 summarises the Ca/P ratios obtained for EDX, XPS and RBS for the Plasma Biotal standard and sputtered thin films. RBS consistently gave the highest Ca/P ratios for the thin films, followed by EDX and XPS yielding the lowest values. All techniques recorded a decrease in Ca/P ratio from sample 1 to 3. A clear difference was observed between the two XPS instruments with the Kratos values being on average 28 % higher than unetched ESCAlab XPS values. After argon etching (section 3.3.5.) on the ESCAlab instrument higher Ca/P ratios were recorded than from the unetched samples.

Sample	EDX All elements	XPS Kratos	XPS ESCAlab	XPS ESCAlab Etched	RBS
Standard[a]	1.63±0.02[b]	1.63±0.03	1.27±0.02	1.32±0.03	1.67±0.04
1	1.94±0.01	1.71±0.01	1.30±0.01	1.78±0.01	2.20±0.02
2	1.82±0.02	1.50±0.00	1.14±0.01	1.69±0.01	1.98±0.03
3	1.79±0.06	1.35±0.01	1.11±0.01	1.64±0.02	1.89±0.01

Table 4-6. A summary of Ca/P ratios of all calcium phosphate coatings. [a]P120 Plasma Biotal HA powder Ca/P = 1.70 calculated using X-ray fluorescence analysis for major compound components (appendix table A15), [b] Ca/P calculated from prexisting apatite standards. Data presented is the mean ± standard error of mean, where n = 3 in terms of scans. This was calculated from data obtained from instrument readings. Uncertainty due to instrument accuracy has not been included.

A positive correlation between coating thickness and Ca/P ratio was observed by all techniques. The addition of oxygen to the sputtering environment aided to lower the Ca/P ratio, by an average of 0.16 Ca/P units, which was confirmed by all analytical techniques.

4.6. Chemical and Structural Characterisation of UDP HA and SiHA Thin Films

Due to the large number of samples required for investigating the *in vitro* cellular response and characterisation two batches of coatings were produced for set of run parameters. For the purpose of this section the batches with the same run parameters have been combined. Details of all coatings are provided in chapter 3, table 3-1, however in this section coatings will be referred to as HA (runs 8082 + 8084), SiHA1 (runs 8092 + 8095), SiHA2 (runs 8099 + 8102) and SiHA3 (runs 8230 + 8231).

4.6.1. Film Thickness

Coating thickness was measured using a ball crater technique. For the HA and SiHA films thickness was estimated to be approximately 200 nm with increasing thickness with increasing silicon addition. However, such a method is likely to have an accuracy of approximately ± 25 nm. Therefore, thicknesses were checked using an HA thin film by a FIB-SEM and a sample was then transferred to a TEM (section 3.3.7.). Figure 4-21a shows a cross section of a HA thin film on a CPTi disc annealed at 600°C in flowing argon. SAED was used to confirm that the substrate and the coating was indeed CPTi and polycrystalline HA. A protective tungsten film was placed over the sample by CVD (section 3.3.7.). Moreover, the film can be seen to be uniform in thickness, free of voids or defects and 185 ± 4 nm in thickness confirming the ball crater method was suitable. Figure 4-21b shows a SiHA3 thin film on CPTi cross section. This film was measured to have a thickness of 216 ± 5 nm indicating films became thicker with increasing silicon content. SAED patterns again indicated crystalline CPTi and W layer. The SiHA3 films were amorphous, however the electron beam appeared to interfere with the SiHA3 film and so a semi-crystalline structure was observed indicating the beam may locally recrystallise the film.

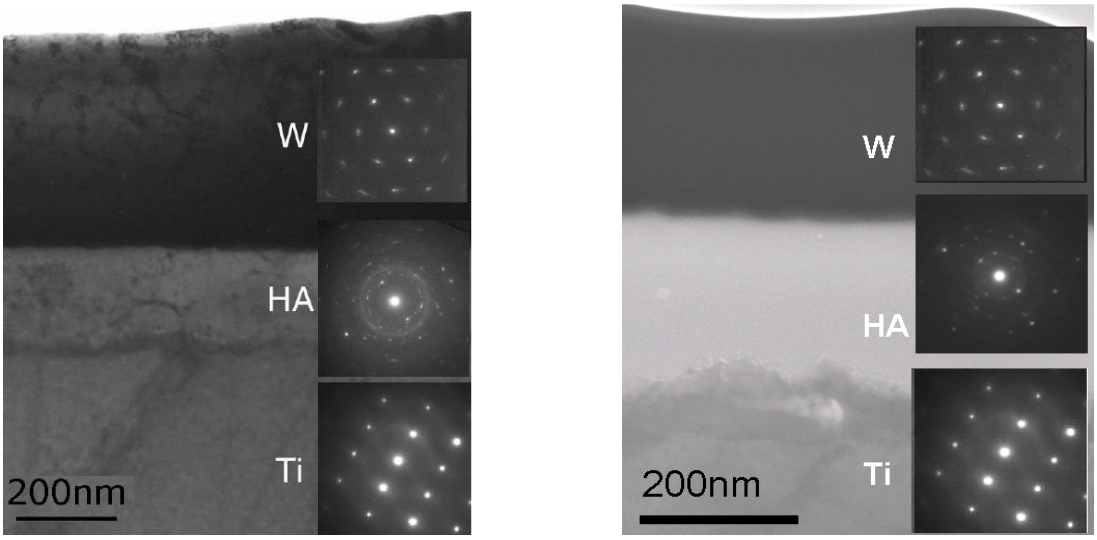

a **b**

Figure 4-21. Bright field TEM image of a) the tungsten/HA/Ti lamellar showing the HA thin film deposited on a CPTi substrate with associated selected area electron diffraction (SAED) patterns of the crystalline W protective coating, polycrystalline HA coating and crystalline Ti substrate and b) the tungsten/SiHA3/Ti lamellar showing an amorphous SiHA3 coating on a CPTi substrate and associated SAED.

A qualitative approach may also be used to show that film thickness increased with increasing silicon addition. Thin films were visually coloured differently which can be related to thickness. Depending on coating thickness light reflecting from the film/substrate interface or layers within the films differ in wavelength leading to variations in the visual spectrum. HA films were seen to be a deep blue colour that generally changed to green/yellow for the SiHA3 films due to distructive interference effects.

4.6.2. Film Morphology

SEM was taken of 20 samples from the batch of approximately 100 for each silicon addition. All films exhibited similar morphologies in as-deposited and heat treated states following the topography of the CPTi substrates. Figure 4-22 shows representative as-deposited HA film showing a smooth dense coating without voids or defects. After a heat

treatment at 600˚C thin films all HA and silicon containing films looked similar in morphology with no notable differences with respect to silicon addition. At 700˚C films became notably more textured with distinct features rising from the films as shown in figure 4-22c.

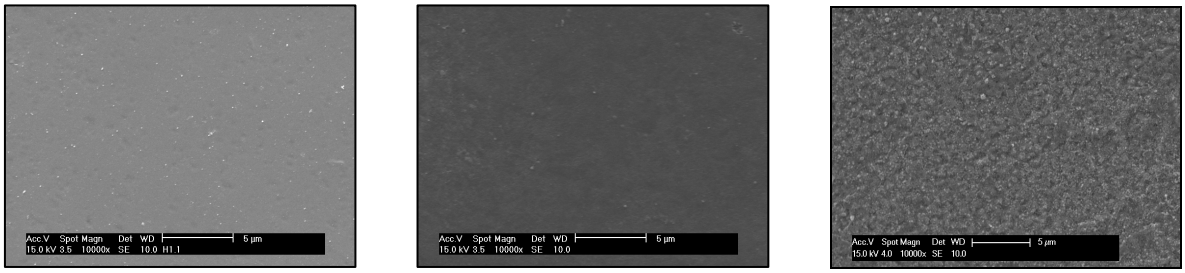

Figure 4-22. Representative SEM micrographs displaying the surface morphology of HA and SiHA thin films where a) is an as-deposited thin film on a CPTi substrate, b) annealled at 600˚C in flowing argon for 2 h and C) 700˚C in flowing argon for 2 h. Images taken from HA samples.

4.6.3. Surface Roughness

Stylus profilometry (section 3.3.1.) was performed on coatings to assess surface roughness and morphology. Figure 4-23 shows measured R_a values for uncoated polished CPTi, HA and SiHA coated discs. Uncoated CPTi discs had an R_a value of 16 nm. After heat treatment at 600˚C 2 h samples increased in roughness to a value of 25 nm. Heat treatment at 700˚C for 2 h led to a R_a value of 70 nm. As-deposited HA and all SiHA coatings exhibited similar roughness' which was slightly increased to a R_a value of 20 nm when compared to the uncoated CPTi. This suggested films closely followed the CPTi surface. After Heat treatments at 600˚C for 2 h HA films had the highest roughness value at 41 nm, decreasing with increasing silicon content. This effect was also observed for all films at heat treatments of 700˚C for 2 h but at significantly higher roughness values than the samples heat treated at 600˚C, with HA films having a roughness of 78 nm and the SiHA3 samples being measured at 32 nm.

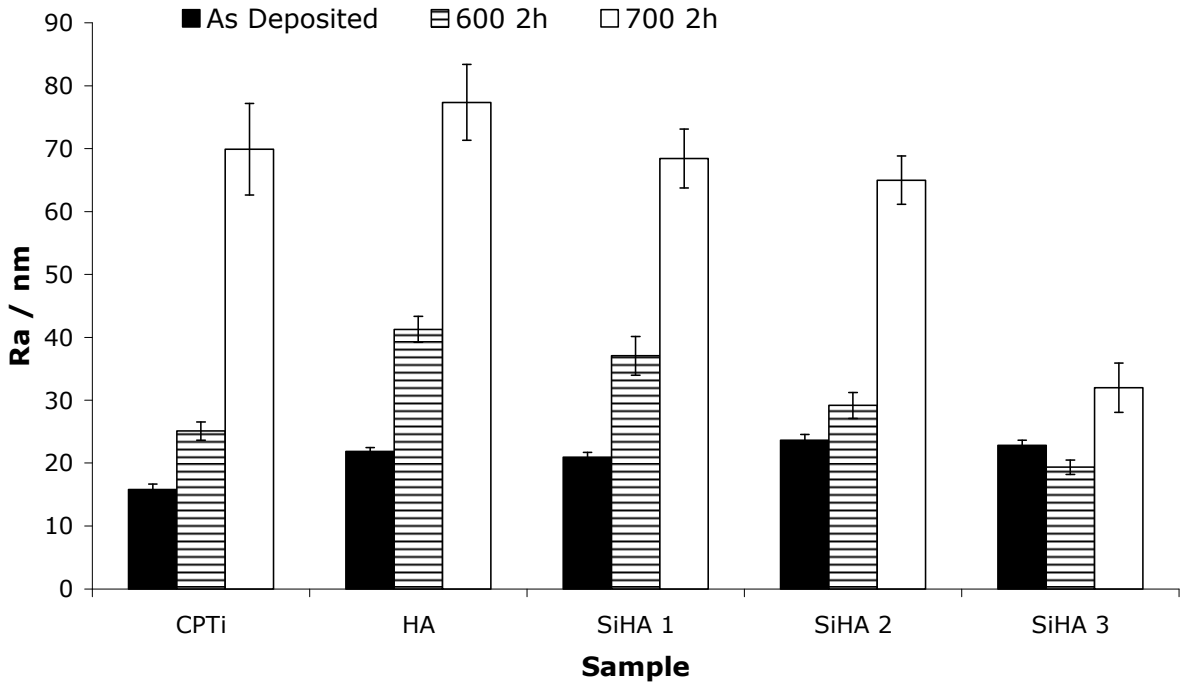

Figure 4-23. R_a roughness values for CPTi, HA and SiHA thin films as received and heat treated at 600 and 700˚C in flowing argon for 2 h.

4.6.4. Energy Dispersive X-ray Analysis (EDX)

While EDX compositional analysis can only be considered as semi-quantitative for the measurement of thin films, it is a quick and accessible means of assessing film composition. This concept has already been discussed in section 4.5. Table 4-7 shows averaged Ca/P ratios of all coatings, and plasma sprayed targets. All samples were significantly higher than the stoichiometric value of bulk HA (1.67), however, were significantly lower than the Ca/P ratio of the target material. It may also be seen that the standard error of the mean increases with increasing silicon content. Silicon content was seen to increase with increasing power density applied to the silicon target.

Sample	Silicon Target Density / Wcm^{-2}	Ca/P Ratio	Silicon Content / Wt%
Stoichiometric HA	n/a	1.67	n/a
Plasma sprayed HA target	n/a	1.9±0.02	0.0±0.1
HA	n/a	1.76±0.03	0.0±0.1
SiHA1	6.6×10^{-4}	1.74±0.03	1.8±0.3
SiHA2	1.6×10^{-3}	1.79±0.08	4.2±0.7
SiHA3	3.3×10^{-3}	1.68±0.09	13.4±1.4

Table 4-7. A summary of combined silicon content of HA and SiHA thin films batches as measured by EDX_n. Values displayed are the mean ± standard error of the mean, where n = 6.

4.6.5. Fourier Transform Infrared Spectroscopy (FTIR)

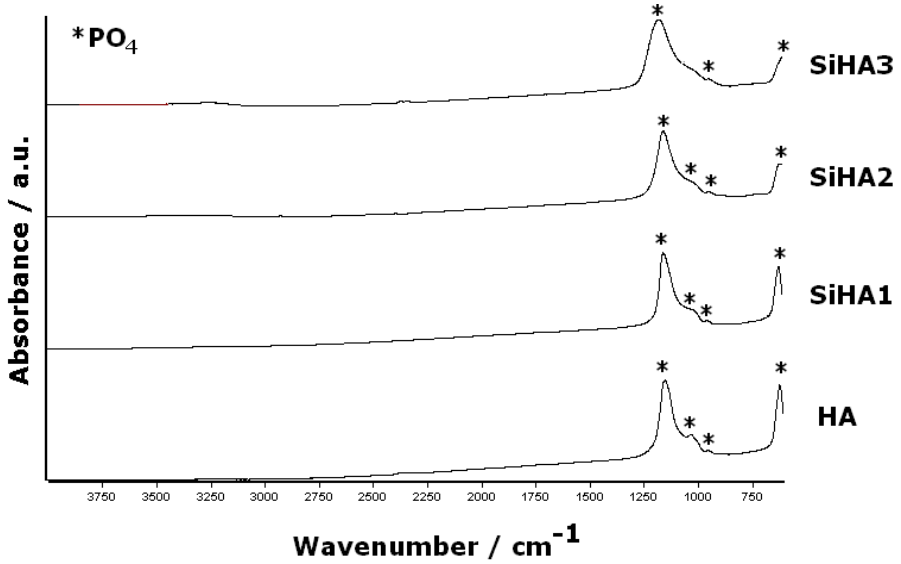

Figure 4-24. Infrared spectra for as-deposited HA and SiHA thin films on CPTi substrates. See appendices table A2 for further details.

FTIR was used to assess the chemical bonding in RF magnetron sputtered thin films. Figure 4-24 shows infrared spectra for as-deposited HA and SiHA thin films sputtered onto CPTi. The HA film exhibited four distinct peaks at wavenumbers 1147, 1028, 950

and 617 cm^{-1} which are indicative of υ_3 P-O stretching. All phosphate bonding peaks were present in SiHA1 and SiHA2. In the SiHA3 samples a reduction in the number of phosphate bands was seen, with only peaks at 1147, 950 and 617 cm^{-1} present.

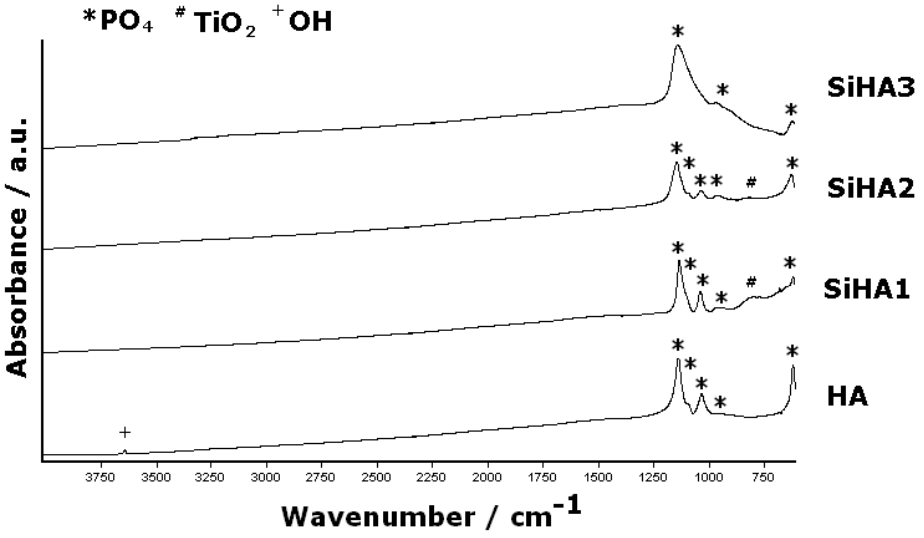

Figure 4-25. Infrared spectra for HA and SiHA thin films on CPTi substrates heat treated at 600˚C for 2 h in argon. See appendices table A2 for further details.

Figure 4-25 shows infrared spectra for HA and SiHA films annealed at 600˚C for 2 h in flowing argon. After heat treatments for 600˚C the HA films showed sharper peaks in comparison to as-deposited films. The HA films showed an additional phosphate band at 1080 cm^{-1} was seen when compared to the as-deposited HA film. Moreover, a small OH peak was seen at 3643 cm^{-1}. The SiHA1 sample showed all phosphate bonds exhibited by the recrystallised HA sample, however, bands were slightly broader. Furthermore, a new peak was seen at 820 cm^{-1}. The SiHA2 sample showed broader phosphate bands, however, the intensity of the peak at 820 cm^{-1} was reduced. The SiHA3 sample only showed three broad phosphate bands at 1147, 950 and 617 cm^{-1}. This spectrum was very similar to the as-deposited spectrum recorded. Hydroxyl (OH) bonding was not seen on any of the SiHA samples.

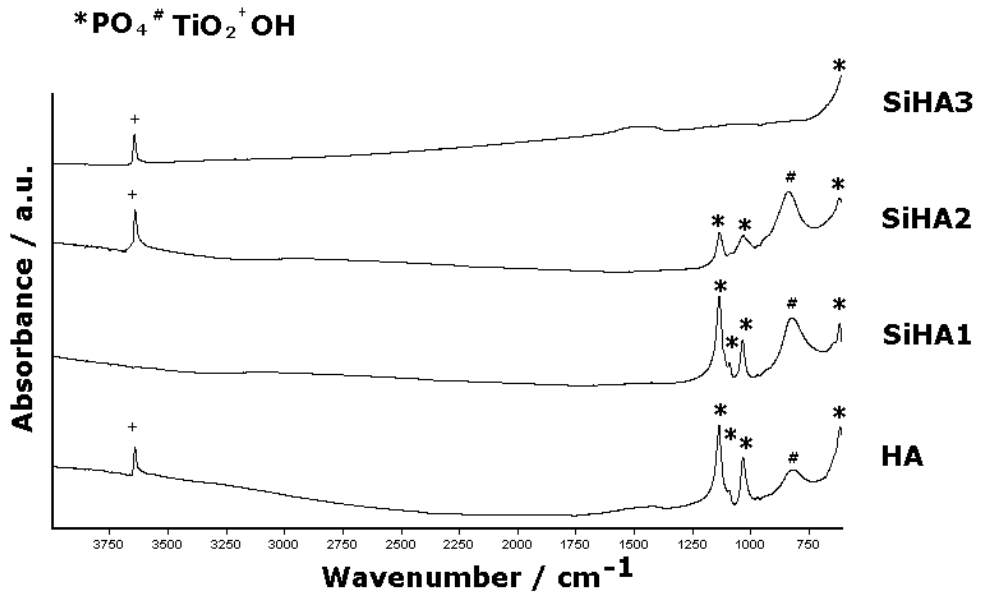

Figure 4-26. Infrared spectra for HA and SiHA thin films on CPTi heat treated at 700˚C for 2 h in flowing argon. See appendices table A2 for further details.

Figure 4-26 shows infrared spectra for HA and SiHA thin films heat treated at 700˚C for 2 h in an argon atmosphere. In comparison to the HA film heat treated at 600˚C, the HA film treated at 700˚C shows increasingly sharper phosphate bands. The set of five phosphate bands was observed at 1147, 1080, 1028, 950 and 617 cm^{-1}. An OH band was also seen at 3643 cm^{-1} which was more intense than the HA samples heat treated at 600˚C. The broad peak at 820 cm^{-1}, observed in some of the 600˚C samples was now present in the HA sample. The SiHA1 sample was similar to the HA sample, however, no OH band was observed, but reappeared in the SiHA2 and SiHA3 sample. SiHA2 showed a notable decrease in intensity of the phosphate bands. One phosphate band was seen at 617 cm^{-1} was seen in the SiHA3 sample, however, the broad peak at 820 cm^{-1} was not observed. For all details of peak assignment see appendix table 1.

4.6.6. X-ray Diffraction (XRD)

Figure 4-27 shows representative XRD patterns of as-deposited films, HA and SiHA thin films sputtered onto silicon (100) wafers heat treated for 2 h at 600 ˚C in argon. All as-deposited coatings were X-ray amorphous; however a distinct hump could be seen at

27.5 ° 2θ. Following heat treatments at 600°C for 2 h in argon HA, SiHA1 and SiHA2 films recrystallised forming a single phase HA structure matching ICDD card 09-432. Preferential orientation was seen along the (002) reflection when compared to a randomly orientated sample as shown in figure 4-1. Peak intensity of films decreased with increasing silicon content. This was seen by peak broadening which was particularly noticeable along the (002), (211), (112) and the (300) planes. The SiHA3 samples remained amorphous.

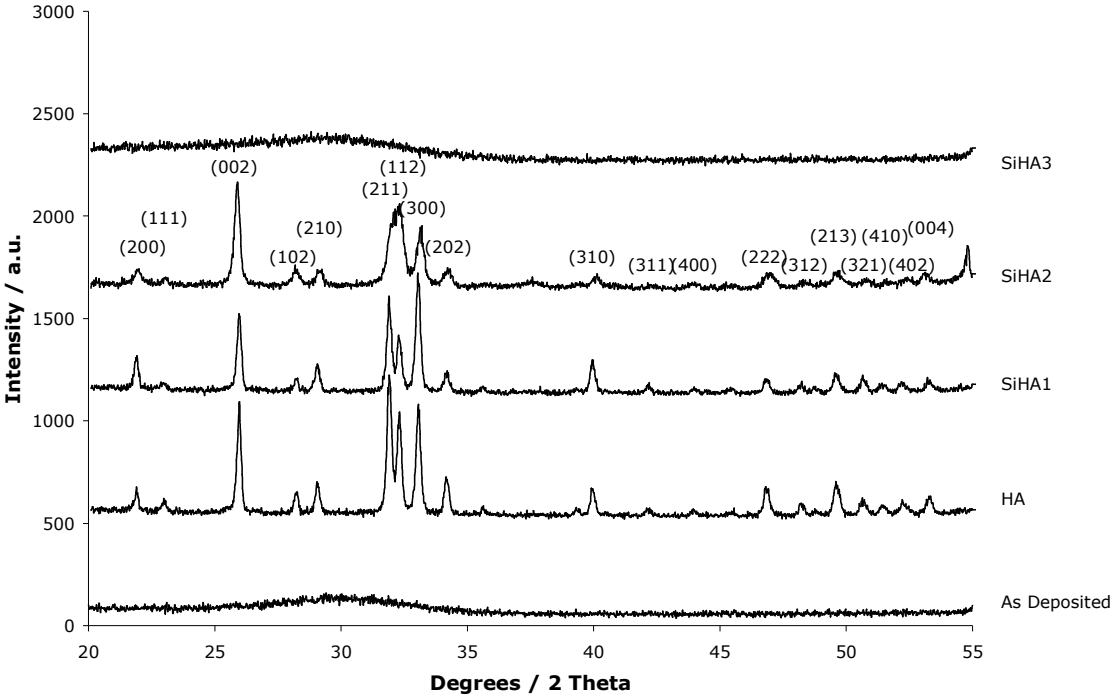

Figure 4-27. Representative XRD plots of as-deposited HA and HA and SiHA thin films on silicon (100) wafers heat treated at 600°C in argon. See appendices table A10 for full details.

XRD plots for thin films heat treated at 700°C on silicon (100) wafers are shown in figure 4-28. A similar trend was observed as with the samples heat treated at 600°C, with HA, SiHA1 and SiHA2 films recrystallising showing a single phase HA. Preferential orientation along the (002) plane was seen. Again a decrease was seen in peak intensity with increasing silicon content.

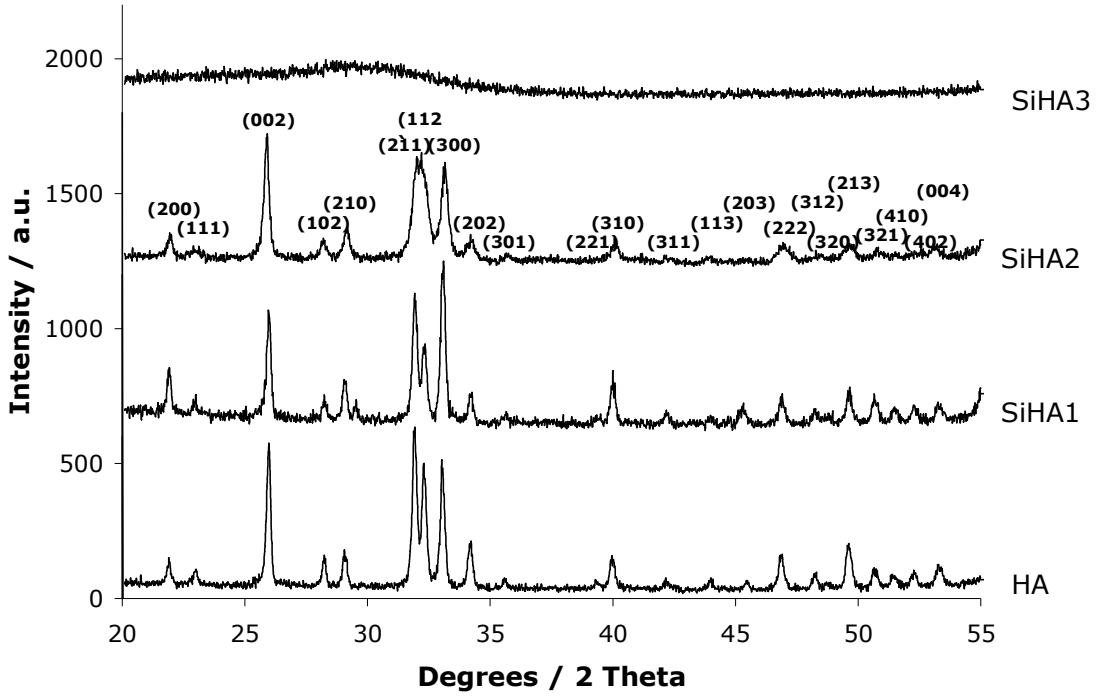

Figure 4-28. Representative XRD plots of HA and HA and SiHA thin films on silicon (100) wafers heat treated at 70˚C in argon. See appendices table A11 for full details.

The silicon addition to SiHA3 clearly has an effect on the recrystallisation transitional temperature of the HA structure. Therefore, a sequential heat treatment investigation was carried out to establish if the film could achieve recrystallisation and if so at what temperature this occurred. Figure 4-29 shows that heat treating the film up to 700˚C did not alter the structure. At 800˚C a single phase HA structure matching ICDD card number 09-432 was observed. Preferential orientation along the (002) plane was no longer observed, with the (211) plane being the most intense. For further heat treatments up to 1000˚C, the intensity of the (002) increased and peaks sharpened indicating crystal growth.

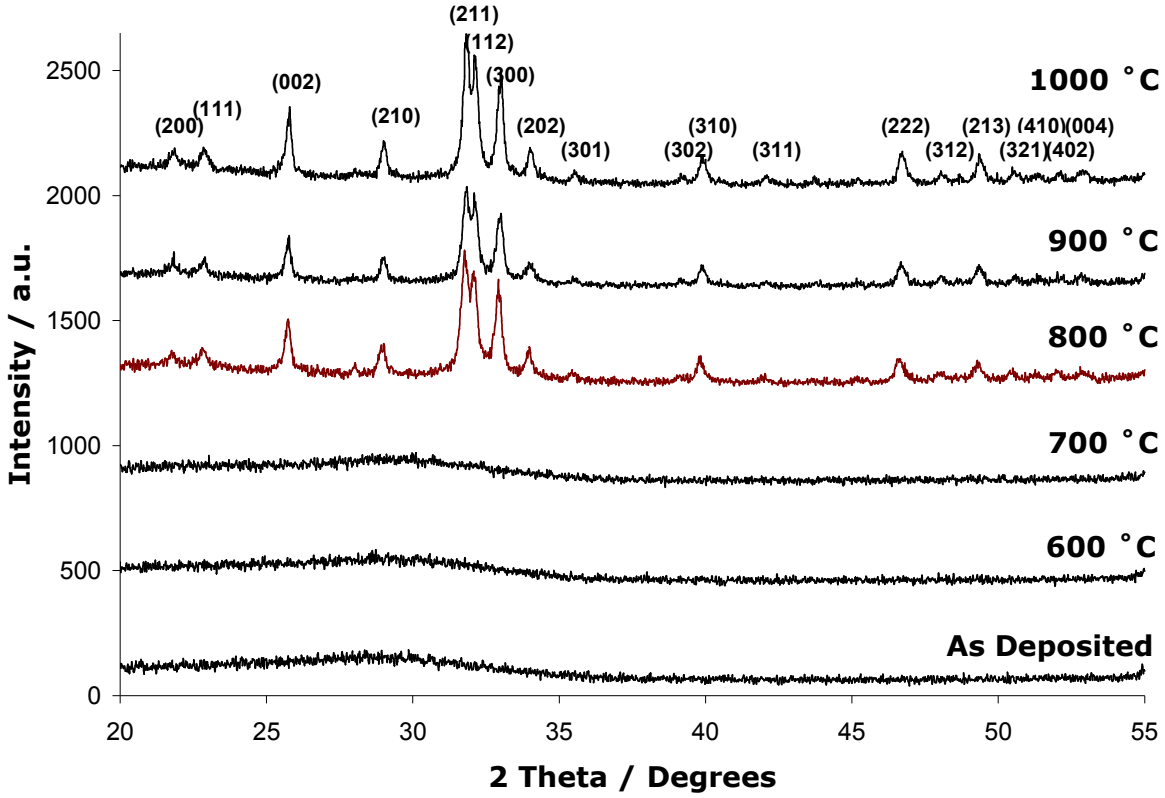

Figure 4-29. XRD plots of successive heat treatments on SiHA3 on silicon (100) wafer. See appendices table A12 for full details.

The effect of heat treatments on recrystallisation was also investigated on the CPTi coated discs. Figure 4-30 shows XRD plots of HA and SiHA thin films sputtered onto CPTi discs after heat treatments of 600°C in argon. The plot is dominated by the substrate titanium material with peaks present at 2θ values of 35.1, 38.4, 40.2 and 53.0 ° corresponding to planes (100), (002), (101) and (102) matched with ICDD card 044-1294. All other peaks are related to HA diffraction planes matching with ICDD card 09-432. These peaks are much less intense than the titanium peaks, which is due to the low thickness of the film causing the film to penetrate into the substrate material. It can be seen that the HA sample is the most crystalline and this decreases with increasing silicon content. The underlying titanium substrate remains generally unchanged with increasing silicon. After heat treatments of 700°C HA peaks were seen to be more intense than the samples heat treated at 600°C (figure 4-31).

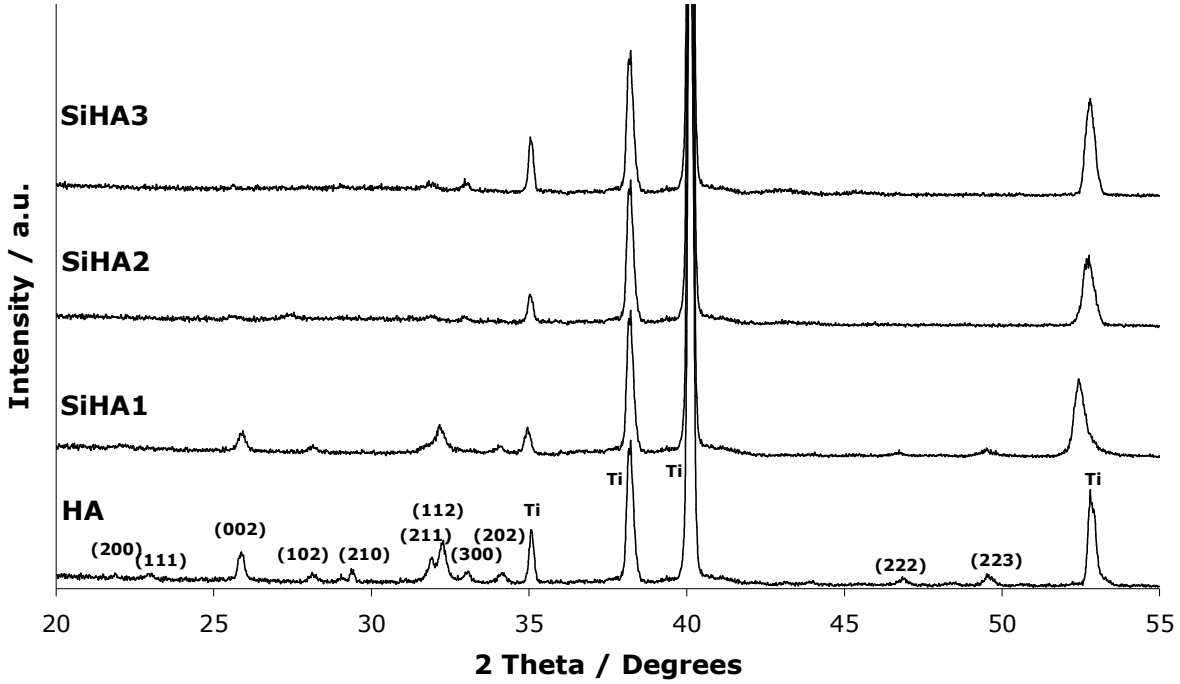

Figure 4-30. XRD plots of HA and SiHA thin films deposited onto CPTi discs and annealed for 2h in flowing argon at 600˚C. See appendices table A13 for full details.

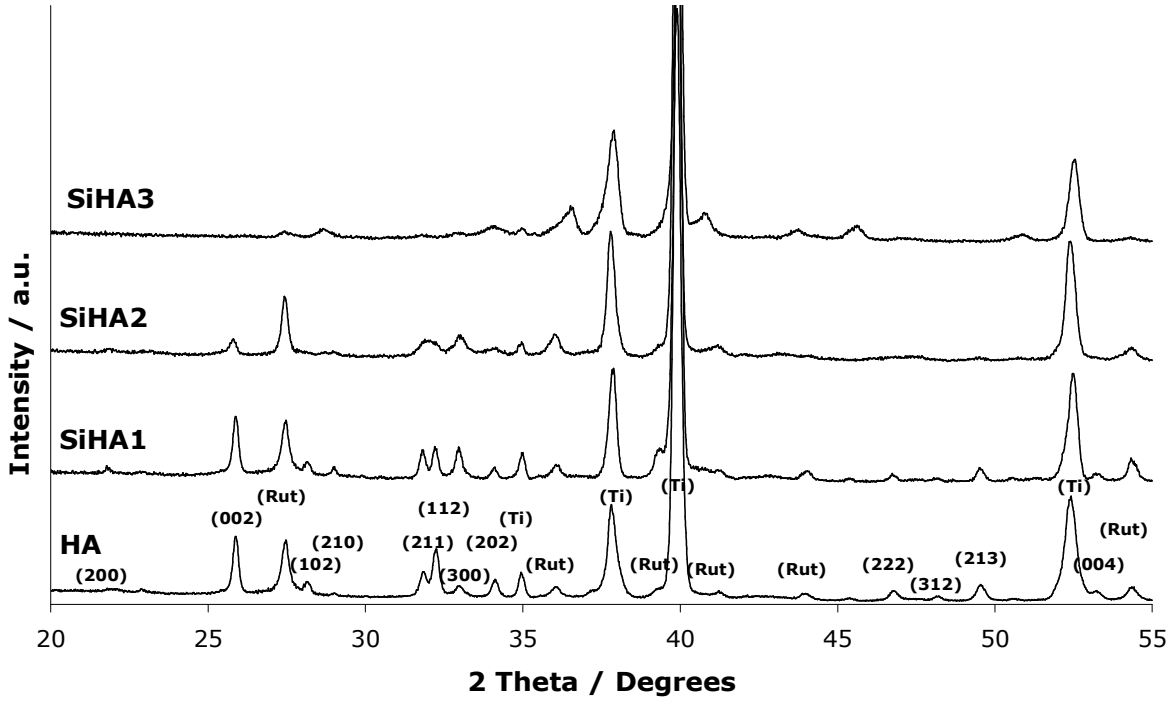

Figure 4-31. XRD plots of HA and SiHA thin films deposited onto CPTi discs and annealed at 700˚C for 2 h in flowing argon. The HA phase is indexed while titanium is denoted 'Ti' and rutile is denoted 'rut'. See appendices table A14 for full details.

The intensity of the HA (002) plane was significantly larger than XRD plots for the 600˚C sample. This was seen to reduce with increasing silicon content, and less intense than the (211) plane in SiHA2. A rutile crystal structure matching to ICDD card 76-1939 was also observed which is likely to be due to the titanium substrate oxidising. The rutile peaks also became less intense with increasing silicon content.

Table 4-8 lists particle sizes of annealed HA and SiHA thin films on CPTi and silicon (100) wafers calculated by the Scherrer equation (section 3.3.3.1.). HA particle size on CPTi discs was 80 nm following annealing at 600°C which increased by 63 % at a temperature of 700°C. Respective values were seen to decrease with increasing silicon content. Particle size could not be calculated for SiHA2 sample annealed at 600°C as peak intensity was too low for accurate data. Particle size could not be calculated for SiHA3 at either annealing temperature as both films were amorphous. Particle calculations for HA and SiHA films were measured between 78 and 89 nm, however, correlation was noted between annealing temperature or silicon content.

Sample	**HA particle size on CPTi discs / nm**		**HA particle size on Si (100) wafers / nm**	
Heat Treatment	**600˚C**	**700˚C**	**600˚C**	**700˚C**
HA	80 ± 6	131 ± 17	78 ± 16	89 ± 16
SiHA1	59 ± 3	117 ± 6	65 ± 14	71 ± 14
SiHA2	n/a*	77 ± 11	71 ± 23	86 ± 31
SiHA3	n/a	n/a	n/a	n/a

Table 4-8. A summary of HA crystallite size calculated by the Scherrer equation (section 3.3.3.1.) for HA and SiHA thin films sputtered onto silicon (100) single crystal wafer and CPTi discs using the <001> planes. * peaks were observed however data could not be obtained.

4.6.7. Reflective High Energy Electron Diffraction (RHEED)

a b

Figure 4-32. Typical RHEED diffraction patterns for a) a polished CPTi discs and b) an as-deposited HA thin film onto a CPTi disc.

Reflective high energy electron diffraction (RHEED) patterns for polished CPTi substrates indicated that the sample surface was amorphous (figure 4-32a). All as-deposited samples were amorphous (figure 4-32b). RHEED was performed on annealed HA and SiHA samples to evaluate the surface crystallinity and phase purity. Preliminary experiments established that plasma cleaning of substrates prior to RHEED experiments led to unexpected effects. On viewing RHEED patterns showed distinct rings which became diffuse after a few seconds of exposure to the electron beam. This phenomenon will be discussed in section 5.6.3. After annealing at a temperature of 600°C diffraction rings could be observed suggesting the surfaces of the coatings were polycrystalline. Typical diffraction patterns are shown in figure 4-33 for HA and SiHA samples after a heat treatment at 600°C for 2 h in argon. Due to the low accuracy of the RHEED measurements and the large number of HA diffractions it proved difficult to index the rings. Therefore, only the most intense rings have been indexed with confidence, with the first ring corresponding to the (002) plane and the second broader ring corresponding to the (211), (112) and (300) planes. With increasing silicon content the number of rings present was reduced. The SiHA1 sample, figure 4-33b, exhibited only two hazy rings corresponding to the d-spacings at 2.9 and 2.7 Å. The first ring was

assigned to the (002) plane and the second broader ring is a combination of the (211), (112) and the (300) planes. The SiHA2 samples, figure 4-33c again displayed these rings but they were less intense. The SiHA3 samples however showed no rings indicating these samples were amorphous.

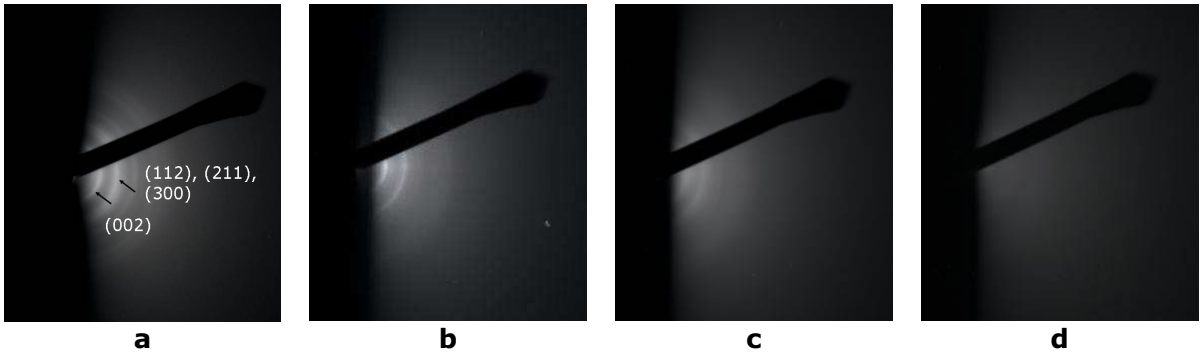

Figure 4-33. RHEED diffraction patterns of HA and SiHA thin films sputtered onto CPTi discs and annealed at 600˚C in flowing argon for 2 h. Images were obtained at 200 KeV. a) HA, b) SiHA1, c) SiHA2 and c) SiHA3.

After heat treatments of 700˚C for 2 h, all samples showed sharper diffraction rings. RHEED patterns for samples annealed at 700˚C are shown in figure 4-34. The HA samples (figure 4-34a) displayed a very similar RHEED pattern to the samples heat treated at 600˚C, however, rings appeared more intense. The SiHA1 sample (figure 4-34b) saw the presence of additional rings. It is thought that these were related to a combination of HA and rutile present at the surface. Figure 4-35 displays expanded RHEED patterns for the SiHA1 sample HA and rutile surface produced at 750˚C in air for 1 h. All rings present for the rutile sample are seen in the SiHA1 sample. Additional rings were also seen in the SiHA1 sample suggesting two phases present at the immediate surface. For the higher silicon content coatings, as in sample SiHA2 and SiHA3, the number of rings is then reduced appearing to revert back to an HA system, however it may be seen that in SiHA2 (figure 4-34b) some rings relating to rutile remain. This was also the case for the SiHA3 (figure 4-34c) sample but the rings were more diffuse.

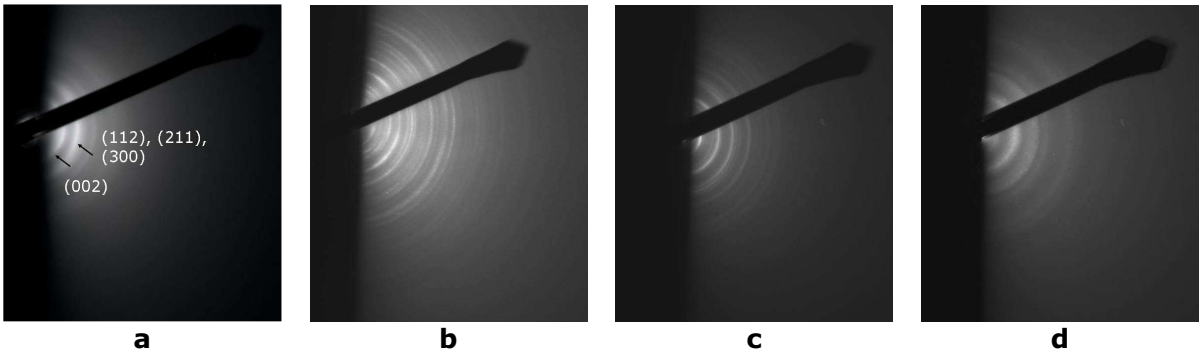

Figure 4-34. RHEED diffraction patterns of HA and SiHA thin films sputtered onto CPTi discs and annealed at 700˚C in flowing argon for 2 h. Images were obtained at 200 KeV. a) HA, b) SiHA1, c) SiHA2 and c) SiHA3.

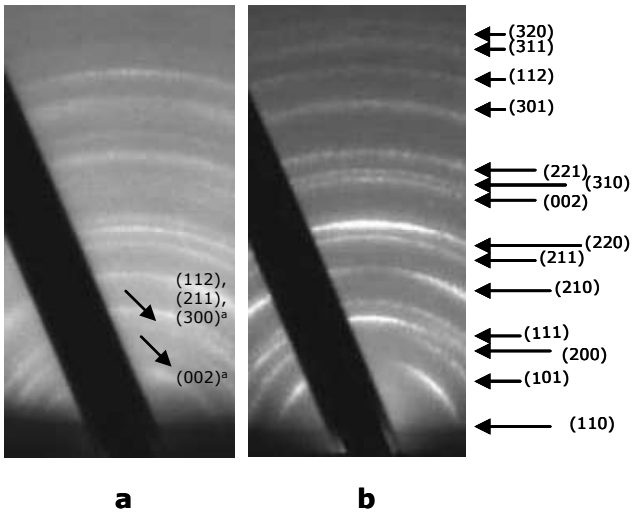

Figure 4-35. Comparisons of RHEED patterns for a) SiHA1 film on a CPTi disc annealed at 700˚C in flowing argon for 2 h and b) CPTi sample annealed in air at 750˚C for 1 h. All indexed planes match to ICDD card 76-1939 (Rutile) unless indexed with a superscript b and diagonal arrows indicating possible HA reflections matching to ICDD card 09-432 (HA).

4.6.8. X-ray Photoelectron Spectroscopy (XPS)

XPS was carried out using a Kratos Axis Ultra XPS instrument to investigate the top few atomic layers of HA and SiHA thin films. Figures 4-36, 4-37, 4-38, 4-39, and 4-40 display typical Ca 2p, P 2p and C 1s high resolution XPS spectra for as-deposited and annealed HA and SiHA samples. All atomic percentages and binding energies are quoted in tables 4-9 and 4-10 respectively. Carbon contamination ranged from 17.9 – 38.7 at.% for all

samples. A general increase in carbon content was seen after annealing, which may be due to contamination introduced by the furnace, however, no correlation was seen between annealing temperature or silicon content and surface carbon present. The C 1s region was fitted with three components at binding energies 285.0, 286.6 and 288.7 eV attributed to adventitious carbon, C-O and C=O and [180]. A calcium doublet was observed separated by 3.55 eV and fitted with two components at peak positions of 347.5 and 351.0 eV for Ca $2p_{1/2}$ and Ca $2p_{3/2}$ respectively [180]. Calcium was in low concentrations in the as-deposited films (4.3 - 6.8 at.%) but increased after annealing at both temperatures (12.1 - 18.0 at.%). Where present, the phosphorus P 2p peak was fitted as a doublet [179] with separation energy of 0.84 eV. Phosphorus was seen to decrease with both increasing annealing temperature and silicon content. Interestingly, no phosphorus was seen on any of the HA thin films annealed at 600°C but was seen on HA samples annealed at 700°C. C 1s, Ca 2p and P 2p component binding energies did not appear to be notably affected by either heat treatment or increases in silicon concentration.

The O 1s peak for the as-deposited samples was fitted with two components at 531.0 eV and 532.5 eV corresponding to PO_4 [200] groups and C-O [200] or SiO_2 groups [240] respectively. The second C-O component became larger with increasing silicon content. Therefore, it is thought that this is related to SiO_2 binding [240]. After annealing at 600 or 700°C the O 1s peak could only be fitted to a single component at 531.0 eV which corresponded to PO_4 bonds. Furthermore, a reduction in oxygen content was seen in all films after annealing, however, no differences were observed between the oxygen content of films annealed at 600 or 700°C. In the HA samples annealed at 600°C (which showed no phosphorus present on the surface) no shift in the binding energy of the component at 531 eV was seen, however, it has also been reported that this may be related to Ca-O bonds [240]. The loss of the SiO_2 component present at 532.5 eV suggested that the silicon in the annealed structure had changed electronic configuration.

The Si 2p silicon peak was fitted to a single component. As already shown by the EDX data, the silicon content of thin films increased with increasing power density applied to the silicon target. These values, however, were in poor agreement with the EDX being consistently lower. It was also seen that 0.37 – 0.52 at.% silicon was present on undoped HA samples suggesting some silicon contamination was present on the surface of the films. It is likely that this is residual silicon present in the XPS high vacuum chamber which would further contribute to the oxygen content. Furthermore, fluorine was also observed in some wide scan spectra (data not shown) which is another common contaminant, that is difficult to remove from vacuum systems. In the as-deposited samples the chemical shift for the Si 2p were found to depend on the silicon content of the film, with lower binding energies measured for the samples with lower silicon concentrations. The relationship between silicon concentration and binding energy is shown in figure 4-38. At concentrations in the region of 1 - 2 at.% there is a large increase in binding energy but at concentrations greater than 2 at.% the rate of increase lowers with all binding energies being measured at approximately 103 eV. After annealing at both temperatures all Si 2p peak positions were in the region of 101.5. This relationship between silicon concentration and binding energy for annealed samples is shown in figures 4-38. Silicon content did not vary after annealing at 600°C, compared with the as-deposited samples, however, after a heat treatment of 700°C only very small quantities were seen on all of the SiHA samples, which was comparable to residual silicon observed on the undoped HA samples.

XPS for all samples annealed at 700°C revealed the presence of titanium at the surface of the films. This was seen to be at a value of 5 at.% for the SiHA1 samples, but approximately 0.3 at.% for all other samples. A Ti 2p doublet observed with Ti $2p_{3/2}$ present at 458.3 and Ti $2p_{1/2}$ present at 464.2 eV using a doublet separation energy of 5.8 eV. This corresponded to a new component appearing at 529.6 eV in the O 1s region for the SiHA1 sample (figure 4-40), which was related to a TiO_2 rutile phase. Rutile O 1s was not detected by XPS on any of the other films annealed at 700°C.

The Ca/P ratio decreased with increasing silicon content from 1.43 in the HA samples to 1.03 in the SiHA3 samples for the as-deposited samples. After heat treatments of 600°C the Ca/P ratio increased. This increase was higher for higher concentration silicon containing HA films. Following annealing at 700°C a further increase in Ca/P ratio was seen. This was due to smaller quantities of phosphorus being detected on the surface.

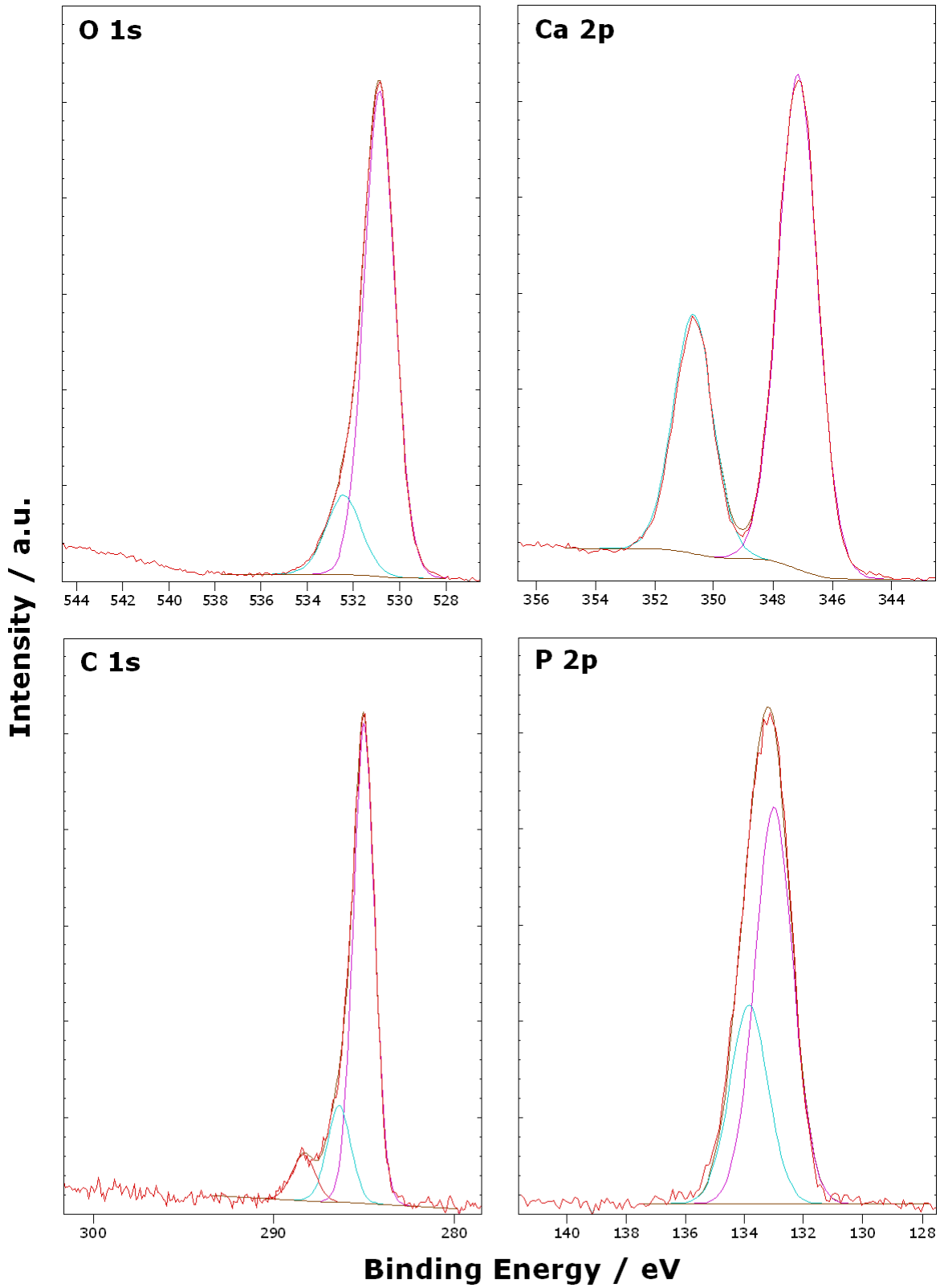

Figure 4-36. Representative high resolution XPS spectra for O 1s, Ca 2p, P 2p and C 1s regions for the surface of an as-deposited HA thin film showing subtracted backgrounds and fitted components.

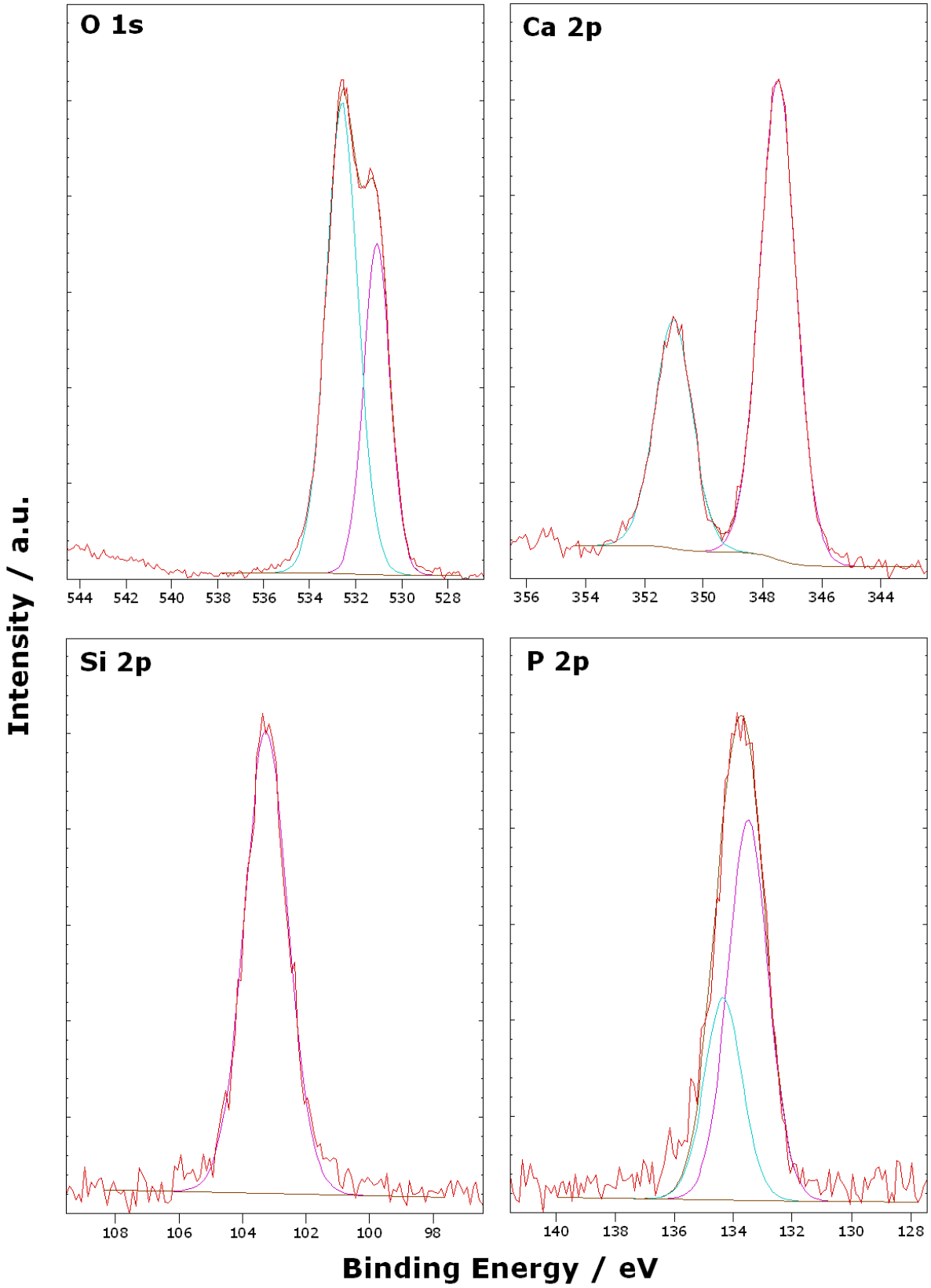

Figure 4-37. Representative high resolution XPS spectra for O 1s, Ca 2p, P 2p and Si 2p regions for the surface of an as-deposited SiHA sample. Spectra have been taken from SiHA3. Note C 1s in the previous figure has been replaced with Si 2p in the current image.

Sample	Region	As-deposited	±	Annealled 600˚C	±	Annealled 700˚C	±
HA	O 1s	58.21	2.28	47.05	0.76	48.08	0.65
	Ca 2p	6.77	0.41	18.01	0.83	14.69	1.84
	C 1s	29.88	2.99	34.42	1.48	32.64	1.44
	P 2p	4.72	0.22	n/a	n/a	3.76	0.21
	Si 2p	0.42	0.1	0.52	0.21	0.37	0.24
	Ti 2p	n/a	n/a	n/a	n/a	0.45	0.12
	Ca/P	**1.43**	**0.03**	**n/a**	**n/a**	**3.96**	**0.62**
SiHA1	O 1s	64.17	1.89	41.01	3.73	48.08	1.14
	Ca 2p	6.2	0.34	13.29	1.72	12.07	1.40
	C 1s	23.61	2.13	38.67	6.12	27.72	3.02
	P 2p	5.03	0.12	6.02	0.93	5.14	1.78
	Si 2p	0.99	0.13	1.01	0.23	1.17	0.40
	Ti 2p	n/a	n/a	n/a	n/a	5.83	1.73
	Ca/P	**1.23**	**0.05**	**2.21**	**0.3**	**5.95**	**3.73**
SiHA2	O 1s	63.18	2.31	50.82	1.29	46.45	1.85
	Ca 2p	5.52	0.12	18.06	0.98	19.39	4.22
	C 1s	23.31	2.7	22.04	2.60	32.49	4.68
	P 2p	4.77	0.24	5.73	0.65	0.46	0.36
	Si 2p	3.21	0.54	3.36	0.21	0.91	0.31
	Ti 2p	n/a	n/a	n/a	n/a	0.30	0.20
	Ca/P	**1.16**	**0.06**	**3.15**	**0.2**	**58.25**	**39.86**
SiHA3	O 1s	67.45	1.32	39.70	3.26	45.22	2.88
	Ca 2p	4.27	0.38	13.42	1.70	14.14	1.00
	C 1s	17.9	1.89	36.49	5.76	38.43	1.75
	P 2p	4.4	0.49	3.69	0.53	1.34	1.88
	Si 2p	5.98	0.83	6.71	0.73	0.55	0.12
	Ti 2p	n/a	n/a	n/a	n/a	0.33	0.19
	Ca/P	**1.03**	**0.13**	**3.63**	**0.4**	**54.56**	**25.11**

Table 4-9. High Resolution XPS atomic percentages and Ca/P ratios HA and SiHA thin films of different compostions and post deposition treatments.

Sample	Region	Component	As-deposited	±	Annealed 600˚C	±	Annealed 700˚C	±
HA	O 1s	PO_4	530.8	0.15	531.5	0.10	531.7	0.06
		C-O	532.7	0.07	-	-	-	-
		TiO_2	-	-	-	-	-	-
	Ca 2p	3/2	347.0	0.11	347.2	0.09	347.5	0.07
		1/2	350.5	0.11	350.8	0.09	351.0	0.07
	C 1s	Adventitious C	285.0	0.02	285.0	0.02	285.0	0.03
		C-O	286.6	0.11	286.5	0.02	286.5	0.08
		C=O	288.7	0.09	289.8	0.12	288.6	0.07
	P 2p	P 2p 3/2	132.9	0.10	n/a	n/a	133.4	0.06
		P 2p 1/2	133.8	0.10	n/a	n/a	134.3	0.06
	Si 2p	Si 2p	102.0	0.17	101.6	0.07	101.2	0.05
	Ti 2p	3/2	-	-	-	-	458.3	0.06
		1/2	-	-	-	-	464.2	0.11
SiHA1	O 1s	PO_4	530.6	0.05	531.5	0.09	531.5	0.11
		C-O/SiO_2	532.5	0.09	-	-	-	-
		TiO_2	-	-	-	-	529.6	0.10
	Ca 2p	Ca 2p $_{3/2}$	347.1	0.04	347.3	0.14	347.2	0.29
		Ca 2p $_{1/2}$	350.6	0.04	350.9	0.14	350.8	0.29
	C 1s	Adventitious C	285.0	0.01	285.0	0.03	285.0	0.04
		C-O	286.5	0.08	286.5	0.03	286.6	0.11
		C=O	288.5	0.08	290.2	2.66	288.6	0.10
	P 2p	P 2p $_{3/2}$	132.9	0.01	133.3	0.11	133.1	0.29
		P 2p $_{½}$	133.8	0.01	134.2	0.11	134.0	0.29
	Si 2p	Si 2p	102.1	0.10	101.3	0.24	101.4	0.15
	Ti 2p	3/2	-	-	-	-	458.6	0.09
		½	-	-	-	-	464.5	0.06
SiHA2	O 1s	PO_4	531.2	0.02	531.3	0.13	531.6	0.06
		C-O/SiO_2	532.6	0.03	-	-	-	-
		TiO_2	-	-	-	-	-	-
	Ca 2p	Ca 2p $_{3/2}$	347.5	0.05	347.1	0.11	347.1	0.24
		Ca 2p $_{1/2}$	351.0	0.05	350.7	0.11	350.6	0.24
	C 1s	Adventitious C	285.0	0.05	284.9	0.07	285.0	0.02
		C-O	286.6	0.06	286.4	0.07	286.7	0.14
		C=O	288.8	0.08	289.0	0.27	288.7	0.07
	P 2p	P 2p 3/2	133.3	0.09	133.2	0.09	132.9	0.17
		P 2p 1/2	134.1	0.09	134.0	0.09	133.8	0.17
	Si 2p	Si 2p	102.9	0.14	101.1	0.11	101.6	0.18
	Ti 2p	3/2	-	-	-	-	458.4	0.07
		½	-	-	-	-	464.2	0.10
SiHA3	O 1s	PO_4	531.2	0.09	531.3	0.18	531.7	0.02
		C-O/SiO_2	532.7	0.06	-	-	-	-
		TiO_2	-	-	-	-	-	-
	Ca 2p	Ca 2p $_{3/2}$	347.5	0.05	347.3	0.10	347.3	0.02
		Ca 2p $_{1/2}$	351.1	0.05	350.8	0.10	350.8	0.05
	C 1s	Adventitious C	285.0	0.03	285.0	0.03	285.0	0.00
		C-O	286.6	0.07	286.5	0.03	286.6	0.16
		C=O	290.6	1.51	288.7	0.09	288.7	0.12
	P 2p	P 2p $_{3/2}$	133.4	0.03	133.4	0.09	133.1	0.05
		P 2p $_{1/2}$	134.3	0.03	134.2	0.09	134.2	0.03
	Si 2p	Si 2p	103.2	0.04	101.7	0.14	101.6	0.16
	Ti 2p	3/2	-	-	-	-	458.4	0.11
		½	-	-	-	-	464.2	0.08

Table 4-10. Peak positions for components fitted to high resolution XPS data for HA and SiHA thin films.

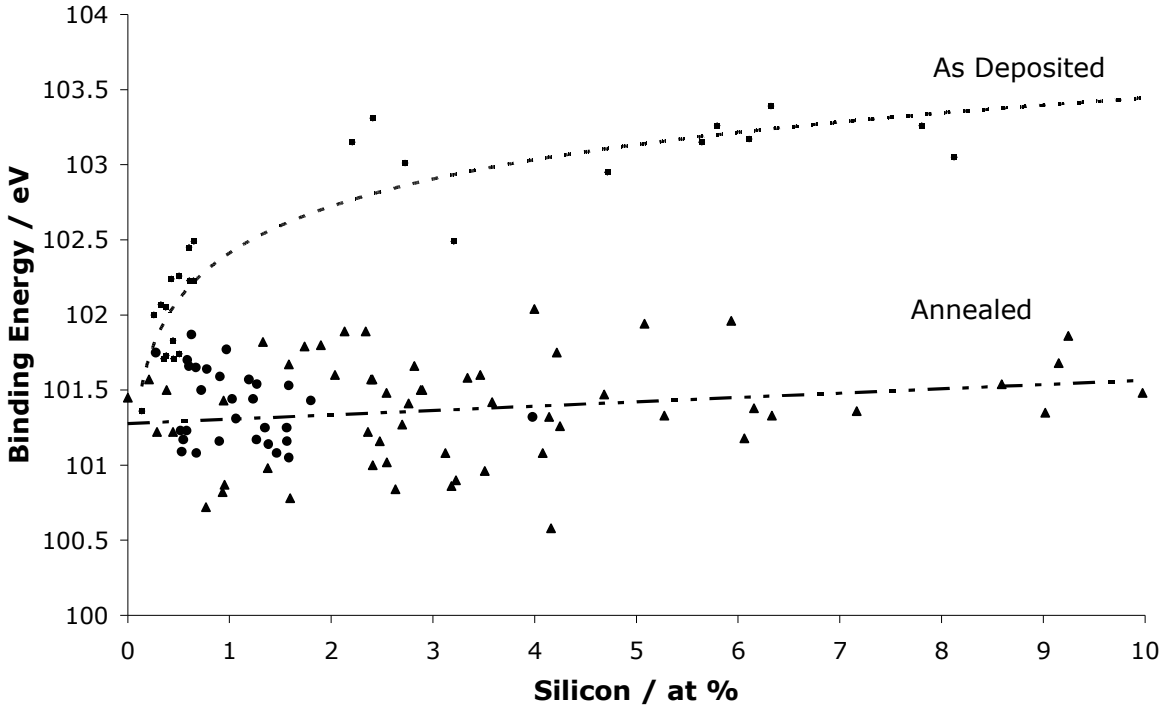

Figure 4-38. The comparison of atomic percentage of silicon content of films against binding energy taken from Si 2p high resolution XPS data for as-deposited HA and SiHA thin films. Data have been obtain from >10 samples of different silicon content which have not been included in this study. Typically 3 scans were taken per sample with good agreement between composition.

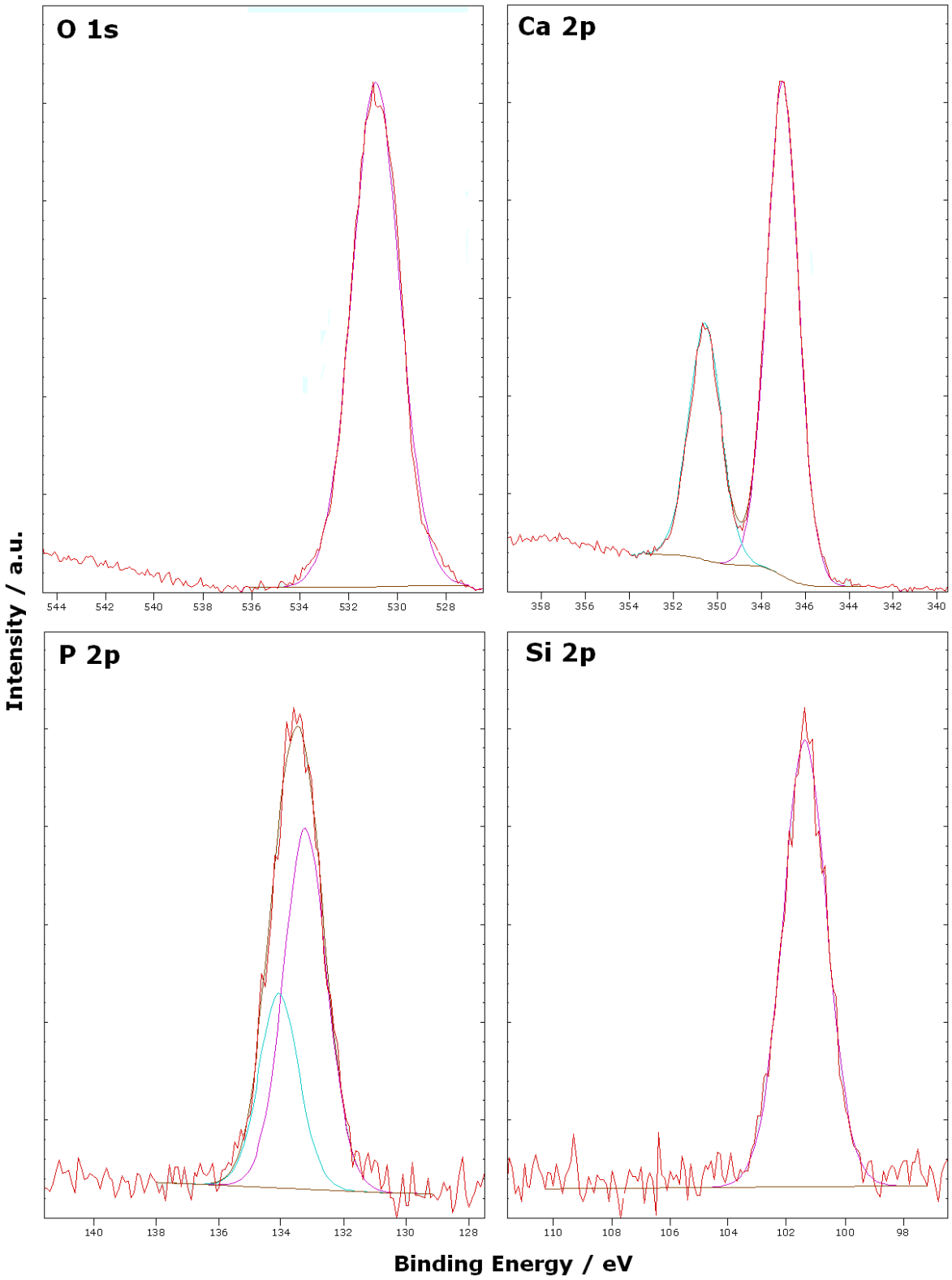

Figure 4-39. Representative high resolution XPS spectra for O 1s, Ca 2p, P 2p and Si 2p regions for the surface of high silicon content SiHA thin film annealed at 600˚C showing subtracted backgrounds and fitted components.

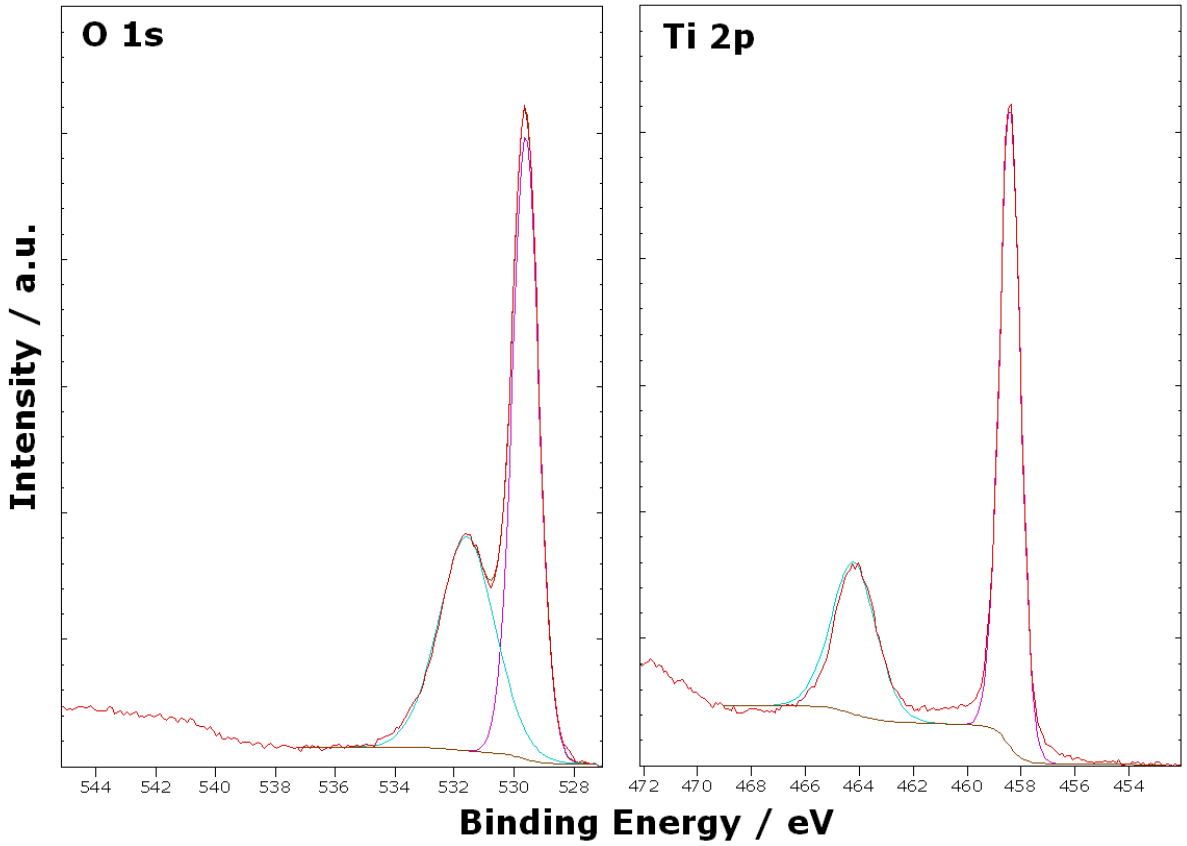

Figure 4-40. Representative high resolution XPS spectra for O 1s and Ti 2p regions for the surface of SiHA1 thin film annealed at 700˚C in flowing argon for 2 h.

4.6.9. Film Wettability

Contact angle testing was performed to establish the relative surface hydrophobicity or hydrophilicity of thin film samples. Figure 4-41 shows measured contact angles for HA and SiHA thin films. All silicon doped samples exhibited lower contact angles than the HA films whether in an as-deposited or annealed state. The as-deposited HA film had a contact angle of 67 ˚ which decreased with increasing silicon content down to an angle of 27 ˚ for the SiHA3 samples. Following heat treatments at 600˚C for 2 h in argon, the contact angle for all samples decreased when compared to the as-deposited samples to values of 54, 41, 31 and 26 ˚ for the HA to SiHA3 respectively. Following heat treatments of 700˚C an increase in contact angle was seen for all samples when compared to either the as-deposited or samples heat treated at 600˚C, measuring 69, 56, 42 and 36 ˚ for the HA to the SiHA3 samples. Figure 4-41 also shows digital images

taken of water droplets on as-deposited HA and SiHA surfaces. It can be seen that the hydrophobicity decreases with increasing silicon content.

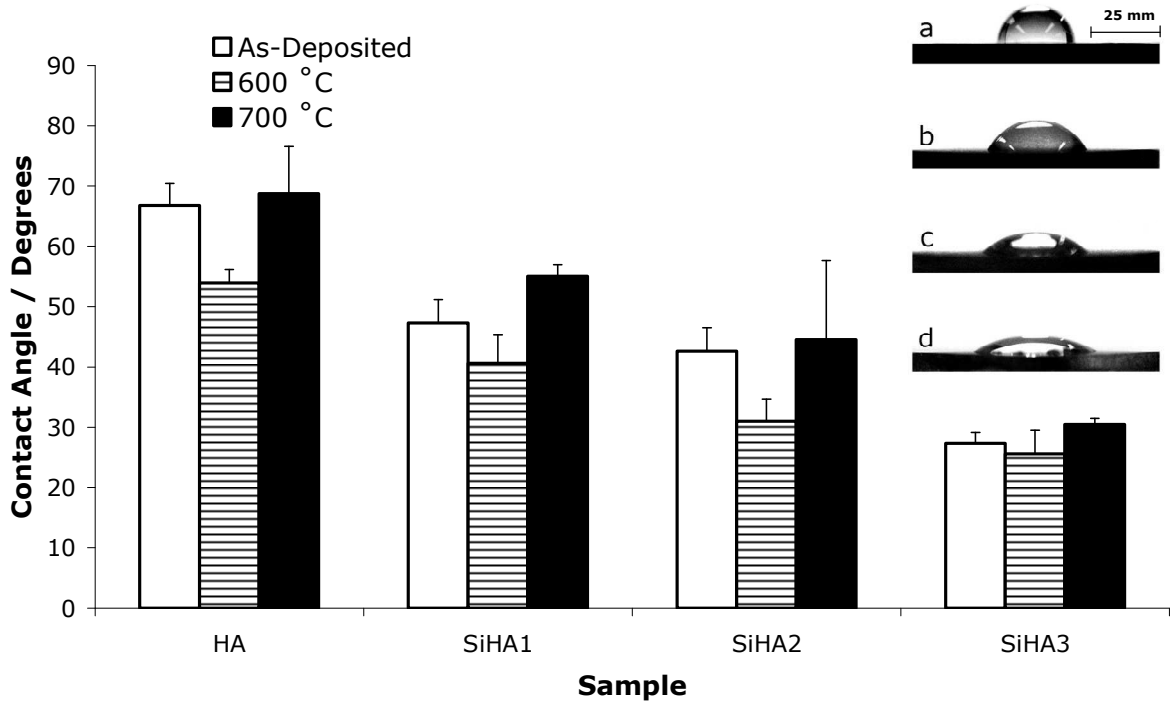

Figure 4-41. Measured contact angles of water droplets on HA and SiHA thin films sputtered on to CPTi substrates. Mean ± standard error of the mean where n ≥ 6, n = number of photographs taken. Also shown are digitally enhanced representative grayscale photographs of a water droplets on a) HA b) SiHA1 c) SiHA2 and c) SiHA3 thin films sputtered onto CPTi discs showing the effect of silicon doping on the contact angle of water. Photographs taken from as-deposited sample set.

4.6.10. The Solubility of HA and SiHA Thin Films in Relation to *In Vitro* Cell Culture

A qualitative investigation was carried out to assess the rate of dissolution of HA and SiHA thin films during *in vitro* culture conditions. Due to a shortage of samples EDX analysis was performed on samples after cell culture assays were performed rather than using new samples (as in figure 4-42). This introduces a large degree of uncertainty with the results as surfaces will have been exposed to cells and changing media conditions. Moreover, EDX analysis can only be considered a semi-quantitative technique to measure the composition of thin films with a thickness lower than the penetration depth of the electron beam.

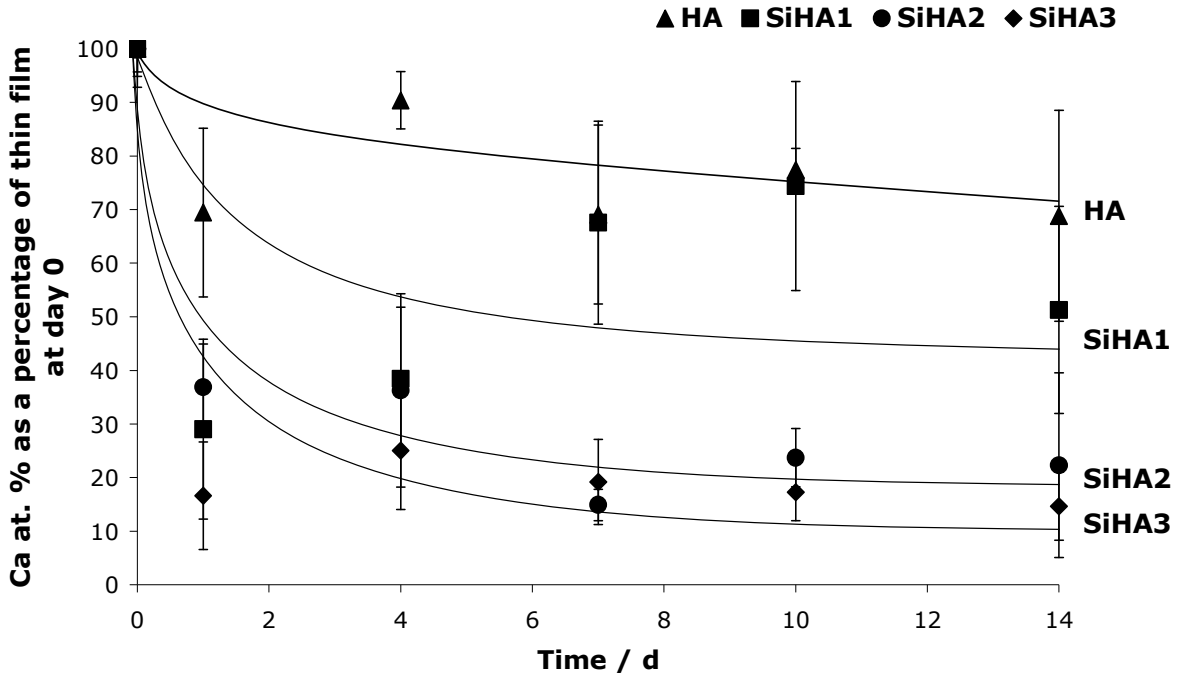

Figure 4-42. Percentage of HA and SiHA thin films annealed at 600˚C for 2 h in flowing argon remaining as a percentage of original coating Ca content. Data plotted is mean ± standard error of the mean, where n = 4. Best fit lines are fitted manually for visual enhancement.

Figure 4-42 illustrates that silicon content of the films is proportional to film solubility in culture conditions. It can be seen that most film dissolution occurred between day 0 and day 1. The HA film underwent some dissolution appearing to remain approximately 80% of its original content after 14 days. The addition of silicon had a dramatic effect on film stability with the SiHA1 sample only retaining approximately 55 % of its original thickness. The SiHA2 and SiHA3 samples had approximately 20 and 10 % of the original coating; however, due to the uncertainty associated with this data it is thought that dissolution rate would be significantly lower for the SiHA3 samples as XPS data (data not shown) obtained for films immersed in media for 48 h showed the presence of titanium (approximately 1 at.%). Calcium and phosphorus content was slightly reduced, however, almost no silicon was detected in any of the thin films suggesting that this had dissolved after preferentially.

4.6.11. Mechanical Characterisation

The hardness and adhesion of HA and SiHA as-deposited and annealed films (700°C for 2 h in flowing argon) were investigated using nano-hardness and nano-scratch testing (sections 3.3.11. and 3.3.12. respectively). Preliminary investigations were performed to measure the hardness values of coatings on CPTi discs. Thin films were found to be harder than the underlying substrate and therefore the substrate material heavily affected the hardness results of the coating.

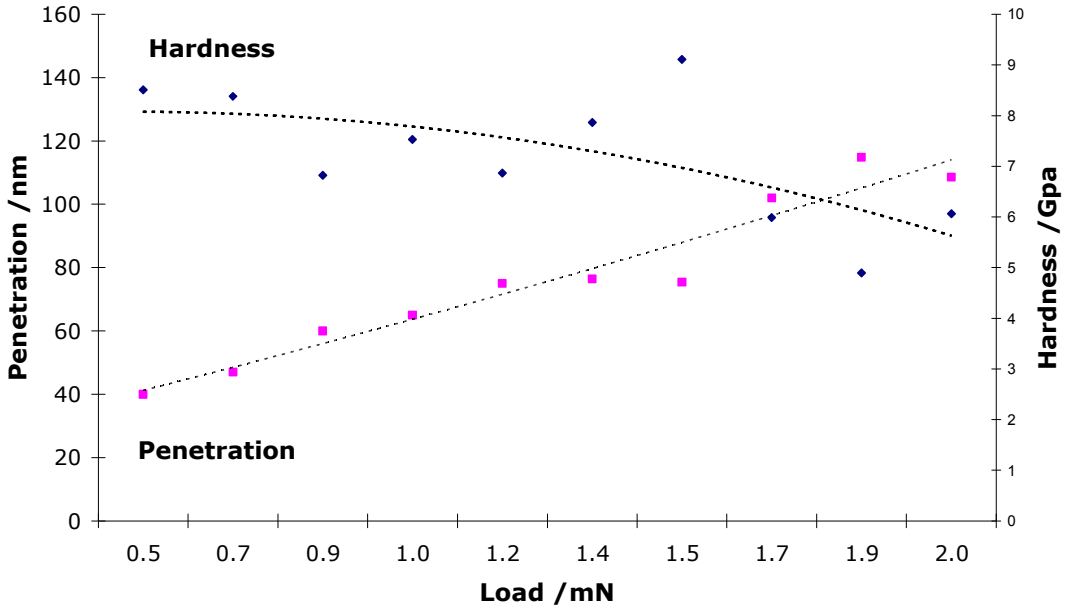

Figure 4-43. A typical plot for the variation of hardness with increasing load on an as-deposited HA thin film on a CPTi disc showing the effect of tip penetration on hardness measurements.

Figure 4-43 shows the measured hardness with increasing load on a CPTi disc coated with HA. It can be seen at higher loads, that the tip penetration into the sample increased, and as a net effect, calculated hardness decreased. In fact this is a well known phenomenon in nano-hardness testing and occurs because the substrate is affecting the hardness measurement more than the coating material due to stress fields produced in the tip extending through the coating to the underlying substrate material. Therefore, the hardness of CPTi discs and (001) silicon wafers was measured to be 3.1 ± 1.3 and 13.8 ± 3.4 GPa, and so silicon wafers were chosen for accurate hardness measurements.

Figure 4-44 shows hardness values obtained for HA and SiHA thin films sputtered onto single crystal (100) orientated silicon wafers in as-deposited and annealed at 700˚C state. There was no significant difference (P>0.05) in hardness values for any of the coating compositions indicating that the addition of silicon had no effect on the hardess of HA coatings. For all compositions the average hardness of as-deposited coatings was 5.7 GPa and the annealed samples were on average 11 % harder with a value of 6.3 GPa. The modulus can also be calculated from tip penetration data. As-deposited and annealed data are displayed in figure 4-45. All moduli ranged from 100-110 GPa. No significant difference (P>0.05) was observed for either heat treatment or composition variations.

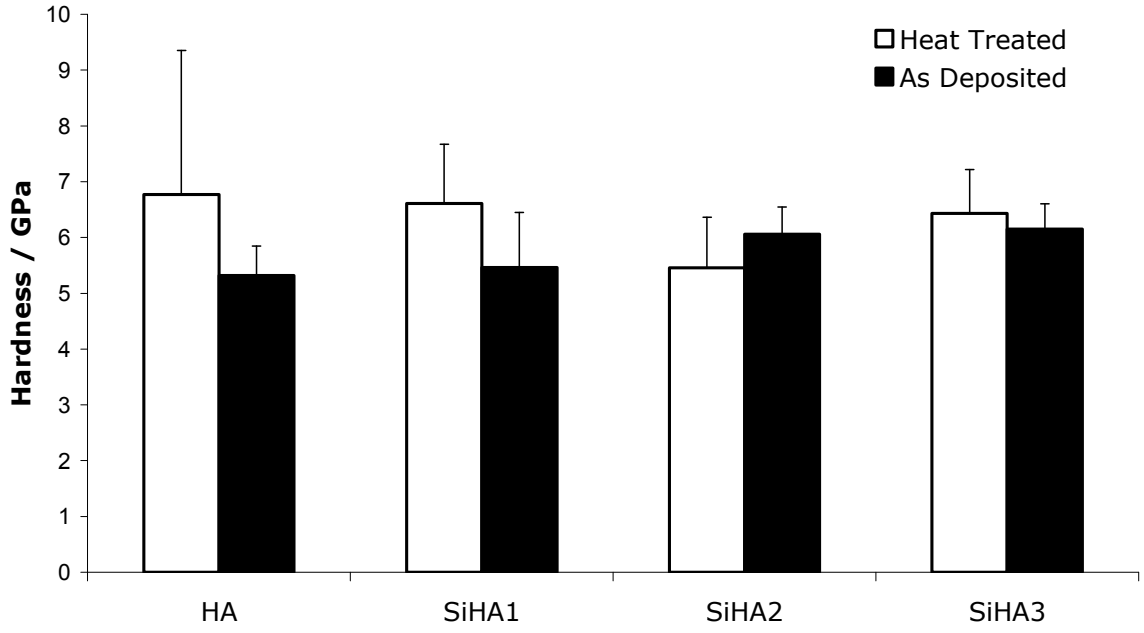

Figure 4-44. Hardness values of HA and SiHA thin films on silicon (100) wafers in as-deposited state and after annealing at 700˚C for 2 h in flowing argon as measured by nanoindentation.

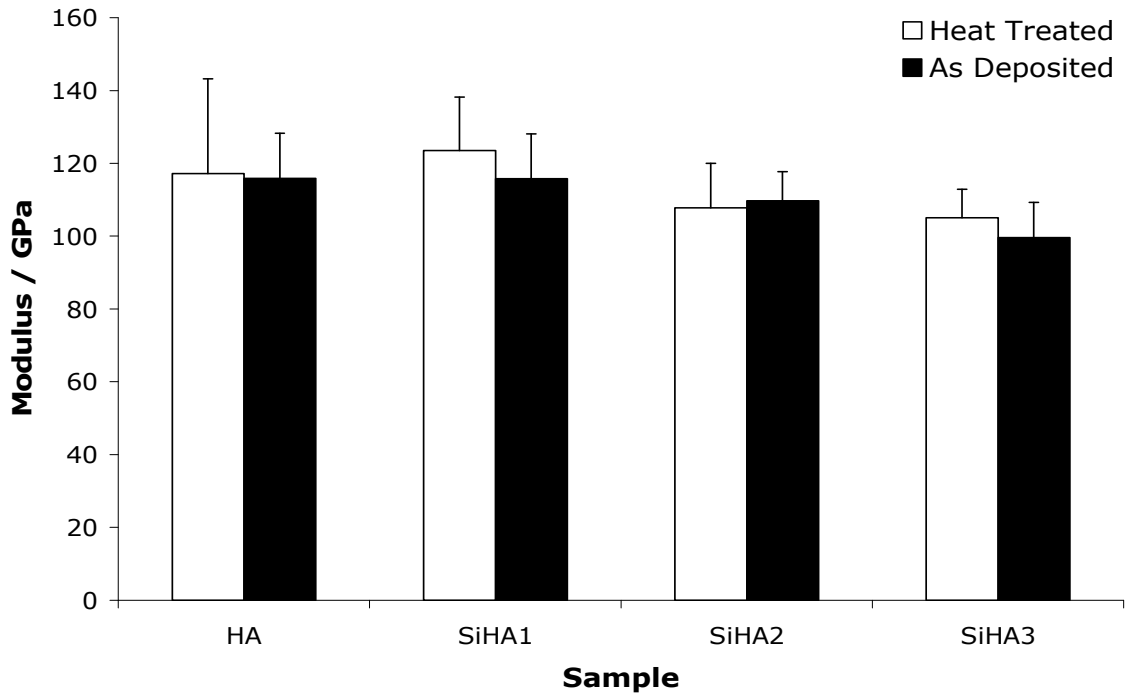

Figure 4-45. Modulus values of HA and SiHA thin films on silicon (100) wafers in as-deposited state and after annealing at 700˚C for 2 h in flowing argon as measured by nanoindentation.

As HA and SiHA thin films were found to have similar hardness and moduli values only HA films were tested for adhesion to the substrate. Nano-scratch testing was performed on HA thin films sputtered onto CPTi discs. Scratches were carried out across the sample surface at varied loads ranging from 30 to 120 mN using a 10 μm diameter Berkovic indenter. The load was ramped linearly over 500 μm. At lower loads no erratic changes could be seen for either the load or penetration depth suggesting that the thin film was well adhered and no failure had occurred. Successive increases in load showed similar results, however, the penetration depth exceeded the coating thickness of 200 nm. Optical microscopy was employed to image scratches at higher loads. Figure 4-46 shows a typical post scratch image of an HA coated CPTi disc. The scratch depth was approximately 2 μm and the film appears to be undamaged following the topography of the groove created by the pathway of the tip. The same test was then repeated on an uncoated CPTi disc. Typical results are shown in figure 4-47. As the tip has traversed the sample it can be seen that titanium debris has been expelled from the groove as indicated by the arrows. This showed that coatings were well adhered and single pass

scratch testing up to 120 mM could find no evidence of failure. As a value of failure could not be obtained attention was turned to (100) silicon substrates as a comparison. Ramping up to loads of 200 mN identified no failure signs in depth or friction plots (figure 4-48). At loads of up to 400 mN a small changes were seen at the same time in depth and friction plots (figure 4-49). The coating was estimated to crack at 200 mN load. Interestingly at 500 mN (figure 4-50) the films failed at 350 mN, suggesting that the load rate was important in coating failure. Figure 4-51 shows optical micrographs for the failure of HA coatings on silicon (100) wafers. It can be seen that although coatings fractured at the failure point, delamination did not occur. In conclusion thin films could not be found to fail on CPTi substrates but did on (100) silicon wafers in the region of 200-350 mN indicating that the adhesion of HA to CPTi substrates is well in excess of 350 mN, however, a value cannot be obtained.

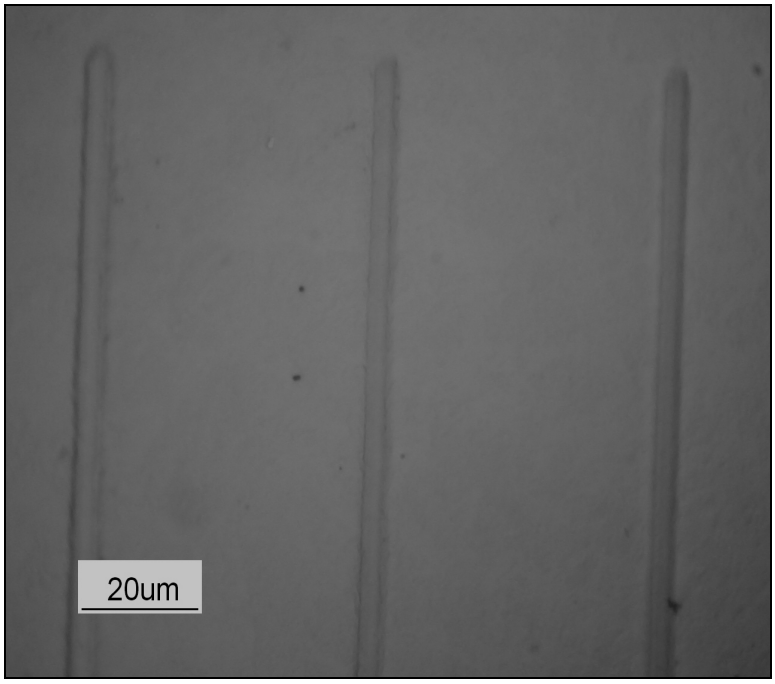

Figure 4-45. A typical light micrograph of an as-deposited HA coated CPTi disc after scratch testing at a load of 120 mN using a 10 μm tip.

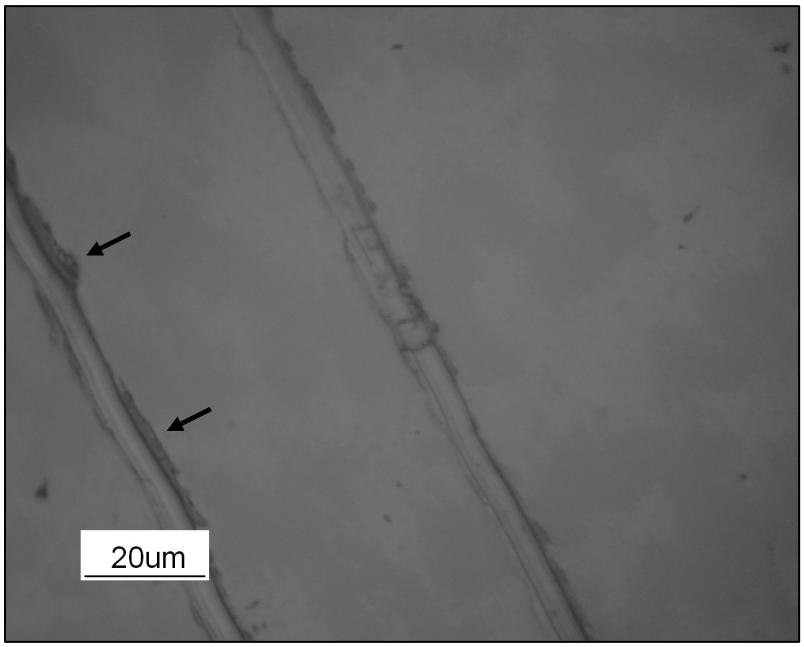

Figure 4-47. A typical light micrograph of an uncoated CPTi disc after scratch testing at a load of 120 mN using a 10 μm tip. The arrows indicate debris created from the scratch groove.

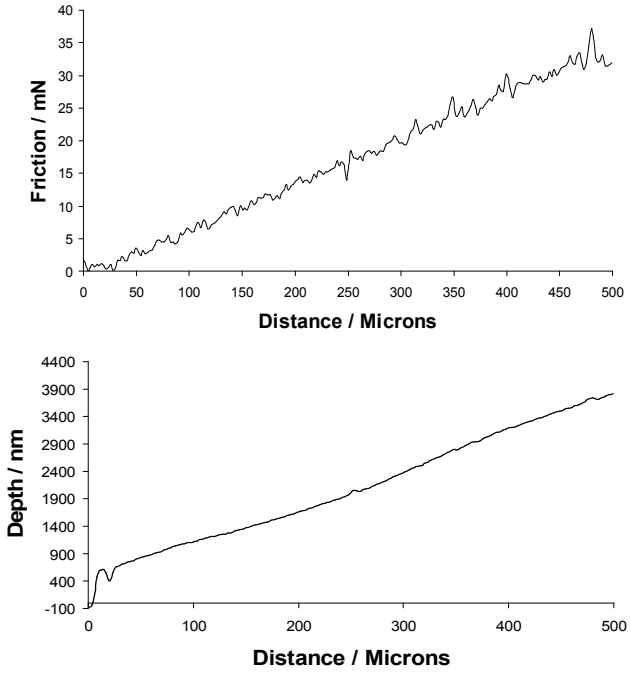

Figure 4-48. Typical depth and friction plots for nano-scratching of a HA coating on a silicon (100) single crystal silicon wafer ramping to a maximum load of 200 mN.

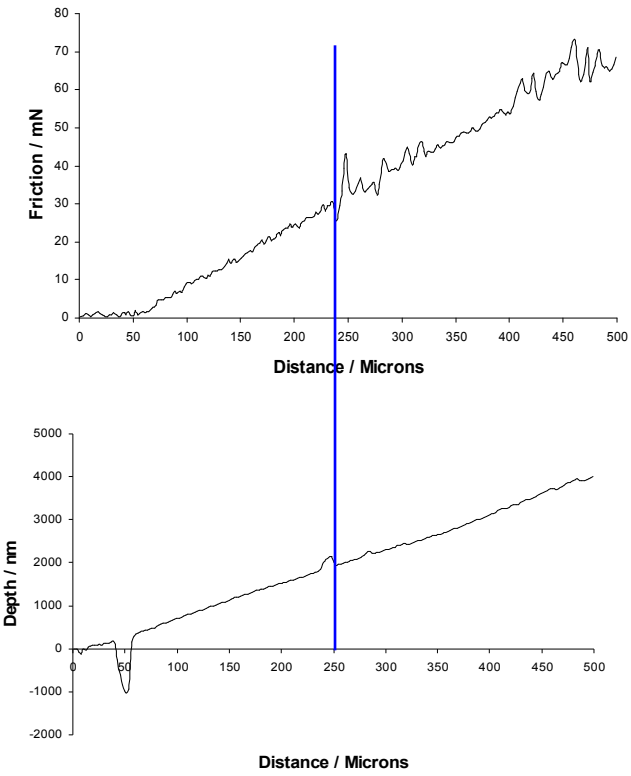

Figure 4-49. Depth and friction plots for nano-scratching of a HA coating on a silicon (100) single crystal silicon wafer ramping to a maximum load of 400 mN. The line indicated possible failure at 200 mN.

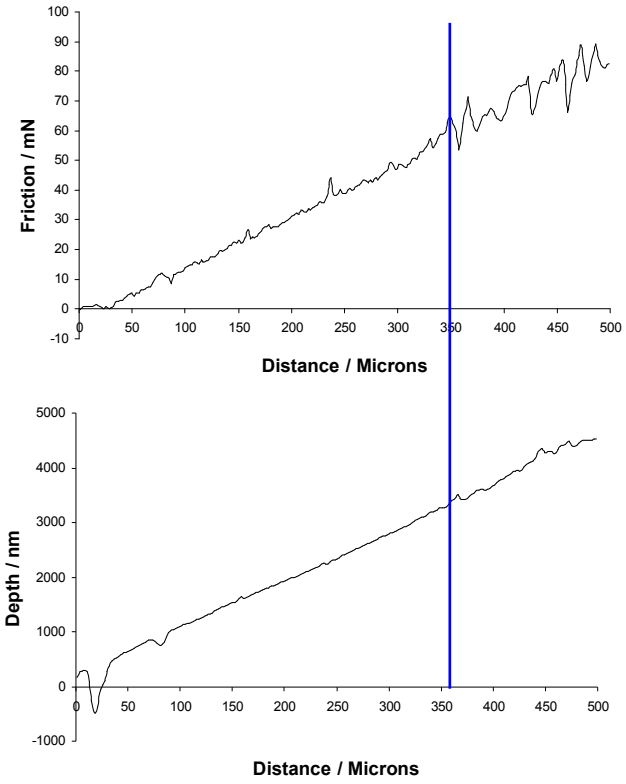

Figure 4-50. Depth and friction plots for nano-scratching of a HA coating on a silicon (100) single crystal wafer ramping to a maximum load of 500 mN. The line indicated possible failure at 350 mN.

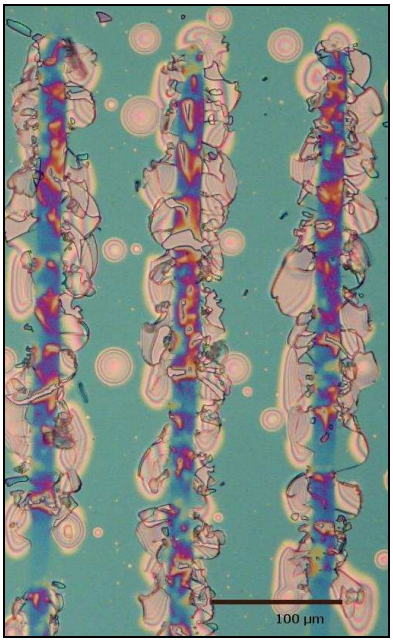

Figure 4-51. Optical micrograph of an HA thin film on a silicon (100) single crystal wafer after scratch testing at 500 mN.

4.7. In Vitro Cytocompatibility Testing of UDP HA and SiHA Thin Films

4.7.1. Elution Testing

An *in vitro* cytotoxicity test was performed using an Alamarblue™ and DNA Hoechst stain assay to assess the possible toxic effect of silicon dopant which could act to lower the cellular response to silicon containing samples.

4.7.1.1. Cellular Activity

Figure 4-52 shows the metabolic activity of HOB cells seeded onto Thermanox slides after 24 h of being exposed to media containing the dissolution products of HA and SiHA thin films. There was no significant difference ($P>0.05$) between either the control Thermanox samples or the samples in HA and SiHA sample. This was confirmed by the Hoechst DNA staining assay which is shown in figure 4-53, in which there was no significant difference ($P>0.05$) in DNA content of HOBs grown in the dissolution products of any of the sample surfaces.

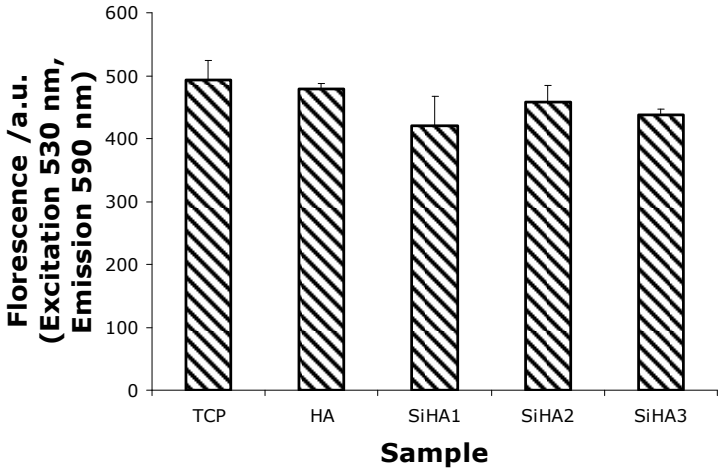

Figure 4-52. The metabolic activity of pre-seeded HOB cells exposed to media containing the dissolution products of HA and SiHA thin films for 24 h. Data plotted is mean ± standard error of the mean where n = 6.

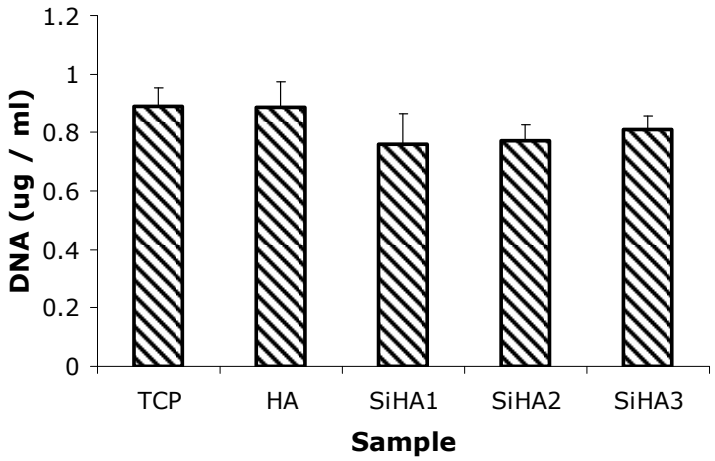

Figure 4-53. The DNA content of pre-seeded HOB cells on TCP exposed to media containing the dissolution products of HA and SiHA thin films for 24 h. Data plotted is mean ± standard error of the mean where n = 6.

4.7.1.2. Cell Morphology

The cell morphology of HOB cells grown on Thermanox slides for 24 h in media containing the dissolution products of HA and SiHA thin films is shown in figure 4-54.

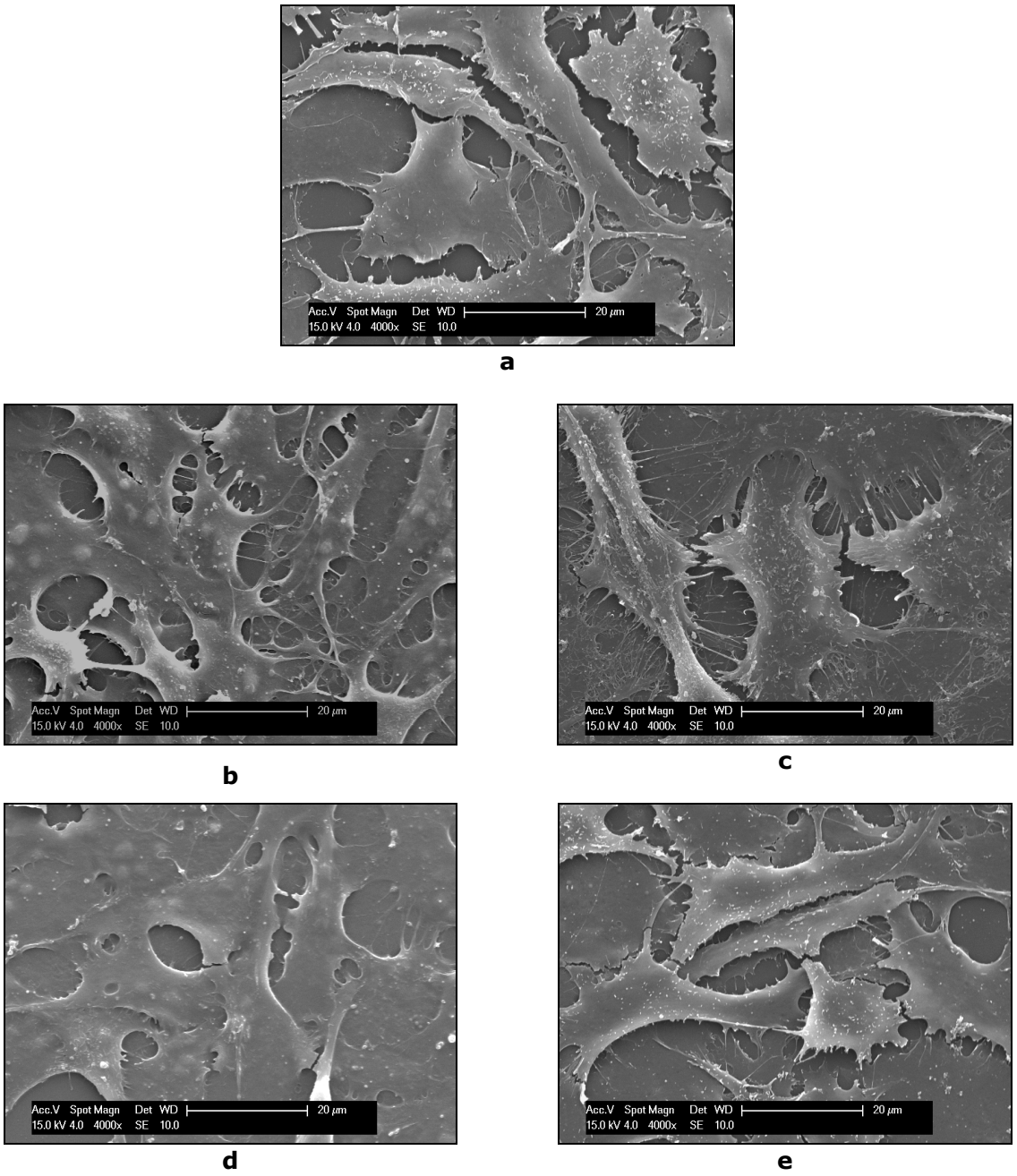

Figure 4-54. SEM micrographs of HOB cell morphology on Thermanox slides after 24 h of culture in a) fresh media, media containing the dissolution products of b) HA, c) SiHA1, d) SiHA2 and c) SiHA3 thin films.

Cell morphologies for the control and all samples appeared similar showing a monolayer over the Thermanox surface. Cells were well spread appearing to have similar cell areas. Filopodia and lamellapodia were also observed indicating cell spreading was occurred successfully. In conclusion the SiHA samples did not demonstrate cytotoxicity in either

Alamarblue™ or DNA assays due to no significant (P>0.05) differences being found in either of the assays conducted when compared to the TCP control samples. Furthermore, cell morphology indicated no differences for osteoblast cells grown in either of the elution culture medium.

4.7.2. Initial Attachment

The initial attachment of HOB cells to as-deposited and annealed (600°C for 2 h) HA and SiHA thin films was performed to see what quantity of HOB cells attached to surfaces after 90 min giving an indication of the suitability of surfaces for cell growth. Figure 4-55 shows the adhesion of HOB cells as a percentage of a TCP control. As-deposited and heat treated HA thin films showed good 90 min attachment with values of 51 and 91 % of the control and were found to be significantly different (P<0.05). As-deposited and heat treated SiHA1 and SiHA2 samples showed poor attachment which was less than 20 % of the control. All values for these samples were significantly lower than the heat treated HA thin film (P<0.05).

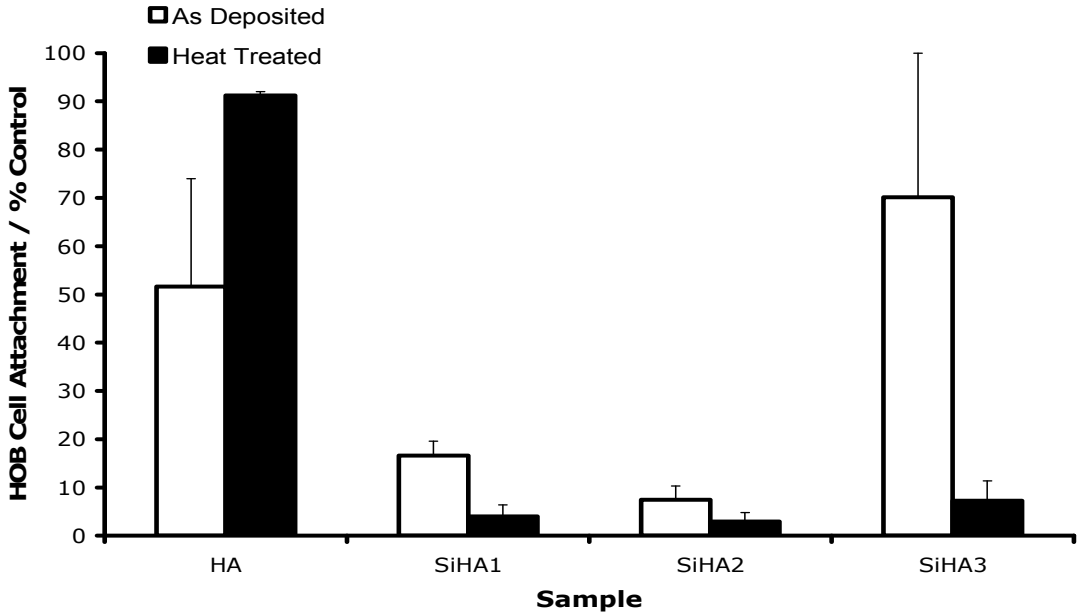

Figure 4-55. The 90 min attachment of HOB cells to as-deposited and heat treated HA and SiHA films at 600°C for 2 h in argon. Values are mean ± standard error where n = 6.

The as-deposited SiHA3 samples showed good attachment compared to the as-deposited and annealed SiHA1 and SiHA2 samples but was not significantly different from the heat treated HA samples ($P<0.05$). Large amounts of variation were seen for this sample type with some samples showing excellent attachment, others were poor. This may be observed by the large value of standard error calculated for this sample. Following heat treatments at 600 °C for 2h, the SiHA3 sample showed poor cell adhesion which was 7 % of the attachment seen on the control surface.

4.7.3. Proliferation and Differentiation Studies

4.7.3.1. Cellular Activity

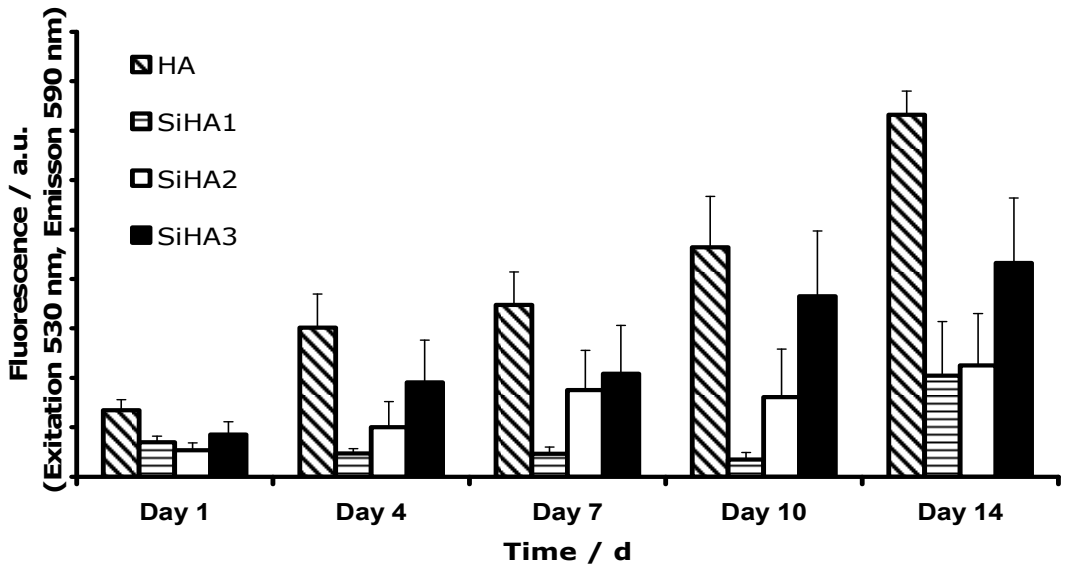

Figure 4-56. The metabolic activity as measured by Alamar Blue™ of HOBs on HA and SiHA surfaces heat treated at 600˚C for 2 h. Plotted values are mean ± standard error of the mean where n = ≥ 6.

The metabolic activity of HOB cells on HA and SiHA surfaces at selected timepoints was measured using an Alamarblue™ assay. Figure 4-56 shows relative metabolic activity of HOBs over a 14 day period for HA and SiHA surfaces heat treated at 600˚C. The HA surface showed the highest cellular metabolic activity at every time point. The lowest activity was recorded on the SiHA1 samples. There appeared to be no increase in metabolic activity until day 14 where cell activity significantly increased. The SiHA2

samples showed higher cellular activity compared to the SiHA1 samples, with the SiHA3 samples showing the highest of all the SiHA samples. Metabolic activity increased with increasing silicon content of SiHA samples.

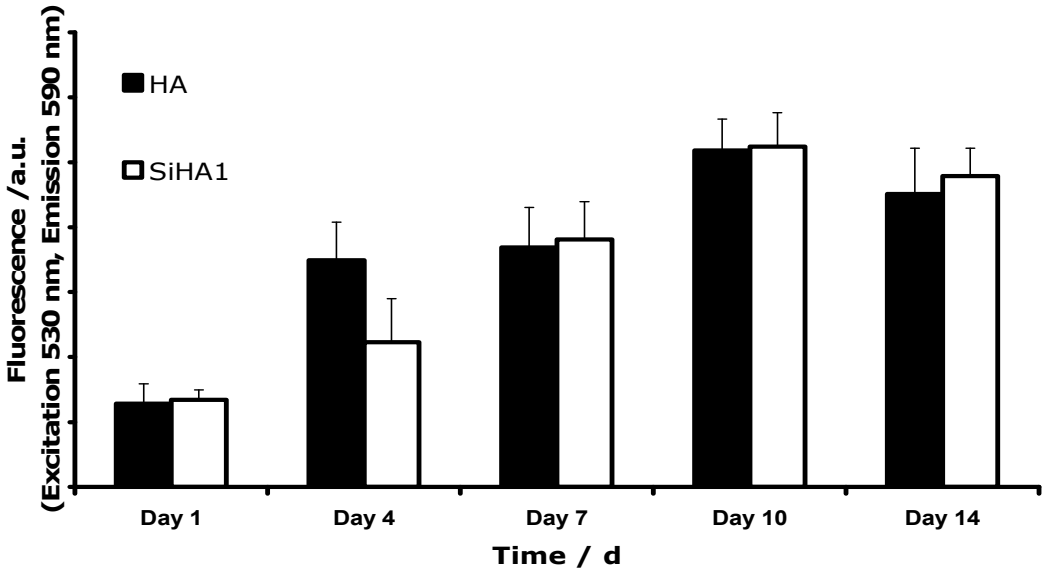

Figure 4-57. The metabolic activity of HOB cells on HA and SiHA1 samples heat treated at 700˚C in flowing argon for 2 h after 14 days of culture. Plotted values are mean ± standard error of the mean where n = ≥ 6.

The metabolic activity of HOB cells on HA and SiHA1 surfaces annealed at 700˚C in flowing argon is shown in figure 4-57. After 1 day of culture there was a small increase in metabolic activity on the SiHA1 surface compared to the HA surface, however, there was no significant difference ($P>0.05$). At day 4 the HA sample exhibited higher proliferation than the SiHA1 sample but again not significantly different ($P>0.05$). At days 7, 10 and 14 measured proliferation was not different between the two samples. At day 14 a slight reduction in the overall proliferation of both samples was seen compared to day 10.

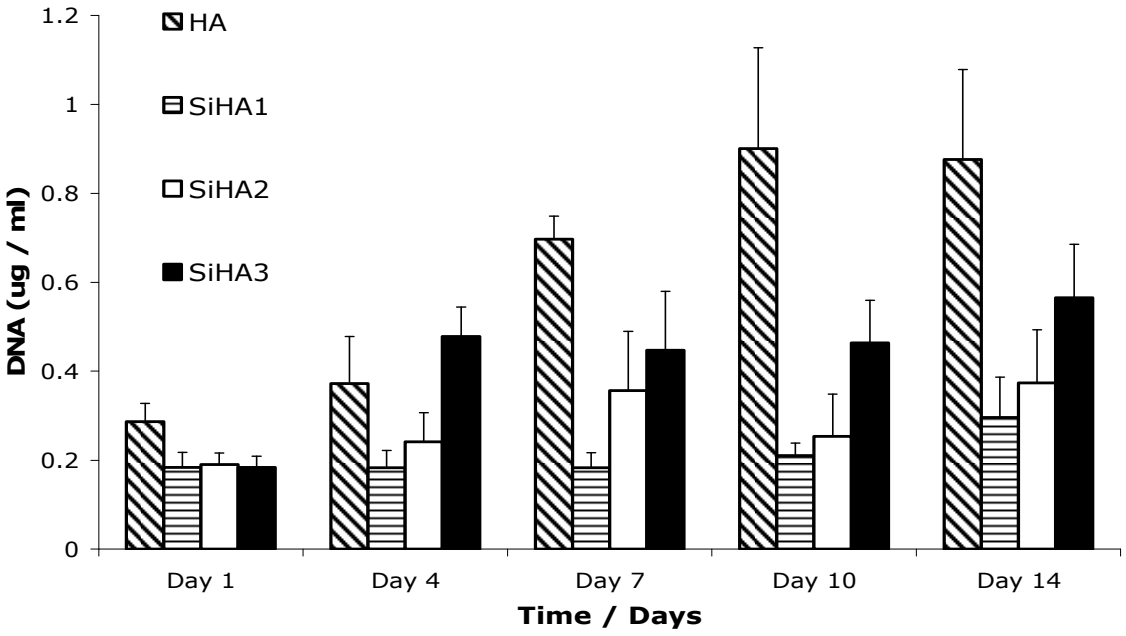

Figure 4-58. DNA content of HOB cells on HA and SiHA surfaces heat treated at 600˚C in flowing argon for 2 h. Plotted values are mean ± standard error of the mean where n = ≥ 6.

The measured DNA content of HOBs on the HA and SiHA surfaces confirmed the trend shown by the Alamarblue™ assay. DNA content of HOB cells on HA and SiHA surfaces annealed at 600 °C in flowing argon for 2 h are displayed in figure 4-58. HA showed the highest DNA content. HA consistently showed higher DNA values than all other samples. Little change in DNA content was seen from days 1 to 10 for the SiHA1 sample but a small increase was seen at day 14. The SiHA2 samples elicited increasing DNA content up to day 10. There was then a small decrease at day 10 which increased again at day 14 however no significant difference was seen between day 7, 10 or 14 for this sample set. The SiHA3 sample showed an increase in DNA content from day 1 to 4 but stabilised at all other time points. These samples exhibited the highest DNA content of all the SiHA samples.

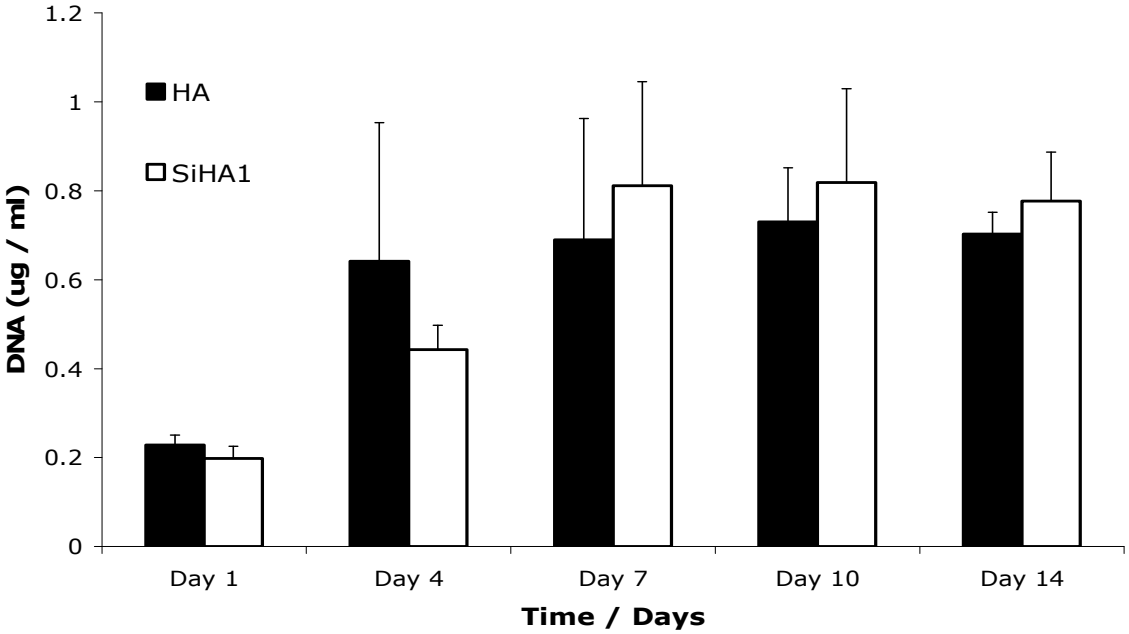

Figure 5-59. DNA content of HOB cells on HA and SiHA thin film surfaces heat treated at 700˚C for 2 h. Plotted values are mean ± standard error of the mean where n = ≥ 6.

The DNA content of HOBs on HA and SiHA1 surface annealed at 700˚C showed no significant difference between either of the samples at any time point (figure 5-59). However, at day 4, as with the Alamarblue™ data the HA was at a higher value than the SiHA1 samples. At days 7, 10 and 14 this was reversed with SiHA1 measurements being slightly higher than the HA samples.

4.7.3.2. Alkaline Phosphatase Activity

Figure 4-60 presents data for ALP activity normalised to DNA content for HOB cells grown on HA and SiHA surfaces heat treated at 600˚C. The ALP activity was neglilable for all surfaces after 7 days of culture. At 10 and 14 days a significant increase ($P<0.05$) in ALP activity was seen for the HA samples compared to the ALP actity at day 7. All silicon containing HA thin films did not show any significant difference in ALP activity at any of the timepoints assessed.

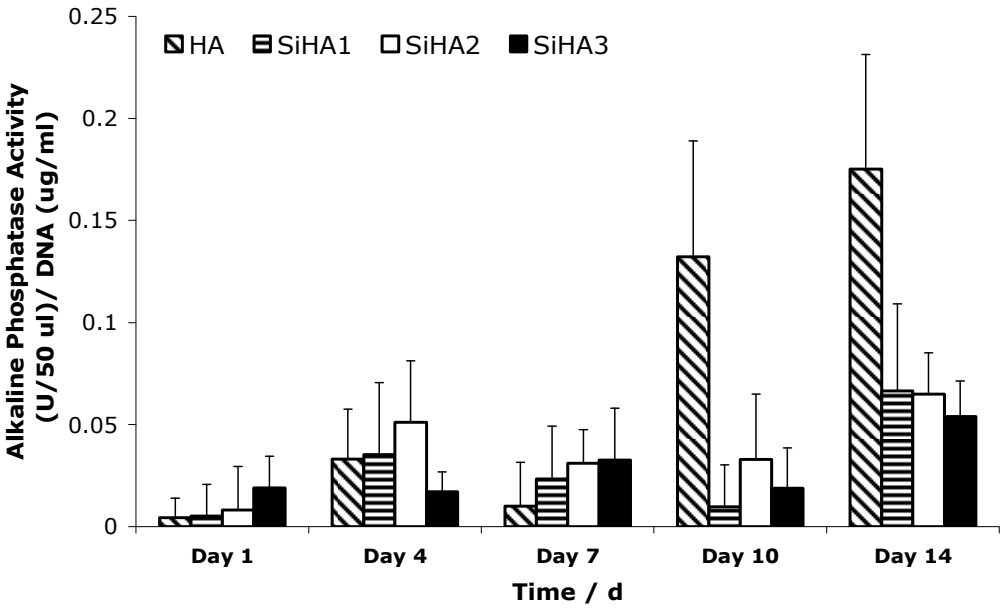

Figure 4-60. Alkaline Phosphatase activity normalised to DNA content for HOBs on HA and SiHA films heat treated at 600˚C for 2 h in argon. Plotted values are mean ± standard error of the mean where n = ≥ 6.

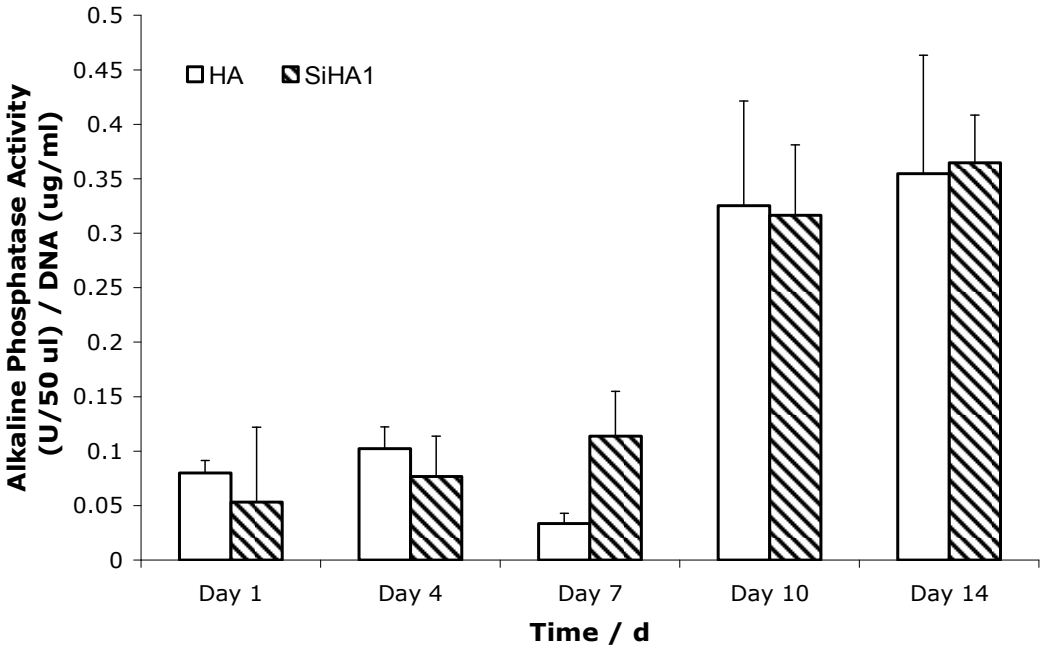

Figure 4-61. Alkaline Phosphatase activity normalised to DNA content for HOBs on HA and SiHA films heat treated at 700˚C for 2 h in flowing argon. Plotted values are mean ± standard error of the mean where n = ≥ 6.

Figure 4-61 shows ALP normalised to DNA content for HOB cells grown on HA and SiHA1 surfaces annealed at 700°C in flowing argon for 2 h. ALP was not expressed in the HA samples until day 10, noted by a significant increase ($P<0.05$) in activity from day 7 to day 10. Values at day 14 were not significantly different from that at day 10. The SiHA1 samples followed this trend, however, there was no significant difference ($P>0.05$) in ALP activity between the two compositions.

4.7.3.3. Cell Morphology

The cell morphology of HOB cells was examined by SEM. This section shows representative images at selected time points.

Figure 4-62 shows typical morphologies of HOBs after 1 day on Thermanox, HA and SiHA samples heat treated at 600°C in flowing argon for 2 h. The Thermanox slides showed the greatest number of cells attached to the surface. These cells appeared well spread forming a monolayer over the sample surface. Cells on the HA surface showed fewer cells than the control samples with cells being slightly more spread over the surface of the thin film. Very few cells were seen on the SiHA1 samples, however cells that did attach had comparable morphologies to the HA and control samples. Interestingly the thin films on some on the SiHA1 samples appeared to delaminate in areas. Delaminating films are shown in more detail in figure 4-63. Figure 4-63a show that delamination is consistent over the sample while figure 4-63b shows the delaminated film patches rounded in shape which could possibly coincide with the underlying titanium grains. The SiHA2 samples supported increased cell growth compared to the SiHA1 samples, with a greater number of cells appearing spread and flat on the surfaces. Cells on the SiHA3 samples appeared to be thin and elongated. The morphology of cells on Thermanox slides, HA and SiHA3 samples at day 14 are shown in figure 4-64. Only these images are shown as cells were not seen on SiHA1 or SiHA2 surface. HOBs on all featured surfaces appeared to mulitlayer indicating desirable osteoblast cell growth.

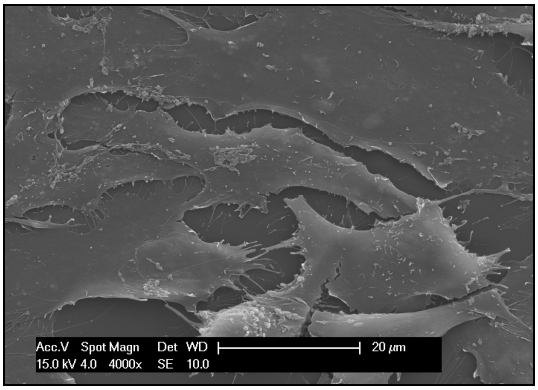

a

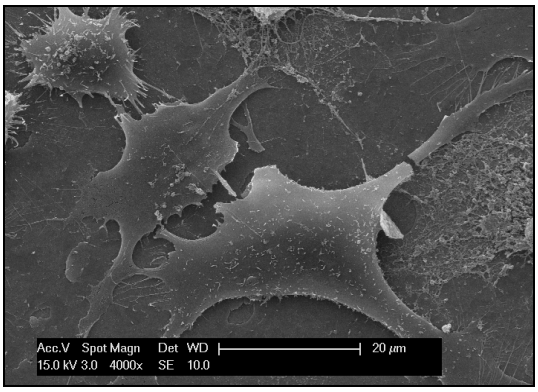

b

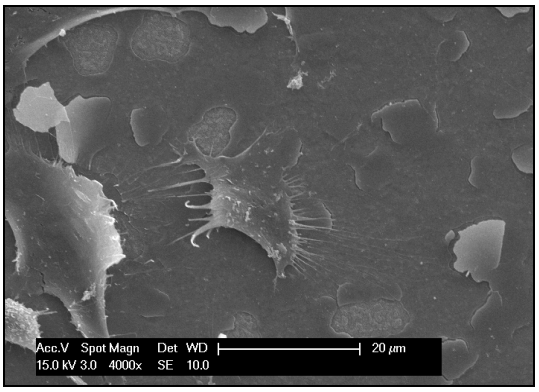

c

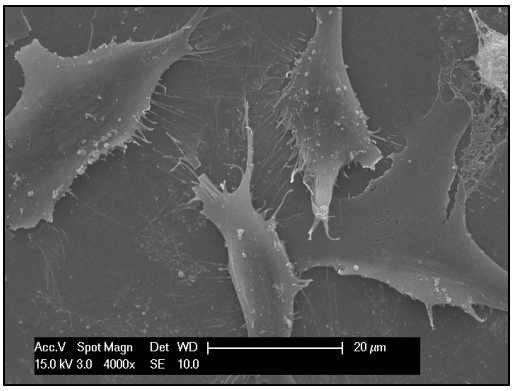

d

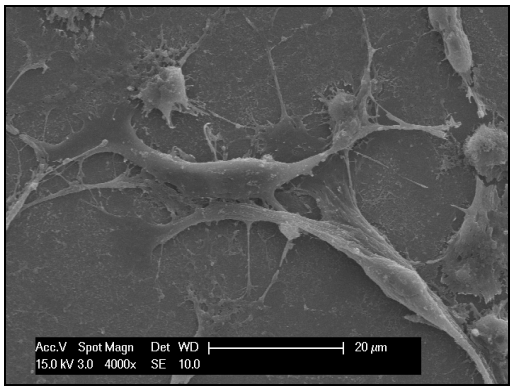

e

Figure 4-62. Typical HOB cell morphology at day 1 on HA and SiHA surfaces heat treated at 600˚C for 2 h in flowing argon, where a) Thermanox (control), b) HA, c) SiHA1, d) SiHA2 and e) SiHA3 surfaces.

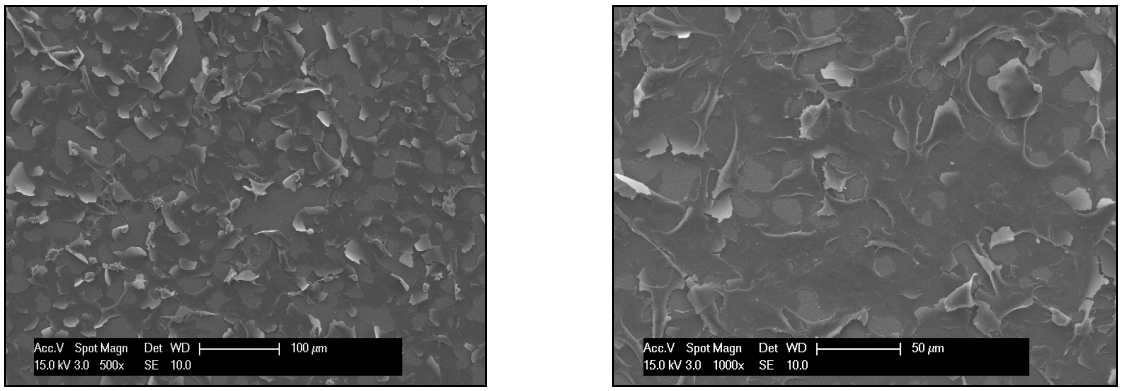

a **b**

Figure 4-63. Delamination of SiHA1 thin films after day 1 of cell culture.

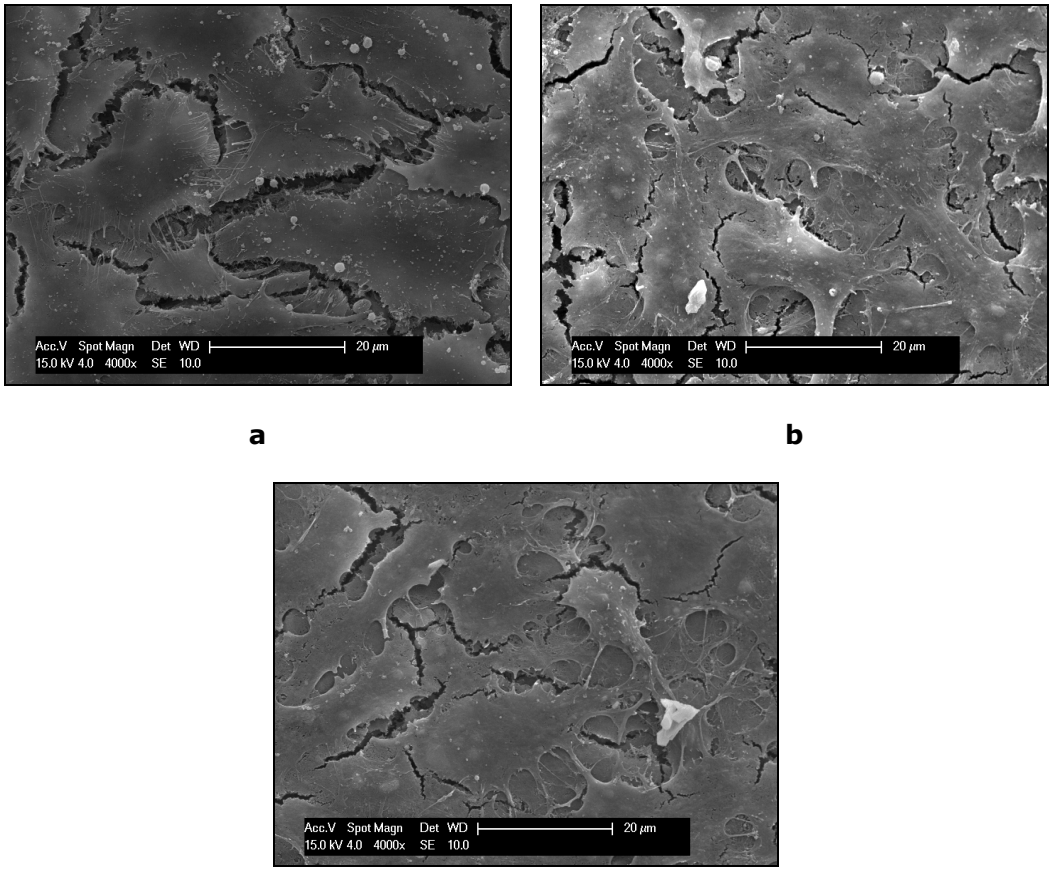

a **b**

c

Figure 4-64. Typical HOB cell morphology at day 14 on Thermanox, HA and SiHA3 surfaces heat treated at 600˚C in flowing argon for 2 h, where a) Thermanox (control), b) HA and c) SiHA3 surfaces.

The morphology of cells after day 1 on HA and SiHA1 surfaces heat treated at 700°C for 2 h is displayed in figure 4-65a and 4-65b respectively. Both HA and SiHA1 surfaces appeared to be more textured than samples heat treated at 600°C, which corresponds to roughness values measured by stylus profilometry. This was more pronounced on the HA sample. Cells appeared to react to this topography in the case of both samples by larger numbers of extending extra cellular processes compared to 600°C sample, which attached to raised areas of the surface.

Figure 4-65c and 4-65d displays HOB cell morphology for the HA and SiHA1 samples annealed at 700 °C after 7 days of cell culture respectively. Cells on both samples cover the sample surfaces and multilayering had occurred, and no differences were seen between the two samples. Cracks were also seen in both cell samples which is due to the dehydration protocol adopted. Figure 4-65e and 4-65f shows HOB cell morphologies on HA and SiHA1 surfaces after 14 days of cell culture respectively. Cracks could again be seen but no difference in morphologies was seen.

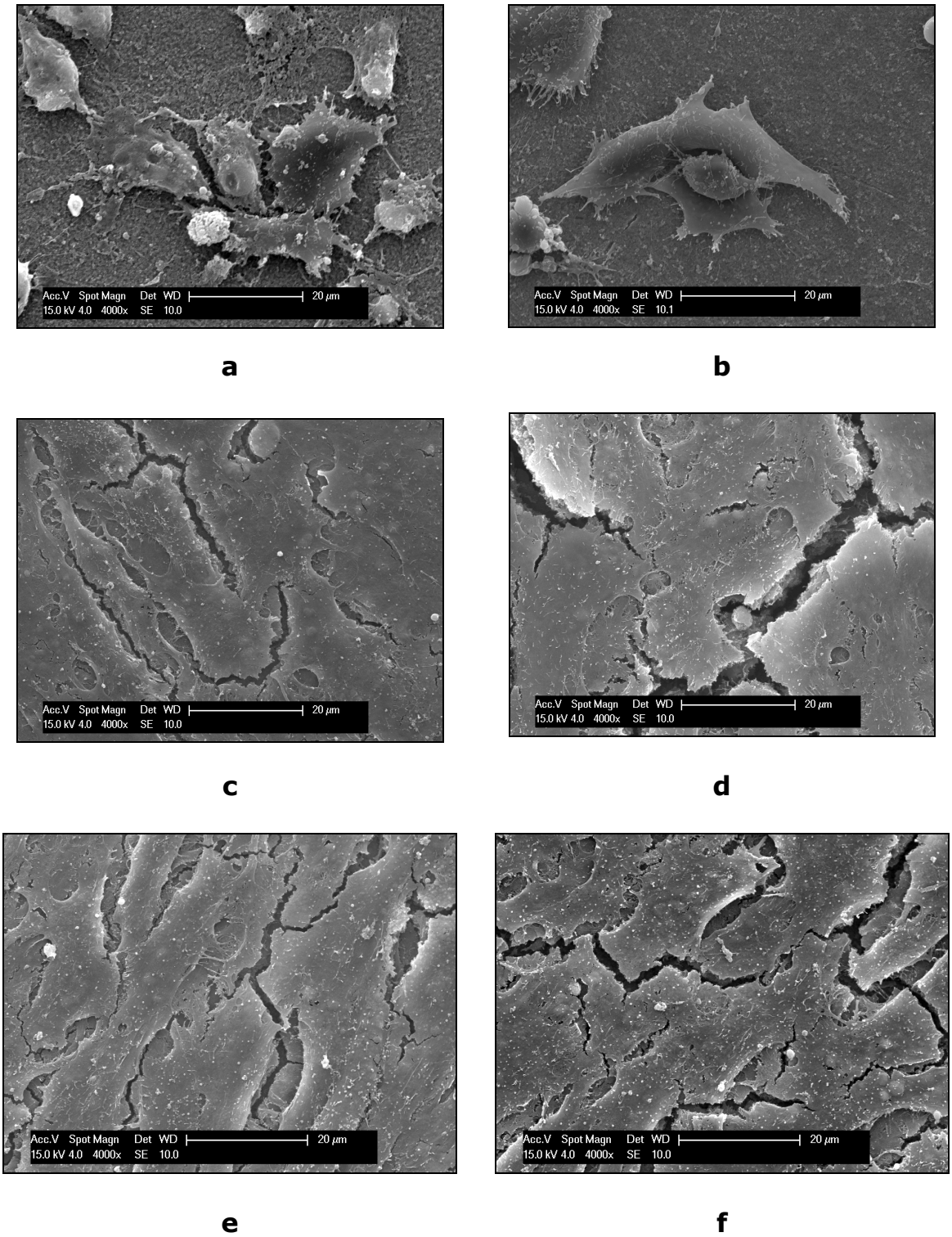

Figure 4-65. Typical HOB cell morphology on a) HA thin films heat treated at 700˚C in flowing argon for 2 h after day 1, b) SiHA1 thin films surfaces heat treated at 700˚C in flowing argon for 2 h after day 1, c) HA thin films heat treated at 700˚C in flowing argon for 2 h after day 7, d) SiHA1 thin films heat treated at 700˚C in flowing argon for 2 h after day 7, e) HA thin films heat treated at 700˚C in flowing argon for 2 h after day 14 and f) SiHA1 thin films heat treated at 700˚C in flowing argon for 2 h after day 14.

4.8. Summary

This chapter has detailed the results obtained from all relevant experiments carried out in this study. Investigations into post-deposition heat treatments on HA films found that coatings began to exhibit a single phase HA crystal structure after annealing temperatures of 500°C for 2 h in an inert atmosphere (helium or argon). Increasing annealing temperature acted to increase crystallinity and it was concluded that a annealing temperature of 600°C for 2 h in flowing argon allowed suitable recrystallisation of HA thin films.

HA coatings and thin films system are commonly non-stoichiometric. In the case of RF magnetron sputtering, deposition parameters can be altered to achieve stoichiometric compositions. It was found that power supply type, deposition power density, and gas composition all influenced film composition. Moreover, the inclusion of 12 % oxygen to the sputtering atmosphere actively lowered the Ca/P ratio allowing the production of stoichiometric HA thin films.

The ability to accurately measure the composition, or more specifically, the Ca/P ratio of HA thin films has been questioned. An investigation into the effectiveness of EDX, XPS and RBS to measure such values has been investigated. Unsurprisingly it found that each technique gave a different Ca/P value for the same surface. Furthermore, it was found that the techniques gave Ca/P values from lowest to highest in order of XPS>EDX>RBS. Standard materials were used to identify error and uncertainties related to each of the techniques.

HA and SiHA thin films, ca. 200 nm in thickness, of different silicon content were successfully produced using a RF magnetron sputtering method. Films were then characterised using multiple techniques in order to study surface roughness, chemistry, structure and composition. Some general findings can be summarised. All as-deposited

coatings were amorphous. After heat treatments all films exhibited a single phase HA structure matching to standard ICCD cards with the exception of the SiHA3 samples. The addition of silicon to the HA system reduced crystallinity. This effect was found to be dose dependant. Moreover, the presence of silicon reduced the formation of phosphate and hydroxyl bonding in HA films. Surface analysis showed that silicon was in the form of polymeric silicon in the as-deposited SiHA film. After annealing at 600 or 700°C silicon transformed to a monomeric silicate system.

From the work presented here, it is proposed that, in post-plasma-deposited heat treated films, silicon substitutes as silicate species into the HA lattice. As-deposited SiHA1, SiHA2 and SiHA3 (containing 1.8, 4.2 and 13.4 wt.% Si by EDX, respectively) thin films were found to have a polymeric Q^4 silicate configuration as determined by XPS. Furthermore, XRD analysis gave evidence that all as-deposited films were amorphous. These two results suggest that, in as-deposited SiHA1, SiHA2 and SiHA3 thin films, silicate groups may be randomly distributed throughout the amorphous film. After post-deposition annealing at 600 or 700°C for 2 h in an argon atmosphere, XPS investigations indicated that in SiHA1, SiHA2 and SiHA3 films silicate groups had substituted for phosphate tetrahedra in the HA lattice, evidenced by a monomeric Q^0 silicate structure. Furthermore, in SiHA1 and SiHA2 films, an HA-like phase was found to be present as shown by XRD; in contrast, the SiHA3 films annealed at 600 or 700°C for 2h in an argon atmosphere exhibited an amorphous structure. Contrary to these findings, FTIR analysis of SiHA1, SiHA2 and SiHA3 films did not manifest any silicate-based bands. This may, however, be due to the fact that the ATR evanescent technique only samples a very small amount of material and, due to the low doping quantities of silicon in the HA films, this may have lead to practical difficulties in detecting these bands. Further contradictory evidence to the proposal of substitution of silicate into HA is that Ca/P ratios consistently differed from the stoichiometric value of HA (1.67) as determined by both XPS and EDX. It should also be mentioned that, although phosphate bands were observed by FTIR for the heat-treated crystalline SiHA1 and SiHA2, no phosphate bands were found for the

amorphous SiHA3 films after post-deposition annealing at 700°C. This combined evidence raises the question of whether the post-deposition heat-treated films have a true HA-like structure. However, the change from Q^4 in the as-deposited films to Q^0 silicate in the heat-treated films and the HA-like structure found by XRD is strong evidence that silicate substitution of HA has occurred for the lower levels of silicon addition. More work is required in order to truly understand the structures present in plasma-deposited, heat-treated SiHA thin films.

Films were found to be more hydrophilic with increasing silicon content suggesting SiHA films to have a more negative charge than HA films. Solubility was also investigated demonstrating films became more soluble with increasing silicon content.

Initial attachment studies indicated that HOB cells attached well to as-deposited and HA thin films annealed at 600°C. However, cells did not attach well to all silicon doped HA thin films with the exception of the SiHA3 as-deposited sample. Cellular activity studies on HA and SiHA thin films annealed at 600°C for 2 h in flowing argon showed cell growth could be maintained on all surfaces, however, the HA surface showed the highest amount of cell activity when compared to all SiHA samples. While all SiHA samples showed lower cellular activity, an increase was seen in accordance with the silicon content of SiHA thin films. Elution tests carried out on HA and SiHA samples annealed at 600°C after 1 day of exposure to media showed not significant differences ($P>0.05$) suggesting elution products are non-cytotoxic. Cellular response was not significantly different ($P>0.05$) on HOBs grown on HA surfaces annealed at 700°C when compared to HA films annealed at 600 °C, however, a significant increase in cellular response was noted from HOBs on SiHA1 samples annealed at 700°C when compared to SiHA1 sample annealed at 600°C. Moreover, the SiHA1 samples annealed at 700°C were not significantly different ($P>0.05$) from HA films annealed at the sample temperature. Cell morphology studies illustrated that HOB morphologies on all surfaces did not vary significantly and that cells were well spread showing filopodia and lamelapodia.

5. Discussion

5.1. Introduction

Recent studies on bulk SiHA and thick and thin film coatings have identified them as eliciting an enhanced cellular and tissue response compared to HA [126, 141, 219, 220]. The characterisation of thin film materials is currently limited. As a result, the role of silicon in the HA crystal structure is still not fully understood and moreover how this interacts with cells. It is hoped that this discussion section will contribute in part to this understanding. This chapter provides an interpretation of the results disclosed in the previous results chapter and relates these findings to those of other authors. This is divided into the following discussion topics. Section 5.2. discusses the basic characterisation of both HA target types used for RF magnetron sputtering. Section 5.3. looks at the effect of post deposition heat treatments on thin films crystallinity. Section 5.4 discusses the role of deposition parameters and how these may be adjusted in order to optimise coating compositions with respect to the Ca/P ratio. Section 5.5. discusses the accuracy of three techniques used to investigate thin film compostion. Section 5.6. considers in detail the properties of HA and SiHA thin films related to surface chemistry, composition, topography, wettablilty, stability and mechanical properties and their importance with respect to cellular response. Section 5.7 discusses the data relating to cellular response referring this back to the characterisation of the thin film surfaces to understand why HOB cells react in a particular way.

5.2. Characterisation of Target Materials

Powders obtained from Plasma Biotal have previously been well characterised [241], however batch variation may occur and therefore the sample composition was assessed. The as received powder was found to be a single phase HA before and after sintering (figure 4-1). The material remained phase stable up to 1350°C owing to its purity. HA has been shown to decompose forming calcium phosphates such as β-TCP at a temperature range between 1200 and 1350°C [242]. Particle size increased after sintering which can be explained by growth of HA crystallites.

Plasma-spraying of HA powders often leads to the thermal decomposition of HA materials due to the high temperatures involved during the deposition process which can result in a mixed phase coating [63]. In this study plasma sprayed targets obtained from Plasma Biotal showed a very small quantity of α-TCP which is consistent with the literature [63]. α-TCP has a Ca/P ratio of 1.5 so this would act to lower the overall Ca/P ratios. However, amorphous calcium phosphate phases can have Ca/P ratios in the range of 1.2 - 2.0 (table 2-3) which would increase the overall Ca/P ratio and remain undetected by XRD due to the amorphous nature of the material. Also it is important to note that $Ca_2P_2O_7$ melt to an amorphous phase with a Ca/P =1.0. As the Ca/P ratio was measured to be high it is likely that amorphous material was present which would have increased the Ca/P ratio from 1.67. Furthermore, as will be discussed in section 5.5. the characterisation technique used to perform this anaylsis had error associated with the calculation of the Ca/P ratio which could also lead to misleading Ca/P ratios. Moreover, the crystallite size was measured to be 23.4 nm which would support this hypothesis. A strong crystallographic preferential orientation along the (002) and the (004) diffraction planes was observed on the plasma sprayed targets (figure 4-4). This means the XRD apparatus was effectively 'seeing' more (002) orientated crystallites [180]. This is typical of HA plasma-sprayed coatings [216, 243], and also occurs naturally in bone [244]. This orientation in HA materials means the c-axis is perpendicular to the substrate resulting in predominantly a columnar grain structure. Furthermore, orientating along this axis allows

the coating to achieve the lowest strain possible [191]. Preferential orientation increases with coating thickness [243]. As more material is deposited increasing strain is generated providing the driving energy for the film to peferentially orientate. Coating morphology was of a typical splat formation for plasma sprayed HA coatings, which has been well documented [63]. Cracks could also be seen across the coating which is probably likely due to a combination of thermal expansion mismatch of HA and the copper backing disc and residual stresses induced in the coating process due to high temperature, high velocity particle impinging the copper surface and then cooling rapidly thus going through thermal shock. Indeed, HA has a thermal expansion co-efficient of 14 μm m^{-1} K^{-1} while copper is measured at 16.5 μm m^{-1} K^{-1}.

5.3. The Effect of Post-deposition Annealing on BPM HA Thin Films

BPM RF magnetron sputtered thin films produced with sintered HA powder targets and annealing was carried out at various temperatures to see the effect on thin films. The deposited films were found to be amorphous, which has been shown to be common in RF magnetron sputtered systems at lower power densities, below 10 W cm^{-2} [86]. Post-deposition heat treatments at 400°C in a static inert helium atmosphere did not lead to film recrystallisation (figure 4-6), but this did occur at 600°C in the same environment (figure 4-7). When the temperature of post-deposition heat treatments was altered at 25°C steps recrystallisation was seen to start occurring at 500°C (figure 4-8). Other researchers have reported temperatures which correspond to this value [178, 184] but this is the first instance in which *in situ* XRD has been used to identify this transition temperature for RF magnetron sputtered HA thin films. Boyd *et al*. [180] found HA thin films to partially recrystallise at 400°C. They, however, used a sputtering pressure of 100 mTorr (13.3 Pa) with a deposition rate of 60 nm h^{-1} which is a much higher sputtering pressure and rate than used in the current study. This would have lead to increased film bombardment and localised target and substrate heating which may have aided lowering of the recrystallisation temperature due to higher residual stress present in the films. Figure 5-1 shows literature values and data from the current study to compare the deposition rate with the initial recrystallisation rate. It can be seen that there was a weak correlation between these two factors. This correlation is masked due to the large other number of factors which will have affected substrate heating during deposition such as the sputtering pressure and target to substrate distance. Bulk materials have been also indicated at 850°C. It is thought that as the deposition rate is lowered this recrystallisation temperature will approach this value.

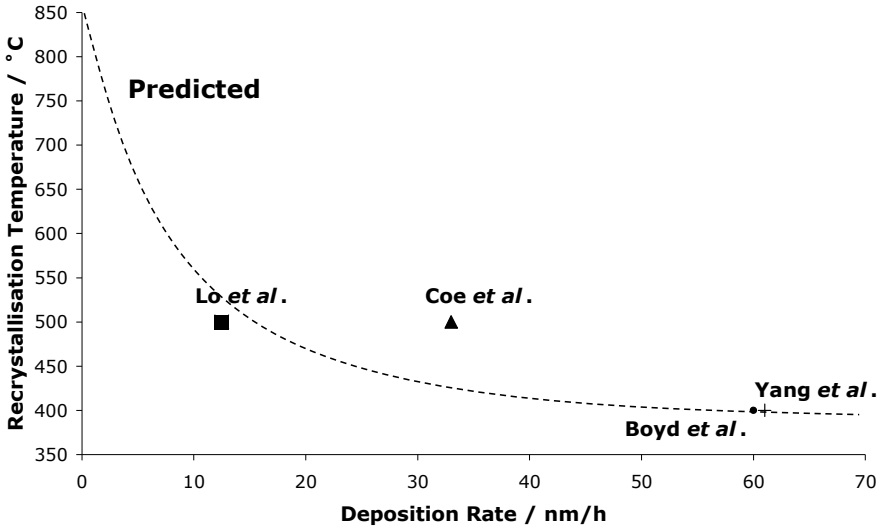

Figure 5-1. The effect of deposition rate on the initial recrystallisation temperature for RF magnetron sputtered HA thin films. Data calculated and compiled from [180, 183, 184, 195]. Curve is only to give a guide to the eye.

In the work presented here, XRD peak intensity grew with increases in temperature of post-deposition heat treatments which directly corresponds to crystallite growth (figure 4-8). *In situ* XRD did have limitations; in glancing angle mode the signal to background ratio is lower and this is further worsened by the use of an inert environment and a kapton window. The signal to background was 6 times higher for the *ex situ* XRD than the *in situ* XRD. Nevertheless, *in situ* XRD provided a time saving method to obtain information about the effect of post-deposition heat treatments. It is suggested that *ex situ* XRD is also used in conjunction to provide more detailed analysis of diffraction patterns, as was carried out in this study, due to a higher signal to background ratio.

FTIR was used to study the effect of heat treatments on the thin film chemistry. As-deposited films showed characteristic HA phosphate bands, that upon heat treatment became more defined with new phosphate bands appearing after heat treatments of 500°C (figure 4-9). Furthermore, hydroxyl species were detected on the surface of all heat treated samples which also became more prominent with higher annealing temperatures. This has been shown by researchers working with HA thin film materials

[180, 184]. Lo *et al*. [195] investigated annealing temperatures from 80 – 500°C and found OH bonding was not present until heated to 500°C This may be due to the dissociation of water molecules at this temperature which reform on the thin film surfaces when cooled. Atomic mobility increases at higher temperatures, thus allowing for easier bond formation. In addition, carbonate bonding was observed in the films annealed at 500 and 600°C. This was unexpected but carbon may have originated from either the inside of the sputtering apparatus or from the target materials.

5.4. Optimisation of UDP HA Thin Films

Many authors have reported differences in composition for HA thin films deposited via RF magnetron sputtering using similar parameters but for different rigs. Therefore, it is essential to optimise thin film deposition parameters for individual apparatus. Three key areas were identified from the literature which contributed to final thin film composition. These were target power supply, target power density and gas composition. A combination of XRD and EDX analysis was performed to assess film crystallography and compositional analysis.

The choice of power supply mode was seen to have an effect on the resultant thin films. The pulsed DC power supply (operated at 6.8 W cm^{-2}) yielded a lower deposition rate of 1.7 nm min^{-1} compared with the RF power supply with a deposition rate of 2.5 nm min^{-1} (operated at 6.8 W cm^{-2}). This factor will have been further affected by the settings of the power supply; however the ionisation of RF plasmas is generally higher than that of DC plasmas [189] as most of the energy input into DC plasmas is lost as heat, thus explaining the higher deposition rate. Moreover, RF power supplies are connected capacitively to the target via a 50 Ω matching unit. This allows automatic micro-adjustments of voltage and current to reduce the reflecting power to a minimum, whereas pulsed DC supplies are not matched [245]. This factor may have further contributed to the increased deposition rate seen for the RF power supply. As-deposited pulsed DC coatings were amorphous showing two distinct humps in the XRD plot (figure 4-11), however, after a heat treatment of 600°C in flowing argon no formation of a crystal structure was observed, yet RF sputtered films did recrystallise at 600°C. Neither of the peaks (figure 4-11) could be associated with an HA type amorphous hump at 27.5° 2θ or any other amorphous like calcium phosphate phase. This can be explained by the use of longer duty cycles and lower frequencies used for pulsed DC power supplies compared with RF leading to lower substrate heating and subsequently higher recrystallisation temperatures. Moreover, in the pulsed DC power supply the power is

averaged over the duty cycle whereas for the RF the power is continuous over the duty cycle. The former allows the coating more time to cool down more between switching to positive and negative bias thus lowering the total residual stress in the pulsed DC films when compared to RF films. A higher residual stress would tend to lower the recrystallisation temperature of the films compared to values of the bulk material. It is therefore expected that the pulsed DC film will recrystallise at a higher temperature than 600°C. The as-deposited RF sputtered coating was also amorphous but formed a single phase HA crystal structure after annealing at 600°C for 2 h in flowing argon (figure 4-12). A preferential orientation was seen along the (002) plane when compared to a randomly orientated powder (figure 4-1). This occurrence has been discussed already in relation to plasma-sprayed coatings (section 5.2.). This may indicate a higher stress within the thin film which was not seen in the pulsed DC thin film, which ultimately aids to lower the recrystallisation temperature of HA thin films.

Increasing target power density from 6.8 to 11.3 W cm^{-2} showed three notable differences in film structure and deposition properties; an increase in deposition rate, an increase in Ca/P, and the formation of a semi-crystalline as-deposited coating. With increasing power density the flux of positive particles colliding with the target will increase thus increasing the sputtering yield Y [189]. Therefore, the probability that a single atom will impinge on the substrate is higher, increasing the deposition rate. It is thought that at increased powers more ions bombard the substrate surface. Moreover, more ions are back-sputtered from the surface and as phosphorus (RAM= 30.97) has a lower atomic mass than calcium (RAM = 40.08) ions it is thought that phosphorus is more easily pumped away leaving a localised calcium rich environment [183]. Freddes *et al*. [208] demonstrated that at low partial pressures negative oxygen particles were responsible for the back-sputtering of phosphorus, which will contribute to the increase in Ca/P ratios. Semi-crystalline as-deposited thin films, in the current study, arose as significant energy is provided by the extra bombardment due to higher power densities and therefore particle kinetic energies to overcome the crystallisation threshold

temperature. Therefore, temperatures approaching the recrystallisation temperature of HA thin films (~ 500°C) could easily be achieved thus causing a semi-crystalline or crystalline as-deposited thin film. Moreover, increased film stress will also act to lower the recrystallisation temperature.

Previous authors have used the inclusion of oxygen into the sputtering environment to aid the production of HA coatings [181, 202]. This resulted in three effects in this study; the Ca/P ratio became lower, the deposition rate was lowered, but a more randomly orientated HA structure was detected by XRD (figures 4-14 and 4-15). The addition of oxygen allows reactive sputtering to occur between phosphorus and oxygen forming heavier phosphate bonds $(PO_4)^{3-}$, reducing the re-sputtering effect and the chance of phosphorus being pumped away, thus improving the stoichiometry of the films [181]. Unfortunately the use of oxygen also lowers the deposition rates. Oxygen is an electron scavenger removing electrons from the system; hence the number of electrons available for ionisation of argon gas is reduced lowering the sputter yield [181]. Lower thicknesses and lower deposition rates led to less preferential orientation and hence an increase in the number of total diffraction planes will be seen. Oxygen aids to fill vacancies that may be in the HA crystal structure not only by the inclusion of P but also O itself. This will give rise to increased reflections present in the XRD plots which are shown in figures 4-14 and 4-15.

5.5. Accurate Measurement of Ca/P ratios for Calcium Phosphate Thin Films

Ca/P ratios for calcium phosphate thin film materials are often calculated without any real consideration for the accuracy of the given technique or quantification parameters used. This means that researchers may be testing materials with uncertain Ca/P ratios. As discussed in section 2.3.2 the Ca/P ratio can lead to altered material properties and cellular response of these types of materials. This study was undertaken to review two commonly, used characterisation techniques in the biomaterials field, XPS and EDX, in conjunction with RBS spectroscopy highlighting key problems and uncertainty associated with recording Ca/P ratios. While all techniques can be highly powerful tools for quantification of many materials they must be chosen appropriately. It has been shown that these three techniques all give notably different values for a given thin film. Considerations should be given to the fact that not all techniques are available in all research institutions.

RBS gave the highest Ca/P ratios for the three thin films followed by EDX, with XPS giving the lowest values. RBS is ideal for the measurement of thin film material composition partly because of its ability to give accurate information about lower layers without removal of surface atoms and partly because it requires no standards for compositional calibration which eliminates a further source of error. Furthermore, all analysis steps are traceable and accountable, which was confirmed by the accurate measurement, within 2 % of a HA powder sample with a known Ca/P ratio of 1.7 (table 4-6). Some problems have previously been associated with the ability of RBS to resolve elements of similar relative atomic masses. Ide-Ektessabi *et al.* [82] detected argon in calcium phosphate films with particle induced X-ray emission (PIXE). RBS cannot discriminate between argon and calcium as they have similar atomic weights, 39.95 and 40.08 amu respectively. However, in this study argon was below the detectable limit of XPS and EDX suggesting the Ca/P ratios required no adjustment. A further limitation of

RBS is the depth resolution which is ~ 750 nm for accurate analysis. Therefore, if the film is inhomogeneous with changes occurring over 750 nm this will not be dectected. For the measurement of thin films this is not a problem as all were measured to have thickness values lower than 750 nm. However, for the P120 HA standard material this may mean that an accurate measurement of the whole sample was not possible casting some uncertainty over the result obtained. In fact this may be why the value obtained for the P120 standard by RBS was not closer to the certified value. This could further be due to the carbon coating added to the P120 HA standard sample for EDX calibration. Some Z dependant absorption of backscattered particles could have occurred though this layer which may have led to some uncertainty.

A small quantity of tungsten (0.1 wt%) was found at the interface of the two UDP calcium phosphate thin films. This is likely to have arisen from impurities in the as received CPTi discs. This is consistent with data published online by Timet [246].

The atomic densities of thin films were calculated using approximate thickness measurements, resulting in the values 11 ± 1, 12 ± 1 and 14 ± 4 (x 10^{23} atoms cm^{-3}) for samples 1 to 3 respectively (table 4-3). All densities were higher than the value of single phase HA which is 9.4 x 10^{23} atoms cm^{-3} [182]. While standard error was accounted for, this approximation was probably too low. Furthermore, samples 1 and 2 showed some compositional differences through the depth of the film. As the density was calculated on the average of these values this may have led to some inaccuracies. In the current study no significant difference was found between the densities of any of the thin films deposited at various parameters. This is consistent with the work of van Dijk *et al*. [182] who found that HA thin films annealed at 550 ºC had densities between 6.2 and 9.0 x 10^{23} atoms cm^{-3} with no relationship was found with density, discharge power or argon partial pressure which is reinforced by this study.

If it is assumed that RBS is the most accurate method for compositional analysis of calcium phosphate thin films, EDX obtains results on average within 10 % of the actual composition when good quality standards are used. However, there were a number of problems associated with EDX when quantifying spectra in the current study. In sample 3, sputtered onto a silicon (100) wafer (section 4.5.), Si Kα lines overlapped with P Kα lines due the deposition of this film onto a silicon substrate, thereby limiting the accuracy that the P content of the film could be calculated, and probably leading to overestimation of this value. This was not a problem with films on titanium substrates as peak overlaps did not occur (section 4.5.). More significant still, material standards used to calculate standard profiles for quantification are often created using materials with very little in common with the analysis material. When GaP and wollastonite standard profiles were used to assess the Ca/P ratio of the P120 HA powder a value of 1.63 ± 0.01 was returned (table 4-6). However, in this study the P120 powder was used to create profiles which were more relevant to the thin films than the GaP and wollastonite standard profiles.

ZAF corrections used in EDX can also induce error, which are also used with the assumption that samples are homogeneous leading to equal matrix effects throughout the depth of the sample. For the thin film deposits this is not the case as the beam will penetrate much further than the film thickness leading to substrate material being analysed. Figure 5-2 shows Monte Carlo simulations using Casino v2.42 for all three samples. For these simulations HA was assumed to be fully dense (3.219 g cm^{-3}). Electron beam voltage was set to 20 KeV with a beam size of 10 μm and 200 electron trajectories were calculated. The energy of the electrons within the sample is represented by colour. The lighter the greyscale the more energy electrons have at that position. It can be seen that the depth penetration of electrons in samples 1 and 2, on titanium substrates, are similar with maximum depth of 2100 nm. This predicts, as indeed the EDX spectra illustrate, that Ti will be present in the spectra (figure 4-16). While the actual part of the spectra that we are interested in is only small, the electrons do not

start spreading laterally until past the depth of the coating. Sample 3, on a silicon substrate, (section 4.5.) shows a much greater penetration depth of approximately 4000 nm. This means the Si Kα signal will be large, further complicating quantification.

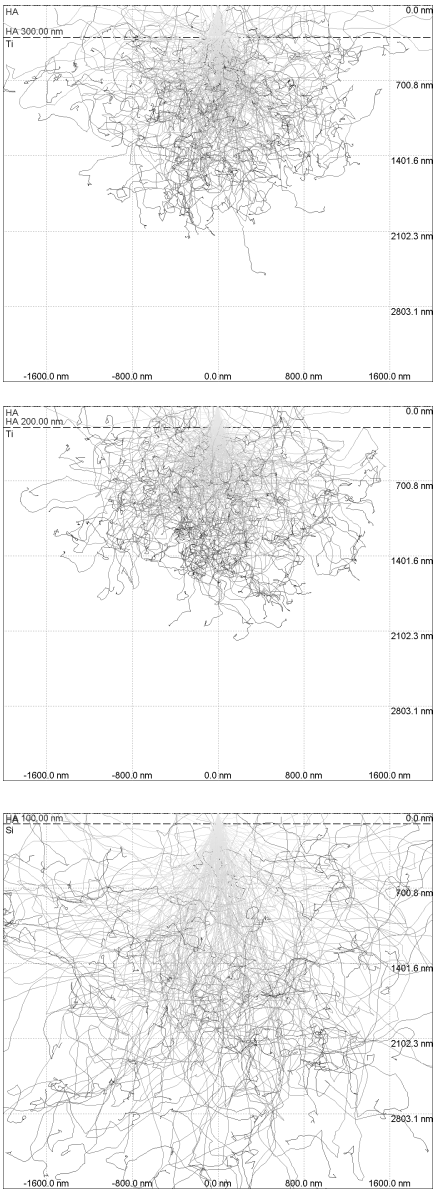

Figure 5-2. Monte Carlo simulations of electron depth penetration for a) Sample 1, b) Sample 2 and c) Sample 3 at 20 KeV with a working distance of 10 mm and an assumed fully dense HA thin film.

The inclusion of substrate material will result in a fluorescence effect which is probably the main contributor to the error when considering the use of EDX with thin films. Briefly, the characteristic X-rays given off from Ti will excite the Ca and P in the coating affecting

quantification [89, 228]. As P is excited at a lower KeV to the Ca it will be excited by Ti and Ca Kα X-rays further increasing the P signal. An overestimation of P will give a lower than expected Ca/P ratios when compared to other techniques. The electron voltage can be lowered to reduce this effect as penetration depth is reduced however counts are lost and standards must be taken at this accelerating voltage for quantitative analysis.

Dedending on the XPS instrument used an accuracy of such measurements were within 25 and 41 % of RBS values for the Kratos and ESCAlab instruments respectively. As XPS, like EDX, uses standards to calculate RSF. Often RSF are created with standards which are not similar to the material that is analysed. In the current study we have used two independent XPS instruments and found that the Kratos instrument obtained values on average 28 % higher than the ESCAlab instrument. It is probable that this is mainly related to RSFs, however, other factors such as count rate and instrument setup can also influence values. This may explain variation of reported Ca/P ratios for calcium phosphate materials of similar manufacturing methods [179, 182, 183]. Argon etching experiments performed on the ESCAlab instrument showed that surface composition of the top few atomic layers varies from the bulk of the coating material. The Ca/P ratio was seen to increase, on average by 44 %, after etching. However, this may not be a real observation as preferential etching of P atoms from the surface may occur which would increase the Ca/P ratio. However, the same experiment was carried out on the P120 HA powder. No significant difference was found between the Ca/P ratio before or after etching (table 4-6). This suggests that etching at 4 KeV for 10 min with argon does not lead to significant preferential sputtering, and that RF magnetron sputtered calcium phosphate thin films have an increased concentration of P present at the surface compared with the bulk of the thin film. In fact this has been suggested for other calcium phosphate materials [247]. Interestingly, however the Ca/P ratios obtained for the etched films was still lower than both the EDX and the RBS results, which can again be attributable to the geometry adjusted Schofield RSFs used for the ESCAlab instrument used to quantify obtained spectra.

Figure 5-3 shows a model illustrating the penetration depth of XPS, EDX and RBS. It can be seen that each technique analyses to different depths which can lead to different results than expected without consideration to designing an experiment to best measure the compositional values at a particular area within the material.

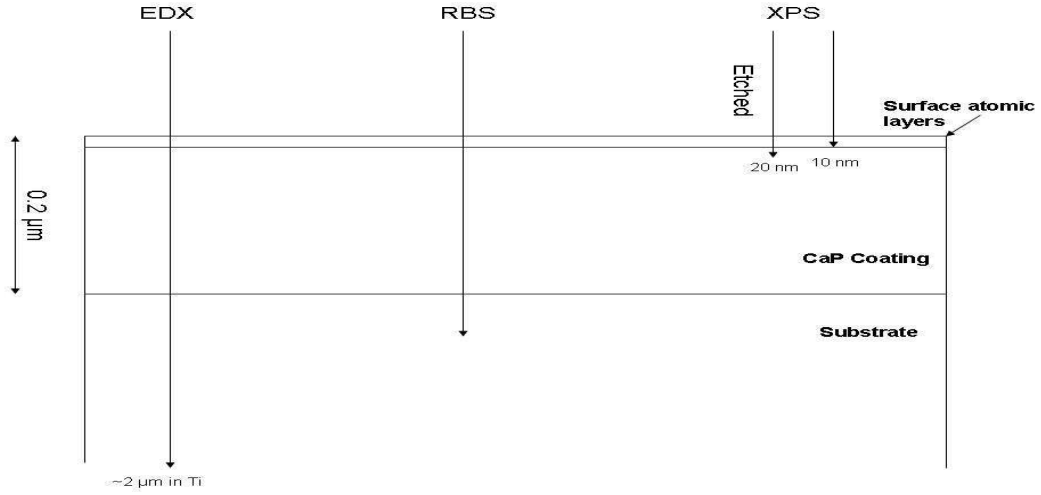

Figure 5-3. Schematic model showing a 200 nm thick calcium phosphate thin film on an undefined substrate. Analysis depths for XPS, RBS and EDX are shown.

Regardless of the accuracy of all the techniques, they are still extremely useful at showing general trends and this is obviously the intention of many researchers when using them. Similarly in this study trends have been observed between coatings with all or most techniques being in agreement. Surfaces are often very different from the bulk of the material.

The addition of oxygen to the sputtering environment has been shown to be beneficial in lowering the Ca/P ratio of coatings. The idea was first carried out by van Dijk *et al.* [181] showing Ca/P ratios declined with increasing oxygen addition to a value of about 10 vol.% oxygen. Increased oxygen levels allows P to bind more easily in the form of PO_4 groups at the substrate surface lowering the chance of P being backsputtered or pumped away. A drop of 0.2 with RBS and EDX (0.1 units with XPS) in the Ca/P ratio was also observed in sample 1 compared to sample 2 (table 4-6). Although reducing the Ca/P

ratio, the use of oxygen lowered the deposition rate. In this instance the deposition rate dropped from 2.5 to 1.1 nm min^{-1} for sample 1 and 2 respectively (table 4-2). This is because oxygen acts to reduce the discharge current lowering the number of ions bombarding the target and therefore lowering the deposition rate [181]. The addition of oxygen did not alter the binding energies of the P 2p peaks or alter peak shape, indicating oxygen had no effect on the type of phosphate in the coating.

Increasing power density, as in samples 1 and 3, has been shown in the literature to increase the Ca/P ratio [183]. However, in the current study sample 3 had a lower Ca/P ratio than sample 1. Samples 1 and 3 are 300 and 100 nm thick respectively (table 4-2) due to sputtering time, and it has been shown that thicker coatings give higher Ca/P ratios. Since the mass of calcium is greater than argon or phosphorus higher quantities will be implanted into the substrate surface. Furthermore as the calcium particle arrives at the surface it will sputter phosphorus away from the substrate thus increasing the Ca/P ratio. Over longer time periods increasingly more calcium will be present at substrate surface than phosphorus thus increasing the Ca/P ratio [182].

Chusuei *et al*. [231] observed a change in surface composition when exposing a calcium phosphate powder to X-rays in an XPS system for 1 h suggesting that Ca was ejected lowering the Ca/P ratio. However, the present study demonstrated that no change in composition was measured even after 3.5 h exposure time when a Kratos instrument was operated at 10 KeV with a Al Kα (1486.6 eV) anode (figure 4-20). Chusuei *et al*. used a Mg Kα (1253.6 eV) anode operated at 12 KeV. The use of a higher energy may explain why they observed detrimental effects to their samples, but without more information this is difficult to conclude this hypothesis.

5.6. Characterisation of UDP HA and SiHA Thin Films

This section aims to interpret results obtained from the characterisation of HA and SiHA thin films sputtered onto CPTi discs and silicon (100) wafers (section 4.6.). This information helps in understanding the osteoblast response to the thin films associated with each composition or heat treatment.

5.6.1. Chemical and Compositional Analysis

Cells respond to chemical and topographical stimuli. Both of these factors are material dependant, however it is important to investigate both parameters fully in order to understand why cells react the way they do to a particular surface. For SiHA materials it has been shown that the silicon structural configuration is important when trying to enhance osteoblast response [135]. Silicate in the form of SiO_4^{4-} is considered to be soluble whereas silica (SiO_2) is insoluble in water. Balas *et al*. [135] found that substituted silicate (soluble) generated a more favorable cellular response than un-substituted insoluble silica. This increased solubility may invoke a more desirable cellular response than silica configurations. Silicon configurations were identified in SiHA thin films using high resolution XPS spectroscopy of the Si 2p peak (figures 4-37 and 4-39). The current study found that in as-deposited coatings the binding energy of the Si 2p peak was related to surface silicon content (table 4-10); increasing in binding energy with increasing silicon content. Okada *et al*. [248] looked at silicon chemical shifts in XPS of different silicon containing apatites, finding that with increasing silicon content an increasing XPS binding energy was observed. If fewer silicon atoms are present on the surface it is more probable that surface silicon will bond to oxygen. As the silicon concentration increases silicon will begin to bond using fewer bridging oxygen atoms. Stevenson *et al*. [249] also found that increased surface silicon led to increasing XPS binding energies, however they studied silicon concentrations of 2.2 – 22.0 at.% for oxide-silicate-silica layers on titanium substrates thus only observing the linear proportion of this trend. Their findings are shown graphically in figure 5-4 with relation to

Si 2p binding energies and kinetic energies and related compounds, this effect also occurs in natural silicon containing compounds.

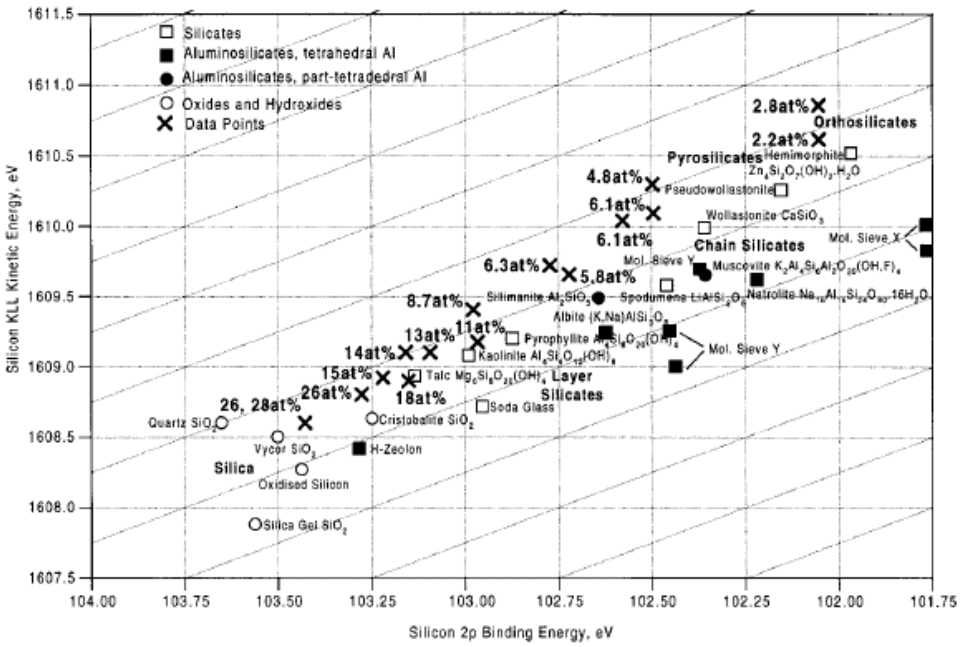

Figure 5-4. Silicon chemical state plot showing XPS binding and kinetic energies of structures with varying surface silicon concentrations. Taken from [249].

An increase in binding energy signifies a chemical change in Si-O bonding from a polymeric SiO_2 structure to a monomeric SiO_4 structure. This can be denoted in terms Q^n where n represents the number of bridging oxygen atoms per SiO_4 tetrahedron. Figure 5-5 shows three dimensional ball and stick diagrams for these different configurations, where a Q^0 structure is shown in figure 5-5a and a Q^4 structure is shown in figure 5-5b.

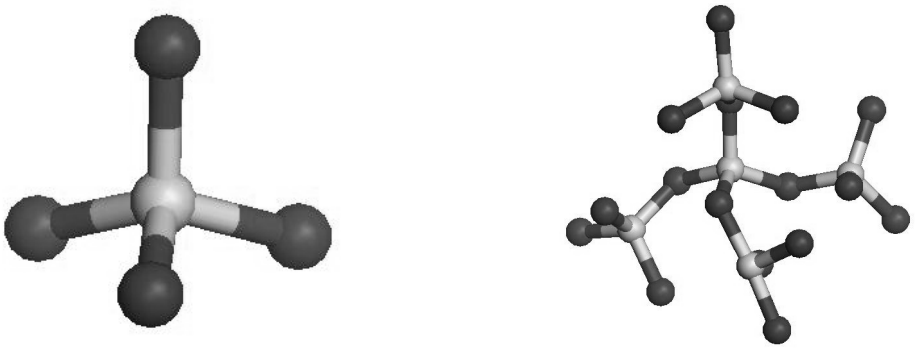

a **b**

Figure 5-5. Ball and stick diagrams of silica tetrahedral with an a) Q^0, SiO_4^{4-} and b) Q^4, $(SiO_2)_n$ configurations. Black – Oxygen, Grey - Silicon.

Post-annealing at both the 600 and 700°C all SiHA samples exhibited binding energies of approximately 101.5 eV (table 4-10), suggesting silicon had adopted a Q^0 structure. Two independent studies [135, 136] have demonstrated that in bulk 0.8 wt.% silicon substituted HA the Si 2p peak had a binding energy of 101.5 and therefore a Q^0 configuration. It was concluded that SiO_4^{4-} had successfully substituted for PO_4^{3-} groups. However, Balas *et al.* [135] demonstrated that this effect only occurred up to 1.6 wt.% silicon addition in bulk materials, above which, it reverted back to a Q^4 configuration with a binding energy of 103 eV. This may be explained as Balas *et al.* used a controlled crystallisation method opposed to that proposed by Gibson *et al.* [126] which has proved to be a very successful method of producing SiHA powders. In the current study however, up to 13.4 wt.% (EDX/bulk)/ 6 at.% (XPS/surface) (tables 4-7 and 4-10 respectively) was successfully substituted into the HA films allowing the production of a 'super-saturation' state as suggested by the Q^0 structure of silicon. This could lead to further enhancement of the bioactive nature of HA materials. Theoretically, in equilibrium systems such as bulk SiHA, a value of 5 wt.% SiO_4^{4-} ions can be substituted for PO_4^{-3} tetrahedra [250]. However, in the case of an RF magnetron sputtered system a metastable material system has been created and regenerated from an amorphous state and therefore more silicon can be potentially substituted into the structure. While this is the first instance that super-saturation has been shown in SiHA materials, metastable

thin film systems are well documented within the field of superconducting films [251-253]. An example of super-saturation in sputtered coatings is MgB_2 superconducting films [251]. Furthermore, Ma [254] has discussed in detail many other immiscible element systems with a large range of applications. Other methods to manufacture super-saturated systems include ball milling and rapid solidification processes. Figure 5-6 shows a schematic for the equilibrium phase boundary for different materials processing methods illustrating how sputtering can allow for the creation of metastable systems.

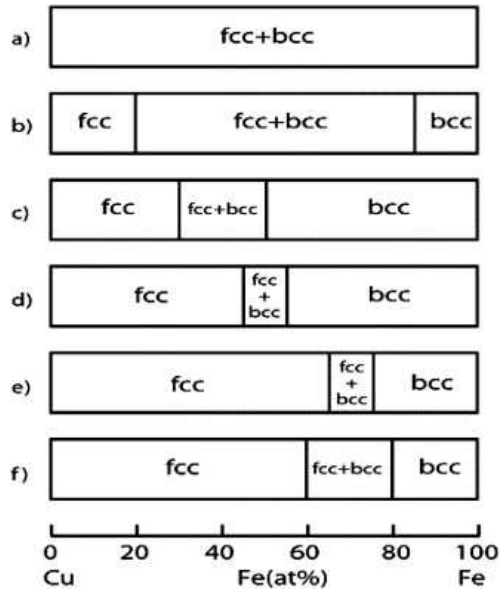

Figure 5-6. Schematic diagram (a) the equilibrium phase boundary at room temperature. Included for comparison are the phase boundaries obtained by (b) liquid quenching, (c) thermal evaporation, (d) sputtering, (e) sputtering on cryogenic substrates, and (f) mechanical alloying for a Cu-Fe alloy system. Taken from [254].

The position of the silicate tetrahedra may occupy PO_4^{3-} vacancies however without further proof this cannot be assumed and it may be that SiO_4^{4-} occupies other sites such as in $Ca_5(PO_4)_4(SiO_4)_2$ (ICDD card 40-393) which could be possible as no OH groups are seen in SiHA samples from FTIR analysis. However, the above phase would be detected in the XRD and FTIR data, but this was not the case, giving further evidence of a silicate substituted hydroxyapatite structure. While the position and configuration of silicon within the HA structure is important in relation to cellular response other compositional

values should also be accounted for such as the Ca/P ratio. This has already been discussed in detail in section 5.5., however this was not with respect to SiHA thin films.

Compositional analysis of RF magnetron sputtered coatings can often lead to differences compared to stoichiometric bulk HA materials, due to the complexity of the physics involved during the deposition process. EDX was used to calculate the Ca/P ratio and silicon content of films. The Ca/P ratio of HA and SiHA thin films varied from 1.68 – 1.80 as seen in table 4-6. No batch run was significantly different from any other, however all runs were higher than the stoichiometric value of 1.67 for HA (table 4-7). Long *et al*. [255] carried out spectroscopy on HA containing plasmas finding the predominant species was CaO. This equally would give rise to a higher than expected Ca/P ratio. Boyd *et al*. [179] investigated the effect of target Ca/P on resultant films concluding that the Ca/P ratio of films was independent of target starting Ca/P ratio and so sputtering parameters, such as power density will have more effect on this value. The HA target, in the current study, was run at set run parameters for each coating type and therefore no significant changes in the amount of calcium or phosphorus was expected (table 3-1). When batch data was combined into HA and SiHA groups it was seen that with increasing silicon content the standard error of the mean for the Ca/P ratio increased from 0.01 to 0.06 (table 4-7). This is because with increasing silicon content the Si Kα will impinge on the P Kα peak thus making quantification harder to be accurately achieve. Moreover, calculation of the silicon content will be more uncertain with increasing silicon content potentially explaining why the reproducibility of silicon content in HA coatings was poor. Other factors which may lead to this is silicon contamination in the SEM/EDX chamber giving variable silicon content or the possibility that the silicon content of individual discs altered and as only n = 4 this may have been too low for accurate silicon content analysis.

Ca/P ratios obtained from XPS data for as-deposited thin films were all lower than EDX values. This topic is discussed in detail in section 5.5 but briefly is likely to be due to an

increase in phosphate groups preferentially residing at the surface of the thin films [247]. The Ca/P ratios of the as-deposited samples decreased with increasing silicon from 1.43 to 1.03 (table 4-9). It may be hypothesised that the sputtering environment allows the formation of a [P-Si-O] species or unit-containing molecule. This is a likely scenario as a large number of Ca-P, Ca-O and P-O like species have been found in HA plasmas [255]. It has already been shown that oxygen can increase the amount of P reaching the substrate surface as this allows the creation of a heavier molecule than P, making it easier to bind to the surface of the film [181, 202]. Therefore, in a similar mechanism, the binding of silicon to this phosphate group increases the atomic weight further, and so increases the sputtering potential leading to more P reaching the surface. As more silicon is made available due to increasing bias on the silicon target more P-Si-O groups may form, hence an increasing amount of these groups can reach the surface, thus lowering the Ca/P ratio. EDX data showed the Ca/P ratios for HA and SiHA thin films, when increasing the silicon content, were not significantly different (table 4-7). This may be because firstly, EDX is not an accurate enough technique to spot such small Ca/P differences and secondly, as has already been discussed Ca/P ratio uncertainty increases with increasing silicon content as silicon and phosphorus peaks are in close proximity making deconvolution more erroneous (section 5.5). It was seen that on annealing the Ca/P ratio increased due to a loss of phosphorus (table 4-9). Lo *et al.* [195] and Boyd *et al*. [256] have both observed this. It has been documented that evaporation of volatile phosphorus products during annealing occurs [179, 195, 256]. As increasing silicate groups substitute into the HA lattice, phosphate tetrahedra will be either partially bound or free in the structure. However, if phosphate bonds have been expelled from the HA lattice, less energy will be required for their removal from the surface. This is supported by the fact that at a given annealing temperature it was seen that silicon content had a direct effect on the Ca/P ratio (table 4-9).

Undoped HA surfaces were shown to have a small quantity of surface silicon (table 4-9). This amount remained approximately constant throughout the as-deposited and annealed

samples. This is likely to be due to residual silicon present in the XPS chamber associated with hydrocarbon contamination or XPS analysis of silicon containing samples. F contamination was also seen to be present on the sample due to the use of the XPS instrument for F containing materials (section 4.6.8.). Such contaminants may increase the uncertainty in quantitative calculation of Si 2p contents. There was no significant difference between the silicon content in as-deposited SiHA thin films and films annealed at 600°C (table 4-9). Post deposition annealing at 700°C resulted in almost no notable surface silicon for the samples (table 4-9). Two possible scenarios could account for this; either in a similar mechanism to the phosphate groups silicate groups were evaporated, or silicon has diffused away from the surface. Currently not enough data are available to support either mechanism, although as silicon oxides are generally fairly stable compounds it is more likely that silicon diffused to lower layers of the samples.

HA and SiHA thin films annealed at 700°C showed the presence of a small amount of titanium at the surface of thin films (0.3 - 5.0 at.%) as detected by XPS surface analysis (table 4-9). A significant increase in titanium was seen at the surface of SiHA1 samples (table 4-9, figures 4-34b and 4-35). This is likely to be due to two reasons; with increasing silicon content the coatings will become thicker. The HA film was seen by TEM and a ball crater technique to have a film thickness of 185 ± 4 nm (figure 4-21a and table 3-1). This increased up to a thickness of 216 ± 5 nm for the SiHA3 thin films (figure 4-21b). This increase in thickness will have had a dramatic effect on the amount of titanium that appeared at the surface. However, HA and SiHA1 have similar thicknesses but more titanium was present at the surface of the SiHA1 samples (table 4-9). This is because of the smaller crystallite size allowing a larger number of grain boundaries and crystal lattice defects which will act as diffusion paths thus allowing titanium an easier diffusion passage [257].

FTIR analysis of as-deposited thin films showed the appearance of PO_4 bonding in all films (figure 4-24). Previous FTIR work has shown the presence of Si-O bonds in silicon containing HA coatings and bulk materials [126, 219]. However, it is argued that in this study due to the low thickness (ca. 200 nm) of the films and the use of glancing angle mode only a low signal was achieved and so no Si-O bonds were observed. With increasing silicon content the PO_4 bands widened (figure 4-24). This suggests that bond formation is inhibited by the addition of silicon. After annealing at 600°C all samples showed phosphate bands which have sharpened compared to the as-deposited samples, however with increasing silicon the bands broadened (figure 4-25). The HA sample showed OH^- bonding, which disappeared in the SiHA samples (figure 4-25). When SiO_4^{4-} species are substituted for PO_4^{3-} bonds a charge imbalance of -1 is created. The most energetically favorable method of reducing this effect is to reduce the number of OH groups associated with the molecule [126]. The numbers of substitutions will be inversely proportional to the number of OH groups. XPS had shown films to be in a super-saturated state (section 4.6.8.) which may explain why no OH^- was seen, opposed to just a reduction in OH peak intensity. This effect has also been shown in other apatite systems [258]. A small broad peak at 820 cm^{-1} wavenumber, was seen on the SiHA1 and the SiHA2 samples (figure 4-25). Ong *et al*. [178] identified a broad peak at the same wavenumber for calcium phosphate coatings on titanium substrates. In the aforementioned study a fluoroapatite target was used for the production of films and an annealing temperature of 600°C in air. It was suggested that this band was due to P-F stretching indicating a phosphorofluoridate phase. In the current study HA targets were used and therefore this is unlikely be the case. More recently, Boyd *et al*. [256] investigated HA/TiO_2 RF magnetron sputtered hybrid coatings observing a peak at approximately 820 cm^{-1} and linking it to a rutile structure. Interestingly, rutile was not seen on the HA or the SiHA3 samples annealed at 600°C. It was most abundant on the SiHA1 samples with a small quantity observed on the SiHA2 samples (figure 4-25). As thin films were annealed in an inert environment it is suggested that the only available oxygen resource for the formation of the rutile phase was from the HA coatings.

Moreover, we can see from table 5-1 that oxygen associated with calcium bonds requires the least amount of energy to disassociate and the formation of the rutile phase is energetically viable.

Molecule	Dissociation Energy / KJ mol^{-1}
Si-O	799.6 ± 13.4
Ti-O	688
Ca-O	383.3 ± 5.0
P-O	599.1 ± 12.6

Compound	$\Delta_f G$ / kJ mol^{-1}
TiO_2	-888.8
SiO_2	-856.3
CaO	-603.3
$Ca_3O_8P_2$	-3884.7
PO	-51.9[a]
SiO	-126.4[a]

Table 5-1. Bond strength dissociation energies and Gibbs free energies at room temperature and atmospheric pressure of formation for components at the HA/Ti interface. Values compiled from [259]. [a] figures quoted in gaseous form due to solid state information being unavailable.

It is well known that silicon inhibits HA crystallite growth [141]. In the HA samples the crystallite size was calculated to be approximately 80 nm (table 4-8). This became smaller with increased silicon content. If titanium diffuses into the HA films then it takes the easiest pathway which will be the grain boundaries, reacting with oxygen along the way. Therefore, higher silicon containing films will allow an easier diffusion path than undoped HA thin film samples. Another potential mechanism can be proposed; in a less crystalline structure loosely bound oxygen (confirmed by FTIR PO_4 peak broadening with increasing silicon content) will be more readily available to react with titanium atoms. Furthermore, Li *et al*. [260] showed that the diffusion of Ca, P and O into titanium occurs more easily than titanium into HA, which supports the dynamic nature of the system at elevated temperatures. Therefore, in the more crystalline HA structure diffusion at the HA/Ti interface will be lower than diffusion at the SiHA/Ti interface. However, it is also

known that silicon species can strongly inhibit rutile formation [261], hence reducing rutile in the SiHA2 samples (figure 4-25) and totally inhibiting its presence in the SiHA3 sample (figure 4-26). After annealing at 700°C the PO_4 bands sharpened and peak intensity increased, indicating a further increase in phosphate bonding (figure 4-26). More OH bonding was seen on the HA compared to the HA film annealed at 600°C but again OH was not seen on the SiHA films (figures 4-25 and 4-26). Rutile was seen in all samples except SiHA3 (figure 4-26). No data are available for the diffusion of titanium into HA. Therefore, attentions have been turned to a simplified model of titanium in titanium.

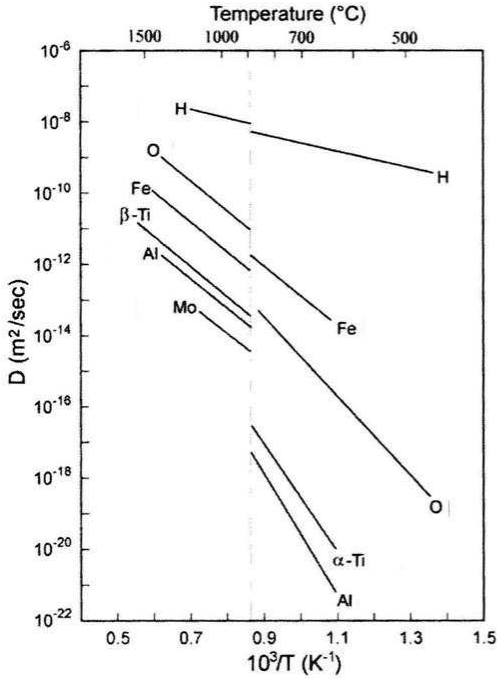

Figure 5-7. Diffusion data for common elements through titanium at elevated temperatures. Taken from [262].

Figure 5-7 shows diffusion data for elements through titanium phases. From this figure it can be calculated that at 700°C titanium diffuses a distance of 85 nm in 2 h compared to negligible diffusion at 600°C. This distance is likely to be greater in HA due to a lower density, difference in structure and vacancies present. Moreover, the XPS data shows

titanium present on the surface of SiHA1 films annealed at 700°C indicating a diffusion distance of at least 200 nm (table 4-9).

5.6.2. Wettability and Surface Energy

Contact angle measurements can give an idea of how cells will interact with a surface in the initial attachment stages. Wettabilty testing showed that the incorporation of silicon into the HA lattice led to a more hydrophilic surface (figure 4-41). Furthermore, Samples became more hydrophilic with increasing silicon content. This validates the work of other authors who also found the inclusion of silicon lowers the contact angle. Vandiver *et al*. [263] and Botelho *et al*. [136] showed that SiHA has a more negative surface charge and increased surface adhesion than HA. Thian *et al*. [221] compared HA and 0.8 wt.% SiHA surfaces measuring contact angles of 47.6 and 29.5 ° respectively for films annealed at 600°C in flowing moist argon for 3 h. In the current study a higher contact angle was measured for HA annealed at 600°C (figure 4-41) which may be due to slightly different sputtering parameters and the post deposition annealing method resulting in a different surface chemistry. For example the use of moist argon may lead to a larger number of surface OH groups resulting in a more negatively charged surface and so a lower contact angle. Takeda and Fukawa [264] found OH^- groups were a major factor governing surface chemical properties of oxide thin films. Higher contact angles were obtained for as-deposited samples than samples annealed at 600°C (figure 4-41). When the samples were annealed residual stresses can be reduced thus lowering the total surface energy. This can be confirmed by the fact that only a small difference was seen between the measured contact angles of as-deposited and 600°C SiHA3 samples as this sample did not recrystallise at this temperature (figure 4-41). Moreover, the switch from a Q^4 silicon configuration to a Q^0 configuration, as shown by a lowering in binding energy from 103 to 101.5 eV measured by XPS analysis (table 4-10), may be partly responsible for this trait, however, this argument cannot be used for the HA samples. After annealing at 700°C contact angles were higher than both the as-deposited and 600°C samples for all films

(figure 4-41). This is likely to be due to the appearance of titanium and rutile phases at the surface of these samples. In fact it has been shown that titanium has a higher contact angle than HA surfaces [265].

5.6.3. Crystallography

Cellular response can be affected by sample crystallinity [2]. XRD and RHEED were used to investigate the crystallinity of HA and SiHA thin films (sections 4.6.6. and 4.6.7.). As-deposited HA and SiHA thin films were shown to be amorphous. Post-annealing, all samples except the SiHA3 samples recrystallised showing a single phase HA structure (figures 4-27, 4-28, 4-30, 4-31, 4-33 and 4-34). The SiHA3 samples were shown to recrystallise after post-deposition heat treatments of 800°C on silicon (100) wafers showing a single phase HA structure (figure 4-29). Gibson *et al*. [126] and others have shown that introducing silicon into HA lowers the thermal stability. It has commonly been shown that silicon additions of 5 wt.% or more causes HA, on sintering, to decompose into undesirable phases like CaO and α- or β-TCP. However, no secondary phases were found in any of the films at any annealing temperature. This evidence, in conjunction with the XPS data (section 4.6.8.), further suggests that higher amount of silicon may be substituted in the HA thin film structure than previously reported elsewhere.

Problems were encountered with preliminary RHEED experiments (section 4.6.7.). Substrate electron beam damage occurred reducing the quality of images. This was due to charging of the HA thin films and it was found plasma cleaning further worsened this effect, as the adventitious carbon layer was present on the surfaces acts to carry negative charge build up away from the surface.

Crystallinity decreased with increasing silicon content (sections 4.6.6. and 4.6.7.). This was observed by Zou *et al*. [137] who found the introduction of silicon reduced crystallinity but thereafter no change was found at different silicon concentrations.

However, in this study silicon contents from 1.8 - 13.4 wt.% were investigated, whereas Zou *et al.* [137] only investigated from 0.8 - 2.0 wt.%, which may explain this discrepancy. Interestingly this was seen more clearly with films deposited onto the CPTi substrates but not on the (100) silicon wafers (figures 4-27, 4-28, 4-30 and 4-31). It is known that a thermal expansion coefficient mismatch leads to residual stresses which can aid recrystallisation. Unfortunately this does not explain the difference in crystal growth on the CPTi and silicon (100) wafers as HA has a thermal expansion coefficient of 14 μm m^{-1} K^{-1}, titanium 8.6 μm m^{-1} K^{-1} and silicon 2.5 μm m^{-1} K^{-1}. These figures suggest that the opposite trend should be observed. It is therefore more likely that crystallite grow is due to the grains present in the CPTi allowing recrystallisation nucleation points whereas the silicon (100) wafers are single crystals with far less nucleation points. In this study we measured crystallite size along the <001> (table 4-8). Some confusion has been associated with choosing the correct diffraction planes to calculate particle size. It is most common to measure the <001> direction but other authors have measured the <111> direction with the (211) plane - due to it being the most intense direction line in bulk HA powders in accordance to ICDD card 09-432. In this study it was found that the (002) plane was most affected by the addition of silicon on CPTi substrates (figures 4-27 and 4-28) whereas the (211), (112) and the (300) planes were more affected on the silicon (100) wafers (figures 4-30 and 4-31). However, if we calculated the particle size using the (211), (112) and the (300) reflections they cannot be compared to each other or <001> reflections because HA crystallites are not spherical and each reflection is attributable to a different direction within the crystal.

After annealing at 700°C the SiHA1 samples showed rutile diffraction patterns (figure 4-35). This was confirmed by the XPS data (figure 4-40). Titanium was only present at 0.3 at.% at the surface of all other films annealed at this temperature and therefore was not detected by RHEED. Moreover, the XPS data for the O 1s peaks did not reveal a rutile component at 529.6 eV. The RHEED data presented for the SiHA3 samples annealed at 700°C showed diffraction rings suggesting this sample was crystalline whereas the XRD

data for SiHA3 films on both silicon (100) wafers and CPTi samples showed this film to be amorphous. XPS analysis showed that only a small amount silicon (0.5 at.%) was present at the surface of the SiHA3 films after annealing at this temperature and therefore HA crystallisation could not be inhibited, allowing some crystal growth preferentially at the surface of the SiHA3 film.

5.6.4. Topography

A combination of SEM and stylus profilometry showed the effects of silicon content and annealing temperature on HA thin films (figures 4-22 and 4-33 respectively). Films were smooth flat and followed the topography of the CPTi substrates. This agrees with current literature which has also shown that substrate pits and defects can also be filled in by sputtered films. Boyd *et al*. [180] prepared a titanium surface with a P1200 SiC grit which had a roughness of 83 ± 1 nm. After sputtering HA onto the surface the roughness decreased to 33 ± 0.7 nm (figure 4-23). The as-deposited films in the current study were of comparable roughness to that of Boyd *et al*. [180] even with different starting substrate roughnesses. Silicon content had no effect on the as-deposited film roughness but an increase in roughness was seen after annealing in flowing argon at 600°C on all but sample SiHA3, which remained at approximately the same value as the as-deposited samples (figure 4-23). At higher annealing temperatures of 700°C roughness increased dramatically on all samples typically doubling in R_a value (figure 4-23). As crystals grow an increase in surface roughnesses will be observed. Furthermore, the higher the recrystallisation temperature the larger the crystallite size and in turn the more textured the surface. In addition silicon inclusion has been shown by a number of authors to inhibit the crystallite growth of HA in both bulk and coatings [126]. Therefore, roughness increases by a smaller amount for each increase in silicon addition to the point where the 13.4 wt.% SiHA shows no change in surface roughness. At the annealing temperature of 700°C FTIR data showed rutile was present in all samples. This grain growth would lead to an increase in roughness when compared to the films annealed at 600°C (figure 4-

23). As previously discussed silicon inhibits rutile growth and this will lead to a decrease in roughness. The 13.4 wt.% sample annealed at 700°C showed almost no increase in roughness which consistent with this hypothesis because this film had not recrystallised.

5.6.5. Dissolution Properties

Many authors argue that the success of SiHA materials is related to an increased solubility potential [141, 219]. This was found to greatly affect cellular response in the current study. Dissolution properties of HA and SiHA thin films annealed at 600°C were investigated by a qualitative EDX method to give an idea of how stable films were in cell culture conditions (figure 4-42). This study, while only being qualitative, clearly illustrates the effect of cell culture conditions on HA and SiHA thin films. Film solubility was proportional to silicon content with SiHA1, SiHA2 and SiHA3 retaining 55, 20 and 10 at.% respectively of the Ca present in the as received films (figure 4-42). Interestingly, even the HA sample showed a small amount of dissolution in the 14 day time period retaining approximately 80 % of the original film (figure 4-42). Boyd *et al*. [180] found that HA thin films slightly dissolved after 1 h in solution but did remain stable over the course of 30 days. This was quantified by changes in roughness as measured by AFM. After 1 h the films increased in roughness from 33 ± 0.7 to 42 ± 1.1 nm. After 30 days this increased to 48 ± 1.9 nm, suggesting initial surface dissolution of the film was at a faster rate than when the film had been immersed for 30 days. Thian *et al*. [222] measured Ca, P and Si ion content in parts per million (ppm) in SBF over a 30 day period for a 0.8 wt.% SiHA film. It was found that the quantity of ions was highest at days 1-5 and decreased thereafter. He investigated formation of an apatite layer on the surface of such films suggesting that the silicon aided dissolution of the coating and furthermore the silicate ions acted as nucleation points of the new apatite layer.

5.6.6. Mechanical Properties

RF magnetron sputtering is an attractive coating method because the resultant films are well adhered, dense, void free films [86]. However, in the case of HA and SiHA films only a few studies have investigated properties such as hardness and adhesion, probably because of the low thicknesses making testing difficult without the aid of a nanotesting unit. It was found that hardness testing on CPTi substrates was inaccurate as stress fields spread into the substrate lowering hardness values. In this study, we obtained hardness values by using silicon (100) wafers, measuring an average hardness of 5.7 GPa and 6.3 GPa was obtained for all as-deposited and annealed films respectively using a 0.3 mN load (figure 4-44). Average reduced moduli for HA and SiHA were measured at 113 and 110 GPa for the heat treated and as-deposited films (figure 4-45). Saha *et al*. [266] also found that substrate has a large impact in nano-hardness testing, concluding underlying substrates harder than thin films gave more accurate results than hard films on soft substrates. No significant difference was found between either the HA or the SiHA compositions suggesting the inclusion of silicon into the HA lattice has no effect on hardness. Neih *et al*. [205, 267] looked at as-deposited RF magnetron sputtered HA thin films finding a hardness of 7.8 GPa and a modulus of 120 GPa which is higher than the results in the current study, although not notably different. Fully dense HA sintered at 1300°C to have a hardness of 6.5 GPa [267] which suggests HA and SiHA films are also approaching full density here which can be supported by the densities calculated by the RBS data (table 4-3). Nelea *et al.* [165] obtained hardness values lower than both Neih *et al.* [205, 267] and the current author in the range of 4.5 - 5.2 GPa, however, Nelea *et al.* [165] measured a modulus of 150 GPa. This may be explained by the use of a very low sputtering power density (0.8 W cm^{-2}), employed to reduce target cracking, which would result in lower density films. Chen *et al*. [265] found silver containing HA thin film to have hardnesses between 6.5-7.0 GPa and a modulus of 125 GPa for as-deposited films with a thickness of 4 μm. This supports the current study's results in terms of lower doping values, illustrating the addition of small quantities of dopants have no enhancing or detrimental effect on hardness or modulus. Elsewhere, Liu *et al*. [268] obtained similar

hardness values (6-9 GPa) when looking at biomimetic calcium phosphate coatings on titanium, but moduli were not recorded. In comparison to nano-testing work carried out by Rho *et al*. [40, 269] on bone, and RF magnetron sputtered thin films well exceed the hardness and modulus values of bone which are in the region of 0.52 - 0.74 GPa and 15 - 25.7 GPa respectively. This is due to the high density of RF magnetron sputtered films, whereas bone varies and is generally more porous.

The current study did not manage to obtain an adhesion value for HA and SiHA thin films on CPTi substrates. However, it was concluded that thin film fracture would occur at > 350 mN load (section 4.6.11.). Nevertheless, it has been proved that RF magnetron sputtered thin films are well adhered in comparison to other commonly used techniques such as plasma spray [185]. Equally, other studies have not found a definite failure point for RF magnetron sputtered coatings on titanium. Neih *et al*. [267] simply concluded HA films on titanium substrates exhibited good adhesion whereas HA films on silicon wafers did not. Microstructural and EDX chemical analysis was performed across the surface interface revealing Ti and TiO_2 in the HA coatings caused by diffusion bonding, whereas this did not occur with the HA on silicon substrate hence the poor bonding ability.

5.7. *In Vitro* Cytocompatability

Characterisation has shown that both silicon content and post-deposition annealing significantly changed the surface chemistry and crystallinity of HA and SiHA thin films (section 4.6.). Initial cell adhesion studies carried out on as-deposited and HA thin films annealed at 600°C demonstrated cells preferentially adhered to HA surfaces, with poor adhesion on all SiHA surfaces, with the exception of the SiHA3 as-deposited samples, which showed no significant difference in adhesion when compared to the as-deposited and annealed HA thin films (figure 4-55). Furthermore, the 14 day Alamarblue™, DNA and ALP assays using HA and SiHA samples annealed at 600°C provided further evidence that HOB cells preferred HA to the SiHA surfaces (figures 4-56, 4-58 and 4-60). Osteoblasts on HA surfaces showed increased proliferation but also showed evidence of osteoblast maturation, indicated by the activity of alkaline phosphatase. This effect was not seen on any of the SiHA surfaces after 14 days. This result was considered surprising as a large amount of literature has been published demonstrating SiHA ceramics led to increased proliferation and differentiating activity of osteoblast cells with both bulk and coating materials *in vitro* and *in vivo*. Elution DNA and Alamarblue™ assays ruled out that the samples had any negative cytotoxic effect on cells (figures 4-52 and 4-53), moreover, studies have shown that increased quantities of silicon (0.1–0.2 mg ml^{-1}) in cell media can lead to the up-regulation of genes that aid cell proliferation and differentiation over a period of 48 h [119, 122], however, effects on cell morphology or growth were not measured, and therefore cannot be compared to the current study. It is likely no enhancing effects were seen in our elution study because the test only exposed osteoblasts to media for a period of 24 h and protein expression was not investigated. Furthermore, it is hypothesised the quantity of silicon present in the media from the SiHA discs did not even exceed 0.5 mg ml^{-1} as no measurement was taken. While no figure has been suggested for the minimum amount of silicon needed to have an affect on bone cells, *in vivo* a minimum of 2-20 mg ml^{-1} is required for normal growth [99, 101].

The stability of SiHA thin films in culture media must be considered to be responsible for the poor adhesion and therefore the low proliferation of HOB cells on SiHA films compared with HA films. Qualitative EDX carried out on films annealed at 600°C (figure 4-42) showed that the SiHA thin films dissolved at rates dependant on silicon content and XPS of samples used for the elution test study confirmed that after 48 h in media the titanium substrate was observed at the surface of the SiHA3 samples annealed at 600°C for 2 h. While not quantitative data, this indicated that SiHA surface annealed at 600°C are unstable; dissolving in cell culture media within hours for the highest doped sample. Cells have been shown to attach poorly to highly soluble (bioactive) surfaces. Burling [270] carried out work on soluble phosphate glasses and showed that more stable glasses supported a higher degree of cell growth. Furthermore, other soluble glasses such as Bioglass™ can lead to poor cellular attachment and proliferation dependant on dissolution rates in solution, which is further related to composition [2]. It is argued that in this study a similar effect has occurred. Cell-matrix adhesion has already been discussed is section 2.2.7, however, it is summarised here for the purpose of this discussion. *In vitro*, proteins such as fibronectin and vitronectin have been shown to be involved in *in vitro* osteoblast cell adhesion [271]. Cells do not adhere to a naked material either *in vitro* or *in vivo*, however, upon implantation or *in vitro* testing, the material is conditioned by biological fluid components from either tissue fluid or serum respectively [272]. Some of the proteins involved in osteoblast adhesion, e.g. fibronectin, vitronectin and type I collagen, possess an Arg-Gly-Asp (RGD) peptide sequence which is specific to the fixation of cell membrane receptors such as integrins. RGD peptide coated surfaces have demonstrated to induce significantly higher calvarial cell adhesion, as deduced by radial flow, compared to a RGE (Arg-Gly-Glu) peptide coated surface [273]. The sites of adhesion between cultured cells and the adsorbed protein substrate surfaces are called focal contacts or adhesion plaques. The extracellular face of focal adhesions present specific receptor proteins, such as integrins, while the cytoplasmic side involves proteins such as talin, paxillin, vinculin and tensin which are involved in mediating interactions between actin filaments and integrins [49]. Many proteins such as protein

kinases, phosphatases and signalling molecules are colocalised with vinculin and talin, and are involved in signal transduction. If the interaction between integrins and the extracellular matrix is disrupted, e.g. by the addition of specific antibodies or a change is conformation of adhesion protein, osteoblast differentiation and mineralisation will not occur. This is especially true for integrins which involve the binding of the ligands present on collagen and fibronectin. The interaction between extracellular ligands and integrins is necessary for the expression of osteoblastic genes, however, this signal transduction pathway is not yet fully understood [44]. The above information applies to stable surfaces such as the HA thin films is the current study. Adhesion may not be so readily possible on an unstable surface such as the SiHA films. It is likely that a conditioning layer will be deposited onto the films as this occurs in a matter of seconds. This will be a continual process with as the thin film dissolves in the media which the conditioning layer being continually renewed. Cells may attach to this conditioning layer through ligand based binding. If the conditioning layer and the cell are subsequently removed via dissolution the adhesion protein may change conformation as this is no longer anchored to the biomaterial surface [274]. This change in conformation may lead to the cell becoming detached from the protein. This may happen on multiple occasions and cells may be constantly reattaching to the surface as it dissolves, hence not given the chance to spread and then proliferate until a stable surface for protein mediated cell adhesion become available such as the underlying CPTi substrate. Alternatively, cells may be constantly reacting to the dissolving surface and thus lowering proliferation activity and cell maturation [270].

Even though cells preferred HA surfaces, it was shown that cell number was higher on the higher content SiHA thin films than the lower doped films in the order of SiHA3>SiHA2>SiHA1 (figure 4-56). The SiHA1 sample showed no increase in proliferation or DNA content between time points until day 14 (figure 4-56). In the case of the SiHA1 compositions cells do not adhere to the CPTi substrate until day 10, but the dissolution rate of the thin film was high enough to inhibit long term adhesion until this

point. SiHA2 however showed increasing proliferation with time demonstrated by both the Alamarblue™ and the DNA assay (figures 4-56 and 4-58). Qualitative EDX data (figure 4-42) showed SiHA2 samples dissolved between day 1 and day 4 and so some titanium patches would be available in this time period for cell adhesion. Qualitative EDX data showed that 30 % of the SiHA3 thin film remained after 2 days in culture media. Furthermore, it was observed in the contact angle testing (section 4.6.9.) experiments that some film dissolution would occur even when exposed to water for a few minutes. These observations and measurements may explain why initial adhesion of HOB cells is possible and sustainable on the as-deposited and 600°C SiHA3 films. Essentially the CPTi substrates are revealed to cells which act as a stable protein mediated adhesion site. Initial adhesion studies comparing titanium and HA surfaces have demonstrated that titanium surfaces show a better response in a 90 min attachment period [275], but this was not seen in the case of the as-deposited SiHA3 samples which is thought to occur due to some cells undergoing apoptosis or programmed cell death during the prolonged attachment time. It is well known that cell adhesion via proteins allows signaling which can inhibit apoptosis [276].

It has been shown both in this study and other studies that SiHA bulk and thin film materials have a higher dissolution potential than HA [148, 222]. Moreover, the staining protocol required for the initial adhesion may further affect the stability of the surface owing to numerous washing steps involved (section 3.3.4.) which would accelerate dissolution of the films and some adhered cells may be removed. In the current study we investigated silicon contents higher than previously reported, ranging from 1.8 - 13.4 wt.%. Thian *et al*. [219, 277] looked at a range of silicon contents from 0.4 – 4.9 wt.% stating that the 4.9 wt.% SiHA film did not allow cells to adhere well due to coating instability. In the aforementioned study, coating thicknesses were higher which tends to lead to higher residual stress in the films and on recrystallisation will give a higher crystallinity. Thian *et al*. used moist argon during annealing; the inclusion of water molecules in the annealing atmosphere have been shown to lead to higher crystallinities

[184] due to water molecules having a higher thermal conductivity than argon at a given temperature. Data are not available for 600°C however, at 327°C (600 K) water has a thermal conductivity of 44.1 mW m^{-1} K and argon has a value of 30.6 mW m^{-1} K [259]. Moreover, water is a reactive vapour which can lead to the formation of OH groups on the film surface which could allow easier crystal formation than argon, which is inert. Ultimately this will lead to a more stable surface which cells can more easily attach. In comparison to bulk materials Arcos *et al*. [250] investigated the *in vitro* response of osteoblast cells to bulk high quantity silicon doped apatites. It was found that high silicon content apatite (low crystallinity) showed poor cell proliferation over a seven day period. This was explained by cells poorly adapting to their environments, however, it is more likely that this is due to surface dissolution inhibiting cell adhesion. Figure 5-8 shows a proposed relationship between the amount of silicon content added and the *in vitro* cellular response in terms of adhesion, proliferation and differentiation, above that of a base level based on HA. This illustrates that silicon doping can have a beneficial effect but as our results suggest a detrimental effect is observed at higher silicon contents due to surface instability. Currently, the optimum area of this diagram has not been accurately calculated. Many authors have suggested 'optimum' silicon doping values, but often such values are in disagreement.

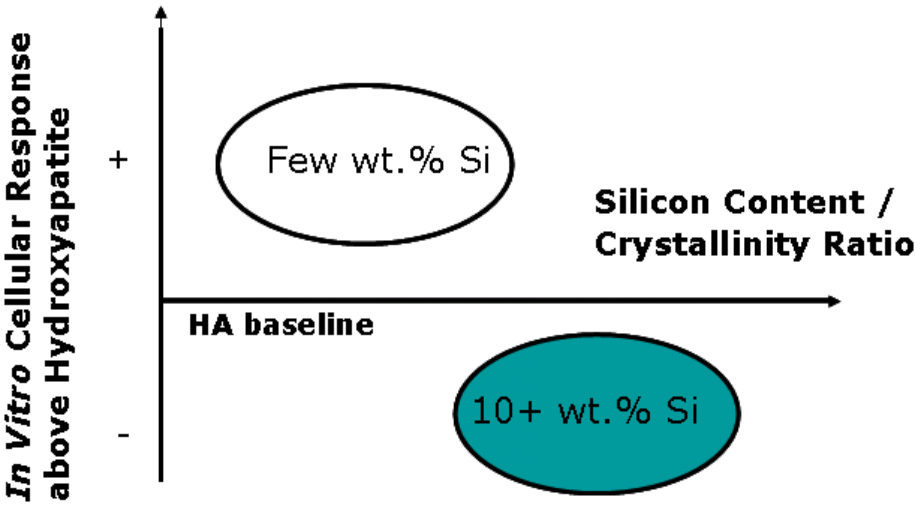

Figure 5-8. The affect of silicon content at enhancing in vitro cellular response above that of a HA baseline.

In order to overcome high dissolution rates of samples annealed at 600°C the cellular response of samples annealed at 700°C in flowing argon were investigated (figures 4-57, 4-59 and 4-61). Proliferation and differentiation on SiHA1 surfaces was slightly higher than on HA surfaces, however, this was not significantly different ($P>0.05$) (figure 4-57). This conflicts with a large number of studies providing strong evidence that SiHA materials elicit an enhanced response when compared with HA materials [133, 141, 147, 148, 199, 218-224, 277]. This may be explained by the presence of a HA/rutile phases at the surface of samples annealed at 700°C (sections 4.6.5., 4.6.6., 4.6.7. and 4.6.8.). Moreover, a much lower silicon content was seen on the surface of the samples annealed at 700°C compared to that of those annealed at 600°C (table 4-9). Even so, it has been shown that even 0.4 wt.% silicon addition to HA can have a pronounced effect on adhesion and proliferation [199]. Only a small amount of silicon (~0.5 at.%) was present on the SiHA1 after annealing at 700°C for 2 h (table 4-9). It would be expected that this surface will have a low dissolution rate as no silicon is avaible to destabilise the HA lattice. Therefore, cell adhesion will remain unaffected. Moreover, this small silicon quanitity may, in fact, have a beneficial effect on cell leading to the slightly increased

cellular response. However, because sample chemistry and texture differ for the HA and the SiHA samples it can not be concluded that the silicon alone had any benefical effect.

Commonly in the literature it has been shown that increasing the post-deposition temperature of HA ceramics increases the cell proliferation and differentiation in both bulk and thin film systems [2, 211, 275]. Roughness, topography, chemistry and surface energy are all known to influence cell response to a given surface [278]. Data obtained would suggest that in the current study cells have reacted to the roughness and chemistry. The majority of studies concerned with topography have concentrated on the micron scale with only a few authors concentrating on the nanometre scale. This is mainly due to a lack of knowledge of how to produce such surfaces, however, Affrossman *et al*. [279] have used polymer demixing to achieve nanotopographies. It has been reported that cells can detect changes as small as 5 nm and *in vivo* cells commonly respond to 66 nm banding on collagen fibrils [280]. In this study there was a roughness difference of 35 nm (figure 4-23) with cells appearing to display increasing numbers of lamellapodia and filopodia. However, no significant difference ($P>0.05$) in cell number or metabolic activity was noted, suggesting that roughness values on this scale have no major affects on cellular response. Recently, Kahn *et al*. [281] used neural cells to investigate several surface textures ranging from 10 to 250 nm in roughness. Values between 20-100 nm promoted cell adhesion and longevity, however, surfaces led to a decrease in attachment at values > 100 nm. Similar trends have been found in other studies using different cells [282], but it is often the case that differences as low as 30 nm did not yield any notable difference. Dalby *et al*. [283] studied the effect of nano-islands on polystyrene materials with fibroblasts. It was found that islands as low as 13 nm high led to increased adhesion, proliferation and cytoskeletal development when compared to flat controls. Conversely, nano-islands 95 nm in height lead to unusual, stellate morphologies with poorly formed cytoskeletons [284]. Intermediate islands (45 nm) showed no difference in cell area from the control, however, the cytoskeleton was less well formed. Studies have shown that RF magnetron sputtered HA surfaces show no

significant difference ($P>0.05$) when compared with titanium substrates at initial time points [220, 285] and the current study agrees with such work. It may however, be that because phosphorus was not found at the top few atomic layers the cellular response was impaired (table 4-9). While not directly comparable it has been shown that cells respond preferentially to surfaces with stoichiometric Ca/P values [72]. The literature confirms that surface texture and chemistry are important but it is still under debate which has a more positive effect.

Overall, the combination of nanotopography and change in surface chemistry has led to small changes in cell morphology and proliferation over a 14 day time period, however, such differences in the HA and SiHA1 surfaces annealed at 700°C for 2 h were too subtle to be significantly different.

5.8. Summary

Post-deposition annealing showed films could be recrystallised at 500°C, however, 600°C was the chosen temperature of recrystallisation due to higher crystallinities. Furthermore at this temperature OH peaks were detected. The importance of optimisation of the sputtering deposition process for the UDP thin films has been demonstrated. Power supply, power density and sputtering environment are all important factors which should be considered as these parameters alter the HA plasmas produced which ultimately affect the final thin film properties.

It has been shown that in this study a super-saturated SiHA thin film has been created as confirmed by XRD and XPS. This is possible as thin films can achieve non-equilibrium states and therefore stoichiometries can be achieved that are not possible in bulk materials. Variation in annealing temperature has led to very different surface chemistries and topographies. Moreover, it was found that at the highest annealing temperature titanium was found to diffuse to the surface of HA thin films leading to a hybrid dual phase surface.

Cellular response to biomaterial surfaces are predominantly governed by surface chemistry and topography [278]. In this study a further parameter must be considered; sample stability. It is well known that low silicon SiHA ceramics lead to an increased cellular response compared with HA. This study did not concur with the literature, however, it was found that factors such as silicon content and crystallinity of thin films ultimately affected the bioactivity of SiHA materials. SiHA thin films annealed at 600°C have an increased dissolution potential which limits cell attachment and proliferation. The highest silicon doped HA sample dissolved in media within 24 h allowing cells to adhere to the underlying CPTi substrate maintaining a level of growth, however, this was lower than the HA control samples. Dissolution rate was proportional to silicon content and therefore cellular response.

After annealing at 700°C a cellular response was higher on SiHA1 samples than HA samples, however this was not significant ($P>0.05$). This occurred due to a dual phase surface now appearing in which a larger proportion of rutile phase was found on the surface of the SiHA1 samples than the HA surface. In addition surface silicon was drastically reduced compared to the as-deposited and 600°C SiHA1 samples. Moreover, a slight reduction in surface roughness was seen on the SiHA1 surface compared to the HA. The combination of altered surface chemistry and small changes in roughness may have reduced cellular response compared with literature values.

6. Conclusions

The work performed in this study looked at HA and SiHA RF magnetron sputtered thin films for the application of orthopaedic materials as coatings for load bearing implant devices. A broad range of sub-topics has been investigated to provide knowledge on all aspects of HA and SiHA thin films ranging from accurate characterisation, post deposition annealing and *in vitro* cellular response testing. Due to the diversity of this study many conclusions may be drawn contributing to the overall furthering of this research area, however, equally this has highlighted many areas in which mechanisms are poorly understood allowing a great deal of scope for future work.

HA and SiHA thin films were deposited successfully onto CPTi and silicon (100) single crystal wafers using BPM and UDP rigs with powder HA, plasma sprayed HA and solid silicon target materials.

Structural observations obtained by XRD, TEM and RHEED showed BPM as-deposited HA thin films to be amorphous or nanocrystalline, following *in* and *ex situ* annealing it was found that films recrystallised at 500°C when heated in flowing argon for 2 h by XRD. It was found OH group formation was in accordance with this recrystallisation temperature as measured by FTIR.

The addition of oxygen to the sputtering environment was found to be beneficial in lowering the Ca/P ratio of HA thin films towards the stoichiometric value of bulk HA material (1.67).

Investigations into the accurate measurement of the Ca/P ratio of thin films was carried out using XPS, EDX and RBS. It was found that XPS gave the lowest value, followed by EDX and finally RBS. Calcium phosphate thin film materials have preferentially P rich surfaces which could account for the low Ca/P ratio returned by XPS. In EDX analysis the

electron beam penetrates into the substrate material dependant on accelerating voltage, but is typically > 2 μm which is greater than the depth of the thin film. Therefore, the titanium X-rays can over excite the Ca and P X-rays leading to a lower Ca/P ratio than expected. It was found that RBS gave the highest Ca/P value but this is thought to be the most accurate. This was confirmed by the measurement of a standard bulk HA material.

The effect of silicon doping on HA thin films was investigated using a range of analytical techniques. XRD confirmed all as-deposited UDP HA and SiHA thin films deposited onto CPTi and silicon (100) single crystal wafers were amorphous or nanocrystalline. After annealing at 600°C in flowing argon for 2 h all films with the exception of the SiHA3 samples recrystallised exhibiting a single phase HA structure matching to ICDD card 09-432. Subsequent post deposition *ex situ* XRD showed that the SiHA3 thin film did not recrystallise until 800°C, but again showing a single phase HA structure. Furthermore, the addition of silicon to HA thin films inhibited HA crystallite growth as demonstrated by crystallite sizes calculated from XRD line broadening.

UDP HA and SiHA thin films were found not to have significantly different Ca/P ratios when measured with EDX, returning a value of approximately 1.8. Conversely, Ca/P ratios measured by XPS showed this value decreased with increasing silicon content in the as-deposited thin films. This was thought to occur due to the creation of a P-Si-O chemical species during the plasma deposition allowing P to reach the substrate more readily. After annealing, however, the Ca/P ratio increased with increasing temperature which is likely to be due to the evaporation on volatile phosphate species which is facilitated by the inclusion of silicon into the HA thin film structure destabilising the HA structure allowing P to be released more easily.

XPS chemical analysis showed as-deposited SiHA thin films to contain a polymerised silicate network which transformed to a monomeric state after annealing at 600°C in

flowing argon for 2 h. This suggested that SiO_4^{4-} groups had substituted in the HA lattice for PO_4^{3-} chemical species. FTIR spectra showed as-deposited UDP HA and SiHA thin films exhibited broad phosphate bonding but no OH bonding was observed. After annealing at 600°C in flowing argon for 2 h OH bonding was seen on the HA thin film but not any of the silicon containing films. This is in keeping with the theory suggested by Gibson *et al*. [126] which states that when silcon substitutes for phosphate bonds a charge balance effect occurs which requires the loss of OH bonds.

From the work presented here, it is proposed that, in post-plasma-deposited heat treated films, silicon substitutes as silicate species into the HA lattice. As-deposited SiHA1, SiHA2 and SiHA3 (containing 1.8, 4.2 and 13.4 wt.% Si by EDX, respectively) thin films were found to have a polymeric Q^4 silicate configuration as determined by XPS. Furthermore, XRD analysis gave evidence that all as-deposited films were amorphous. These two results suggest that, in as-deposited SiHA1, SiHA2 and SiHA3 thin films, silicate groups may be randomly distributed throughout the amorphous film. After post-deposition annealing at 600 or 700°C for 2 h in an argon atmosphere, XPS investigations indicated that in SiHA1, SiHA2 and SiHA3 films silicate groups had substituted for phosphate tetrahedra in the HA lattice, evidenced by a monomeric Q^0 silicate structure. Furthermore, in SiHA1 and SiHA2 films, an HA-like phase was found to be present as shown by XRD; in contrast, the SiHA3 films annealed at 600 or 700°C for 2h in an argon atmosphere exhibited an amorphous structure. Contrary to these findings, FTIR analysis of SiHA1, SiHA2 and SiHA3 films did not manifest any silicate-based bands. This may, however, be due to the fact that the ATR evanescent technique only samples a very small amount of material and, due to the low doping quantities of silicon in the HA films, this may have lead to practical difficulties in detecting these bands. Further contradictory evidence to the proposal of substitution of silicate into HA is that Ca/P ratios consistently differed from the stoichiometric value of HA (1.67) as determined by both XPS and EDX. It should also be mentioned that, although phosphate bands were observed by FTIR for the heat-treated crystalline SiHA1 and SiHA2, no phosphate bands were found for the

amorphous SiHA3 films after post-deposition annealing at 700°C. This combined evidence raises the question of whether the post-deposition heat-treated films have a true HA-like structure. However, the change from Q^4 in the as-deposited films to Q^0 silicate in the heat-treated films and the HA-like structure found by XRD is strong evidence that silicate substitution of HA has occurred for the lower levels of silicon addition. More work is required in order to truly understand the structures present in plasma-deposited, heat-treated SiHA thin films.

The roughness of the UDP HA and SiHA thin films was shown to be similar for all the as-deposited films, which was measured to be approximately 20 nm R_a. This illustrated that the thin films followed the topography of the CPTi substrates which were found to have a similar value. After annealing at 600°C in flowing argon for 2 h the roughness increased, but this was inversely proportional to the silicon content. Silicon inhibition of the HA crystallite growth was responsible for this effect. After annealing at 700°C in flowing argon for 2 h a similar affect was seen but the roughness of all films at least doubled, which is likely to be due to the rise of rutile grain growth and HA crystallite growth, however, silicon is also known to inhibit rutile growth, thus explaining the lowering in roughness with increasing silicon content.

Water contact angle testing of the as-deposited and annealed UDP HA and SiHA thin films showed the addition of silicon to the HA structure increased the sample surface energy allowing droplets to become more spread with increasing silicon content.

Mechanical characterisation carried out on the UDP as-deposited and annealed HA and SiHA thin films showed hardness was not affected by silicon content or annealing. A value of about 6 GPa was obtained for all films with a modulus of 110 GPa. Adhesion testing showed HA thin films were so well adhered to the CPTi substrates that a quantitative failure measurements could not be made. In comparison adhesion testing of HA thin films

on silicon (100) single crystal wafers found the film to delaminate at loads of 350 mN. Therefore it was concluded that HA on CPTi substrates failed at > 350 mN loads.

A HOB cell model was used to assess the *in vitro* cellular reposnse to UDP HA and SiHA thin films. Initial adhesion, proliferation and differentiation assays all suggested HOBs signicantly favoured HA to the SiHA surfaces. It is thought that as the silicon doping destabilises the HA thin films they dissolve in the cell culture media. This acts to remove the protein conditioning layer and adhered cell. Alternatively, the cell is constantly adapting to the dissolving surface thus reducing cell proliferation. HOBs on the highest silicon doped HA thin films annealed at 600°C in flowing argon for 2 h showed some proliferation due to the stable CPTi substrate surface becoming available for protein mediated cell adhesion. After annealing at 700°C in flowing argon for 2 h no significant difference ($P>0.05$) was then seen between the HA and the SiHA1 surfaces suggesting crystallinity levels in SiHA thin films was able to enhance cellular adhesion, proliferation and defferentiation compared to lower crystalline SiHA thin films which were annealed at 600°C for 2 h in flowing argon.

7. Future Work

HA thin film materials are a well established material system, however, it has only been a recent development to dope HA thin films with silicon. This means there are a vast number of studies that could still be performed to obtain a better understanding of SiHA thin films. This chapter aims to highlight some of the areas which could be studied further to aid successful development of a commercial material.

Recrystallisation temperature of HA thin films was related to deposition rate of sputtered HA coatings. However, it is likely that other deposition parameters can also affect this property. This should be investigated by varying factors such as different substrate materials and *in situ* heating of substrates. Such substrates could include Co-Cr alloys also used in TJR. A combination of *in* and *ex situ* XRD should be used to investigate this comprehensively.

An investigation into the accuracy of commonly used characterisation techniques was carried out. Other useful techniques could also be investigated such as PIXE, ERD, EDX with thin film analytical software and wavelength dispersive X-ray analysis (WDX). Furthermore, calcium phosphate thin film standards should be used rather than bulk standards to ascertain if any difference in accuracy occurs due to a thin film system opposed to a bulk material system.

Recently Nottingham University has installed a Nanotechnology and Nanoscience Centre housing a FIB-SEM allowing fast an accurate removal of thin film cross sections for TEM analysis. In this study some results have been produced, but only to check thickness measurements. Much more detailed investigations could be carried out to look at the atomic structure of the SiHA thin films for comparison with analysis carried out by Porter *et al*. [147, 148] on bulk systems. Furthermore, in the current study it was found that thin films were in a super saturated state. High resolution TEM and electron energy loss

spectroscopy (EELS) analysis could be used to investigate how a super saturated state is achieved and the location of silicate species are situated in the HA lattice.

XPS revealed some interesting surface compositional alterations with varied silicon content. Some of these effects were put down to phenomenon occurring during deposition. Plasma spectroscopy could be used during the deposition of SiHA thin films to support such hypotheses or identify exactly what species are present in this complicated deposition mixture. In fact, only a few studies have concerned themselves with intricacies in relation to the plasma deposition of HA thin films.

Finally, it is evident that silicon concentration in HA thin films has a profound affect on the *in vitro* cellular response. This appears to also closely be related to HA crystallinity. It is suggested that more attachment studies are undertaken to investigate the initial celluar reaction to the SiHA thin films. Phallodin staining could be used to see the cell actin configuration with respect to silicon concentration and HA crystallinity. Furthermore, time lapsed differential interference contrast (DIC) microscopy could be used to see how HOB cells react to highly unstable surfaces. Alamarblue™, DNA, ALP and protein attachment studies are required with a large range of silicon compositions and crystalliniies to identify the optimum silicon composition and crystallinity to obtain the most favorable cellular response. Moreover, it is still not clearly understood how silicon may change the cellular response although it is thought to be related to the increased surface dissolution of SiHA thin films in comparison to HA thin films, however, this study has shown that high silicon doping can be detrimental to cellular response.

Appendices

hkl reflection	ICDD 09-432 (HA) 2θ	I	As-received HA 2θ	I	Sintered HA 2θ	I
100	10.839	12				
101	16.840	6				
110	18.830	4				
200	21.776	10	22.18	4	21.98	5
111	22.862	10	23.22	5	23.02	6
201	25.364	2				
002	25.864	40	26.10	31	25.96	34
102	28.116	12	28.38	8	28.24	11
210	28.940	18	29.18	15	29.06	16
211	31.779	100	32.00	100	31.86	100
112	32.187	60	32.42	49	32.3	57
300	32.918	60	33.12	63	33	65
202	34.057	25	34.30	23	34.16	27
301	35.471	6	35.76	5	35.62	6
212	39.199	8	39.52	5	39.34	8
310	39.817	20	40.06	23	39.92	24
221	40.457	2	40.84	1	40.78	2
311	42.008	10	42.34	5	42.16	6
302	42.330	4				
113	43.854	8	44.24	4	44.03	7
400	44.392	2	45.54	5	45.4	7
203	45.31	6				
222	46.704	30	46.92	32	46.82	33
312	48.093	16	48.34	14	48.2	15
320	48.619	6	48.98	5	48.86	4
213	49.477	40	49.70	34	49.58	38
321	50.505	20	50.76	18	50.6	19
410	51.290	12	51.56	12	51.4	14
402	52.091	16	52.34	14	52.2	15
004	53.178	20	53.4	14	53.3	18
104	54.445	4	54.8	2	54.7	2
322	55.883	10	56.18	6	56.08	6
313	57.131	8	57.50	4	57.32	5
501	58.063	4	58.52	3	58.44	3
420	59.966	6	60.30	4	60.22	5
331	60.442	6	60.82	2	60.66	4
214	61.676	10	61.92	8	61.82	7
502	63.009	12	63.32	7	63.14	9
510	63.449	4				
304	63.974	13				
323	64.171	13	64.36	10	64.24	11
511	65.042	9	65.40	7	65.2	8
422	66.401	4				
413	66.422	4	66.80	3	66.46	5
512	69.707	3	70.00	2	70	2

Table A1. XRD 2θ and intensity data for as-received and sintered Plasma Biotal HA powders (refer to figure 4-1).

Band	Experimental Wavenumber cm^{-1}	Literature Wavenumber cm^{-1}	Reference
Water	1500-1400[a]	1640	[180, 256, 286]
PO_4	1136[a], 1147[b]	1120	[180, 256, 286]
PO_4	1012[a], 1028[b]	1020	[180, 256, 286]
OH^-	688[a]	630	[180, 256, 286]
CO_3^{2-}	1406[a]	1550-1400	[180, 256, 286]
PO_4	1084[a], 1080[b]	1078	[180, 256, 286]
PO_4	940[a], 950[b]	960	[180, 256, 286]
CO_3^{2-}	874[a]	880-850	[180, 256, 286]
OH^-	3642[a], 3643[b]	3570	[180, 256, 286]
PO_4	617[b]	609	[180, 256, 286]
TiO_2	820[b]	820	[256]

Table A2. FTIR band assigments and relevant references for FTIR sections 4.3.1.3 [a]. and 4.6.5 [b].

hkl reflection	ICDD 09-432 (HA) 2θ	I	Target 2θ	I
100	10.839	12	11.02	1
101	16.840	6	17.32	1
110	18.830	4		
200	21.776	10	22.28	1
111	22.862	10	23.58	7
201	25.364	2		
002	25.864	40	26.14	100
102	28.116	12	28.52	14
210	28.94	18	29.52	7
211	31.779	100	32.44	32
112	32.187	60	33.4	9
300	32.918	60	34.56	9
202	34.057	25		
301	35.471	6		
212	39.199	8	39.78	4
310	39.817	20	40.5	4
221	40.457	2	41.18	6
311	42.008	10	42.72	3
302	42.330	4		
113	43.854	8		
400	44.392	2	44.44	5
203	45.310	6	45.72	5
222	46.704	30	47.24	7
312	48.093	16		
320	48.619	6	48.74	4
213	49.477	40	49.86	16
321	50.505	20		
410	51.290	12		
402	52.091	16		
004	53.178	20	53.7	48
104	54.445	4	54.82	5
322	55.883	10		
313	57.131	8		
501	58.063	4		
420	59.966	6		
331	60.442	6		
214	61.676	10	62.14	4
502	63.009	12		
510	63.449	4		
304	63.974	13		
323	64.171	13	64.5	6
511	65.042	9		
422	66.401	4		
413	66.422	4		
512	69.707	3		

Table A3. XRD 2θ and intensity data for the plasma-sprayed HA target used for UDP experiments (refer to figure 4-4).

			Time / min			
			0	208	608	800
hkl reflections	ICDD 09-432 (HA) 2θ	Experimental 2θ	I	I	I	I
102	28.116	28.1	45	31	35	37
211	31.771	31.8	100	100	100	100
112	32.187	32.1	90	73	77	78
300	32.918	32.9	5	4	8	7

Table A4. XRD 2θ and relative intensity data for *in situ* heat treatments of HA thin films deposited onto silicon (100) wafer and held at 600˚C under helium for 800 min (refer to figure 4-7).

hkl reflections	ICDD 09-432 (HA) 2θ	I	500˚C 2θ	I	600˚C 2θ	I
102	28.116	12	28.3	13	28.3	35
210	28.940	18	29.4	27	29.1	3
211	31.779	100	32	100	31.9	55
112	32.187	60			32.3	100
300	32.918	60	33.1	27	33.0	10
202	34.057	25	34.1	13	34.1	20

Table A5. XRD 2θ and relative intensity data for HA thin films deposited onto CPTi discs following post-deposition heat treatments at 500 and 600˚C in an argon atmosphere (refer to figure 4-9).

hkl reflection	ICDD 09-432 2θ	I	600˚C 2θ	I
100	10.839	12		
101	16.840	6		
110	18.830	4		
200	21.776	10		
111	22.862	10		
201	25.364	2		
002	25.864	40	25.9	100
102	28.116	12	28.2	24
210	28.940	18		
211	31.779	100		
112	32.187	60	32.2	66
300	32.918	60		
202	34.057	25	34.2	20
301	35.471	6		
212	39.199	8		
310	39.817	20		
221	40.457	2		
311	42.008	10		
302	42.330	4		
113	43.854	8	44.0	6
400	44.392	2		
203	45.31	6	45.3	3
222	46.704	30	46.8	4
312	48.093	16		
320	48.619	6		
213	49.477	40	49.6	20
321	50.505	20		
410	51.290	12		
402	52.091	16		
004	53.178	20	53.3	29
104	54.445	4		
512	69.707	3		

Table A6. XRD 2θ and intensity data for HA thin film (Ref. 7017, see table 3-1) deposited onto silicon (100) wafer following post-deposition heat treatment 600˚C in an argon atmosphere (refer to figure 4-12).

hkl reflection	ICDD 09-432 2θ	I	As-Deposited	I	600˚C 2θ	I
100	10.839	12				
101	16.840	6				
110	18.830	4				
200	21.776	10				
111	22.862	10				
201	25.364	2				
002	25.864	40	25.4	100	25.9	100
102	28.116	12	27.8	24	28.3	12
210	28.940	18				
211	31.779	100	31.6	70	32.3	30
112	32.187	60				
300	32.918	60				
202	34.057	25	33.4	24	34.2	7
301	35.471	6				
212	39.199	8				
310	39.817	20				
221	40.457	2				
311	42.008	10				
302	42.33	4				
113	43.854	8				
400	44.392	2			44.0	3
203	45.310	6			45.5	1
222	46.704	30			46.8	2
312	48.093	16				
320	48.619	6	48.8	21		
213	49.477	40			49.6	10
321	50.505	20				
410	51.29	12				
402	52.091	16	52.5	26	53.4	14
004	53.178	20				
104	54.445	4				
CaO[a]/200	37.361	100			37.2	12
B-TCP[b]/1211	37.329	11			37.2	12

Table A7. XRD 2θ and intensity data for as HA thin films (Ref. 7019, see table 3-1) deposited onto silicon (100) wafer following post-deposition heat treatment 600˚C in an argon atmosphere (refer to figure 4-13). [a] = CaO/ICDD card 004-0777, [b] = β-TCP/ICDD card 09-0169.

hkl reflection	ICDD 09-432 2θ	I	600˚C 2θ	I
100	10.839	12		
101	16.840	6		
110	18.830	4		
200	21.776	10		
111	22.862	10	22.9	5
201	25.364	2	24.2	2
002	25.864	40	25.9	100
102	28.116	12	28.2	17
210	28.940	18	29.0	1
211	31.779	100	31.8	15
112	32.187	60	32.3	55
300	32.918	60	32.9	5
202	34.057	25	34.1	17
301	35.471	6		
212	39.199	8	39.2	2
310	39.817	20	39.8	1
221	40.457	2		
311	42.008	10		
302	42.330	4		
113	43.854	8	43.9	4
400	44.392	2		
203	45.310	6	45.4	3
222	46.704	30	46.7	6
312	48.093	16	48.1	2
320	48.619	6		
213	49.477	40	49.6	17
321	50.505	20		
410	51.290	12		
402	52.091	16	52.1	2
004	53.178	20	53.3	16
104	54.445	4		
β-TCP[a]/02$\underline{10}$	31.027	100	30.7	8

Table A8. XRD 2θ and relative intensity data for as HA thin films (Ref. 7125, see table 3-1) deposited onto silicon (100) wafer following post-deposition heat treatment 600˚C in an argon atmosphere (refer to figure 4-14). [a] = β-TCP/ICDD card 09-0169.

hkl reflection	ICDD 09-432 2θ	I	600˚C 2θ	I
100	10.839	12		
101	16.840	6		
110	18.830	4		
200	21.776	10	21.8	8
111	22.862	10	22.9	15
201	25.364	2		
002	25.864	40	25.9	51
102	28.116	12	28.1	13
210	28.94	18	28.9	12
211	31.779	100	31.8	100
112	32.187	60	32.2	70
300	32.918	60	32.9	47
202	34.057	25	34.7	30
301	35.471	6	65.5	4
212	39.199	8	39.2	4
310	39.817	20	39.9	14
221	40.457	2		
311	42.008	10		
302	42.330	4	42.3	3
113	43.854	8	43.9	3
400	44.392	2		
203	45.310	6	45.3	3
222	46.704	30	46.7	20
312	48.093	16	48.1	7
320	48.619	6		
213	49.477	40	49.5	21
321	50.505	20	50.5	7
410	51.290	12	51.3	6
402	52.091	16		
004	53.178	20	52.1	8
104	54.445	4		
β-TCP[a]/02$\underline{10}$	31.027	100	30.7	7

Table A9. XRD 2θ and intensity data for as HA thin films (Ref. 7128, see table 3-1) deposited onto silicon (100) wafer following post-deposition heat treatment 600˚C in an argon atmosphere (refer to figure 4-15).

hkl reflections	ICDD 09-432 2θ	I	HA 2θ	I	SiHA1 2θ	I	SiHA2 2θ	I
100	10.839	12						
101	16.840	6						
110	18.830	4						
200	21.776	10	21.9	16	21.9	25	22.1	11
111	22.862	10	23.1	10	23.1	1	23.2	3
201	25.364	2						
002	25.864	40	26.0	83	26.0	70	25.9	100
102	28.116	12	28.3	13	28.3	3	28.3	13
210	28.940	18	29.1	23	29.1	16	29.3	11
211	31.779	100	31.9	100	31.9	80	32.1	59
112	32.187	60	32.3	75	32.3	41	32.3	79
300	32.918	60	33.1	76	33.0	100	33.2	58
202	34.057	25	34.2	26	34.2	13	34.3	16
301	35.471	6	35.7	4	35.7	1		
212	39.199	8	40.0	18	40.0	24	40.2	5
310	39.817	20						
221	40.457	2						
311	42.008	10	42.3	3	42.3	1	42.4	1
302	42.330	4			44.2	1	44.1	1
113	43.854	8						
400	44.392	2	44.5	1	47.0	6	47.1	9
203	45.310	6						
222	46.704	30	46.9	19	48.4	2	48.4	1
312	48.093	16	48.3	7	49.7	11	49.7	10
320	48.619	6						
213	49.477	40	49.7	22				
321	50.505	20	50.7	11	50.7	7	50.9	3
410	51.290	12	51.6	5	51.6	2	51.8	2
402	52.091	16	52.4	8	52.3	2	52.5	6
004	53.178	20	53.4	11	53.3	7	53.4	8
104	54.445	4						

Table A10. XRD 2θ and intensity data for HA, SiHA1 and SiHA2 thin films deposited onto silicon (100) wafer following post-deposition heat treatments at 600˚C an argon atmosphere (refer to figure 4-27).

hkl reflection	ICDD 09-432 2θ	I	HA 2θ	I	SiHA1 2θ	I	SiHA2 2θ	I
100	10.839	12						
101	16.840	6						
110	18.830	4						
200	21.776	10	20.9	21	21.9	1	22	19
111	22.862	10	23.0	16	23.0	12	23.16	7
201	25.364	2						
002	25.864	40	26.0	91	26.0	65	25.92	100
102	28.116	12	28.3	23	28.3	8	28.26	14
210	28.940	18	29.1	23	29.1	21	29.2	22
211	31.779	100	31.9	100	31.9	79	32.14	76
112	32.187	60	32.3	79	32.4	43	32.2	85
300	32.918	60	33.0	81	33.1	100	33.16	78
202	34.057	25	34.2	34	34.3	14	34.3	15
301	35.471	6	35.8	8	35.7	8	35.84	3
212	39.199	8						
310	39.817	20	39.5	7	39.5	7	39.6	3
221	40.457	2						
311	42.008	10	42.0	23	40.0	28	40.22	9
302	42.330	4	42.3	9	42.3	1	42.4	1
113	43.854	8	44.1	7	44.2	7	40.04	2
400	44.392	2						
203	45.310	6	45.5	9	45.3	7	45.68	1
222	46.704	30	46.9	23	46.9	9	47.1	6
312	48.093	16	48.3	15	48.4	1	48.4	3
320	48.619	6	48.9	9	48.9	8	49.04	2
213	49.477	40	49.7	29	49.7	17	49.82	11
321	50.505	20	50.8	16	50.8	7	50.96	3
410	51.290	12	51.6	12	51.6	2	51.7	1
402	52.091	16	52.3	15	52.4	3	52.52	4
004	53.178	20	53.4	17	53.4	4	53.22	12
104	54.445	4						

Table A11. XRD 2θ and intensity data for HA, SiHA1 and SiHA2 thin films deposited onto silicon (100) wafer following post-deposition heat treatments at 700˚C in an argon atmosphere (refer to figure 4-28).

hkl reflection	ICDD 09-432 2θ	I	SiHA 800˚C 2θ	I	SiHA 900˚C 2θ	I	SiHA 1000˚C 2θ	I
100	10.839	12						
101	16.840	6						
110	18.830	4						
200	21.776	10	21.9	19	21.9	20	21.9	18
111	22.862	10	22.9	22	23.0	23	23.0	18
201	25.364	2						
002	25.864	40	25.8	39	25.8	40	25.8	52
102	28.116	12						
210	28.940	18	29.0	23	29.0	30	29.0	28
211	31.779	100	31.8	100	31.9	100	31.9	100
112	32.187	60	32.1	80	32.1	88	32.1	86
300	32.918	60	32.9	78	33.0	71	33.0	242
202	34.057	25	34.0	22	34.1	23	34.0	22
301	35.471	6	35.6	4	35.6	7	35.6	6
212	39.199	8	39.3	2	39.3	3	39.4	2
310	39.817	20	39.9	13	40.0	16	40.0	16
221	40.457	2						
311	42.008	10	42.0	5	42.1	5	42.2	2
302	42.330	4						
113	43.854	8						
400	44.392	2						
203	45.310	6						
222	46.704	30	46.7	14	46.8	18	46.8	18
312	48.093	16	48.2	4	48.2	9	48.1	5
320	48.619	6						
213	49.477	40	49.4	10	49.4	17	49.4	17
321	50.505	20	50.7	3	50.7	9	50.5	8
410	51.290	12	51.4	6	51.5	6	51.5	2
402	52.091	16	52.1	3	52.2	11	52.2	5
004	53.178	20	53.0	4	52.9	11	53.0	7
104	54.445	4						

Table A12. XRD 2θ and intensity data for SiHA3 thin films deposited onto silicon (100) wafer following post-deposition heat treatments at 800, 900 and 1000˚C in an argon atmosphere (figure 4-29).

hkl reflection	ICDD 09-432 2θ	I	HA 2θ	I	SiHA1 2θ	I	SiHA2 2θ	I	SiHA3 2θ	I
100	10.839	12								
101	16.840	6								
110	18.830	4								
200	21.776	10	22.0	28	22.0	46				
111	22.862	10	23.1	31						
201	25.364	2								
002	25.864	40	25.9	80	26.0	74	25.8	89		
102	28.116	12	28.2	33	28.3	32				
210	28.940	18	29.5	35						
211	31.779	100	32.0	62			32.0	100	32.0	100
112	32.187	60	32.3	100	32.2	100				
300	32.918	60	33.2	31	33.3	29	33.1	73	33.1	95
202	34.057	25	34.2	30	34.1	39				
301	35.471	6								
212	39.199	8								
310	39.817	20								
221	40.457	2								
311	42.008	10								
302	42.330	4								
113	43.854	8								
400	44.392	2								
203	45.31	6								
222	46.704	30	46.9	23	46.9	19				
312	48.093	16								
320	48.619	6								
213	49.477	40	49.7	19	49.6	20				
321	50.505	20								
410	51.29	12								
402	52.091	16								
004	53.178	20								
104	54.445	4								
hkl Reflection	**ICDD 44-1294 (Ti) 2θ**	**I**	**HA**	**I**	**SiHA1**	**I**	**SiHA2**	**I**	**SiHA3**	**I**
100	35.094	25	35.1	4	35.0	4	35.1	4	35.1	8
002	38.422	30	38.2	19	38.2	19	38.2	19	38.2	19
101	40.171	100	40.3	100	40.3	100	40.3	100	40.3	100
102	53.005	13	52.9	10	52.5	10	52.8	10	52.8	12

Table A13. XRD 2θ and intensity data for HA, SiHA1, SiHA2 and SiHA3 thin films deposited onto CPTi dics following post-deposition heat treatments at 600˚C in an argon atmosphere (refer to figure 4-30).

hkl Reflection	ICDD 09-432 2θ	I	HA 2θ	I	SiHA1 2θ	I	SiHA2 2θ	I	SiHA3 2θ	I
100	10.839	12								
101	16.840	6								
110	18.830	4								
200	21.776	10	22.0	28	21.9	25	22.0	59		
111	22.862	10								
201	25.364	2								
002	25.864	40	25.9	126	25.9	100	25.9	82		
102	28.116	12	28.3	33	28.2	31	28.2	49		
210	28.940	18	29.1	20	29.1	22	29.1	46		
211	31.779	100	31.9	57	31.9	42	32.0	87		
112	32.187	60	32.3	100	32.3	49	32.3	72		
300	32.918	60	33.1	27	33.0	52	33.1	100	33.0	63
202	34.057	25	34.2	35	34.2	19	34.1	58	34.2	100
301	35.471	6								
212	39.199	8								
310	39.817	20								
221	40.457	2								
311	42.008	10								
302	42.330	4								
113	43.854	8								
400	44.392	2								
203	45.310	6								
222	46.704	30	46.9	20	46.9	11				
312	48.093	16	48.3	11	48.3	8				
320	48.619	6								
213	49.477	40	49.7	29	49.6	18	49.6	24		
321	50.505	20								
410	51.290	12								
402	52.091	16								
004	53.178	20	53.4	18	53.4	15				
104	54.445	4								
hkl reflection	**ICDD 44-1294 (Ti) 2θ**	**I**	**HA 2θ**	**I**	**SiHA1 2θ**	**I**	**SiHA2 2θ**	**I**	**SiHA3 2θ**	**I**
100	35.094	25	35.0	5	35.0	4	35.0	3	35.08	3
002	38.422	30	37.8	17	37.9	17	37.8	22	37.88	27
101	40.171	100	39.9	100	39.9	100	39.9	100	39.9	100
102	53.005	13	52.4	17	52.5	16	52.4	20	52.58	19
hkl reflection	**ICDD 76-1939 (TiO_2) 2θ**	**I**	**HA 2θ**	**I**	**SiHA1 2θ**	**I**	**SiHA2 2θ**	**I**	**SiHA3 2θ**	**I**
110	27.380	100	27.5	100	27.5	100	27.5	100	27.56	35
101	35.993	43								
200	39.101	6	39.34	27	39.4	55	39.4	32		
111	41.142	17	41.34	19	41.4	18	41.3	28	40.86	100
210	43.950	6	44.08	15	44.1	19				
211	54.193	45	54.48	23	54.5	33	54.5	23	54.5	18

Table A14. XRD 2θ and intensity data for HA, SiHA1, SiHA2 and SiHA3 thin films deposited onto CPTi dics following post-deposition heat treatments at 700˚C in an argon atmosphere (refer to figure 4-31).

Compound	Wt.%	Element Wt.%	RAM	Moles
SiO_2	0.34		28.09	
TiO_2	0.01		47.88	
Al_2O_3	0.09		26.98	
Fe_2O_3	0.05		55.85	
CaO	55.1	39.40	40.08	0.98
MgO	0.27		24.31	
K_2O	0.01		39.10	
Na_2O	0.03		22.99	
P_2O_5	41.1	17.96	30.97	0.58
Cr_2O_3	0.005		52.00	
Mn_3O_4	0.01		54.94	
ZrO_2	0.005		91.22	
HfO_2	0.005		178.49	
PbO	0.005		207.20	
ZnO	0.005		65.39	
BaO	0.005		137.33	
SrO	0.04		87.62	
SnO_2	0.005		118.71	
CuO	0.005		63.55	
O	n/a		16.00	
Loss on ignition	2.72			
Total	99.81	57.36	1388.68	1.56
Ca/P	**1.7**			

Table A15. Compositional data determined by XRF of the P120 HA standard. Analysis was performed in July 1993 by M. Homles (Technical Supervisor) at Ceram Research. Data relevant to table 4-6.

References

1. Lysaght, M.J. and O.L. J., *The demographic scope and economic magnitude of contemporary organ replacement therapies.* American Society for Internal Artifical Organs, 2000. **J46**: p. 515-21.
2. Ratner, B.D., et al., eds. *Biomaterials Science: An Introduction to Materials in Medicine*. 1996, Academic Press: San Diego, California.
3. Dixon, T., et al., *Trends in hip and knee joint replacement: socioeconomic inequalities and projections of need.* Annuals of Rheumatoid Disease, 2004. **63**: p. 825-830.
4. *National Joint Registry*. 2007.
5. Shanbhag, A.S., et al., *Composition and morphology of wear debris in failed uncemented total hip replacement.* Journal of Bone and Joint Surgery - Series B, 1994. **76**(1): p. 60-67.
6. Schmalzried, T.P., L.M. Kwong, and M. Jasty, *The mechanism of loosening of cemented acetabular components in total hip arthroplasty. Analysis of specimens retrieved at autopsy.* Clinical Orthopaedics, 1992. **274**: p. 60–78.
7. Maloney, W.J. and P. Peters, *Severe osteolysis of the pelvis in association with acetabular replacement without cement.* Journal of Bone Joint Surgery, 1993. **75A**: p. 1627–1635.
8. Katti, K.S., *Biomaterials in total joint replacement.* Colloids and Surfaces B: Biointerfaces, 2004. **39**(3): p. 133-142.
9. Williams, D.F., *Definitions in biomaterials*. 1 ed. 1987, Amsterdam: Elsevier. 72.
10. Hench, L.L., *Biomaterials: a forecast for the future.* Biomaterials, 1998. **19**(16): p. 1419-1423.
11. www.zimmer.com.au. 2007 [cited 2008 13/03/08].
12. Sauvé, P., et al., *Metal ion levels after metal-on-metal ring total hip replacement.* Journals of Bone and Joint Surgery, 2007. **89-B**(5): p. 586-590.
13. Sieber, H.-P., C.B. Rieker, and P. Kottig, *Analysis of 118 second-generation metal-on-metal retrieved hip implants.* Journal of Bone and Joint Surgery, 1999. **80**: p. 46-50.
14. Wong, L.H., B. Tio, and X. Miao, *Functionally graded tricalcium phosphate/fluoroapatite composites.* Materials Science and Engineering C, 2002. **20**: p. 111– 115.
15. Watari, F., et al., *Fabrication and properties of functionally graded dental implant* Composites Part B: Engineering 1997. **28**(1-2): p. 5-11.
16. Galego, N., et al., *Characterization and application of poly(β-hydroxyalkanoates) family as composite biomaterials.* 2000. **19**(5): p. 485-492
17. Clark, M.E., *Biodegradable Nano-particluate Calcium Carbonate for Fracture Fixation Plates*, in *M3*. 2007, The University of Nottingham: Nottingham. p. 254.
18. Liaoa, S., et al., *The degradation of the three layered nano-carbonated hydroxyapatite/collagen/PLGA composite membrane in vitro.* Dental Materials, 2007 **23**: p. 1120–1128.

19. LeGeros, R.Z., in *Calcium Phosphates in Oral Biology and Medicine (Monographs in Oral Science)* 1991, S Karger: Basel. p. 201
20. Nordin, M. and V.H. Frankel, *Basic Biomechanics of the Musculoskeletal System*. 3rd ed. 2001, Philadelphia: Lippincott Williams & Wilkins.
21. Suchanek, W. and M. Y., *Processing and properties of hydroxyapatite-based biomaterials for use as hard tissue replacement implants.* Journal of Materials Research, 1998. **13**(1): p. 94-117.
22. Brown, P.W., Constantz, B., ed. *Hydroxyapatite and Related Materials*. Biological and synthetic apatites, ed. R.Z. LeGeros. 1994: London.
23. Downey, P.A. and M.I. Siegel, *Bone biology and the clinical implications for osteoporosis.* Physical Therapy, 2006. **86**(1): p. 77-91.
24. Vaughan, J., *The Physiology of Bone* 2nd ed. 1975, Oxford Claredone press.
25. Rho, J.-Y., L. Kuhn-Spearing, and P. Zioupos, *Mechanical properties and the hierarchical structure of bone.* Medical Engineering & Physics, 1998. **20**(2): p. 92-102.
26. Olszta, M.J., et al., *Bone structure and formation: A new perspective.* Materials Science and Engineering R, 2007. doi:10.1016/j.mer.2007.05.001.
27. Gray, H., *Gray's Anatomy* 1974, Philadelphia: Running Press.
28. Thibodeau, G.A. and K.T. Patton, *Structure & Function of the Body*. 12 ed. 2003: Mosby-Yearbook. 547.
29. Noble, B.S. and J. Reeve, *Osteocyte function, osteocyte death and bone fracture resistance.* Molecular and Cellular Endocrinology, 2000. **159**: p. 7-13.
30. Little, K., *Bone Behaviour*. 1973, London: Academic Press.
31. Baron, R., *Molecular mechanisms of bone resorption by the osteoclast.* The Anatomical Record, 1989. **224**: p. 317-324.
32. Teitelbaum, S.L., *Bone resorption by osteoclasts.* Science, 2000. **289**: p. 1504-1508.
33. Marks, S.C. and S.N. Popoff, *Bone cell biology: the regulation of development, structure and function in the skeleton.* Journal of Anatomy, 1988. **183**: p. 1-44.
34. Marks, S.C. and D.C. Hermey, *The structure and development of bone*, in *Principles of Bone Biology*, R.L.R. GA, Editor. 1996, Academic Press: San Diego. p. 3-14.
35. Buckwalter, J.A. and E.B. Hunziker, *Orthopaedics. Healing of bones, cartilages, tendons and ligaments: a new era.* Lancet, 1996. **348**.
36. Bilezikian, J.P., L.G. Raisz, and A.R. Gideon, eds. *Principles of Bone Biology*. 1996, Academic Press: San Diego. 957.
37. Wraighte, P.J. and B.E. Scammell, *Principles of fracture healing.* Surgery (Oxford), 2006. **24**(6): p. 198-207.
38. Shapiro, F. *Bone development and its relation to fracture repair*. in *European Cells and Materials*. 2007.

39. Currey, J., *Incompatible mechanical properties in compact bone.* Journal of Theoretical Biology, 2004. **231**(4): p. 569-580.
40. Rho, J.-Y., T.Y. Tsui, and G.M. Pharr, *Elastic properties of human cortical and trabecular lamellar bone measured by nanoindentation.* Biomaterials, 1997. **18**(20): p. 1325-1330.
41. Wolff, J., *Das Gesetz der transformation der Knochen*. 1892, Berlin: Hirschwald.
42. Ducy, P., T. Schinke, and G. Karsenty, *The osteoblast: a sophisticated fibroblast under central surveillance.* Science, 2000. **289**(1): p. 1501-1504.
43. Stien, G.S., et al., *Transcriptional control of osteoblast growth and differentiation.* Physiological Reviews, 1996. **76**(2): p. 593-629.
44. Franceschi, R.T., *The development control of osteoblast-specific gene expression: role of specific transcription factors and the extracellular matrix environment.* Critical Review of Oral Biology in Medicine, 1999. **10**(1): p. 40-57.
45. Owen, T.A. and M. Aronow, *Progressive development of the rat osteoblast phenotype on vitro:reciprocal relationship in expression of genes associated with osteoblast proliferation and differentiation during the formation of the bone extracellular matrix.* Journal of Cellular Physiology, 1990. **143**: p. 420-430.
46. Ishizuya, T., et al., *Parathyroid hormone exerts disparate effects on osteoblast differentiation depending on exposure time in rat osteoblastic cells.* Journal of Clinical Investigations, 1997. **99**(12): p. 2961-2970.
47. Lynch, M.P., et al., *The influence of type I collagen on the development and maintenance of the osteoblast phenotype in primary and passaged rat calvarial osteoblasts: modification of expression of genes supporting cell growth, adhesion and extra celluar mineralisation.* Experimental Cell Research, 1995. **216**: p. 34-45.
48. Bizios, R., *Mini-review: osteoblasts: an in vitro model of bone-implant interactions.* Biotechnology and Bioengineering, 1994. **43**: p. 582-585.
49. Anselme, K., *Osteoblast adhesion on biomaterials.* Biomaterials, 2000. **21**: p. 667-681.
50. Gronthos, S., et al., *Integrin expression and fucntion of human osteoblast-like cells.* Journal of Bone and Mineral Research, 1997. **12**(8): p. 1997.
51. Alberts, B., et al., *Molecular Biology of The Cell*. 4 ed. 2002, New York: Garland Science.
52. Hynes, R.O., *Integrins: versatility, modulation and signalling in cell adhesion.* Cell, 1992. **69**: p. 11-25.
53. Arima, Y. and H. Iwata, *Effects of surface funtional groups on protien adsorption and subsequent cell adhesion using self-assembled monolayers.* Journal of Material Chemistry, 2007. **17**: p. 4079-4087.
54. Scotchford, C.A., et al., *Growth of human osteoblast-like cells on alkanethiol on gold self-assembled monolayers: the effect of surface chemistry.* Journal of Biomedical Materials Research, 2002. **59**(1): p. 84-99.

55. Keselowsky, B.G., D.M. Collard, and A.J. Garcia, *Surface chemistry modulates fibronectin conformation and directs integrin binding and specificity to control cell adhesion.* Journal of Biomedical Materials Research, 2003. **66A**: p. 247-259.

56. Wertz, C.F. and M.M. Santore, *Abdorption and relaxation kenetics of albumin and fibrinogen on hydrophobic surfaces:single species and competitive behaviour.* Langmuir, 1999. **15**: p. 8884-8894.

57. Gao, M., et al., *Molecular mechanisms of cellular mechanics.* Physical Chemistry Chemical Physics, 2006. **8**: p. 3692-3706.

58. Xiong, J.-P., et al., *Crystal structure of extracellular segment of integrin αVβ3 on complex with Arg-Gly-Asp ligand.* Science, 2002. **296**: p. 151-155.

59. A. Paul Mould, et al., *Role of ADMIDAS cation-binding site in ligand recognition by integrin αVβ3.* Journal of Biological Chemistry, 2003. **278**(51): p. 51622-51629.

60. LeGeros, R.Z., *Calcium phosphates in oral biology and medicine*. biologically relevant calcium phosphates. 1991, New York: Karger. 5-45.

61. Kohn, M.J., J. Rakovan, and J.M. Hughes, eds. *Phosphates - Geochemical, Geobiological and Materials Importance*. Reviews in Mineralogy and Geochemistry, ed. P.H. Ribbe and J.J. Rosso. Vol. 48. 2002: Washington DC. 742.

62. Chou, L., B. Marek, and W.R. Wagner, *Effects of hydroxylapatite coating crystallinity on biosolubility, cell attachment efficiency and proliferation in vitro.* Biomaterials, 1999. **20**(10): p. 977-985.

63. De Groot, K., et al., *Plasma sprayed coatings of hydroxylapatite.* Journal of Biomedical Materials Research, 1987. **21**(12): p. 1375-1381.

64. Webster, T.J., et al., *Increased osteoblast adhesion on titanium-coated hydroxylapatite that forms $CaTiO_3$.* Journal of Biomaterial Materials Research, 2003. **67A**: p. 975-980.

65. LeGeros, R.Z., ed. *Calcium Phosphates in Enamel, Dentin and Bone*. Calcium Phosphates in Oral Biology and Medicine. 1991.

66. Elliott, J.C., *Studies in Inorganic Chemistry 18 - Structure and chemistry of the apatites and other calcium phosphates*. 1994, London: Elsevier.

67. Hughes, J.M., M. Cameron, and K.D. Crowley, *Structural variations in natural F, OH and Cl apatites.* American Mineralogist, 1989. **75**: p. 295-304.

68. Hughes, J.M. and J. Rakovan, *The Crystal Structure of Apatite, $Ca_5(PO_4)_3(F,OH,Cl)$*, in *Reviews in Mineralogy and Geochemistry - Phosphates - Geochemical, Geobiological and Materials Importance*, M.J. Kohn, J. Rakovan, and J.M. Hughes, Editors. 2002: Washington DC. p. 742.

69. Pan, Y. and M.E. Fleet, *Substitution Mechanisms and Controlling Factors*, in *Reviews in Mineralogy and Geochemistry - Phosphates - Geochemical, Geobiological and Materials Importance*, M.J. Kohn, J. Rakovan, and J.M. Hughes, Editors. 2002: Washington DC. p. 742.

70. Ozeki, K., et al., *Phase composition of sputtered films from a hydroxyapatite target.* Surface and Coatings Technology, 2002. **160**(1): p. 54-61.

71. Bohner, *Calcium orthoposhates in medicine: from ceramics to calcium phosphate cements.* Injury, 2000. **31**(4): p. S-D37-47.

72. Wang, C., et al., *Phenotypic expression of bone-related genes in osteoblasts grown on calcium phosphate ceramics with different pase compositions.* Biomaterials, 2004. **25**(13): p. 2507-2514.

73. Lee, I.-S., et al., *Various Ca/P ratios of thin calcium phosphate films.* Materials Science and Engineering C, 2002. **22**: p. 15-20.

74. Wolke, J.C.G., et al., *Study of the surface characteristics of magnetron-sputter calcium phosphate coatings.* Journal of Biomedical Materials Research, 1994. **28**: p. 1477-1484.

75. Yang, Z., et al., *Preparation and thermal stability analysis of hydroxyapatite derived from the precipitation process and microwave irradiation method.* Materials Letters, 2004. **58**(27-28): p. 3586-3590.

76. Tampieri, A., et al., *Characteristics of synthetic hydroxyapatites and attempts to improve their thermal stability.* Materials Chemistry and Physics, 2000. **64**(1): p. 54-61.

77. Cihlar, J., A. Buchal, and M. Trunec, *Kinetics of thermal decomposition if hydroxyapatite bioceramics.* Journal of Materials Science, 1999. **34**: p. 6121-6131.

78. Akao, M., H. Akao, and K. Kato, *Mechanical properties of sintered hydroxyapatite for prosthetic applications.* Journal of Materials Science, 1981. **16**: p. 809-812.

79. Jarcho, M., *Calcium phosphate ceramics as hard tissue prosthetics.* Clinical Orthopaedics, 1981. **157**: p. 259-278.

80. Teraoka, K., et al., *Mechanical properties of hydroxyapatite and OH-carbonated hydroyapatite single crystals.* Journal of Dental Research, 1998. **77**(7): p. 1560-1568.

81. Zeng, H. and W.R. Lacefield, *XPS, EDX and FTIR analysis of pulsed laser deposited calcium phosphate bioceramic coatings: the effects of various process parameters.* 2000. **21**(1): p. 23.

82. Ide-Ektessabi, A.M. and M. Hamdi, *Characterization of calcium phosphate bioceramic films using ion beam analysis techniques.* Surface and Coatings Technology, 2002. **153**(1): p. 10.

83. Ide-Ektessabi, A., T. Yamaguchi, and Y. Tanaka, *RBS and XPS analyses of the composite calcium phosphate coatings for biomedical applications.* 2005. **241**(1-4): p. 685.

84. Russell, S.W., et al., *The application of ion beam analysis to calcium phosphate-based biomaterials.* Journal of Biomedical Materials Research, 1996. **30**: p. 165-174.

85. Freddes, B., et al., *Determination of photoelectron attenuation lengths in calcium phosphate ceramic films using XPS and RBS.* Surface and Interface Analysis, 2003. **35**: p. 287-293.

86. Jansen, J.A., et al., *Application of magnetron sputtering for producing ceramic coatings on implant materials.* Clinical Oral Implants Research, 1993. **4**(1): p. 28-34.

87. Van Dijk, K., et al., *A complete characterization of Ca5(PO4)3OH sputter-deposited films by ion beam analysis: RBS and ERD.* Journal of Biomedical Materials Research, 1998. **42**(2): p. 266-271.

88. Russ, J.C., *Fundamentals of Energy Dispersive X-ray Analysis*. 1984: Butterworths.

89. Goodhew, P.J., J. Humphreys, and R. Beanland, *Electron Microscopy and Analysis*. 3rd Edition ed. 2001, London, New York. 169-212.

90. Potts, P.J., et al., eds. *Microprobe Techniques in the Earth Sciences*. 1st ed. The Mineralogical Society Series, ed. A.P. Jones. 1995, Chapman & Hall: London.

91. Ziegler, J., www.srim.org. 2002.

92. Smith, G.C., *Surface Analysis by Electron Spectrocopy: Measurement and Interpretation*. 1994, London and New York: Plenum Press. 156.

93. Shirley, D.A., *High-resolution X-ray photoemission spectrum of the valence bands of gold.* Physics Reviews B, 1972. **5**(12): p. 4709-4714.

94. Powell, C.J. and M.P. Seah, *Precision, accuracy, and the uncertainty in quantitative surface analyses by Auger-electron spectroscopy and X-ray photoelectron spectroscopy.* Journal of Vacuum Science and Technology, 1990. **A8**(2): p. 735-763.

95. Yoshitake, M. and K. Yoshihara, *Quantitative surface chemical analysis of Au--Cu alloys with XPS* Surface Interface Analysis, 1991. **17**(1010): p. 711-718.

96. *Annual Book of ASTM Standards (American Society for testing and Materials)* Vol. 3.06. 1997, West Conshohocken, PA.

97. Seah, M.P., et al., *Critical review of the current status of thickness measurements for ultrathin SiO_2 on Si Part V: Results of a CCQM pilot study.* Surface and Interface Analysis, 2004. **36**: p. 1269-1303.

98. Powell, C.J. and A. Jablonski, *Evaluation of calculated and measured electron inelastic mean free paths near solid surfaces.* Journal of Physical and Chemical Reference Data, 1999. **28**(1): p. 19-62.

99. Nielsen, F.H., *Ultratrace Minerals*. 1999, Williams & Wilkins: Baltimore, Maryland. p. 283-303.

100. Stewart, S.R., R.J. Emerick, and H. Kayongo-Male, *Silicon-zinc interactions and potential roles for dietary zinc and copper in minimizing silica urolithiasis in rats.* Journal of Animal Science, 1993. **71**: p. 946-954.

101. Carlisle, E.M., *Silicon*. In: Handbook of Nutritionally Essential Mineral Elements, ed. B.L. O'Dell and R.A. Sunde. 1997, New York: Marcel Dekker Inc. 603-608.

102. Sripanyakorn, S., et al., *Dietry silicon and bone health.* British Nutrition Foundation, 2005. **30**: p. 222-230.

103. Jugdaohsingh, R., et al., *Dietary silicon intake and absorption.* American Society for Clinical Nutrition, 2002. **75**: p. 887-893.

104. Yokoi H and E. S., *Effect of degree of polymerization of silicic acid on the gastrointestinal absorption of silicate in rats.* Chemical and Pharmaceutical Bulletin, 1979. **27**: p. 1733-1739.

105. Loeper, J., et al., *The antiatheromatous action of silicon.* Actherosclerosis, 1979. **33**: p. 397-408.

106. Lassus, A., *Colloidal silcic acid for oral and topical treatment of aged skin, fragile hair and brittle nails in females.* Journal of Internation Medical Research, 1993. **21**: p. 209-215.

107. Carlisle, E.M., *Silicon: A possible factor in bone calcification.* Science, 1970. **167**(916): p. 279-280.

108. Carlisle, E.M., *An essential element for the chick.* Science, 1972. **178**(4061): p. 619-621.

109. Schwarz, K. and D.B. Milne, *Growth-promoting effects of silicon in rats.* Nature, 1972. **239**: p. 333-334.

110. Kayongo-Male, H. and X. Jia, *Silicon bioavailability studies in young rapidly growing rats and turkeys fed semipurified diets: a comparative study.* Biology Trace Element Research, 1999. **67**: p. 173-186.

111. Calomme, M.R. and D.A.V. Berghe, *Supplementation of calves with stabilised orthosilicic acid effect on the Si, Ca, Mg and P concentration in serum and the collagen concentration in skin and cartilage.* Biology Trace Element Research, 1997(56): p. 153-165.

112. Seaborn, C. and F.H. Nielsen, *Silicon deprivation and arginine and cystine supplementation affect bone collagen and bone and plasma trace mineral concentrations in rats.* The Journal of Trace Elements in Experimental Medicine, 2002. **15**: p. 113-122.

113. Carlisle, E.M., *A relationship between silicon and calcium in bone formation.* Federation Proceedings, 1970. **29**: p. 265.

114. Hott, M., C.D. Pollak, and D. Modrowski, *Short-term effects of organic silicon on trabecular bone in mature ovariectomised rats.* Calcified Tissue International, 1993. **53**: p. 174-9.

115. Rico, H., J.L. Gallego-Lago, and E.R. Hernandez, *Effect of silicon supplement on osteopenia induced by ovariectomy in rats.* Calcified Tissue International, 2000. **66**: p. 53-55.

116. Schiano, A., F. Eisinger, and P. Detolle, *Silicium, tissu osseux et immunite.* Revue du Rhumatisme, 1979. **46**: p. 483-6.

117. Eisinger, J. and D. Clairet, *Effects of silicon, fluoride, etidronate and magnesium on bone mineral density: a retrospective study.* Magnesium Research, 1993. **6**: p. 247-249.

118. Jugdaosingh, R. and K.L. Tucker, *Dietary silicon intake is positively associated with bone mineral density in men and pre-menopausal women of the Framingham Offspring cohort.* Journal of Bone and Mineral Research, 2004. **19**: p. 297-307.

119. Reffitt, D.M., et al., *Orthosilicic acid stimulates collagen type 1 synthesis and osteoblastic differentiation in human osteoblast like cells in vitro.* Bone, 2003. **32**: p. 127-135.

120. Hench, L., R.J. Splinter, and W.C. Allen, *Bonding mechanisms at the interface of ceramic prothetic materials.* Journal of Biomedical Materials Research Symposium, 1971. **2**(1): p. 117-141.

121. Cao, W. and L.L. Hench, *Bioactive materials.* 1996. **22**(6): p. 493.

122. Xynos, I.D., et al., *Gene-expression profiling of human osteoblasts following treatment with the ionic products of Bioglass 45S5 dissolution.* Journal of Materials Research, 2001. **55**: p. 151-157.

123. Keeting, P.E., M.J. Oursler, and K.E. Wiegand, *Zeolite A increases proliferation, differentiation, and transforming growth factor beta production in normal adult human osteoblast-like cells in vitro.* Journal of Bone and Mineral Research, 1992. **7**: p. 1281-1289.

124. Bloyer, D.R., et al., *Fabrication and characterization of a bioactive glass coating on titanium implant alloys.* Acta Materialia, 1999. **47**(15-16): p. 4221-4224

125. Mardare, C.C., et al., *Deposition of bioactive glass-ceramic thin-films by RF magnetron sputtering.* Journal of the European Ceramic Society 2003. **23**(7): p. 1027-1030.

126. Gibson, I.R., S.M. Best, and W. Bonfield, *Chemical characterization of silicon-substituted hydroxyaptite.* Journal of Biomedical Materials Research, 1999. **44**(4): p. 422-428.

127. Ruys, A.J., *Silicon doped hydroxyapatite.* Journal of Australian Ceramic Society, 1993. **29**: p. 71-80.

128. Tanizawa, Y. and T. Suzuki, *X-ray photoelectron spectroscopy study of silicate-containing apatite.* Phosphorus Research Bulletin, 1994. **4**: p. 83-88.

129. Sugiyama, K., T. Suzuki, and T. Satoh, *Bactericidal activity of silicate-containing hydroxyapatite.* Journal of Antibacterial and Antifungal Agents, 1995. **23**: p. 67-71.

130. Boyer, L., J. Carpena, and J.L. Lacout, *Synthesis of phosphate-silicate apatites at atmospheric pressure.* Solid State Ionics, 1997. **95**: p. 121-129.

131. Leshkivich, K.S. and E.A. Monroe, *Solubility characteristics of synthetic silicate sulphate apatites.* Journal of Materials Science, 1993. **28**: p. 9-14.

132. Leventouri, T., C.E. Bunaciu, and V. Perdikatsis, *Neutron powder diffraction studies of silicon-substituted hydroxyapatite.* 2003. **24**(23): p. 4205.

133. Hing, K.A., et al., *Effect of silicon level on rate, quality and progression of bone healing within silicate-substituted porous hydroxyapatite scaffolds.* 2006. **27**(29): p. 5014.

134. Best, S.M., et al., *Silicon-substituted Apaties and Process for the Preparation Therof*. 1996.

135. Balas, F., J. Perez-Pariente, and M. Vallet-Regi, *In Vitro bioactivity of silicon-substituted hydroxyapatites.* Journal of Biomedical Materials Research, 2003. **66A**: p. 364-375.

136. Botelho, C.M., et al., *Structural analysis of Si-substituted hydroxyapatite:zeta potential and X-ray photoeletron spectroscopy.* Journal of Materials Science: Materials in Medicine, 2002. **13**(12): p. 1123-1127.

137. Zou, S., et al., *Crystal imperfection studies of pure and silicon substituted hydroxyapatite using Raman and XRD.* Journal of Materials Science: Materials in Medicine, 2005. **16**: p. 1143-1148.

138. Vallet-Regi, M. and D. Arcos, *Silicon substtituted hydroyapatites. A method to upgrade calcium phosphate based implants.* Journal Of Materials Chemistry, 2005. **15**: p. 1509-1516.

139. Porter, A.E., et al., *Effect of sintered silicate-substituted hydroxyapatite on remodelling processes at the bone-implant interface.* Biomaterials, 2004. **25**: p. 3303-3314.

140. Gibson, I.R., et al. *Enhanced in vitro cell activity and surface apatite layer formation on novel silicon-substituted hydroxyapatites*. in *Proceedings of the 12th International Symposium on Ceramics in Medicine*. 1999. Nara, Japan.

141. Gibson, I.R., et al., *Enhanced in vivo response to silicate-substituted hydroxyapaptite.* Key Engineering Materials, 2002. **218-220**: p. 203-206.

142. Patel, N., et al., *A comparative study on the in vivo behaviour of hydroxyapatite and silicon substituted hydroxyapatite granules.* Journal of Materials Science: Materials in Medicine, 2002. **13**: p. 1199-1206.

143. Patel, N., et al., *In vivo assessment of hydroxyapatite and silicate-substituted hydroxyapatite granules using an ovine defect model.* Journal of Materials Science: Materials in Medicine, 2005. **16**: p. 429-440.

144. Porter, A.E., S.M. Best, and W. Bonfield, *Ultrastructural comparison of hydroxyapatite and silicon-substituted hydroxyapatite for biomedical applications.* Journal of Biomedical Materials Research, 2003. **68A**(1): p. 133-141.

145. Wen, S. and Q. Liu, *High resolution electron microscopy investigations of interface and other structure defects in some ceramics.* Microscopy Research and Technique, 1998. **40**: p. 177-186.

146. Nelson, D.G.A., J.D. McLean, and J.V. Sanders, *A high-resolution electron microscope study of synthetic and biological carbonated apatites.* Journal of Ultrastructure Research 1983. **84**(1): p. 177-186.

147. Porter, A.E., et al., *Ultrastructural comparison of dissolution and apatite precipitation on hydroxyapatite and silicon-substituted hydroxyaptite in vitro and in vivo.* Journal of Biomedical Materials Research, 2004. **69A**(4): p. 670-679.

148. Porter, A.E., et al., *Comparison of in vivo dissolution processes in hydroxyapatite and silicon-substituted hydroxyapatite bioceramics.* 2003. **24**(25): p. 4609.

149. Porter, A.E., et al., *Bone bonding to hydroxyapatite and titanium surfaces on femoral stems retrieved from human subjects at autopsy.* Biomaterials, 2004. **25**(21): p. 5199-5208.

150. Ducheyne, P. and Q. Qiu, *Bioactive ceramics: the effect of surface reactivity on bone formation and bone cell function.* 1999. **20**(23-24): p. 2287.

151. Canham, L.T., et al., *The effects of DC electric currents on the in vitro calcification of bioactive silicon wafers.* Advanced Materials, 1996. **8**(10): p. 847-849.

152. Amarh-Bouali, S., et al., *Surface modifications of hydroxyapatite ceramics in aqueous media.* Biomaterials, 1994. **15**(4): p. 269–272.

153. Porter, A.E., *Nanoscale characterization of the interface between bone and hydroxyapatite implants and the effect of silicon on bone apposition.* Micron, 2006. **37**(8): p. 681-688.

154. Tanizawa, Y. and T. Suzuki, *Effects of silicate ions on the formation and transformation of calcium phosphates in neutral aqueous solutions.* Journnal of the Chemical Society, Faraday Transactions 1995. **91**: p. 3499 - 3503.

155. Webb, J.C.J. and R.F. Spencer, *The role of polymethylmethacrylate bone cement in modern orthopaedic surgery.* Journal of Bone and Joint Surgery, 2007. **89-B**: p. 851-857.

156. Hench, L., *Bioceramics: From concept to clinic.* Journal of American Ceramics Socitey, 1991. **74**(7): p. 1487-1510.

157. LeGeros, R.Z., *Biodegradation of Bioresorption of Calcium Phosphate Ceramics.* Clincal Materials, 1993. **14**: p. 65-88.

158. Klien, C.P.A.T., et al., *Long-term in vivo study of plasma-sprayed coatings on titanium alloys of tetracalcium phosphate, hydroxyapatite and α-tricalcium phosphate.* Biomaterials, 1994. **15**(2): p. 146-150.

159. Tonino, A., et al., *Hydroxyapatite-coated acetabular components.* Journal of Bone and Joint Surgery, 2001. **83A**(6).

160. Hofmann, A.A., K.N. Bachus, and R.D. Bloebaum, *Comparative study of human cancellous bone remodelling to titanium and hydroxyapatite-coated implants.* Journal of Arthroplasty, 1993. **8**(2): p. 157-166.

161. Anselme, K., et al., *In vitro growth of human adult bone-derived cells on hydroxyapatite plasma-sprayed coatings.* Journal of Biomedical Materials Research, 1997. **34**: p. 247-259.

162. Frayssinet, P., et al., *Comparative biological properties of HA plasma-sprayed coatings having different crystallinitites.* Journal of Materials Science: Materials in Medicine, 1994. **5**(1): p. 11-17.

163. ISO, *Implants for surgery: coating for hydroxyapatite ceramics*. 1996. p. 1–8.

164. Nelea, V., et al., *Growth of calcium phosphate thin films by in situ assisted ultraviolet pulsed laser deposition.* Physics and Chemistry of Advanced Laser Materials Processing, 2003. **208-209**: p. 638.

165. Nelea, V., et al., *Hydroxyapatite thin films grown by pulsed laser deposition and radio-frequency magnetron sputtering: comparative study.* Applied Surface Science, 2004. **228**(1-4): p. 346-356

166. Pramatarova, L., et al., *Ion beam and laser processing for hydroxyapatite formation.* Vacuum, 2004. **76**(2-3): p. 339-342.

167. Ramires, P.A., Wennerberg, A., Johansson, C. B., Consentino, F., Tundo, S., Milella, E., *Biological Behaviour of sol-gel coated dental implants.* Journal of Materials Science: Materials in Medicine, 2003. **14**: p. 539-545.

168. Gan, L. and R. Pilliar, *Calcium phosphate sol-gel-derived thin films on porous-surfaced implants for enhanced osteoconductivity. Part I: Synthesis and characterization.* Biomaterials, 2004. **25**(22): p. 5303-5312.

169. Gan, L., et al., *Calcium phosphate sol-gel-derived thin films on porous-surfaced implants for enhanced osteoconductivity. Part II: Short-term in vivo studies.* Biomaterials, 2004. **25**(22): p. 5313-5321.

170. Kim, H.-W., H.-E. Kim, and J.C. Knowles, *Fluor-hydroxyapatite sol-gel coating on titanium substrate for hard tissue implants.* Biomaterials, 2004. **25**(17): p. 3351-3358.

171. Zhitomirsky, I., *Electrophoretic and electrolytic deposition of cermamic coatings on carbon fibers.* Journal of European Ceramic Socitey, 1998. **18**: p. 849-856.

172. Zhitomirsky, I., *Electrophoretic hydroxyapatite coatings and fibers.* Materials Letters, 2000. **42**(4): p. 262-271.

173. Wang, C., et al., *Thick hydroxyapatite coatings by electrophoretic deposition.* Materials Letters, 2002. **57**(1): p. 99-105.

174. Ducheyne, P., et al., *Calcium phosphate ceramic coatings on porous titanium: effect of structure and composition on electrophoretic deposition, vacuum sintering and in vitro dissolution.* Biomaterials, 1990. **11**(4): p. 244-254.

175. Park, J.-H., et al., *Bioactive calcium phosphate coating prepared on H2O2-treated titanium substrate by electrodeposition.* Surface and Coatings Technology, 2005. **195**(2-3): p. 252-257.

176. Allen, G.C., et al., *Surface and bulk study of calcium phosphate bioceramics obtained by Metal Organic Chemical Vapor Deposition.* Nuclear Instruments and Methods in Physics Research Section B: Beam Interactions with Materials and Atoms, 1996. **116**(1-4): p. 457-460.

177. Ong, J.L., et al., *X-Ray photoelectron spectroscopy charatacterization of ion-beam sputter-deposited calcium phosphate coatings.* Journal of American Ceramics Socitey, 1991. **74**(9): p. 2301-2304.

178. Ong, J.L. and L.C. Lucas, *Post-deposition heat treatments for ion beam sputter deposited calcium phosphate coatings.* 1994. **15**(5): p. 337.

179. Boyd, A., M. Akay, and B.J. Meenan, *Influence of target surface degredation on the properties of r.f. magnetron-sputtered calcium phosphate coatings.* Surface and Interface Analysis, 2003. **35**: p. 188-198.

180. Boyd, A.R., B.J. Meenan, and N.S. Leyland, *Surface characterisation of the evolving nature of radio frequency (RF) magnetron sputter deposited calcium phosphate thin films after exposure to physiological solution.* 2006. **200**(20-21): p. 6002.

181. Van Dijk, K., et al., *Study of the influence of oxygen on the composition of thin films obtained by r.f. sputtering from a Ca5(PO4)3OH target.* 1997. **304**(1-2): p. 191.

182. Van Dijk, K., et al., *Influence of Ar pressure on RF magnetron-sputtered $Ca_5(PO_4)_3OH$ layers.* Surface and Coatings Technology, 1995. **76-77**(Part 1): p. 206-210.

183. Van Dijk, K., et al., *Influence of discharge power level on the properties of hydroxyapatite films deposited on Ti6A14V with RF magnetron sputtering.* Journal of Biomedical Materials Research, 1995. **29**(2): p. 269-276.

184. Van Dijk, K., et al., *Influence of annealing temperature on RF magnetron sputtered calcium phosphate coatings.* Biomaterials, 1996. **17**: p. 405-410.

185. Yang, Y., K.-H. Kim, and J.L. Ong, *A review on calcium phosphate coatings produced using a sputtering process--an alternative to plasma spraying.* Biomaterials, 2005. **26**(3): p. 327-337.

186. Grove, W.R., *On the electro-chemical polarity of gases.* Philosophical Transactions of The Royal Society of London, 1852. **142**: p. 87–101.

187. Rohde, S.L., *Sputter Deposition*, in *ASM Handbook*. 1994: Materials Park, Ohio. p. 573-581.

188. Stuart, R.V., *Vaccum Technology, Thin Films, and Sputtering*. 1983, London: Academic Press. 151.

189. Chapman, B., *Glow Discharge Processes*. 1980: John Wiley & Sons, Inc 406.

190. Wasa, et al., eds. *Thin Film Materials Technology - Sputtering of Compound Materials*. 2004, William Andrew Publishing/Noyes.

191. Ohring, M., *Materials Science of Thin Films*. 2nd ed. 2002, San Diego: Academic Press. 794.

192. Behrisch, R., ed. *Sputtering by Particle Bombardment I*. Physical Sputtering of Single-Element Solids. Vol. 47. 1981, Springer-Verlag: Berlin. 284.

193. Ellmer, K., *Magnetron sputtering of transparent conductive zinc oxide: relation between the sputtering parameters and the electronic properties.* Journal of Physics D: Applied Physics, 2000. **33**: p. R17-R32.

194. Schneider, J.M., et al., *Recent developments in plasma assisted physical vapour deposition.* Journal of Physics D: Applied Physics, 2000. **33**: p. R173–R186.

195. Lo, W.J. and D.M. Grant, *Hydroxyapatite thin films deposited onto uncoated and (Ti,Al,V)N-coated Ti alloys.* Journal of Biomedical Materials Research, 1999. **46**: p. 408-417.

196. Sato, M., et al., *Increased osteoblast functions on undoped and yttrium-doped nanocrystalline hydroxyapatite coatings on titanium.* 2006. **27**(11): p. 2358.

197. Ding, S.-J., C.-P. Ju, and J.-H.C. Lin, *Characterization of hydroxyapatite and titanium coatings sputtered on Ti-6Al-4V substrate.* Journal of Biomedical Materials Research, 1999. **44**(3): p. 266-279.

198. Wan, Y.Z., et al., *Effect of Mg ion implantation on calcium phosphate formation on titanium.* 2006. **201**(6): p. 2904.

199. Thian, E.S., et al., *A new way of incorporating silicon in hydroxyapatite (Si-HA) as thin films.* Journal of Materials Science: Materials in Medicine, 2005. **16**(5): p. 411.

200. Yamaguchi, T., Y. Tanaka, and A. Ide-Ektessabi, *Fabrication of hydroxyapatite thin films for biomedical applications using RF magnetron sputtering.* Ion Beam Analysis - Proceedings of the Seventeenth International Conference on Ion Beam Analysis, 2006. **249**(1-2): p. 723.

201. Jiang, M. and Z. Ning, *Influence of deposition pressure on the structure and properties of fluorinated diamond-like carbon films prepared by RF reactive magnetron sputtering.* Surface Coatings and Technology, 2006. **20**(12-13) p. 3682-3686.

202. Hulshoff, J.E.G., et al., *Interfacial phenomena: An in vitro study of the effect of calcium phosphate (Ca-P) ceramic on bone formation.* Journal of Biomedical Materials Research, 1998. **40**: p. 464-474.

203. Yang, Y., et al., *Effect of post-deposition heating temperature and the presence of water vapor during heat treatment on crystallinity of calcium phosphate coatings.* 2003. **24**(28): p. 5131.

204. Yoshinari, M., et al., *Influence of rapid heating with infrared radiation on RF magnetron-sputtered calcium phosphate coatings.* Journal of Biomedical Materials Research, 1997. **37**: p. 60-67.

205. Nelea, V., et al., *Microstructure and mechanical properties of hydroxyapatite thin films grown by RF magnetron sputtering.* 2003. **173**(2-3): p. 315.

206. Wolke, J.G.C., et al., *Stabilty of radiofrequency magnetron sputtered calcium phosphate coatings under cyclic loaded conditions.* Biomaterials, 1997. **18**: p. 483-488.

207. Ozeki, K., et al., *Crystal chemistry of hydroxyapatite deposited on titanium by sputtering technique* Biomedial Materials and Engineering, 2000. **10**(3-4): p. 221-227.

208. Freddes, B., J.C.G. Wolke, and J.A. Jansen, *Radio frequency magnetron sputtering deposition of calcium phosphate coatings: the effect of resputtering on the coating composition.* Journal of Applied Physics, 2003. **93**(12): p. 9503-9507.

209. Feddes, B., et al., *Bulk composition of RF magnetron sputter deposited calcium phosphate coatings on different substrates (polyethylene, polyfluoroethylene, silicon).* Surface and Coatings Technology, 2004. **185**: p. 346-355.

210. Hulshoff, J.E.G., et al., *Biological evaluation of the effect of magnetron sputtered Ca/P coatings on osteoblast-like cells in vitro.* Journal of Biomedical Materials Research, 1995. **29**: p. 967-975.

211. Lo, W.J., et al., *Physical, chemical, and biological characterization of pulsed laser deposited and plasma sputtered hydroxyapatite thin films on titanium alloy.* Journal of Biomedical Materials Research, 2000. **50**: p. 536-545.

212. ter Brugge, P.J. and J.A. Jansen, *Intial interaction of rat marrow cells with non-coated and calcium phosphate coated titanium substrates.* Biomaterials, 2002. **23**: p. 3269-3277.

213. Vercaigne, S., et al., *A mechanical evaluation of TiO_2-gritblasted and Ca-P magnetron sputter coated implants placed into the trabecular bone of the goat: part 1.* Clinical Oral Implants Research, 2000. **11**(4): p. 305-313.

214. Vercaigne, S., et al., *A mechanical evaluation of TiO_2-gritblasted and Ca-P magnetron sputter coated implants placed into the trabecular bone of the goat: part 2.* Clinical Oral Implants Research, 2000. **11**(4): p. 314-324.

215. Hulshoff, J.E.G., et al., *Mechanical and histologic evaluation of Ca-P plasma-spray and magnetron sputter-coated implants in trabecular bone of the goat.* Journal of Biomedical Materials Research, 1997. **36**(1): p. 75-83.

216. Hulshoff, J.E.G., et al., *Evaluation of plasma-spray and magnetron-sputter Ca-P-coated implants: An in vivo experiment using rabbits.* Journal of Biomedical Materials Research, 1996. **31**(3): p. 329-337.

217. Porter, A.E., et al., *Production of thin film silicon-doped hydroxyapatite via sputter deposition.* Journal of Materials Science, 2004. **39**: p. 1895-1898.

218. Thian, E.S., et al., *Fabrication of hydroxyapatite ceramics via a modified slip casting route.* Key Engineering Materials, 2004. **254-256**: p. 111-114.

219. Thian, E.S., et al., *Silicon-substituted hydroxyapatite: The next generation of bioactive coatings.* 2007. **27**(2): p. 251-256.

220. Thian, E.S., et al., *The response of osteoblasts to nanocrystalline silicon-substituted hydroxyapatite thin films.* Biomaterials, 2006. **27**(13): p. 2692.

221. Thian, E.S., et al., *Surface wettability enhances osteoblast adhesion on silicon-substituted hydroxyapatite thin films.* Key Engineering Materials, 2007. **330-332**: p. 877-880.

222. Thian, E.S., et al., *Novel Silicon-Doped Hydroxyapatite (Si-HA) for Biomedical Coatings: An in vitro study using acellular simulated body fluid.* Journal of B Part B: Applied Biomaterials, 2006. **76B**: p. 326-333.

223. Thian, E.S., et al., *Magnetron co-sputtered silicon-containing hydroxyapatite thin films--an in vitro study.* Biomaterials, 2005. **26**(16): p. 2947-2956.

224. Thian, E.S., et al., *Silicon-substituted hydroxyapatite thin film: Effectof annealing temperature on coating stability and bioactivity.* Journal of Biomedical Materials Research, 2006. **78A**: p. 121-128.

225. Schwarz, M.W., Federation Proceedings, 1974. **33**: p. 1748W.

226. Botterill, N.W., *Deposition and Characterisation of thin film nickel-titanium shape memory alloys for microactuation*, in *M3*. 2002, University of Nottingham: Nottingham. p. 207.

227. Hammond, C., *The basics of crystallography and diffraction*. 2 ed. 2001, New York: Oxford University Press. 336.

228. Friel, J.J. and N.C. Barbi, *X-Ray Microanalysis and Computer-aided Imaging*. 1991, Princeton: PGT. 89.

229. Woodruff, D.P. and T.A. Delchar, *Mordern Techniques of Surface Science*, E.A. Davis, I.M. Ward, and D.R. Clarke, Editors. 1994, Cambridge University Press Cambridge. p. 586.

230. Briggs, D. and J.T. Grant, eds. *Surface Analysis by Auger and X-ray Photoelectron Spectroscopy*. 2003, IM Publications & SurfaceSpectra: Chichester.

231. Chusuei, C.C., et al., *Calcium phosphate phase identification using XPS abd time-of-flight SIMS.* Analytical Chemistry, 1999. **71**: p. 149-153.

232. Chu, W.-K., J.M. Mayer, and M.-A. Nicolet, *Backscattering Spectrometry* 1978, New York: Academic Press.

233. Jeynes, C., et al., *Improved ion beam analysis facilities at the University of Surrey.* Ion Beam Analysis, 1998. **136-138**: p. 1229.

234. Boudreault, G., et al., *Accurate RBS measurement of ion implant doses in silicon.* Surface and Interface Analysis, 2002. **33**: p. 478-486.

235. Edwards, H.K., et al., *Site-specific, cross sectional imaging of biomaterials and the cell/biomaterial interface using focused ion beam/scanning electron microscopy.* Physics Conference Series, 2007. **27**: p. in press.

236. Beake, B.D., G.J. Leggett, and M.R. Alexander, *Characteriation of the mechanical properties of plasma-polymerised coatings by nanoindentation and nanotribology.* Journal of Materials Science, 2002. **37**(22): p. 4919-4927.

237. Beake, B.D., M.J.I. Garcia, and J.F. Smith, *Micro-impact testing: a new technique for investigating fracture toughness.* Thin Solid Films, 2001. **398-399**: p. 438-443.

238. Woodruff, M.A., *Proteomics Techniques for the Intergration into the Biomaterials Field: to study Cell/Surface Interactions*, in *School of Mechanical Materials and Manufacturing Engineering*. 2005, The University of Nottingham: Nottingham. p. 250.

239. Al-Nasiry, S., et al., *The use of Alamar Blue assay for quantitative analysis of viability, migration and invasion of choriocarcinoma cells.* Human Reproduction, 2007. **22**(5): p. 1304–1309.

240. Wagner, C.D., et al., *NIST X-Ray Photoelectron Spectroscopy Database* 2000.

241. Steverson, P. *Plasma Biotal Website*. 2007 [cited 2007 21/10/07]; Available from: http://www.plasma-biotal.com/.

242. Brown, P.W., Constantz, B., ed. *Hydroxyapatite and Related Materials*. Thermal Stability of Synthetic Hydroxyapatite, ed. Y.A. Fang, D. K., Roy, D. M. 1994, CRC Press. 269-282.

243. Tong, W., et al., *Preferred orientation of plasma sprayed hydroxyapatite coatings* Journal of Materials Science, 1995. **31**(14).

244. Clark, S.M. and J.I. Ball, *Orientation of appatite crystals in bone.* Nature, 1954. **174**: p. 399-400.

245. Cooke, K.E., et al., *The industrial application of pulsed DC bias power supplies in closed field unbalanced magnetron sputter ion plating.* Surface and Coatings Technology, 2004. **177-178**: p. 789-794.

246. *www.timet.com*. 2005 [cited 2008 14/01/08].

247. Van Raemdonck, W., P. Ducheyne, and P. De Meester, *Metal and Ceramic Biomaterials*. 1984: CRC Press. 143-146.

248. Okada, K., Y. Kameshima, and A. Yasumori, *Chemical shifts of silicon x-ray photoelectron spectra by polymerization structures of silicates.* Journal of American Ceramics Socitey, 1998. **81**(7): p. 1970-72.

249. Steveson, M., P.A. Arora, and R.S.C. Smart, *XPS studies of low temperature plasma-produced graded oxide-silicate-silica layers on titanium.* Surface and Interface Analysis, 1998. **26**: p. 1027-1034.

250. Arcos, D., et al., *Crystallochemistry, textural properties, and in vitro biocompatability of diffferent silicon-doped calcium phoshates.* Journal of Biomedical Materials Research, 2006. **78A**: p. 762-771.

251. Zhao, Y., et al., *In situ annealling of superconducting MgB_2 films prepared by pulsed laser deposition.* Superconducting Science and Technology, 2003. **16**: p. 1487-1492.

252. Abe, S., et al., *Auger electron spectroscopy of super-doped Si:Mn thin films.* Applied Surface Science, 1999. **142**(1-4): p. 537-542.

253. Kulatov, E., et al., *Electronic struture, magnetic ordering and optical properties of GaN and GaAs doped with Mn.* Physical Review B, 2002. **66**.

254. Ma, E., *Alloys created between immiscible elements.* Progress in Materials Science, 2005. **50**: p. 413-509.

255. Long, J.D., et al., *Structure, bonding state and in-vitro study of Ca-P-Ti film deposited on Ti6Al4V by RF magnetron sputtering.* 2002. **20**(1-2): p. 175.

256. Boyd, A.R., et al., *Characterisation of calcium phosphate/titanium dioxide hybrid coatings.* Journal of Materials Science: Materials in Medicine, 2007. **in press**.

257. Ashby, M.F. and D.R.H. Jones, eds. *Engineering Materials 1: An Introduction to properties, applications and design*. 3rd ed. 2005: Amsterdam. 454.

258. Pan, Y. and M.E. Fleet, *Substitution Mechanisms and Controlling Factors, in Reviews in Mineralogy and Geochemistry - Phosphates - Geochemical, Geobiological and Materials Importance*, J.R. M.J. Kohn, and J.M. Hughes, Editor. 2002: Washington DC. p. 742.

259. Lide, D.R., ed. *CRC Handbook of Chemisrty and Physiscs*. 87 ed. 2007.

260. Li, J., et al., *Study on Interface Reaction and Its Control of Titanium Fiber-Hydroxyapatite Composites.* Key Engineering Materials, 2007. **330-332**: p. 507-510.

261. Okada, K., et al., *Effect of silica additive on the anatase-to-rutile phase transition.* Journal of American Ceramics Socitey, 2001. **84**(7): p. 1591-96.

262. Lutjering, G., ed. *Titanium*. 2003, Springe: Berlin. 379.

263. Vandiver, J., et al., *Silicon addition to hydroxyapatite increases nanoscale electrostatic, van der Waals and adhesive interactions.* Journal of Biomedical Materials Research, 2006. **78A**: p. 352-363.

264. Takeda, S. and M. Fukawa, *Role of surface OH groups in the surface chemical properties of metal oxide films.* Materials Science and Engineering B, 2005. **119**(3): p. 265-267.

265. Chen, W., et al., *In vitro anti-bacterial and biological properties of magnetron co-sputtered silver-containing hydroxyapatite coating.* Biomaterials, 2006. **27**(2): p. 5512-5517.

266. Saha, R. and W.D. Nix, *Effects of the substrate on the determination of thin film mechanical properties by nanoindentation.* 2002. **50**(1): p. 23.

267. Nieh, T.G., A.F. Jankowski, and J. Koike, *Processing and characterisation of hydroxyapatite coatings on the titanium produced by magnetron sputtering* Journal of Materials Research, 2001. **16**(11): p. 3238-3245.

268. Liu, Y., et al., *Biomimetic coprecipitation of calcium phpsphate and bovine serum albumin on titanium alloy.* Journal of Biomedical Materials Research, 2001. **57**: p. 327-335.

269. Rho, J.-Y., et al., *Elastic properties of microstructural components of human bone tissue as measured by nanoindentation.* Journal of Biomedical Materials Research, 1999. **45**(1): p. 48 - 54.

270. Burling, L., *Novel Phosphate Glasses for Bone Regeneration Applications*, in *M3*. 2005, The University of Nottingham: Nottingham. p. 209.

271. El-Amin, S.F., et al., *Integrin expression by human osteoblasts cultured on degradable polymeric materials applicable for tissue engineered bone.* Journal of Orthopaedic Research, 2002. **20**.

272. Bovan, B.D., et al., *Role of material surfaces in regulating bone and cartilage cell response.* Biomoterials, 1996. **17**: p. 137-146.

273. Rezania, A., et al., *The detachment strength and morphology of bone cells contacting materials modified with a peptide sequence found within bone sialoprotein.* Journal of Biomedical Materials Research, 1996.

274. Scotchford, C., *Personal Communication*. 2008.

275. Knabe, C., et al., *In vitro investigation of titanium and hydroxyapatite dental implant surfaces using a rat bone marrow stromal cell culture system.* Biomaterials, 2002. **23**(15): p. 3235-3245.

276. Stupack, D.G. and D.A. Cheresh, *Get a ligand, get a life: integrins, signalling and cell survival.* Journal of Cell Science, 2002. **115**: p. 3729-3738.

277. Thian, E.S., et al., *Silicon-substituted hydroxyapatite (SiHA): A novel calcium phosphate coating for biomedical applications.* Journal of Materials Science, 2006. **41**: p. 709-717.

278. Scotchford, C.A., et al., *Chemically patterned, metal-oxide-based surfaces produced by photolithographic techniques for studying protein- and cell-interactions. II: Protein adsorption and early cell interactions.* 2003. **24**(7): p. 1147.

279. Dalby, M.J., D. Pasqui, and S. Affrossman, *Cell response to nano-islands produced by polymer demixing: a breif review.* IEE Proceedings - Nanobiotechnology, 2004. **151**(2): p. 53-61.

280. Curtis, A. and C. Wilkinson, *Nanotechniques and approaches in biotechnology.* Trends in Biotechnology, 2001. **19**(3): p. 97-101.

281. Kahn, S.P., G.G. Auner, and G.M. Newaz, *Influence of nanoscale surface roughness on neural cell attachement on silicon.* Nanomedicine: Nanotechnology, Biology and Medicine, 2005. **1**: p. 125-129.

282. Ward, B.C. and T.J. Webster, *The effect of nanotopography on calcium and phosphorus deposition on metallic materials in vitro.* Biomaterials, 2006. **27**: p. 3064-3074.

283. Dalby, M.J., et al., *Rapid fibroblast adhesion to 27 nm high polymer demixing nano-topography.* Biomaterials, 2004. **25**: p. 77-83.

284. Dalby, M.J., et al., *Fibroblast reaction to island topography:changes in cytoskeleton and morphology with time.* Biomaterials, 2003. **24**: p. 927-935.

285. Ong, J.L., C.W. Prince, and L.C. Lucas, *Cellular reposonse to well-characterized calcium phosphate coatings and titanium surfaces in vitro.* Journal of Biomedical Materials Research, 1995. **29**: p. 165-172.

286. García, F., et al., *Effect of heat treatment on pulsed laser deposited amorphous calcium phosphate coatings.* Journal of Biomedical Materials Research, 1998. **43**(1): p. 67-76.